FINITE ELEMENT ANALYSIS

OF INDUCTION MOTORS

By

Michael Colin Begg B.Sc.(Eng)

Thesis submitted for
The Degree of Doctor of Philosophy
in the Faculty of Engineering
University of London

Imperial College

London

October 1985

ABSTRACT

This thesis is concerned with the analysis of induction machines using a combined fields and circuits approach.

Chapter Two reviews the work already carried out by others and lays the foundations for the following chapters.

Chapter Three develops an iterative procedure for determining the currents that will flow in the windings of an induction motor if the reluctance of the magnetic circuit and the applied terminal voltages are known. The reluctance of the circuit is determined by a non-linear analysis of the field in the machine using finite elements.

Chapter Four presents the results of applying the techniques of Chapter Three to the analysis of two shaded-pole motors. The theoretical results are compared with experimental data obtained in the laboratory.

Chapter Five derives a technique for the calculation of the bar resistance and leakage reactance of cage rotors with closed slots. The method is then applied to the analysis of several types of closed slot.

Chapter Six outlines a method for the calculation of the resistance of induction motor endrings. The method is compared with other theoretical models of the problem and with experimental results.

ACKNOWLEDGEMENTS

The author would like to extend his thanks to Dr S Williamson of Imperial College for his help and guidance throughout the duration of this project.

I would also like to thank all my fellow postgraduates, especially Dr P J Leonard, for the constructive criticisms and discussions that they provided me with during my stay at Imperial College.

Finally, I wish to thank the Science and Engineering Research Council for my financial support.

LIST OF CONTENTS

		Page
Abstract		1
List of Symbols		6
Acknowledgements		2
Introduction		7
CHAPTER TWO	REVIEW OF THE WORK ALREADY CARRIED OUT BY WILLIAMSON AND RALPH	11
2.1	Introduction	11
2.2	Initial Modelling Considerations	12
2.3	Outline of Methodology Employed by Williamson and Ralph	17
2.4	The Field Solution	20
2.5	Matrix Handling	25
2.6	Storage Considerations	27
2.7	The Reverse Cuthill McKee Algorithm	28
CHAPTER THREE	IMPROVEMENTS TO THE WILLIAMSON AND RALPH ANALYSIS	34
3.1	Replacement of the Nag-Algorithm	34
3.1.1	Introduction	34
3.1.2	The impedance method	35
3.1.3	Stator-stator coupling impedances	37
3.1.4	Stator-rotor coupling impedances	39
3.1.5	Rotor-stator coupling	50
3.1.6	Rotor-rotor coupling	52
3.1.7	Inclusion of iron losses	53
3.1.8	Interbar currents	56
3.2	Alternative Renumbering Schemes	58
3.2.1	The Gibbs Poole and Stockmeyer Algorithm	58
3.3	Alternative Solution Technique	67
3.4	Conclusions to Chapter Three	69
CHAPTER FOUR	RESULTS	70
4.1	Comparison with Previous Work	70
4.2	Analysis of a Shaded Pole Motor	77
4.3	The Test Motors	81
4.4	Experimental Apparatus and Technique	81
4.4.1	Friction and windage	83
4.4.2	Inter-bar resistance	85
4.4.3	Rotor endring resistance	85

		Page
4.5	Comparison of Computed and Experimental Results	86
4.5.1	The full bar model	6
4.5.2	The half bar model	94
4.5.3	Modelling the motor with the wedges in place	94
4.5.4	Comparison of full and half bar results	110
4.6	Conclusions to Chapter 4 and Suggestions for Further work	110
CHAPTER FIVE	CALCULATION OF THE BAR RESISTANCE AND LEAKAGE REACTANCE OF CAGE ROTORS WITH CLOSED SLOTS	115
5.1	Introduction	115
5.2	Theoretical Development	117
5.2.1	General description and consideration of boundary conditions	117
5.3	The Governing Field Equations	121
5.4	The Finite Element Solution	122
5.5	Calculation of the Rotor Leakage Impedance per Bar, $\bar{Z}_b$	124
5.5.1	Bar resistance, R_b	124
5.5.2	Bar leakage inductance	126
5.6	Examples	128
5.6.1	Round rotor bars	128
5.6.2	Parallel-sided bars with rounded ends	139
5.6.3	Elliptical bars	147
5.7	Conclusions	158
CHAPTER SIX	THE CALCULATION OF THE RESISTANCE OF INDUCTION MOTOR ENDRINGS	159
6.1	Introduction	159
6.2	Method of Analysis	163
6.2.1	Model and assumptions	163
6.3	Calculation of Endring Resistance	165
6.4	Experimental Verification	167
6.4.1		167
6.4.2	Comparison between experiment and calculation	171
6.5	Practical Example	176
6.6	Conclusions	181

		Page
CHAPTER SEVEN	REFERENCES	189
CHAPTER EIGHT	APPENDIX	193
8.1	Finite Elements	193
8.2	Modelling of Magnetic Slot Wedges	196
8.3	Incorporation of Complex Periodicity	198
8.4	Derivation of Basic Endring Formulae	201
8.5	Uniqueness of Solution	203
8.6	Power Dissipation	206

List of Symbols

U	Induced e.m.f.
E	Electric field strength or error
A	Magnetic vector potential
B	Magnetic flux density
J	Current density
P	Electrical power
v	velocity
m.m.f.	Magneto-motive-force
ν	Reluctivity
μ_o	Permeability of free space
ρ	Electrical resistivity or density
σ	Electrical conductivity
j	$\sqrt{-1}$
ω	Angular frequency
P	Number of poles
N_{turns}	Number of turns
N_b	Number of bars
N_h	Number of harmonics
W	Length of rotor
ν_k	Harmonic number
θ	Angular displacement
K_{sk}^k	The harmonic skew factor
L	Inductance
X	Inductance reactance
R	Resistance
Z	Impedance
T	Torque
δ	Error measure - either scalar or vector
$\lvert\ \rvert$	Modulus or number of elements contained in
Env	Envelope
b	Bandwidth
Δ	The area of a triangular element
Ω	Area
S	Area or stiffness matrix
$\{\ \}$	Denotes a column vector
$[\ ]$	Denotes a matrix

Complex Quantities

-	Denotes a complex quantity e.g. $\bar{A}$
*	Complex conjugate
R_e	The real part of a complex number
I_m	The imaginary part of a complex number
$\hat{}$	The peak value of a sinusoidal quantity

In general, vector quantities are denoted by capital letters.

INTRODUCTION

In the majority of industrial applications today, the induction motor remains the principal source of rotational horse-power. These machines are manufactured on a large scale ranging from a few watts to many kilowatts. Induction motors are built in many diverse forms to suit the wide range of applications they are required for.

Small single phase induction machines have enjoyed widespread use, as fractional horsepower drives, since their inception at the end of the nineteenth century. The reasons for this popularity are as follows. The machines require no electrical contact to be made with the rotor, which is inherently robust, since it is usually of the squirrel cage type. Construction of small single phase motors is simple and cheap, because the stator laminations can be stamped out and riveted together to form a stack and the rotor can be formed by a pressure dye casting process. The stator windings on these motors are usually simple and the supply to the stator is single phase.

A single phase induction motor produces no starting torque unless external components are added to it. These components may take on a variety of forms. One way is to use a capacitor connected in series with an auxiliary winding, which is disconnected from the circuit once the machine has started by means of a centrifugal switch. Another method which is frequently employed is to wrap one more short circuited copper strip around a portion of the machine's pole tips. This method gives, what is called, a shaded pole motor. The main advantage of shaded pole construction is that there is no need to provide other costly, and potentially troublesome, electrical components to make the machine self starting.

The shaded-pole motor, though attractive, does have some drawbacks. The shading rings, because they are always in the circuit, subtract from the overall efficiency of the motor, since they dissipate power in the form of joule losses. Another disadvantage is that the m.m.f. produced by the salient pole stator is intrinsically high in harmonic content. To reduce the effect of these harmonics the rotors of shaded pole motors are heavily skewed, with skew angles of up to sixty degrees electrical not being uncommon. One of the results of skewing the rotor bars, is to cause an axial redistribution of flux; this produces differential saturation. The elongated pole tips in shaded-pole motors are also known to saturate. Combination of all these effects results in a motor that is not very efficient and runs at high slip, and is notoriously difficult to analyse.

Analysis of shaded-pole motors is difficult, for although their construction is simple, non-linearities make the classical forms of machine analysis invalid when applied to these motors. However many forms of linear analysis have been applied to shaded-pole motors. One of the first of these was carried out by Trickey [1], who uses a two axis model. Other linear approaches were tried by Eastham and Williamson [2],[3], who applied a harmonic technique to the problem. Whilst their method did not account for non-linearities, it was useful in determining and optimising certain parameters associated with the design of shaded-pole motors. Perret and Poloujadoff [4],[5] pointed out shortcomings in the existing treatments of the problem. They suggested that better agreement between theoretical prediction and reality could be achieved by more careful consideration of iron loss and saturation.

More recently further work on the subject has been carried out by Williamson and Ralph [6],[7]. Their approach takes into account some of the non-linear aspects of the problem and mixes classical machine theory with modern numerical analysis, the aim being to produce a useful design tool, which will predict accurately the performance characteristics of small single phase motors fed from constant voltage sources.

This dissertation will be split into two distinct parts. Part one is an extension of the work performed by Ralph and Williamson. It is concerned with improvements and refinements to the technique of analysis developed by Williamson and Ralph and is broken into four chapters.

Chapter two will contain a review of the work already carried out, and will attempt to point out the strengths and weaknesses of it, discussing what room there is for improvement. Chapter Three will take each of the modifications carried out, in turn, and quantify the consequential improvement. In Chapter Four the new approach is compared with experimental results from several test motors and with the previous strategy. All the examples in Chapter Four refer to shaded-pole motors since it is felt that these represent one of the most difficult type of induction motor to analyse. The final part of Chapter Four contains the conclusions reached from the preceding chapters and suggestions for further work.

Part Two of this thesis is concerned with a different, but related, aspect of machine analysis. The determination of machine parameters such as the self inductance and resistance of the rotor, are important if the performance of a given motor, be it three phase or single

phase, is to be predicted. Such parameters are required if predictions are to be made using conventional equivalent circuits or using a numerical analysis of the type described in Part One of this thesis.

Chapter Five presents a general method for calculating the leakage reactance and resistance of rotors. The rotor bars may be of any shape or size. The slot mouths can be open or closed. Non-linear effects are taken into account. Chapter Six introduces a technique for calculating the effective end-ring resistance of cage induction motors. This is useful since the computed value of resistance must be added to the slot resistance obtained in Chapter Five. The result can then be used as a lumped parameter when modelling an induction motor.

CHAPTER TWO

REVIEW OF THE WORK ALREADY CARRIED OUT BY WILLIAMSON AND RALPH

2.1 Introduction

The work described in this thesis is aimed towards developing the ideas already put forward by Williamson and Ralph. To appreciate why this is a worthwhile activity, it is first necessary to understand the underlying background.

Several different techniques are employed to make single phase induction motors self starting and reversible. In applications where reversibility is required often the costly but effective permanent split capacitor motor is used. This type of motor is relatively expensive, and it was thought that a bi-directional form of the cheap and robust shaded-pole motor would be a useful development.

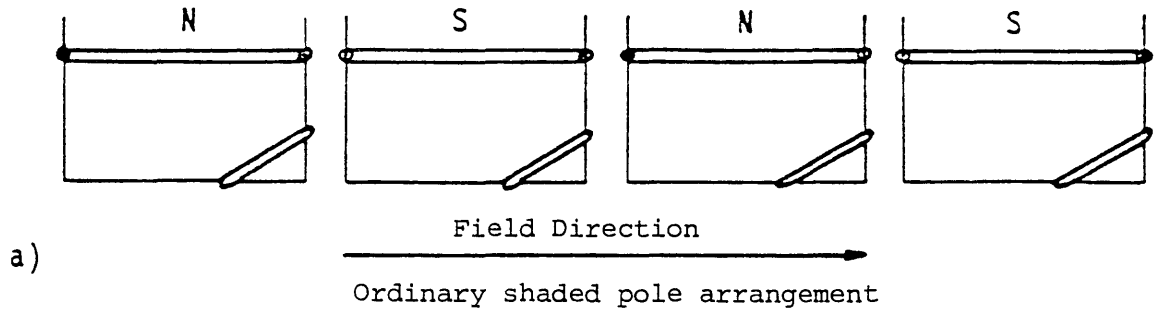
One way of making a shaded-pole motor reversible is to have two sets of wound coils placed on the pole tips and connected in series. The first set is so arranged that the motor starts in the clockwise sense. The second group gives anticlockwise rotation. Hence the direction of motion can be controlled by short circuiting the appropriate shading coils, whilst the other set is on open circuit and vice versa. However, this type of motor has not found favour mainly due to the manufacturing difficulties associated with placing windings in shading ring slots. A simpler and just as effective means of producing a reversing shaded-pole motor was introduced by

Williamson and Ostojic [8]. The new design utilised the concept of "effective ring shift". This way each stator pole is split into two parts termed the 'main pole' and the 'auxiliary pole'. Both portions of the pole carry the stator winding, see Figure 2.1, but only the auxiliary pole carries the shading ring. Bi-directionality is achieved by reversing the polarity of the stator winding around the auxiliary poles. A full discussion of the operating principles of this type of motor can be found in [8].

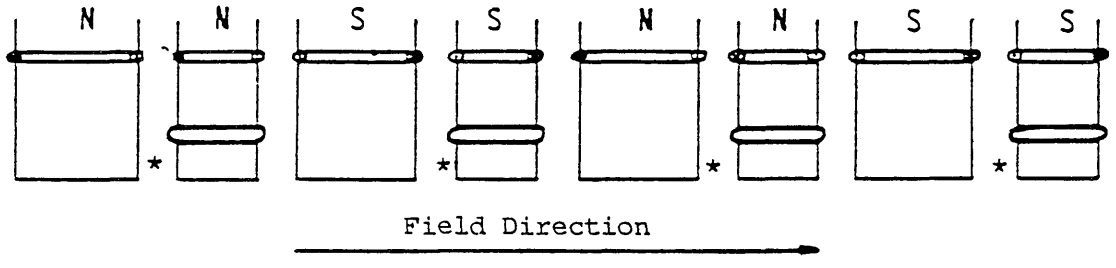
Having put forward a new design of motor, it can then be a fruitful exercise to apply the tools of analysis to the problem of development and improvement of the initial design. It is at this point that it was recognised that there was no existing analysis, which could be reliably applied to the task of predicting the characteristics of this motor. This, then, gave the incentive for the development of a technique of analysis specifically aimed at the analysis of shaded-pole motors. The initial work was thus directed towards modelling the ring shift motor. Later it was realised that the method could, with some improvements, be extended into a more general analysis package, which could be used to analyse induction motors in general.

2.2 Initial Modelling Considerations

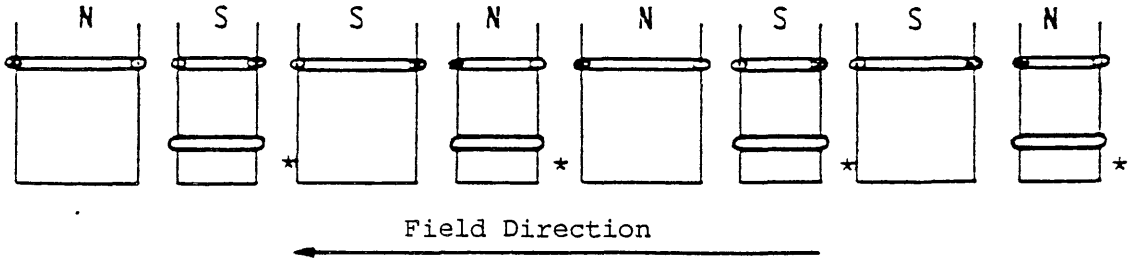
The successful design of induction motors usually relies upon the ingenuity of an experienced designer, who uses data obtained from previous configurations coupled with experience based design factors, which are applied where necessary, to develop a design. The ring-shift motor is of novel construction. There is no previous information on it. For this reason it was decided that a user



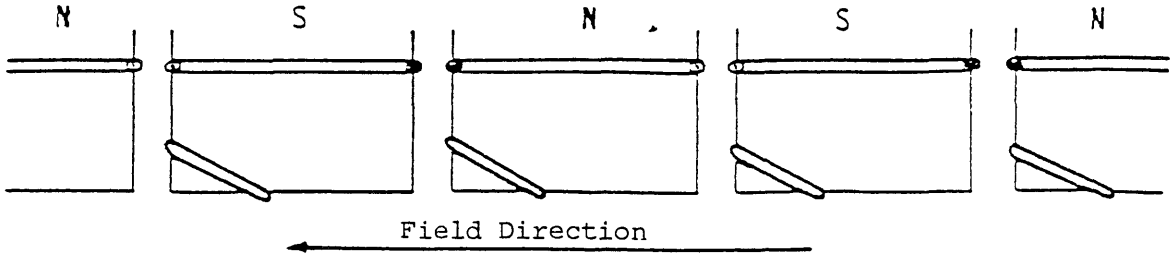
a) Ordinary shaded pole arrangement



b) Equivalent Ring Shift Configuration



c)



d)

Fig. 2.1 Schematic diagram of ring-shift motor operation

independent analysis package would be appropriate, since it would remove the need for many of the experience factors and ingenious assumptions. In their approach to the problem, Williamson and Ralph took advantage of developments in numerical methods, fusing them with the techniques of harmonic analysis and the classical equivalent circuit.

The equivalent circuit method is useful and powerful, when applied to electrical machines. It enables accurate predictions of a motor's performance to be made if the parameters in the circuit are accurately known. One particular strength of this approach lies in the fact that it allows the motor's performance to be calculated when a fixed voltage is applied across its terminals. Nearly all motors are excited from the mains supply, which approximates closely to an infinite bus. A voltage forced solution is therefore of great interest to the user and designer alike. Another advantage of the equivalent circuit method is that it allows three-dimensional effects, which are not readily calculated using field models, such as finite endring resistance, to be incorporated.

Use of the equivalent circuit is in itself not enough to model fully the system under consideration. In order to extract worthwhile information from an equivalent circuit it is necessary to insert the correct values of resistance and reactance. The values of reactance may be obtained from a model of the magnetic field in the machine. The resistances, on the other hand, are calculated, with the exception of the iron loss resistance which can be calculated in the manner shown in Chapter Three, from standard formulae. Having decided to use a field based model of the machine one is then confronted with several choices; these are as follows. Firstly,

should the technique used to solve the field be analytical or numerical? Secondly, is a three dimensional solution to the field necessary or can a smaller number of dimensions be used? Finally, must eddy currents be included in the solution or will a magnetostatic solution suffice?

The method developed by Williamson and Ralph employs a numerical technique to solve the field in the machine. The reasons for this are two fold. Firstly, an electrical machine has a very intricate geometry. This means that any solution of Poisson's equation within the domain of the machine is impossible unless some very gross assumptions are made. The second reason is that a non-linear solution of Poisson's equation is required. Analytical techniques will not cope with this. The finite element method was chosen to solve the magnetic field. There are several factors underlying this choice. Firstly, the finite element method satisfies the boundary conditions imposed on the problem easily. Secondly it is very versatile in accommodating complex geometries with changes in material properties from one subdomain to the next being easily incorporated. It is also a tried and tested technique. Many researchers such as Oden [9], Strang [10] and Demerdash [11] have spent much time in developing the method and proving that for linear problems use of finite elements will give a unique solution.

A two dimensional representation of the field was considered to be a good compromise between ease of application and accuracy. Any three dimensional approach carries with it several penalties. The first of these is that a three dimensional model will necessitate the use of more nodes for a given problem. The number of nodes used is related to the size of the final matrix to be solved. If the matrices to be

handled become very large, they will be, at present, uneconomical to solve. A second difficulty arises with three-dimensional methods, because the formulation of magnetics problems in three dimensions are still at a relatively early stage. Consequently, there are several alternative strategies competing with one another [12],[13],[14],[15] and [16] with no guidelines to say which is best. Furthermore if a three dimensional approach was used then it would be necessary to start considering anisotropic effects in the materials. Finally, because an induction motor is geometrically complex, meshing it would be difficult in three dimensions.

Having opted for a two dimensional model the final choice is then between an eddy current model or a magnetostatic model. Here it was thought that a magnetostatic model was more valid since the effects of endring resistance and rotor bar skew were to be considered. A two dimensional magnetostatic model leads naturally to a harmonic representation of the rotor and allows the influences of endring resistance and skew, which are dependent on pole number, to be accommodated.

The finite element solution of the field utilised first order triangular finite elements. These are developed in Appendix 8.1. Simplex elements were chosen mainly because of their computational simplicity, but also because of the difficulties connected with allowing the flux density, and therefore the permeability, to vary in a complex manner across an element. This variation must necessarily occur if higher order elements are used. Simplex triangles lead to a system of equations, which are easy to assemble with all the required integrations done analytically.

A useful measure of a small motors performance is its steady state behaviour when excited from a constant A.C. voltage source. The analysis carried out previously was accordingly directed towards determination of the steady state characteristics. This restriction leads to a resolution of the rotor currents, which are treated as uniform distributions over the conductors area, into space harmonic distributions. These have been shown to be, [17], important in determining the behaviour of shaded-pole motors. A harmonic approach allows the problems of finite endring impedance and rotor skew to be overcome. It also allows the relative motion of the rotor with respect to the stator, to be readily accounted for by use of a frequency transformation.

From the above discussion it can be seen that blending classical machine theory with a numerical solution of the governing field equations results in a neat and functional solution to the analysis problem. With a balance being struck between computational effort and accuracy of results.

2.3 Outline of Methodology Employed by Williamson and Ralph

Having given a brief insight into the types of method used, it is now necessary to show how these were put together to form a coherent algorithm for the analysis of single phase motors. The basic problem was to find a set of currents which were compatible with the impedances of the machine and the terminal voltage applied to it. This was achieved in the following manner. Firstly, an arbitrary value of current was assumed to flow in each winding of the machine. Having done this the field equations were solved, for this set of

currents, in a complex nonlinear sense, with the reluctivity being the non-linear variable. From the solution of the field equations, which were cast in terms of the magnetic vector potential, $\bar{A}$, the induced e.m.f.'s in the various windings can be calculated taking both the presence of skew and space harmonics into account. When the e.m.f.'s are known they can be used together with the currents to set up error functions of the form

$$e = |\bar{V} - \bar{E} - \bar{I}(R + jX)| \qquad (2.1)$$

A function such as (2.1) was written for each electrical circuit in the machine. For circuits that had no voltage applied to them, such as the shading ring, $\bar{V}$ was set to zero. These equations merely forced the sum of the applied voltages, e.m.f.'s and voltage drops to be zero round any circuit. When this condition was met for all the circuits in the machine, the error functions must all be reduced to zero simultaneously. For the non-linear method to proceed a new set of currentswas required at each step. These were obtained by finding the current that minimised the sum of squares of the error functions. This was accomplished by using Nag algorithm E04FAF [18], which is due to Peckham [19]. The procedure, outlined above, was then repeated until satisfactory convergence of the error functions was achieved. A flow chart of the process is given in Figure 2.2 and a more detailed account of the procedure can be found in [7].

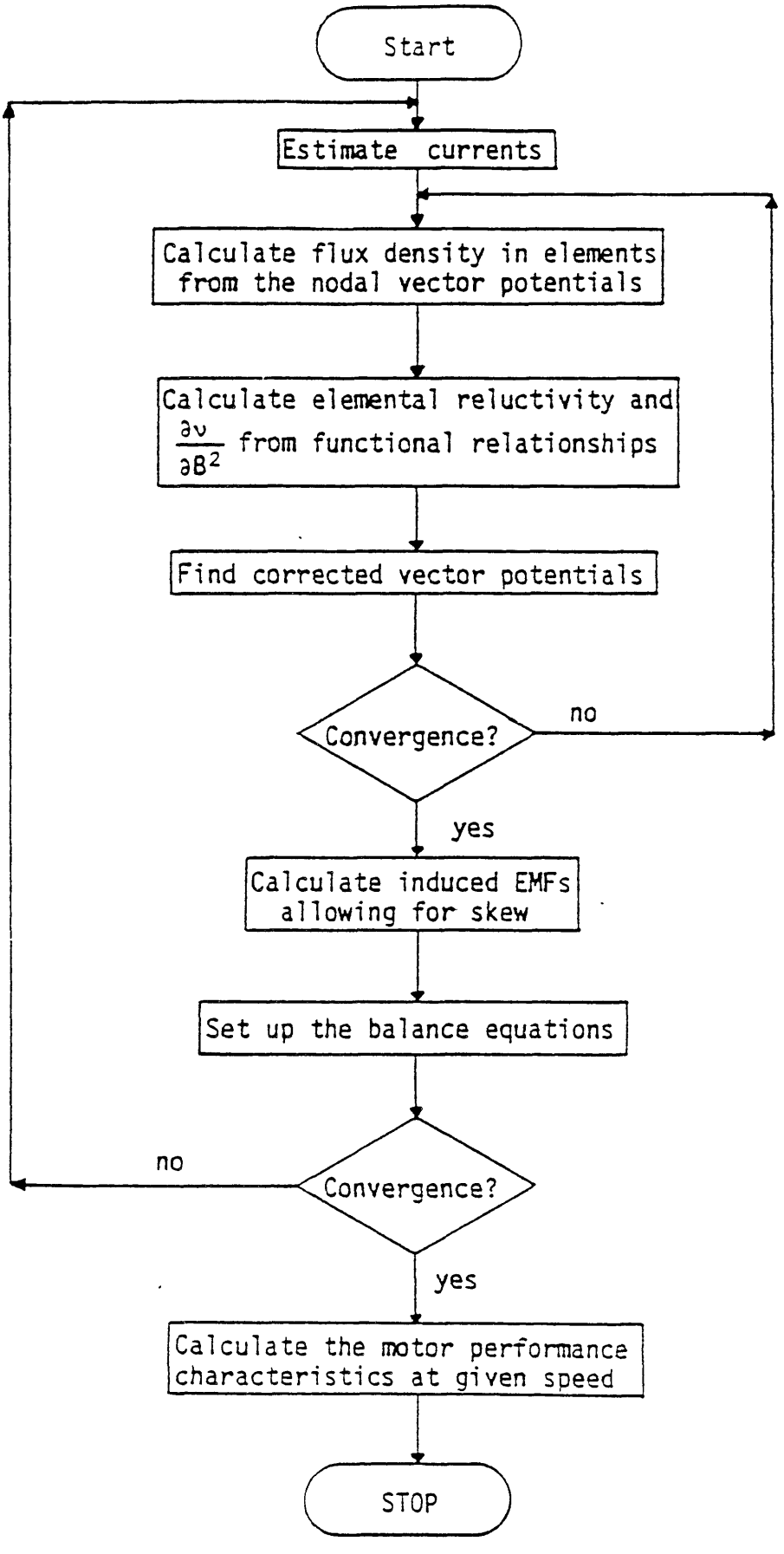


Fig. 2.2 Flow chart for processor

2.4 The Field Solution

The iterative scheme outlined in Section 2.3 requires, at an intermediate stage, a non-linear solution of the two dimensional Poisson equation. In terms of the complex magnetic vector potential this may be written as

$$\frac{\partial}{\partial x}\left(\nu \frac{\partial \bar{A}}{\partial x}\right) + \frac{\partial}{\partial y}\left(\nu \frac{\partial \bar{A}}{\partial y}\right) = -\bar{J} \tag{2.2}$$

$$A = A_z(x,y,t) = \mathcal{R}_e\{\sqrt{2}\ \bar{A}\ e^{j\omega t}\} \tag{2.3}$$

$$J = J_z(x,y,t) = \mathcal{R}_e\{\sqrt{2}\ \bar{J}\ e^{j\omega t}\} \tag{2.4}$$

$$\bar{A} = A_{\mathcal{R}e} + jA_{I_m} \tag{2.5}$$

$$\bar{J} = J_{\mathcal{R}e} + jJ_{Im} \tag{2.6}$$

$$\nu = \nu(B^2) \tag{2.7}$$

It was thus tacitly assumed that A and J have only z components and that they vary sinusoidally in time. This is permissible since a steady state analysis was being undertaken. The sinusoidal variation of A and J was accommodated by use of the complex variables $\bar{A}$ and $\bar{J}$. A non-linear solution to equation (2.2) was obtained by use of finite elements. Solutions of this type of problem by finite elements have been examined by numerous authors. Zienkiewicz [20] reviews general methods for tackling non-linear equations such as (2.2). He concluded that none of the more popular non-linear procedures can guarantee convergence to a solution. The actual method used by Williamson and Ralph was the Newton-Raphson algorithm. This can be justified since many authors have published work [21-23], which utilises this technique successfully.

The finite element method basically minimises the energy of the system of interest over a given domain (see Appendix 8.1). It does this by forming equations of the form

$$\nu[S]\{\bar{A}\} = \{\bar{J}\} \tag{2.8}$$

for all elements which comprise the model. The matrix, [S], is 3x3 and is known as the elementary stiffness matrix. These matrices are packed one at a time into an overall 'global' system of equations, which relate the unknown nodal potentials to the specified field sources. The resulting set of equations have to be solved non-linearly. This is accomplished in the following manner.

Given a set of reluctivities the resulting system of global equations will have the form

$$[G]\{\bar{A}\} = \{\bar{J}\} \tag{2.9}$$

Use of the Newton-Raphson method for a non-linear solution requires the definition of a tangent matrix [T]. This tangent matrix is used together with the present set of potentials to define an error vector $\bar{\delta}$, which is used to refine the solution in $\bar{A}$. This process may be outlined as follows. First, assume that the Kth approximation to the vector $\{\bar{A}\}$ has been found and we wish to obtain the (K+1)th approximation. The steps are then

(1) Determine the Jacobian matrix

$$T^{(k)} = (d/d\{\bar{A}\})^{(k)} \; [[G[\{\bar{A}\}]^{(k)} \tag{2.10}$$

(2) Solve for the error vector $\bar{\delta}^{(k)}$

$$[T]^{(k)} \; \{\bar{\delta}\}^{(k)} = ([G]\{\bar{A}\} - \bar{J}\} \tag{2.11}$$

(3) Refine the solution in $\{\bar{A}\}$ according to

$$\{\bar{A}\}^{(k+1)} = \{\bar{A}\}^{(k)} - \{\bar{\delta}\}^{(k)} \tag{2.12}$$

The above steps are then repeated until $\{\bar{\delta}\}$ becomes small. The variables used in the above equations are all complex. The tangent matrix is assembled from the elementary submatrices. Thus the elemental tangent matrix has the form

$$[T] = d/d\{\bar{A}\}[\nu[S]\{\bar{A}\}] \tag{2.13}$$

This is permissible since the flux density and hence the reluctivity can only have one value in a linear simplex triangle. Differentiating (2.13) gives

$$[T] = \nu[S] + [[S]\{\bar{A}\}]d\nu/d\{\bar{A}\} \tag{2.14}$$

It is the last term of (2.14) which was somewhat problematical. This is because ν is a real variable and $\bar{A}$ is complex. Therefore the derivative of ν with respect to $\bar{A}$ does not satisfy the Cauchy-Riemann equations for differentiability. This problem was circumnavigated by Williamson and Ralph [6]. Rather than trying to perform the differentiation directly they split the potential and its sources into their real and imaginary parts. The elementary submatrices thus took on the form

$$\nu \begin{bmatrix} [S] & [O] \\ [O] & [S] \end{bmatrix} \begin{bmatrix} \{A_{Re}\} \\ \{A_{Im}\} \end{bmatrix} = \begin{bmatrix} \{J_{Re}\} \\ \{J_{Im}\} \end{bmatrix} \tag{2.15}$$

or $$\nu[S']\{A'\} = \{J'\} \tag{2.16}$$

where

$$[S'] = \begin{bmatrix} S_{11} & S_{12} & S_{13} & 0 & 0 & 0 \\ S_{21} & S_{22} & S_{23} & 0 & 0 & 0 \\ S_{31} & S_{32} & S_{33} & 0 & 0 & 0 \\ 0 & 0 & 0 & S_{11} & S_{12} & S_{13} \\ 0 & 0 & 0 & S_{21} & S_{22} & S_{23} \\ 0 & 0 & 0 & S_{31} & S_{32} & S_{33} \end{bmatrix} \tag{2.17}$$

$$\{A'\} = \begin{bmatrix} A_{1Re} \\ A_{2Re} \\ A_{3Re} \\ A_{1Im} \\ A_{2Im} \\ A_{3Im} \end{bmatrix} \tag{2.18}$$

$$\{J'\} = \begin{bmatrix} J_{1Re} \\ J_{2Re} \\ J_{3Re} \\ J_{1Im} \\ J_{2Im} \\ J_{3Im} \end{bmatrix} \tag{2.19}$$

Using equations (2.17), (2.18) and (2.19) the elemental Jacobian matrix may be redefined as

$$[T] = \nu[S'] + \{[S']\{A'\} \frac{\partial \nu}{\partial B^2} \frac{\partial B^2}{\partial \{A'\}}\} \tag{2.20}$$

$$\text{with } B^2 = \{A'\}[\acute{S}]\{A'\}^T \tag{2.21}$$

Differentiation of B^2 with respect to the real and then the imaginary parts of $\bar{A}$ is now possible. The resulting tangent matrix now becomes

$$[T] = \nu[S'] + 2\frac{\partial \nu}{\partial B^2}\{[S']\{A'\}\}\{[S']\{A'\}\}^T \qquad (2.22)$$

the variation of reluctivity with r.m.s. flux density can be derived from manufacturers characteristics. This data can be input to the program in the form of a cubic spline fit from which the derivative $d\nu/dB^2$ and ν can be calculated from the latest solution of the potential. A full derivation of equations (2.17), (2.22) can be found in [6].

The Newton-Raphson algorithm defined above provides a method which converges to a solution in a very few iterations. This is because it is a true second order method since it uses not only the function but also its derivative to find the next approximation to the solution. This in turn suggests that in terms of number of iterations required to converge to a solution, the Newton-Raphson technique should always require fewer iterations than a first order method such as simple iteration.

The disadvantages of Newton-Raphson are two-fold. Firstly, it can be appreciated by examination of the last term of equation (2.22) that the elementary Jacobian matrix exhibits no sparsity. It is a full 6x6 matrix. This means that the corresponding global matrix will, for the non-linear case, require more computer memory for storage than would be necessary if a linear solve were performed. The second disadvantage is that the Newton-Raphson requires far more computer operations when assembling the global matrix than does the linear case. This can be seen by comparing equation (2.22) with equation (2.16). Taking these two factors into consideration the method of simple iteration begins to become a more attractive proposition, since

it requires neither splitting the potential into its real and imaginary parts nor assembly of a tangent matrix. It thus offers potential savings in computer memory and reduction in execution time. However it was found that the Newton algorithm was far more reliable than simple iteration therefore it was used here in preference to simple iteration.

2.5 Matrix Handling

Application of finite elements to a potential problem results in a large sparse system of equations of the form

$$Ax = b \tag{2.23}$$

To obtain a solution to the field the matrix must be solved. There are many ways of doing this [24]. However the techniques of solution may be split into two broad categories, direct methods and iterative techniques. Each approach has its own merits and demerits. The main strengths of direct methods are listed below.

(1) They are well developed and have been thoroughly examined by many authors, for example [24].

(2) Direct methods are very robust and reliable since they are nearly all based on the techniques of Gaussian elimination or triangular factorisation, which are very stable techniques and are in fact equivalent to one another.

It is triangular factorisation that was selected by Williamson and Ralph to solve the matrix equation. The algorithm they used is the same as that used by Zienkiewicz [20]. The algorithm works on the following principles.

Given that

$$Ax = b \tag{2.24}$$

where A is a symmetric positive or negative definite matrix. A may be factored into

$$A = LL^T \tag{2.25}$$

where L is a lower triangular matrix. This is called Choleski's method. Thus (2.24) becomes

$$LL^Tx = b \tag{2.26}$$

therefore

$$L^Tx = L^{-1}b \tag{2.27}$$

The product, $L^{-1}b$, is actually found by introducing another vector c and solving

$$Lc = b \tag{2.28}$$

This presents no difficulty since L is lower triangular. It is also more efficient than explicitly forming $L^{-1}b$.

This brief explanation of Choleski's method brings out one further advantage of using this type of solution. A full Gaussian elimination on a matrix requires approximately N**3/3 computer operations, where N is the order of the matrix. However it can be deduced form equation (2.27) that if the matrix L is remembered then the system described in (2.24) can be solved for as many right hand sides as is necessary at reduced cost. As the Choleski factors are symmetric, L is naturally stored. A re-solve facility is thus available for approximately N**2/2 operations.

In an analysis of induction machines the effects of rotor skew have to be considered when calculating the e.m.f.'s in the various machine windings. Skew is essentially a three dimensional effect and produces axial variations of flux which cannot be represented by a two dimensional field model. However skew may be dealt with by firstly solving the non-linear Poisson equation with both stator and rotor currents present, and then carrying out a series of linear solutions. The first non-linear solution is necessary to set the correct value of reluctivity in each element.

The e.m.f. induced in a given winding can be thought of as being made up of two components. The first of these is due to the unskewed stator originated flux. The second being attributable to the skewed rotor based flux. The e.m.f. in a winding is thus calculated by solving the reduced matrix firstly with only the stator current included in the right hand side and then with each harmonic of rotor current being present separately. The various contributions are accumulated. From this it is obvious that a technique that allows re-solution at reduced cost is useful in this type of analysis.

2.6 Storage Considerations

Having opted for a direct matrix solver another obstacle is encountered immediately. A direct solver normally requires N**2 memory locations to store an NxN matrix. In the work being considered here systems of order 800x800 or more are not uncommon. It would be unrealistic to attempt storage of a matrix of this size. Fortunately

matrices obtained using finite elements are often symmetric and always exhibit sparsity. The former property can be taken advantage of by only storing half the system matrix. The latter feature can be exploited by re-ordering the equations. The motivation for doing this is that the reordered equations may have a smaller envelope or bandwidth than the original system and will therefore require less memory for storage. The algorithm chosen by Ralph and Williamson to achieve this was due to Cuthill and McKee [25].

2.7 The Reverse Cuthill McKee Algorithm

The objective of applying reverse Cuthill-McKee or any other renumbering scheme is to store in an efficient manner a system of equations such as (2.23). To achieve this aim a permutation matrix, P, is applied to the system to rearrange the rows and columns of A in such a way as to reduce the profile or bandwidth of A. The modified set of equations thus has the form

$$PAP^T(Px) = Pb \tag{2.29}$$

It can be seen from (2.29) that P has the property that

$$PP^T = I \tag{2.30}$$

In order to facilitate what follows some definitions are now made. Let A be an NxN symmetric matrix with elements aij. Then for the i^{th} row of A, i=1,...,N the following definitions can be made

$$f_i(A) = \min\{j: a_{ij} \neq 0\} \tag{2.31}$$

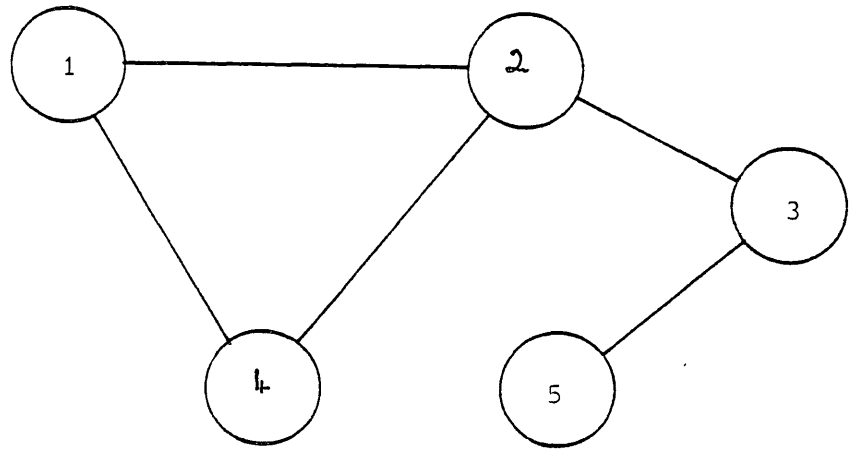
$$p_i(A) = i - f_i(A) \tag{2.32}$$

$$w_i(A) = |\{k: k > i \text{ and } \exists q \leq i \text{ such that } a_{kq} \neq 0\}| \tag{2.33}$$

where $f_i(A)$ is the column subscript of the first nonzero element of the i^{th} row of A, $p_i(A)$ is the bandwidth of the i^{th} row of A, $w_i(A)$ is the front width of the i^{th} row of A and $|X|$ is used to denote the number of elements in X. It is also convenient to introduce here the undirected graph, G(A), of the matrix A. This is best done by example. Consider the matrix

$$A = \begin{bmatrix} x & x & 0 & x & 0 \\ x & x & x & x & 0 \\ 0 & x & x & 0 & x \\ x & x & 0 & x & 0 \\ 0 & 0 & x & 0 & x \end{bmatrix} \tag{2.34}$$

Then its graph, G(A), would be as in Figure 2.3



The graph, G(A), of equation (2.3)

Figure 2.3

Re-ordering the rows and columns of, A, merely corresponds to renumbering the nodes of G(A). From equation (2.32) the bandwidth of A may be defined as

$$b(A) = \max\{|i-j| : a_{ij} \neq 0\} = \max\{p_i(A)\} \tag{2.35}$$

and in the same way as [26] the envelope of A can be defined as

$$Env(A) = \{(i,j) : p_i(A) \leq j \leq i\} \tag{2.36}$$

with the number of locations required to store A being equal to

$$|Env(A)| = N + \sum_{i=1}^{N} p_i(A) \tag{2.37}$$

The degree of a node must also be defined as the number of nodes connected to it. Finally it is necessary to explain the idea of a level structure. A level structure may be generated from the graph of a matrix. It may be rooted at any node on the graph. Starting from this arbitrary node the structure is generated by putting the root node in the first level and all those it is connected to in the second level. The third level will contain all those nodes that are connected to nodes in the second level with the exclusion of those which have already been included; thus a spanning tree is formed. In the case of Figure 2.3 a structure rooted at node two, for example, would have the following form.

Level 1		2	
Level 2	1	4	3
Level 3		5	

Figure 2.4

The width of a particular level is defined as the number of nodes contained in the level. The depth of the structure is equal to the number of levels generated. The Cuthill/McKee algorithm works by taking each node on the finite element mesh, which is itself an undirected graph, and generates a level structure rooted at that node. It measures the maximum width of each structure and isolates those structures of minimal maximum width. New numbers are then assigned to the nodes of each structure in turn, by sweeping through the levels systematically numbering the nodes of each level by degree; the one of highest degree being numbered first. The structure yielding the smallest profile is then regenerated and the nodes numbered accordingly. It can be appreciated from this description that the Cuthill/McKee algorithm reduces the profile of the matrix by attempting to produce the longest thinnest structure possible. This has the effect of making the individual $p_i(A)$'s smaller and hence the sum

$$\sum_{i=1}^{N} p_i(A) \tag{2.39}$$

is reduced and equation (2.37) is diminished in size. Further reductions in profile can sometimes be achieved by taking the final numbering and reversing it. A full mathematical exposition of the preceding discussion can be found in [25] and [26]. From the above it is evident that the main drawback of reverse Cuthill/McKee is the number of level structures that are generated since these take time to generate. However this method has been used widely and successfully on matrices produced by finite element techniques. This is because the graphs which arise from finite elements are not normally complicated or densely coupled. The graph resulting from an isolated simplex finite element is as shown in Figure 2.5. If the problem is

cast in complex form and the node potentials are split into real and imaginary parts this graph becomes as shown in Figure 2.6, where ' is used to denote the imaginary part. This split form is still not difficult for Cuthill/McKee to deal with. However if a scheme such as the Newton-Raphson algorithm is introduced also in a split form then the graph of the element becomes Figure 2.7. This new and complex topology makes the Cuthill/McKee algorithm less effective in reducing the profile. This exposes another difficulty in applying the Newton-Raphson approach to the nonlinear problem.

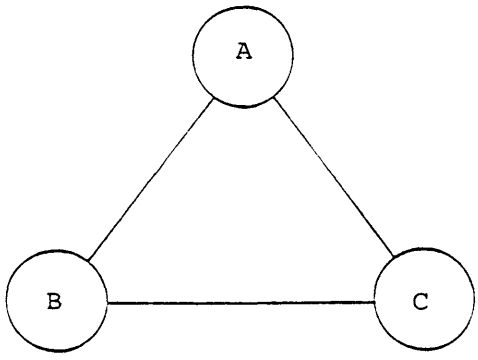


Fig. 2.5 The graph of a single finite element

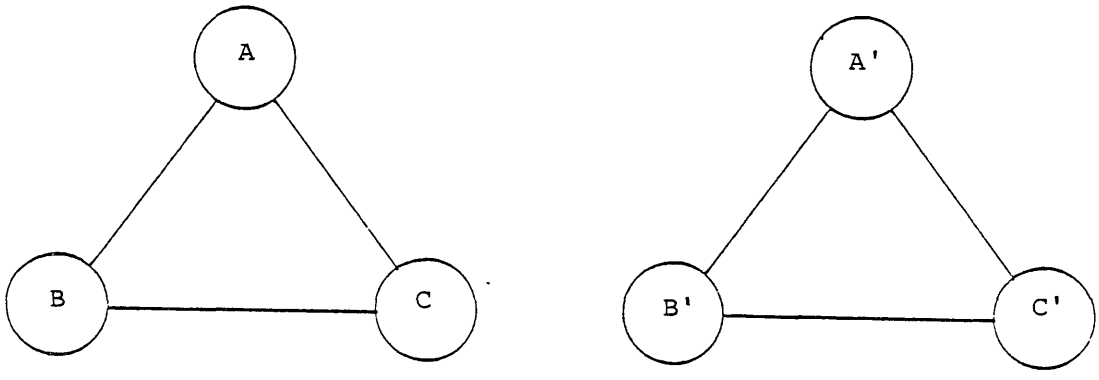


Fig. 2.6 Graph split into real and imaginary parts

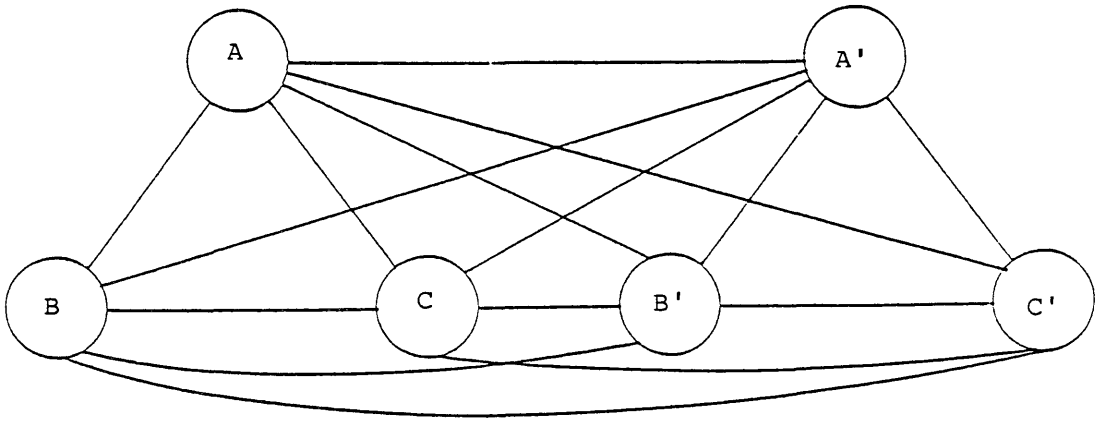


Fig. 2.7 The connection of real and imaginary parts

CHAPTER THREE

IMPROVEMENTS TO THE WILLIAMSON AND RALPH ANALYSIS

3.1 Replacement of the Nag-Algorithm

3.1.1 Introduction: As has already been mentioned in Section 2.3 a new approximation to the actual currents flowing in the windings and bars of the motor is required after each non-linear solution of Poisson's equation. The new current set should more closely match reality than the previous one. This convergent iterative scheme was realised by defining voltage balance equations for each identifiable circuit in the machine. Error functions such as Equation (2.1) in Section 2.3 were then set up to quantify the extent of voltage imbalance. An equation such as (2.1) was written for each electrical circuit and six more were defined for the rotor, since three forwards and three backwards rotating fields were considered. The errors then formed part of the input to Nag Algorithm E04FAF which finds the set of currents that minimise the sum of the squares of the errors. The currents so found were taken as the next approximation to the true currents.

Use of the Nag minimisation subroutine has two major flaws. Firstly, it is very slow. This is because use of a formal minimisation technique relies on mathematical rather than physical considerations when choosing the next current set. Secondly, it makes the analysis package less transportable. This second flaw appears because not all computers support the Nag-Library and it is almost certain that many

machine designers, who mainly use mini-computers, would not have access to it. It was therefore decided that a new method that does not employ minimisation should be developed.

The new technique operates on the idea of linearisation at a point, since if all the reluctivities of the finite elements are known for the latest current set, the impedances of the machine can be calculated for this state. These impedances can then be used to predict the next set of currents.

3.1.2 The Impedance Method: The new technique for updating the winding currents, which is developed below, involves the use of coupled linear circuits. These have recently been applied to induction motor analysis by Williamson [27],[28] and it is from the ideas put forward in these papers that the present technique is derived.

Consider a collection of N coupled linear circuits, each of which carries a sinusoidal current. Then for each circuit a voltage balance equation of the form

$$\bar{V}_n = \sum_{m=1}^{N} \bar{I}_m \bar{Z}_{nm} \qquad (3.1)$$

can be defined where $\bar{Z}_{nm}$ is the coupling impedance between the m-th and n-th circuits. If the voltages applied to each of the N circuits is known and the coupling impedances can be determined then from (3.1) which represents a matrix equation of the form

$$\{\bar{V}\} = [\bar{Z}]\{\bar{I}\} \tag{3.2}$$

the unknown currents flowing in each circuit can be found by inverting (3.2) thus

$$\{\bar{I}\} = [Z]^{-1}\{\bar{V}\} \tag{3.3}$$

The problem can now be regarded as one of finding the coupling impedances. These can be found in the following manner.

Assume firstly that the reluctivity in each finite element of the problem is known, or has been estimated, and the present coupling impedances are to be calculated. Then the most straightforward way of doing this is to reduce all the currents in the windings except one to zero. The non zero current is then set to unity and the magnetic vector potential is solved for using this current as the only source. The e.m.f.'s due to this unit current can then be calculated in all the machines windings and rotor bars. The coupling impedances of the machine can then be calculated, since if $\bar{I}_{j\neq i}=0$ equation (3.1) may be written in the form

$$\bar{Z}_{ji} = \frac{\bar{U}_j}{\bar{I}_i} \tag{3.4}$$

where $\bar{Z}_{ji}$ is the impedance, $\bar{U}_j$ is the induced e.m.f. in the j^{th} winding and $\bar{I}_i$ is the current in the i^{th} winding. This procedure may be adopted to calculate all the coupling impedances. Equation (3.3) may then be solved to give the current set that is fully compatible with the latest estimate of the elemental reluctivities. The currents thus found are used to reset the saturation of the machine, hence an iterative scheme has been defined.

3.1.3 Stator-Stator Coupling Impedances: Consider a pole pitch of a motor such as the one shown in Figure 3.1 with the various windings identified. Let unit current be injected into the main winding, say, and the field in the machine be solved for this current. Then the coupling impedances are calculated as follows.

Faraday's Law may be written

$$\nabla \times \bar{E} = \frac{-\partial \bar{B}}{\partial t} \tag{3.5}$$

Then the magnetic vector potential is defined by

$$\bar{B} = \nabla \times \bar{A} \tag{3.6}$$

Combining (3.5) and (3.6) gives

$$\nabla \times \bar{E} = \frac{-\partial}{\partial t} (\nabla \times \bar{A}) \tag{3.7}$$

(3.7) may be written in an integral form as

$$\iint_{\Omega} (\nabla \times \bar{E}) . \overline{dS} = \frac{-\partial}{\partial t} \iint_{\Omega} (\nabla \times \bar{A}) . \overline{dS} \tag{3.8}$$

applying Stokes' Theorem transforms (3.8) into

$$\phi \bar{E} . \overline{d\ell} = -j\omega\phi \bar{A} . \overline{d\ell} \tag{3.9}$$

Thus the electric field induced between two points in a winding may be obtained from

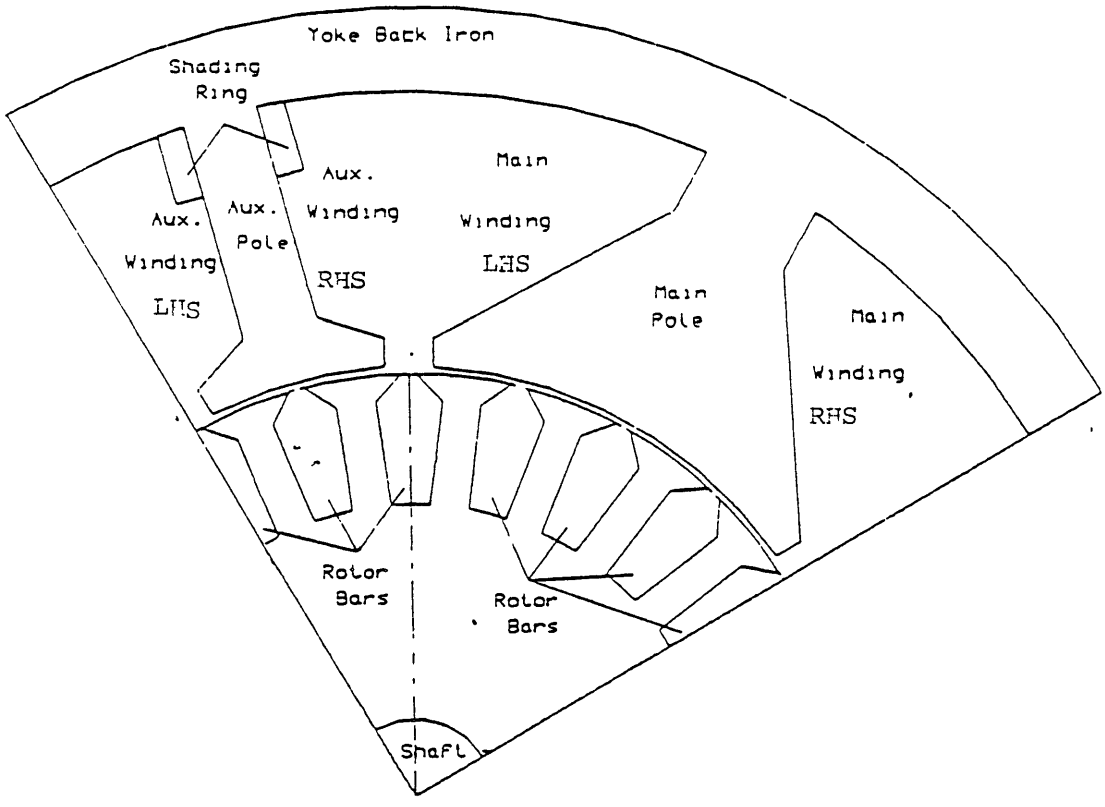

Yoke Back Iron
Shading Ring
Aux. Winding LHS
Aux. Pole
Aux. Winding RHS
Main Winding LHS
Main Pole
Main Winding RHS
Rotor Bars
Rotor Bars
Shaft

Fig. 3.1

$$\bar{E} = j\omega(\bar{A}_{RHS} - \bar{A}_{LHS}) \text{ per metre per turn} \tag{3.10}$$

It is assumed that the slice of the machine being considered is representative of the whole machine, so that

$$\bar{E} = j\omega W(\bar{A}_{RHS} - \bar{A}_{LHS}) \text{ per turn} \tag{3.11}$$

where W is the length of the machine. Thus the average e.m.f. induced over the entire winding may be obtained from

$$\bar{U} = \frac{j\omega WN_{turns}}{\Omega} \iint_{\Omega} (\bar{A}_{RHS} - \bar{A}_{LHS})ds \tag{3.12}$$

writing equation (3.12) in terms of finite elements gives

$$\bar{U} = \frac{j\omega WN_{turns}}{3\Omega} \left\{ \sum^{RHS} \Delta_e \sum_{i=1}^{3} \bar{A}_{ie} - \sum^{LHS} \Delta_e \sum_{i=1}^{3} \bar{A}_{ie} \right\} \tag{3.13}$$

Use of equation (3.13) allows the self and coupling reactances of the main winding and shading ring to be calculated. The resistances of the windings must be calculated separately. The self-impedance of the shading ring, for example, will have the form

$$\bar{Z}_{SR} = \{R_{SR} + jX_{SR}\} \tag{3.14}$$

3.1.4 Stator-Rotor Coupling Impedances: Before detailing the calculation of the stator-rotor coupling impedances it is necessary to define what is meant by a circuit when discussing the rotor. This is because the current flow paths are not uniquely defined in a cage

rotor. But since only symmetrical cages are being considered here, it is convenient to regard the rotor current as a superposition of sinusoidal distributions, each of which would be established in response to a particular rotating sinusoidally distributed airgap field. To characterise any one of these distributions it is sufficient to know the amplitude and phase of the current flowing in one rotor bar, since the whole distribution may then be obtained using a phase shift from one bar to the next that will depend on the number of poles and the sense of rotation of the parent field. The circuit current $\bar{I}_m$ in equation (3.1) is now identified as being the harmonic current in a particular bar of the rotor, which is used as a reference bar. The rotor will have as many unknown currents as there are harmonic current distributions.

For a machine with N_s stator windings, and for which N_h forwards rotating and N_h backwards rotating field harmonics are to be considered, equation (3.1) becomes for the m^{th} stator winding

$$\bar{V}_m = \sum_{n=1}^{N_s} \bar{Z}_{mn}\, \bar{I}_n + \sum_{\nu_k=-N_h}^{N_h} \bar{Z}^k_{mr}\, \bar{I}^k_r \qquad (3.15)$$

The first part of equation (3.15) gives the influence of all the stator winding currents on the m^{th} winding, and the second summation represents the influence of the rotor harmonic current distributions. $\bar{I}_n$ is the current in the n^{th} stator winding, and $\bar{I}^k_r$ is the νk^{th} harmonic current in the reference rotor bar.

Separate voltage balance equations are required for each harmonic component in the reference rotor bar

$$0 = \sum_{n=1}^{N_s} \bar{\bar{Z}}^{k}_{rn} \bar{I}_n + \bar{\bar{Z}}^{k}_{rr} \bar{I}^{k}_{r} \qquad (3.16)$$

The first term of equation (3.16) gives the e.m.f. induced in the reference bar by the νk^{th} harmonic field produced by all N_s stator currents. The last term of (3.16) can be regarded as the impedance drop in the bar when the νk^{th} distribution of currents is flowing.

If there is no variation in the length of the airgap of the machine. then it can be assumed that different rotor current distributions do not couple with each other and the matrix, defined by equation (3.1), is as shown in Figure 3.2 if three forwards and three backwards rotating fields are included. If, however, the stator of the machine is salient, then this effect can be accounted for in the following manner.

Consider a machine with a salient pole stator, which is shown in a linearised form in Figure 3.3. Then the permeance as a function of angular position can be represented graphically as Figure 3.4. This waveform can be resolved into a Fourier series of the form

$$g(\theta) = a_0 + \sum_{n=1}^{\infty} a_n \cos(n\theta) + b_n \sin(n\theta) \qquad (3.17)$$

$g(\theta)$ will be an even function and, with appropriate choice of origin, the sine terms in the series disappear and then equation (3.17) becomes

$$g(\theta) = a_0 + \sum_{n=1}^{\infty} a_n \cos(n\theta) \qquad (3.18)$$

$$\begin{bmatrix} Z_{11} & Z_{12} & Z_{13} & Z_{14} & Z_{15} & Z_{16} & Z_{17} & Z_{18} \\ Z_{21} & Z_{22} & Z_{23} & Z_{24} & Z_{25} & Z_{26} & Z_{27} & Z_{28} \\ Z_{31} & Z_{32} & Z_{33} & 0 & 0 & 0 & 0 & 0 \\ Z_{41} & Z_{42} & 0 & Z_{44} & 0 & 0 & 0 & 0 \\ Z_{51} & Z_{52} & 0 & 0 & Z_{55} & 0 & 0 & 0 \\ Z_{61} & Z_{62} & 0 & 0 & 0 & Z_{66} & 0 & 0 \\ Z_{71} & Z_{72} & 0 & 0 & 0 & 0 & Z_{77} & 0 \\ Z_{81} & Z_{82} & 0 & 0 & 0 & 0 & 0 & Z_{88} \end{bmatrix}$$

Fig. 3.2

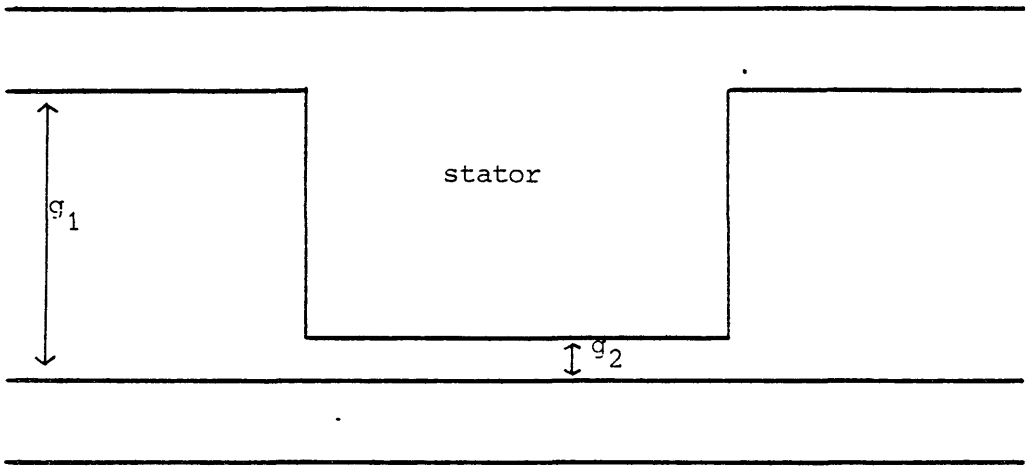


Fig. 3.3 Linearised view of machine pole pitch

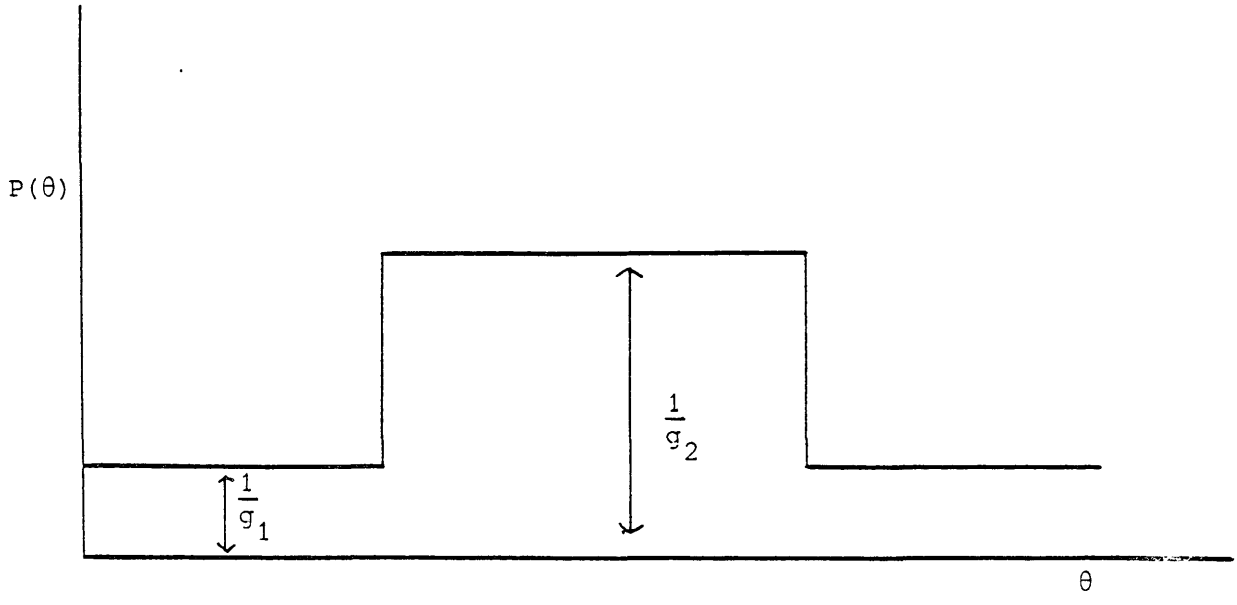


Fig. 3.4 Permeance function corresponding to Fig. 3.3

Consider now the m.m.f waveform, which may originate on either the rotor or the stator but which may be represented in the stator frame of reference by an equation of the same form as (3.17). However the m.m.f. waveform will be an odd function of angular position and time, and can be described by

$$f(\theta,t) = \sum_{m=1}^{\infty} b_m \cos(\omega t - m\theta) \tag{3.19}$$

The airgap flux density of the machine may now be expressed as

$$B_{gap}(\theta,t) = \{a_o + \sum_{n=1}^{\infty} a_n \cos(n\theta)\}\{\sum_{m=1}^{\infty} b_m \cos(\omega t - m\theta)\} \tag{3.20}$$

n only even
m only odd

Taking a typical product of (3.20) gives

$$B_{mn} = \{a_o + a_n \cos(n\theta)\}\{b_m \cos(\omega t - m\theta)\} \tag{3.21}$$

which may be expressed as

$$B_{mn} = \{1 + a'_n \cos(n\theta)\}\{b_m \cos(\omega t - m\theta)\} \tag{3.22}$$

Using certain trigonometric identities (3.22) can be reduced to

$$B_{mn} = a_o b_m \{\cos(\omega t - m\theta) + \frac{a'_n}{2} \cos(\omega t + (n-m)\theta) + \frac{a'_n}{2} \cos(\omega t - (n+m)\theta)\} \tag{3.23}$$

....

To determine the frequency of the harmonics described by (3.23) in the rotor frame of reference it is necessary to transform (3.23) to rotor co-ordinates by

$$\theta = \theta_r + \omega_r t \tag{3.24}$$

Thus (3.23) becomes

$$B_{mn} = a_o b_m \{\cos(\omega t - m(\theta_r + \omega_r t)) + \frac{a_n'}{2} \cos(\omega t + (n-m)(\theta_r + \omega_r t)) + \frac{a_n'}{2} \cos(\omega t - (n+m)(\theta_r + \omega_r t))\} \tag{3.25}$$

If we now define the n^{th} harmonic slip, S_n, in terms of the fundamental slip S, such that

$$S_n = (1 - n(1-S)) \tag{3.26}$$

and

$$\omega_r = \frac{\omega}{n} (1 - S_n) \tag{3.27}$$

Then equation (3.25) may be expressed as

$$B_{mn} = a_o b_m \{\cos(S_m \omega t - m\theta_r) + \frac{a_n'}{2} \cos(S_{m-n} \omega t - (m-n)\theta_r) + \frac{a_n'}{2} \cos(S_{m+n} \omega t - (m+n)\theta_r)\} \tag{3.28}$$

n only even
m only odd

This analysis demonstrates that a given m.m.f. harmonic will not only induce harmonic e.m.f.'s in the rotor of the same pole number as itself, but also an infinite series of other odd harmonics. These

other harmonics however will all be of the slip frequency appropriate to their pole number. For example, the fundamentally distributed stator m.m.f. may interact with the appropriate permeance harmonic to produce a third harmonic distribution of e.m.f. in the bars of the cage. These e.m.f.'s will have the same frequency as the third harmonic e.m.f.'s which arise as a direct result of the third harmonic of stator m.m.f. An important consequence of this is that all the rotor harmonics considered in the analysis will couple together so that the resulting matrix of equation (3.2) will be full. Three forwards and three backwards rotating fields are to be considered and each harmonic e.m.f. induced in the rotor bars must be calculated. Using the complex form a Maxwell's equations it is found from equation (3.7) that

$$\bar{E} = -j\omega\bar{A} + \nabla\phi \tag{3.29}$$

Since periodicity is assumed to apply on the boundaries of the problem gradϕ may be set to zero

$$\text{thus} \quad \bar{E} = -j\omega\bar{A} \tag{3.30}$$

The average e.m.f. induced in a rotor bar may be calculated by integrating [3.30] over the bar area

$$\text{thus } \bar{U} = \frac{W}{S} \iint_S \bar{E}\cdot\overline{dS} \tag{3.31}$$

where S is the bar area. In terms of $\bar{A}$ (3.31) may be written as

$$\bar{U} = \frac{-j\omega W}{S} \iint_S \bar{A}\cdot\overline{dS} \tag{3.32}$$

and (3.32) may be translated into the finite element form and becomes

$$\bar{U} = \frac{-j\omega W}{3S} \sum_{i=1}^{N} \sum_{j=1}^{3} (\bar{A}_j)\Delta_i \qquad (3.33)$$

where $\bar{A}_j$ are the nodal potentials.

The e.m.f. induced in any bar of a squirrel cage is thought of as a superposition of harmonic e.m.f.'s. Therefore if we work out the total e.m.f. in each bar of the cage we are left with N_b samples of the total e.m.f. These samples can be used to decompose the total e.m.f. into its harmonic components by use of a Fourier transform. The total e.m.f. in the n^{th} bar can be represented by

$$\bar{U}_{bn} = \sum_{k=-\nu}^{\nu} U^{-k} e^{jk(\theta_0+(n-1)\alpha)} \qquad (3.34)$$

where $\bar{U}^k$ is the k^{th} harmonic e.m.f. in bar n, θ_0 is the position of the first bar, and k represents the harmonic number which may be positive or negative depending on whether the harmonic is forwards or backwards rotating. Equation (3.34) may be transformed to yield the harmonic components of e.m.f. thus

$$\bar{U}^k = \frac{1}{N} \sum_{k=1}^{N} \bar{U}_{bn} e^{-jk(\theta_0+(n-1)\alpha)} \qquad (3.35)$$

Finally the harmonic coupling impedance may be obtained from

$$\bar{Z}^k = -\frac{1}{\bar{I}_{sN}} \sum_{n=1}^{N} \bar{U}_{bn} e^{-jk(\theta_0+(n-1)\alpha)} \qquad (3.36)$$

where $\bar{I}_s$ is the source current.

An alternative strategy can be used to calculate the rotor-stator impedances. This method relies on the resolution of the airgap flux into a series of forward and backward harmonics and then makes use of the formula

$$\bar{E} = \bar{B}WV \tag{3.37}$$

In effect the method used here calculates the e.m.f. induced in each bar separately, and then recovers the harmonic components by Fourier decomposition. With the alternative method, on the other hand, it is the airgap flux that is resolved into its harmonic components and the harmonic e.m.f.'s are then calculated using the flux cutting rule.

The two techniques have been found by the present author to be equivalent in the case of an open rotor slot. However in the case of a closed rotor slot, such as that shown in Figure 3.5, they do not give the same results. This discrepancy was quantified by looking at the ratios of the stator rotor coupling to the rotor stator coupling. From generalised harmonic analysis a formula relating the ratios can be derived [27]. This formula is as follows

$$\frac{\underline{Z}_{rm}^{k}}{\underline{Z}_{mr}^{k}} = \frac{S_k}{N_b} \begin{Bmatrix} \underline{C}_m^{k} \\ \underline{C}_m^{k*} \end{Bmatrix} \tag{3.38}$$

If the slip in (3.38) is set to unity then since the complex ratio merely represents a phase shift then the ratio

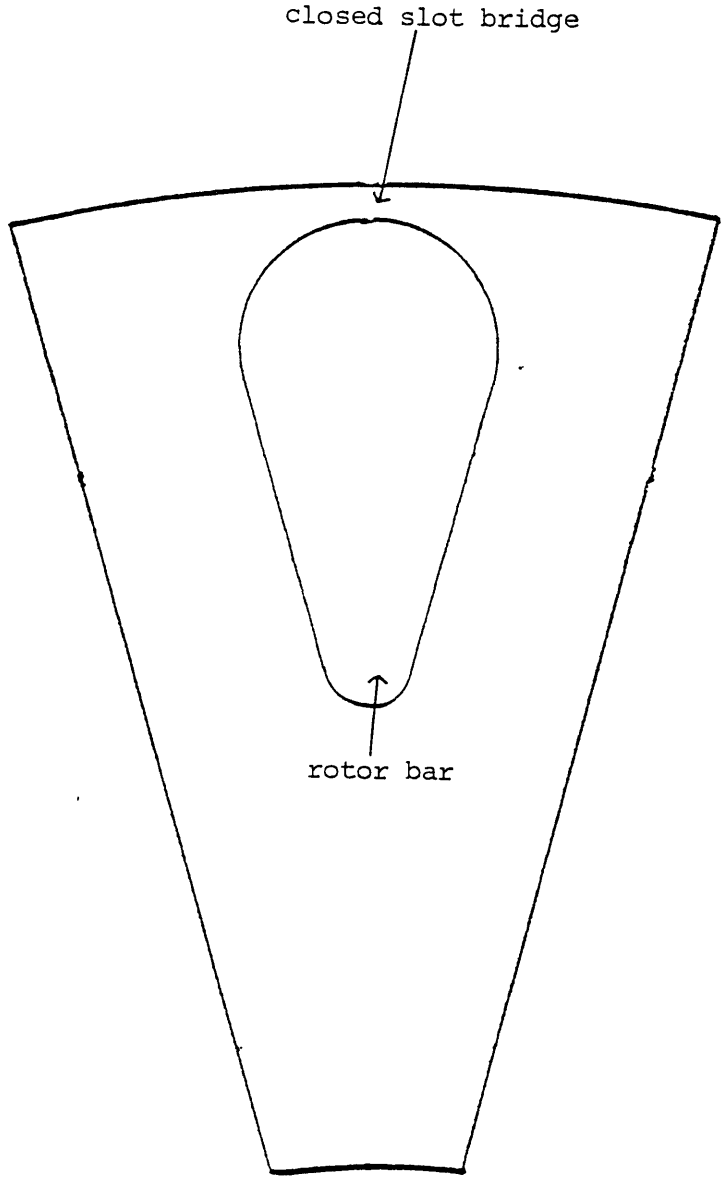


Fig. 3.5 A closed rotor slot

$$\frac{|\bar{Z}^{k}_{mr}|}{|\bar{Z}^{k}_{rm}|} \tag{3.39}$$

should give the number of rotor bars. A table of the ratios is presented for the two methods on page 51 . From this table it can be seen that for the fundamental the two methods are more or less equivalent but for the higher harmonics the alternative method gets progressively worse. Thus integration of the potential over the bar area is the preferred method. A fuller account of the second method of calculation can be found in [7].

The effects of skew on the impedance calculated above may be taken into account by use of a skew factor, K_{sk}, thus the rotor stator coupling impedance is of the form

$$\bar{Z}^{k}_{rm} = \bar{Z}^{k}_{mi}\, K^{k}_{sk} \tag{3.40}$$

3.1.5 Rotor Stator Coupling: The coupling between the rotor and stator may be found by putting harmonic distributions of current in the rotor bars each with a unit amplitude. Thus if a convenient value of current is injected into the reference bar then the current in the n^{th} bar is given by

$$\bar{I}_n = \bar{I}_1\, e^{jk(n-1)\alpha} \tag{3.41}$$

Number of Rotor Bars = 16		
Harmonic Number	Fourier Series of Airgap	Integration of Electric Field over Conductor Area
± 1	15.9	16.0
± 3	17.9	16.0
± 5	17.7	16.0
± 7	5.0	16.0

Table 3.1

Harmonic Ratios

Having put a suitable harmonic distribution of current in the rotor bars the coupling between the rotor and the stator can be calculated by making use of equation (3.13).

3.1.6 Rotor-Rotor Coupling: At the same time as the rotor stator coupling is evaluated the rotor rotor coupling can be calculated by making use of the same equations as were used for the stator rotor coupling. Having evaluated the rotor leakage reactance the effective impedance of the rotor may be found by adding the resistive components due to rotor bars and the endrings to the diagonal terms of the impedance matrix. The net impedance for the K^{th} harmonic is thus given by

$$\underline{Z}_r^k = (R_{bar}^k + R_{ring}^k + jX_r^k) \qquad (3.42)$$

The resistance in (3.42) may be found either from standard formulae or from a numerical model of a rotor slot (see Chapter 5).

Having worked out all the coupling impedances of the machine it is now possible to predict the next approximation to the currents by forming an equation such as (3.43). In the case of the machine shown in Figure 3.1, equation (3.43) will be as follows:

$$\begin{bmatrix} \bar{V} \\ 0 \\ 0 \\ 0 \\ 0 \\ 0 \end{bmatrix} = \begin{bmatrix} \bar{Z}_{11} & \bar{Z}_{12} & \bar{Z}_{13} & \bar{Z}_{14} & \bar{Z}_{15} & \bar{Z}_{16} \\ \bar{Z}_{21} & \bar{Z}_{22} & \bar{Z}_{23} & \bar{Z}_{24} & \bar{Z}_{25} & \bar{Z}_{26} \\ \bar{Z}_{31} & \bar{Z}_{32} & \bar{Z}_{33} & \bar{Z}_{34} & \bar{Z}_{35} & \bar{Z}_{36} \\ \bar{Z}_{41} & \bar{Z}_{42} & \bar{Z}_{43} & \bar{Z}_{44} & \bar{Z}_{45} & \bar{Z}_{46} \\ \bar{Z}_{51} & \bar{Z}_{52} & \bar{Z}_{53} & \bar{Z}_{54} & \bar{Z}_{55} & \bar{Z}_{56} \\ \bar{Z}_{61} & \bar{Z}_{62} & \bar{Z}_{63} & \bar{Z}_{64} & \bar{Z}_{65} & \bar{Z}_{66} \end{bmatrix} \begin{bmatrix} \bar{I}_1 \\ \bar{I}_2 \\ \bar{I}_3 \\ \bar{I}_4 \\ \bar{I}_5 \\ \bar{I}_6 \end{bmatrix} \tag{3.43}$$

Once the currents have been solved they may be used to calculate the steady state torque form

$$T_s = \frac{N_{bars}}{\omega} \sum_{\nu_h=-N_h}^{N_h} \frac{\nu_k}{S_k} \left| \bar{I}_r^k \right|^2 R_r^k \tag{3.44}$$

where in this case ν_k takes the values 1,3,-1,-3. The currents may also be used together with the stator voltage to work out the input power and power factor of the motor. All these quantities may be used at each step of the non-linear procedure to monitor the convergence of the method. Thus when the changes in torque and input power from one iteration to the next become small the method is deemed to have converged.

3.1.7 Inclusion of Iron Losses: Iron losses are known [4] to influence the terminal characteristics and output torque of shaded-pole motors. Since a field based model is being used in this thesis calculation of these losses can be attempted because the flux densities in each finite element are known at every step of the

solution. However, only the stator iron loss will be evaluated here since the fluxes in the rotor vary in a complicated manner because they are the result of superpositions of various harmonic fields.

Manufacturers provide iron loss characteristics in watts per unit weight for a given thickness of lamination, so that the total stator iron loss may be obtained from

$$P_{iron} = N_{poles}\, W\rho \sum_{i=1}^{N_{stator\ elements}} \Delta_i\, f_e\,(|\bar{B}_i|) \qquad (3.45)$$

where Δ_i is the area of the i^{th} triangle, ρ is the density of the iron, W is the length of the machine and $f(|B_i|)$ is the loss curve, which may be stored as a cubic spline, expressed as a function of $|\bar{B}_i|$ the flux density in each element.

Having worked out the power loss it is then necessary to add a parallel resistor to the impedance model, which will dissipate this power. The question now is where to position the resistor in the network. Because of difficulties in separating out the stator leakage reactance from the other components of stator reactance, it was decided to place the iron loss resistor, r_o , in parallel with the stator resistance as is shown in Figure 3.6. This assumes that, for the purposes of loss calculation, the stator leakage reactance is negligible when compared with the stator resistance.

The procedure to obtain the value of the iron loss resistor was as follows:

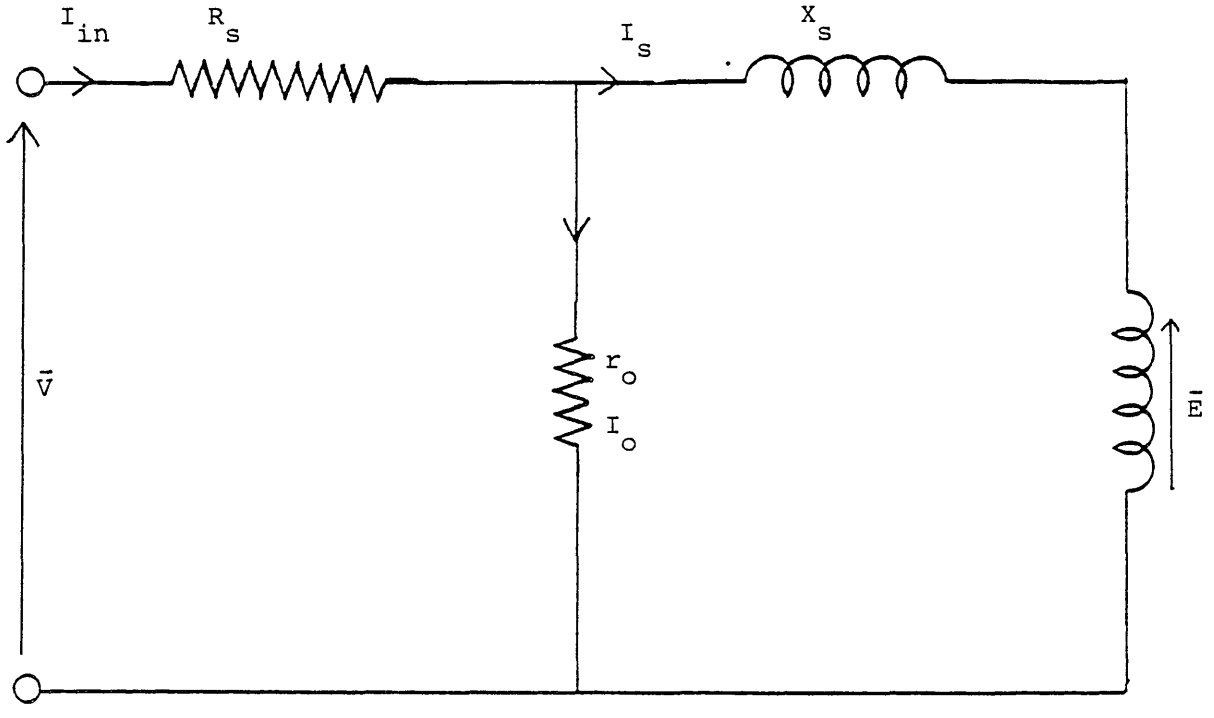


Figure 3.6 Equivalent circuit for iron loss

1. Assume an initial value of r_o

2. Add two more rows and columns to the impedance matrix so that it now looks like the one shown in Figure 3.7.

3. Solve the matrix equation

4. Evaluate the power dissipated in r_o

5. Define $E = P_{iron} - P_{r_o}$

6. Modify r_o according to

$$r_{o_{k+1}} = r_{o_k} - \gamma \left(\frac{E}{|I_o|^2} \right) \qquad (3.46)$$

$$0 < \gamma \leq 1$$

Steps 2 and 6 are then repeated until the value of r_o stabilizes. Typically this only takes a very few iterations, which are not expensive in computer time since the impedance matrix is rarely more than a 10x10 matrix.

3.1.8 Interbar Currents: Interbar currents can be included in the model, by modifying the coupling impedances in equation (3.43). The modification used follows the work of Subba Rao and Butler [45] and can be expressed as

$$\bar{Z}_{bn} = \frac{\bar{Z}_{bn} + W\alpha_n^2 r'_{qn}}{\left\{ 1 - \frac{\bar{Z}_{rn} \cos\left(\frac{W\alpha_n}{2}\right) - \alpha_n r_{qn} \sin\left(\frac{W\alpha_n}{2}\right)}{\bar{Z}_{rn} \cosh\left(\frac{W\gamma_n}{2}\right) + r_{qn} \gamma_n \sinh\left(\frac{W\gamma_n}{2}\right)} \right\}} \qquad (3.47)$$

$$\begin{bmatrix} \bar{V} \\ 0 \\ 0 \\ 0 \\ 0 \\ 0 \\ 0 \\ \bar{V} \\ 0 \end{bmatrix} \quad \begin{bmatrix} jX_S & \bar{Z}_{12} & \bar{Z}_{13} & \bar{Z}_{14} & \bar{Z}_{15} & \bar{Z}_{16} & R_S & 0 \\ \bar{Z}_{21} & \bar{Z}_{22} & \bar{Z}_{23} & \bar{Z}_{24} & \bar{Z}_{25} & \bar{Z}_{26} & 0 & 0 \\ \bar{Z}_{31} & \bar{Z}_{32} & \bar{Z}_{33} & \bar{Z}_{34} & \bar{Z}_{35} & \bar{Z}_{36} & 0 & 0 \\ \bar{Z}_{41} & \bar{Z}_{42} & \bar{Z}_{43} & \bar{Z}_{44} & \bar{Z}_{45} & \bar{Z}_{46} & 0 & 0 \\ \bar{Z}_{51} & \bar{Z}_{52} & \bar{Z}_{53} & \bar{Z}_{54} & \bar{Z}_{55} & \bar{Z}_{56} & 0 & 0 \\ \bar{Z}_{61} & \bar{Z}_{62} & \bar{Z}_{63} & \bar{Z}_{64} & \bar{Z}_{65} & \bar{Z}_{66} & 0 & 0 \\ 0 & 0 & 0 & 0 & 0 & 0 & R_S & r_o \\ 1 & 0 & 0 & 0 & 0 & 0 & -1 & 1 \end{bmatrix} \quad \begin{bmatrix} \bar{I}_S \\ \bar{I}_{SR} \\ \bar{I}_1 \\ \bar{I}_2 \\ \bar{I}_3 \\ \bar{I}_4 \\ \bar{I}_{in} \\ \bar{I}_o \end{bmatrix}$$

Figure 3.7 Modified Impedance Matrix

where $r_{qn}' = \dfrac{r_{qn}}{\sin^2(\frac{\alpha_n}{2})}$

r_{qn} is the interbar resistance per unit length

α_n is the skew in electrical degrees

$\bar{Z}_{rn}$ is the endring impedance for one ring measured between two adjacent rotor bars for the n^{th} harmonic

$\bar{Z}_{bn}$ is the total bar impedance for the n^{th} harmonic

3.2 Alternative Renumbering Schemes

Having opted for a direct method for solving the system of equations it is then desirable to implement a renumbering scheme that will reduce the storage requirements of the solver and increase the speed at which it operates. There are many different re-ordering algorithms available and each one has its own advantages and disadvantages. A survey of the various techniques currently in use can be found in [29]. The R.C.M., which was used by Ralph and Williamson is considered to be among the better strategies. However it was felt that trying out a more recent algorithm, as well as inventing one or two new schemes, would be worthwhile since they may prove to be superior to R.C.M. for cylindrical problems.

3.2.1 The Gibbs Poole and Stockmeyer Algorithm: The first of the alternative techniques tried was the algorithm due to Gibbs Poole and Stockmeyer [30]. This method uses the same concepts as the R.C.M. scheme in that it treats the finite element mesh as an undirected

graph and generates level structures that are rooted at a given node. The main difference between the two strategies is that the G.P.S. generates far fewer tree structures than the R.C.M. and is therefore much faster. Before discussing the G.P.S. further it is necessary to make several additional definitions to those already made in Section 2.7. Consider the graph G(A) to be split into two sets V(G) where the elements of V are the node points or vertices of the mesh and E(G) with the elements of E defined as the edges that join the vertices together. Thus V consists of N vertices $\{V_o$ --- $V_n\}$ and if $\{V_i, V_j\}$ are members of E then V_i and V_j are adjacent or connected to one another. From the above the following definitions can be made.

1. A "path" of length t is a sequence of edges $\{V_0, V_1\}$.... $\{V_{t-1}, V_t\}$ such that $V_i = V_j$ implies that i = j.

2. A graph G(A) is connected if there is a path connecting each pair of vertices.

3. The "distance" between two vertices V_1 and V_n is the length of the shortest path from one to the other.

4. A "diameter" of G(A) is the shortest path connecting two vertices of maximal distance apart.

Using these definitions the fast operation of the G.P.S. can be explained in the following manner. The R.C.M. produces small profiles by finding firstly the longest thinnest level structure it can and then labelling the nodes of the mesh according to this structure. The reason R.C.M. is so slow is that it has to generate many level structures in order to find an optimal one. The G.P.S. also attempts to produce a level structure of maximal depth. However the G.P.S. makes use of the idea of a "pseudo diameter", that is, a

pair of vertices that are at nearly maximum distance apart. Generating a level structure between two nodes which form a diameter has advantages since the structure thus formed should be of maximal depth.

The end points of the pseudo diameter are found in the following way. Firstly a level structure, L_v, is generated from an arbitrary node of minimal degree. Having done this each of the nodes in the last level of L_v is used to generate other level structures. If one of these is found to be deeper than L_v, then the vertex giving this depth is used to generate a new L_v. When this part of the algorithm is completed one vertex, v, of the pseudo diameter has been found and its associated level structure is known. In order to find the other end point, u, of the pseudo diameter the algorithm takes each of the vertices in the last level of L_v and finds which one yields the smallest width of structure. This process of finding a pseudo diameter generally requires only a few level structures to be generated and is very quick. Calculation of the pseudo diameter results in two level structures L_v and L_u with their associated root nodes v and u. These two trees are then merged to form a structure that displays better characteristics than either L_v or L_u and the resulting tree is then numbered in much the same way as the R.C.M. Details of these last two parts may be found in [30]. The present author has found that the G.P.S. algorithm generally yields matrix profiles that are slightly better than the R.C.M. method. The impressive feature of the G.P.S. strategy is that it takes far less time to arrive at its answer. This is because it uses the idea of "pseudo diameter" which obviates the generation of many level structures, thus it is typically five or six times as fast as R.C.M.

Both the G.P.S. and the R.C.M. methods have the advantage that they are fully automatic; this is because they are mathematical methods that depend only on the topology of the mesh not the geometry.

As an alternative to the mathematical techniques the author invented two geometric renumbering schemes which were based on intuitive ideas rather than firm mathematics. The first of these geometric schemes can be explained in the following manner. Consider the reverse Cuthill McKee algorithm which was discussed in Chapter 2; this method operates on the topology rather than the geometry of the mesh. However its action may be interpreted geometrically in terms of a wavefront that spreads out around a central root node. This wavefront will be irregular since its shape will be dependent on the connectivity of the various regions of the mesh. It was therefore thought that a geometrical numbering scheme based on the idea of a circular spreading wavefront centered on a root node, which would be selected in the same way as the root nodes for the reverse Cuthill McKee method, would stand a good chance of working well on a finite element mesh that was circular. The method is outlined below.

1. Find all the nodes likely to produce an optimal profile in the same way as is done in the R.C.M. algorithm. These will be all the nodes of minimum degree.

2. Use each of these nodes in turn as the root node for a circular wavefront as illustrated in Figure 3.8.

3. Select the steplength for the radial increments.

4. Increment the radius of the circle and find all the nodes enclosed between the circle defined by the present value of the radius and the previous value.

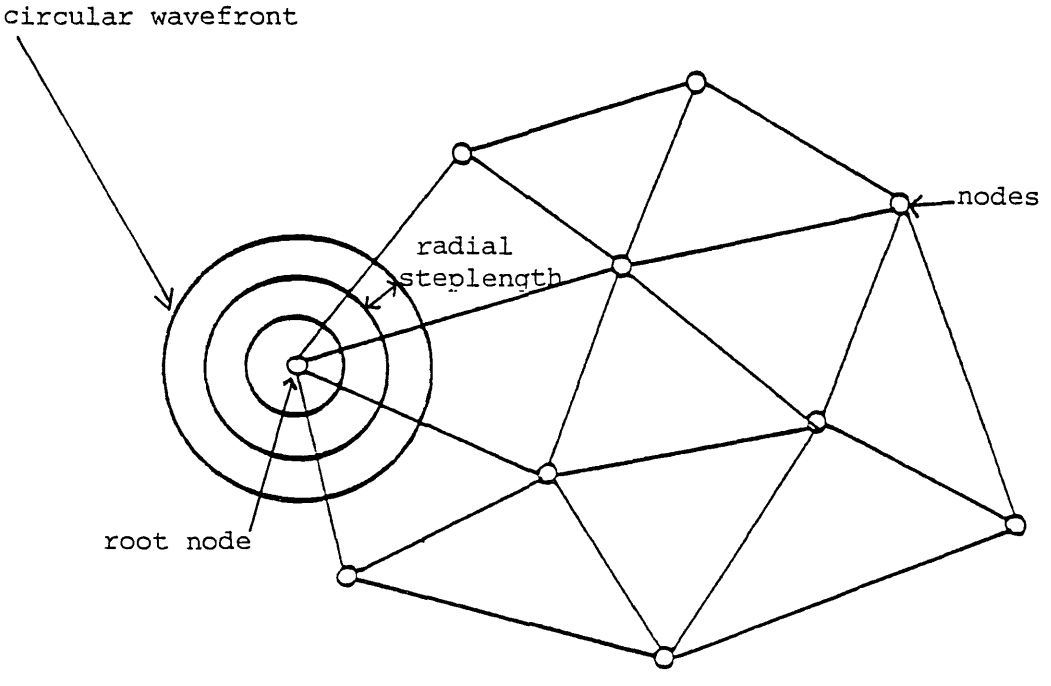


Fig. 3.8 Illustration of a numbering scheme

5. Order the nodes in this band according to increasing theta. If two nodes have the same value of θ they are ordered according to ascending degree.

6. Repeat Steps 4 and 5 until all the nodes have been accounted for.

The second geometric method is based on the motion of two wiper blades sweeping round towards one another on the surface of the a cone. This was thought to be a reasonable idea since most of the finite element grids used represented portions of annuli whose radial boundaries were joined together by a periodicity condition. It can therefore be imagined that the two boundaries are solidly joined forming a cone. The operation of this algorithm may be summarised as follows

1. Work out the angular positions θmax and θmin of the radial boundaries. As is shown in Figure 3.9.

2. Input the angular steplength, θ_s.

3. Define

$$\theta max_{n+1} = \theta max_n - \theta_s$$
$$\theta min_{n+1} = \theta min_n + \theta_s$$

4. Locate all the nodes contained in the zones defined by

$$\theta max_{n+1} \leq \theta \leq \theta max_n$$
$$\theta min_n \leq \theta \leq \theta min_{n+1}$$

These are shown diagrammatically in Figure 3.8.

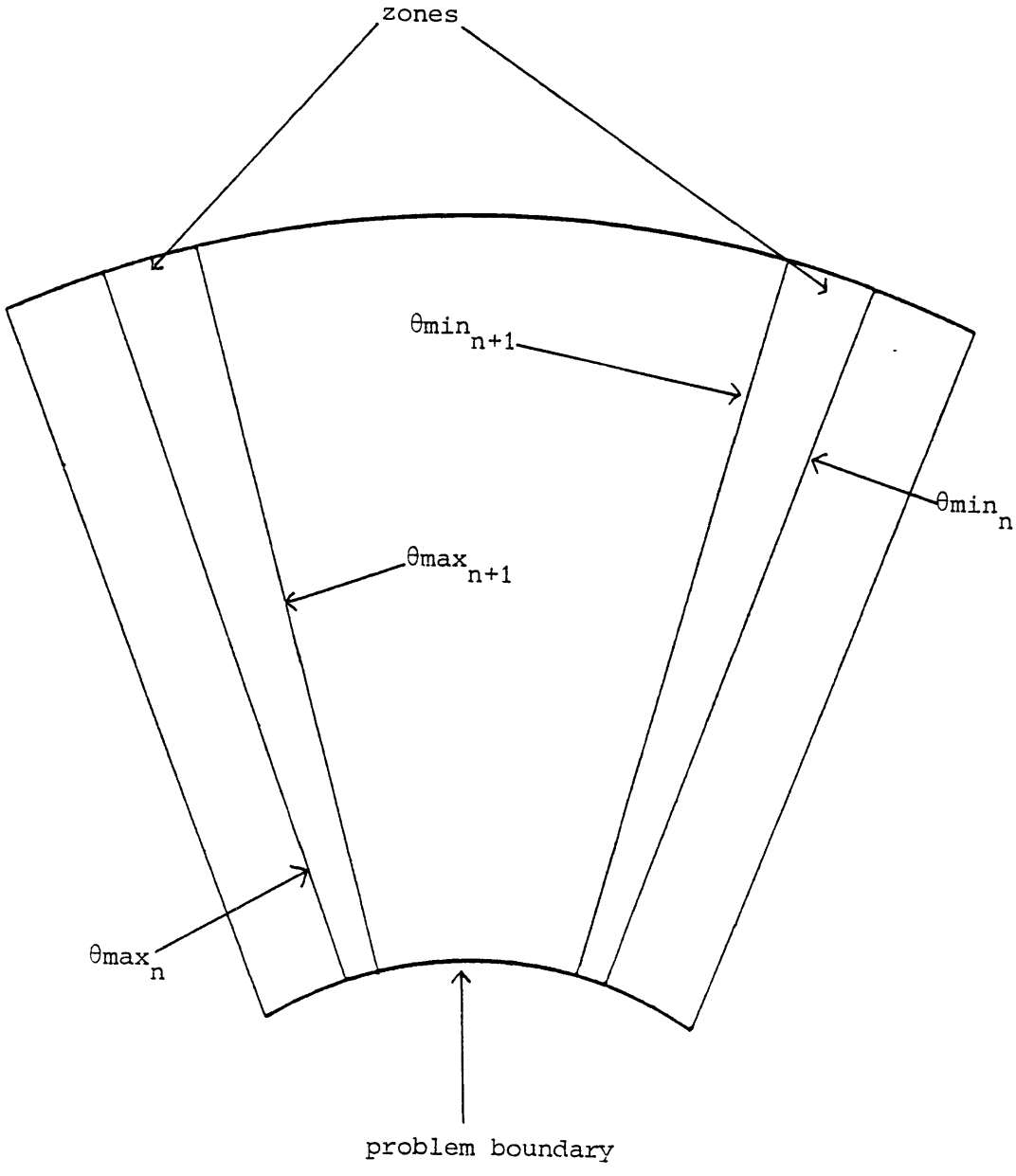


Fig. 3.9

5. Number the nodes found in the zones in terms of increasing radius and if nodes have the same radius then they are arranged in terms of increasing θ.

6. Steps 3-5 are then repeated until all the nodes have been accounted for.

Having implemented four different numbering strategies it is then worthwhile to compare them with one another. This was done by using them to renumber several different finite element meshes. The results of doing this are shown in Table 3.2. From this table it can be seen that on occasions the profiles yielded by the intuitive schemes are smaller than those of the mathematically justifiable techniques. However it is also obvious from this table that the profiles yielded by the G.P.S. method gives consistently good results for a low cost in terms of computer time. It is therefore the preferred method.

From the table the author concludes that for any given mesh geometry it would be possible to concoct a geometrical numbering scheme which would yield a profile that would be slightly better than that obtained by using a mathematical technique. But for overall use the mathematical schemes, and in particular the G.P.S. are more reliable and yield acceptable profiles in nearly all circumstances encountered. However the geometric algorithms are very simple to try out and are not costly to run. It is therefore a good idea to use both types of technique on a given problem and to use the best result.

RENUMBERING SCHEME

Mesh	Number of Equation	Before Renumbering	Gibbs Poole Stockmeyer		Reverse Cuthill McKee		Circular Wavefront		Wiper Blade Motion	
			Profile	Computer Time Taken	Profile	Computer Time Taken	Profile	Computer Time Taken	Profile	Computer Time Taken
1	708	159448	39750	175	39662	562	37134	172	43902	120
2	826	222699	46727	231	53400	650	41547	182	39235	165
3	344	38272	6338	47	7284	132	6388	40	6864	37
4	490	73531	13337	80	13325	170	30899	70	14575	53
5	328	33834	9194	55	8362	145	8352	27	14676	31

Table 3.2

3.3 Alternative Solution Technique

The use of an iterative scheme has one big advantage. This is that no zeros in the system matrix need to be stored on the computer. Consequently, the sparsity exhibited by matrices arising from finite elements can be fully exploited. The main drawback attached to using iterative methods is that they are generally slow to converge to a solution and sometimes they do not converge at all. However it was thought that it was worthwhile to try one out because of the potential savings in computer storage.

The method of conjugate gradients has recently received the attention of numerous authors [31],[32], and because it appeared rather attractive it was decided to implement it. The computer code which was written was based on the work of Jacobs [31] and Kershaw [33] utilising an incomplete Choleski factorisation of the system matrix to reduce its eigenvalues to approximately unity before the iterations started. This is known as preconditioning the system matrix. The conjugate gradient algorithm was compared with a Gaussian elimination technique on a typical matrix arising from a finite element analysis of an electrical machine. The matrix was split into its real and imaginary parts in order that a Newton process could be used to account for the nonlinearity in the ironwork. The results are shown below.

Method	Number of Equations	Computer Storage Required for Method	Time Taken for One Solution of in seconds
Conjugate Gradients	708	25632	3746
Direct Solve	708	39750	45

Table 3.3

Clearly the extra time taken by the conjugate gradients is unacceptable. Furthermore a harmonic analysis of a machine requires several resolves of the system matrix using different right hand sides. When using a Gaussian elimination this is easily done at reduced cost since the triangular factors have been stored. Whereas with an iterative scheme the whole process has to be started again, which will carry a further time penalty.

There seem to be three factors which combine to make the conjugate gradient approach less effective in the problems considered here. The first of these is attributable to the matrix being split into its real and imaginary parts with the two parts being coupled together through the reluctivity. This point is commented on by Jacobs [31]. The second is thought to be due to the intricate arrangement of materials in a machine, which will tend to spread out the eigenvalues of the system matrix and make the Choleksi factors less effective in clustering the eigenvalues of the resultant system round unity. Finally it is well known by users of Conjugate gradients that the algorithm becomes relatively faster as the order of the system being solved goes up. In matrix terms 708 equations represent a fairly low order system.

Development of conjugate gradient methods is still continuing and recently a new and faster algorithm has been reported by Markham [34]. However it is my opinion that these developments will have to go much further before a conjugate gradient algorithm that will compete with Gaussian elimination, on the types of problem described here, is produced.

3.4 Conclusions to Chapter Three

This chapter has discussed the improvements to the method of analysis developed by Williamson and Ralph. The main advance has been the replacement of the Nag subroutine by the impedance method which is based on physical rather than mathematical concepts. This has two advantages. Firstly it makes the package far more general than before and secondly it has been shown, on the test problem, to reduce the computer time required for the analysis by a factor of one hundred. Another significant improvement has been the development of several alternative renumbering strategies which have reduced both the amount of computer time and memory needed for the analysis.

CHAPTER 4

RESULTS

4.1 Comparison with Previous Work

As a first step towards verifying the impedance method of predicting the next current set as opposed to using the Nag minimisation routine it was decided to repeat the analysis of the reversing shaded pole motor presented in [7]. A diagram of the machine is shown in Figure 4.1 and a table of the machine data can be found in Table 4.1.

Using the same machine and analysing it using the same finite element grid as Williamson and Ralph allows their work to be used as a benchmark, in order to determine how well the new scheme is performing. The mesh used in the analysis is shown in Figure 4.2. Figures 4.3-4.5 show the variations of input power, current, and torque with speed, calculated using the method of Williamson and Ralph and the method described in Chapter 3. These curves also include the experimentally measured variations, for purposes of comparison. Examination of Figures 4.3-4.5 shows that the modified method gives good agreement with the experimental results with an error of 5% occurring on the peak torque and errors of less than 10% throughout the characteristics of current and power. It can also be seen from the performance characteristics that an absolute agreement between the two computed curves is not achieved. The author is not entirely sure why this is but considers the match sufficiently good

Rated voltage (rms)		240 V
Frequency		50 Hz
Number of Poles		4
Number of rotor bars		24
Airgap length		0.37 mm
Machine length		50.81 mm
Carter coefficient		1.15
Stacking factor		0.965
Rotor skew (electrical degrees)		60
Number of turns on main pole		411
Number of turns on auxiliary pole		245
Stator winding resistance at 90°C		120 ohm
Stator winding reactance		3 ohm
Resistivity of LM6 at 90°C		6×10^{-8} ohm-m
Rotor bar resistance at 90°C		2.03×10^{-4} ohm
Endring resistance at 90°C		2.94×10^{-4} ohm
Inter bar resistance		5.93×10^{-5} ohm-m
Shading ring details	Actual	Modelled
Length	4.44 mm	3.81 mm
Width	1.25 mm	1.46 mm
Copper area	5.55 mm^2	5.56 mm^2
Resistance		4.43×10^{-4} ohm

Table 4.1

Summary of machine details

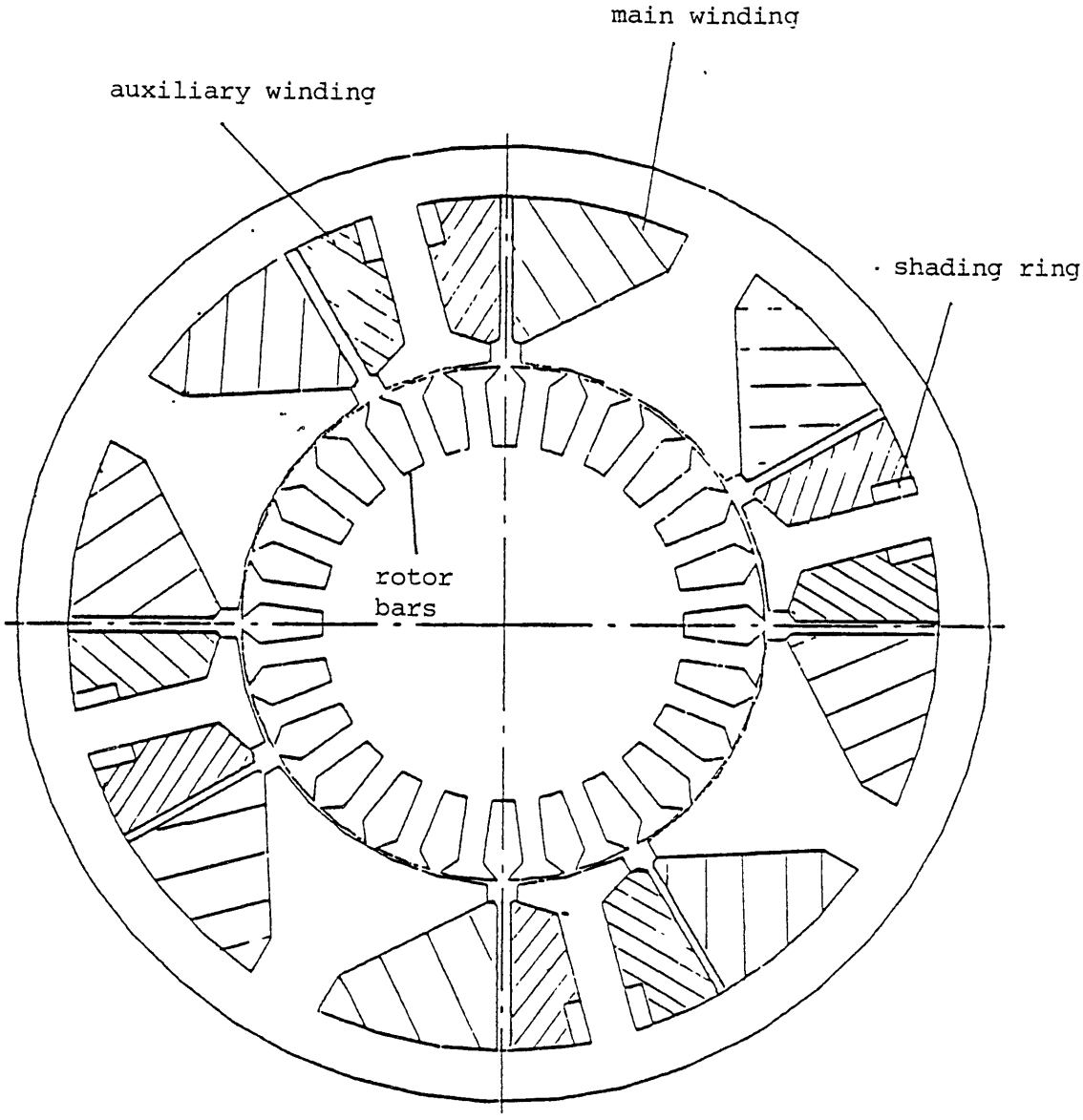


Figure 4.1

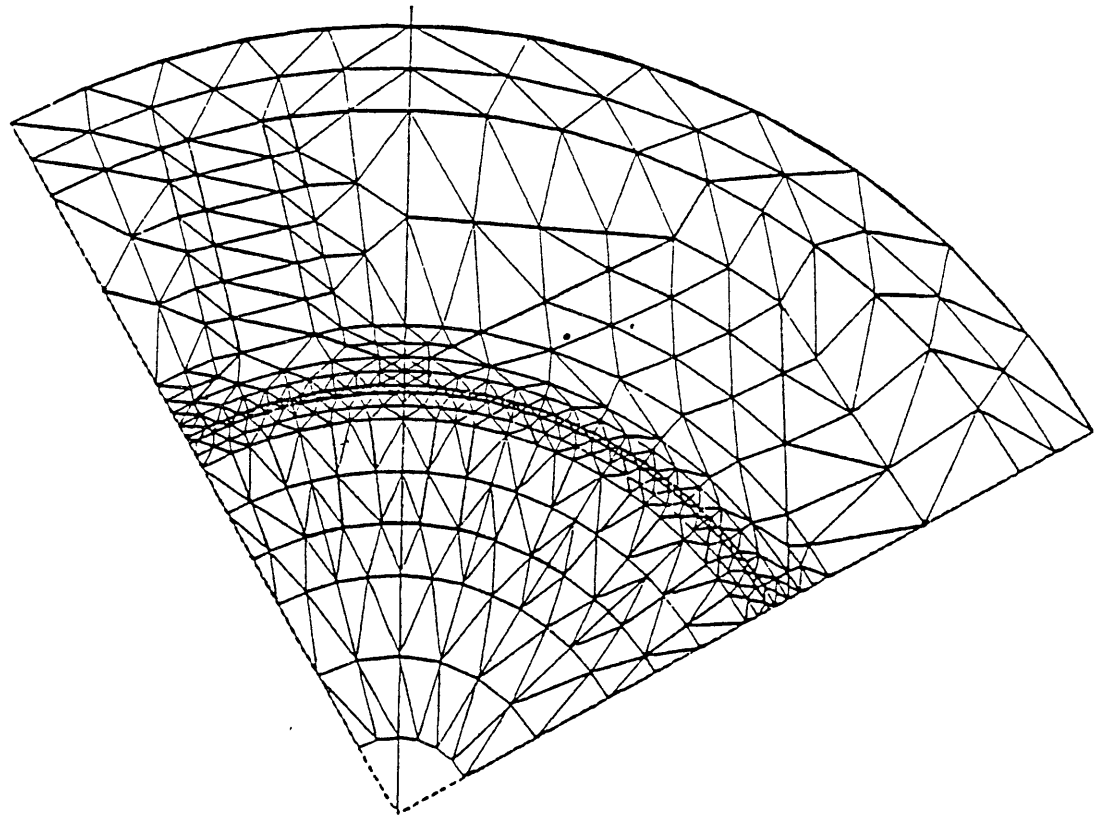


Fig. 4.2 Finite element mesh

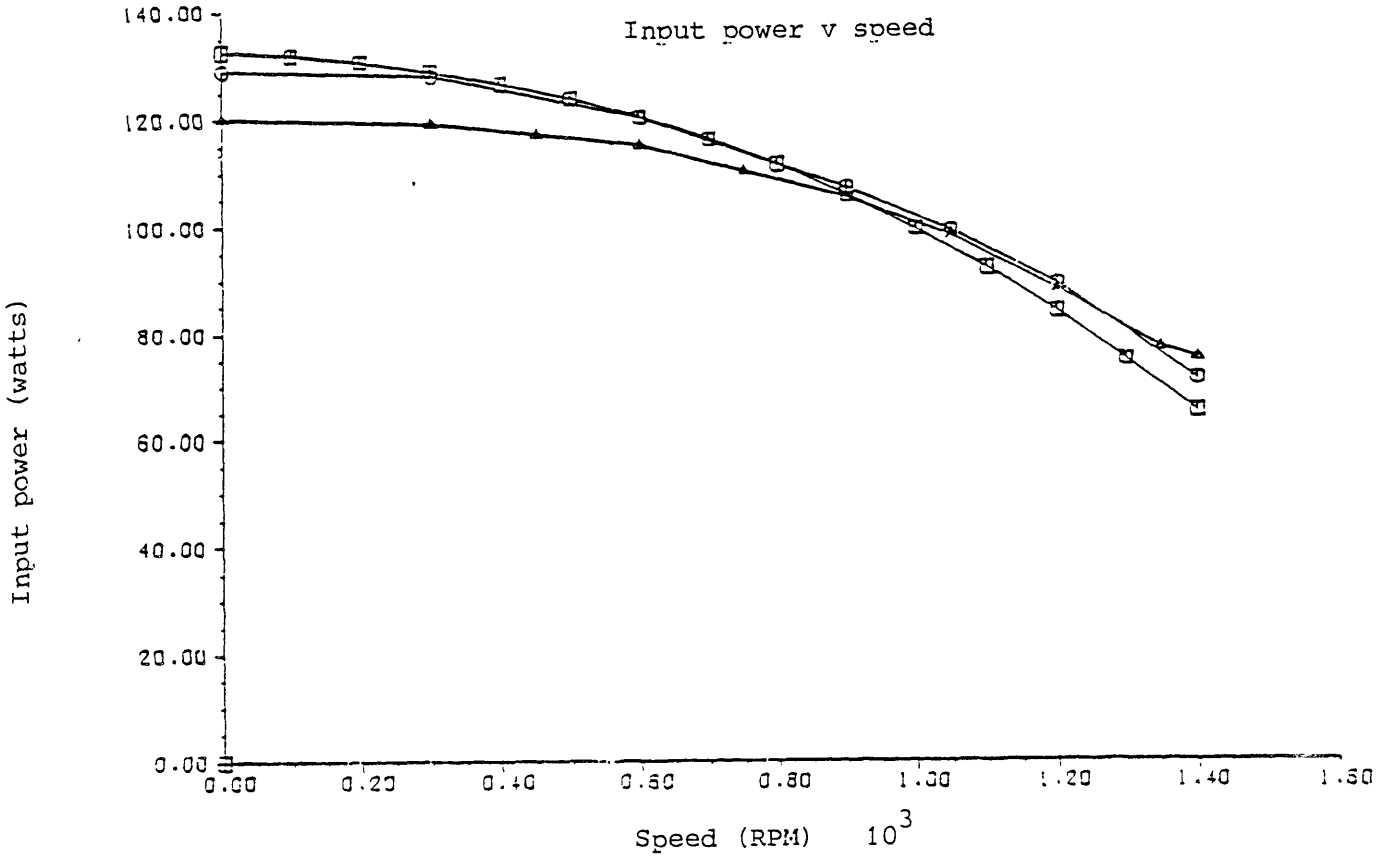


Fig. 4.3

□ impedance method

o previous method

Δ experimental

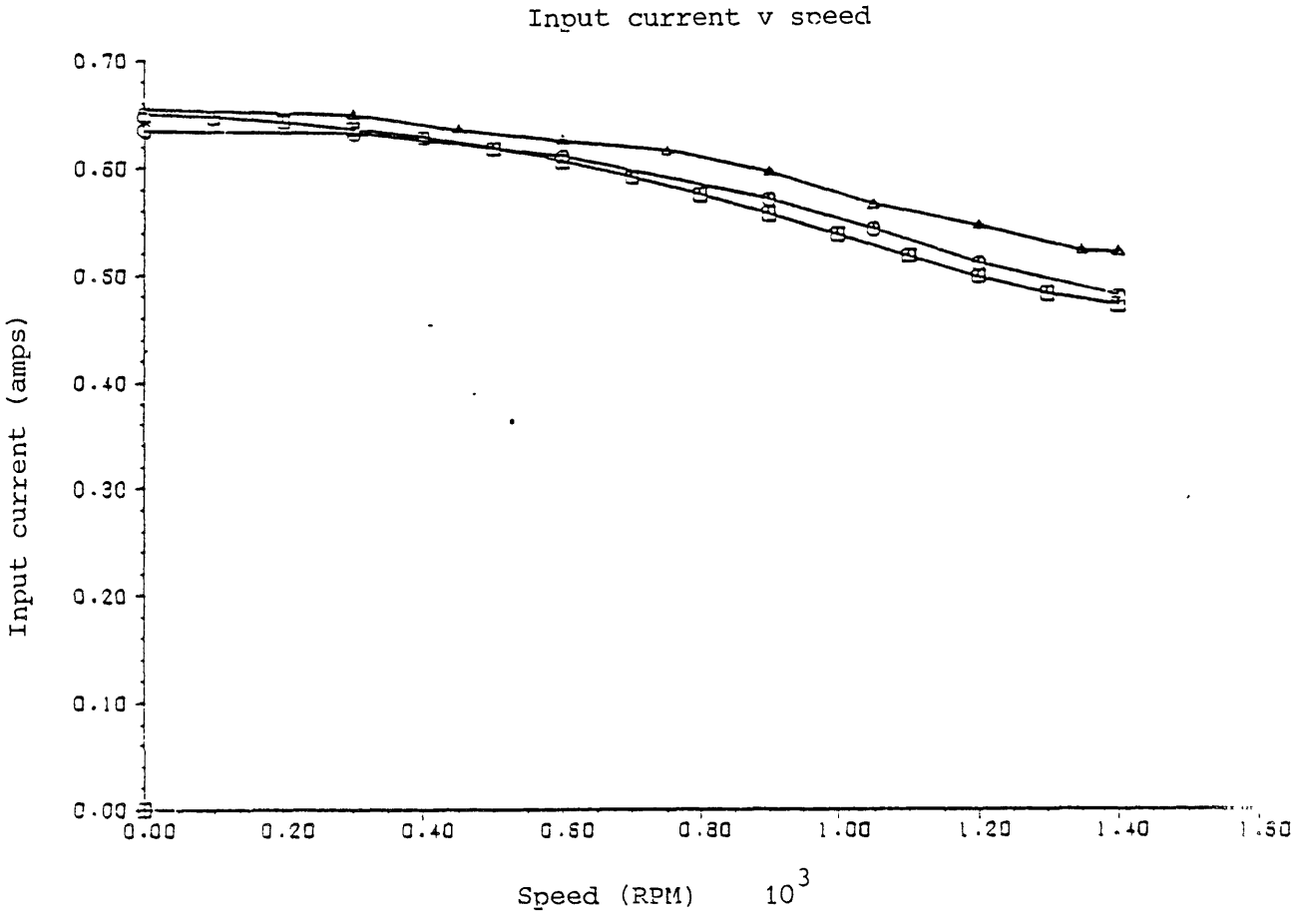


Fig. 4.4

□ Impedance method

o Previous method

Δ Experimental

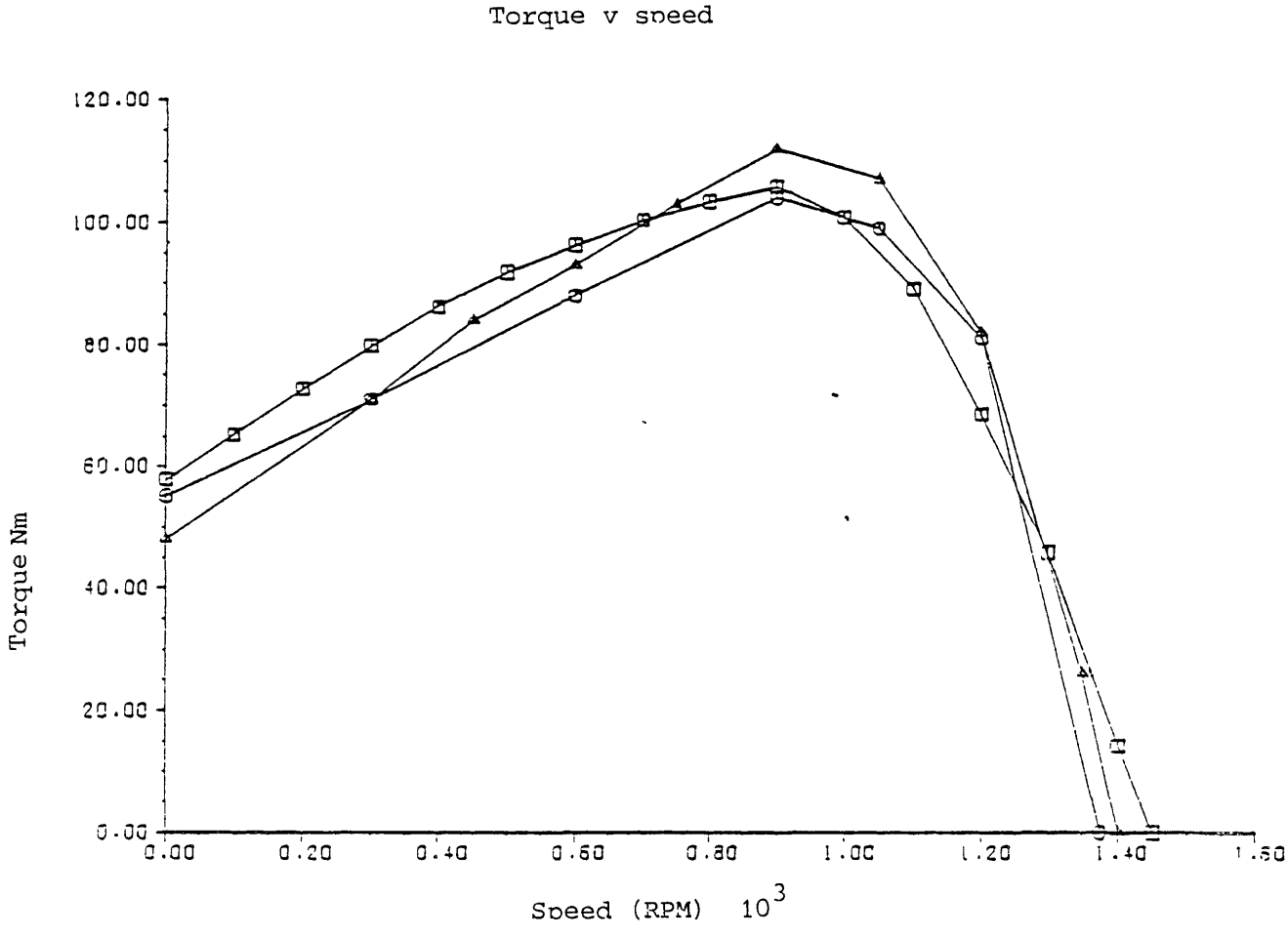


Fig. 4.5

□ Impedance method

o Previous method

Δ Experimental

to enable the technique developed here to be applied with some confidence to other motors. Whilst figures 4.3-4.5 show that the new method gives very much the same computer predictions as the old method, the real advantage of using a minimisation technique based on the physics of the motor rather than a least squares method becomes evident when Table 4.2 is examined. This shows that the impedance based technique is approximately 150 times as fast as the previous method when there is no old solution stored to approximate the next step in the procedure, and is 100 times as quick when going from one point to the next. This decrease in the solution time is important since it makes simulation of these types of devices more economically viable.

4.2 Analysis of a Shaded Pole Motor

Whilst the reversing shaded pole motor provided the impetus for the development of the finite element analysis, it will be appreciated that such a machine must be regarded as something of a novelty. If the finite element analysis is going to be the basis for an industrially-useful tool it is necessary that it should be equally applicable to more commercial types of machine. To this end it was decided that the method should be further tested on a commercial shaded pole motor, which incorporated a number of design features that would make it difficult to analyse by more conventional means. A diagram of the motor chosen is given in Figure 4.6.

The first feature which normally causes difficulty is the use of closed rotor slots, which will saturate and consequently make the rotor leakage reactance highly nonlinear. Secondly it has a magnetic

Method	Time taken to obtain a point on the performance characteristics using CDC 174 machine in seconds	
	No Starting Point	Starting Point
Least Squares	12974	3471
Impedance	85	33

Table 4.2

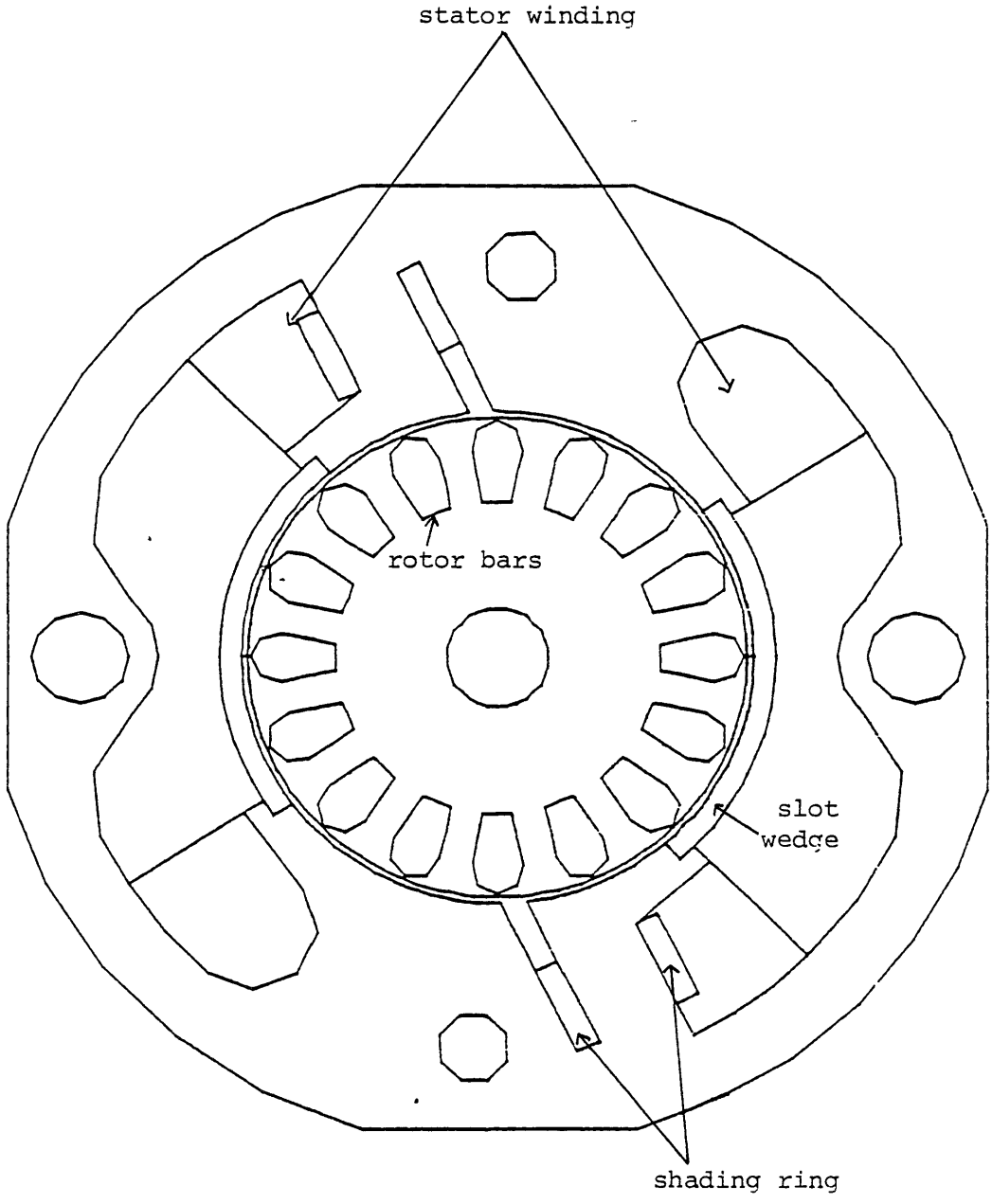


Fig. 4.6 Schematic of shaded pole motor

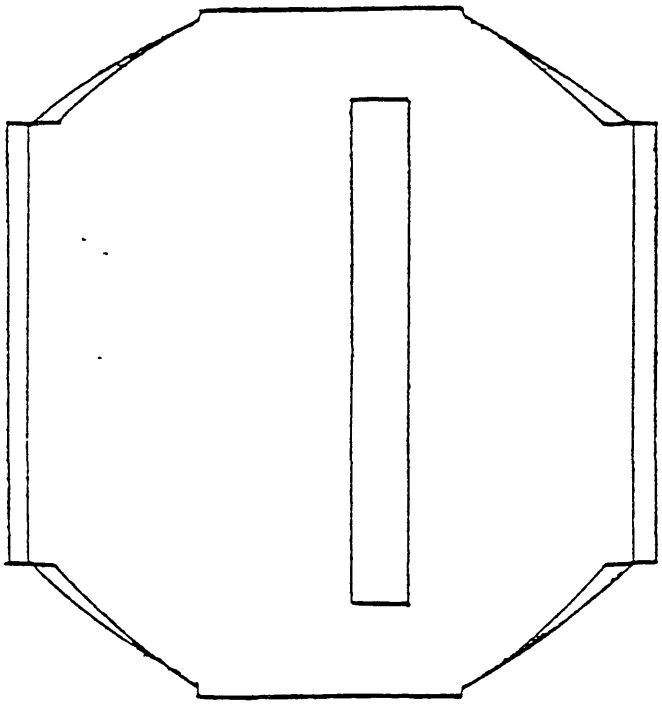


Fig. 4.7 Magnetic slot wedge

slot wedge which is manufactured from mild steel and has a slot cut in it. The wedge is shown as a plan view in Figure 4.7. It will be appreciated that the presence of the cut in the wedge makes it virtually impossible to model the wedge accurately in two dimensions. Therefore it was initially removed to simplify the analysis. Removal of the wedge seriously degrades the performance of the machine and has the effect of making the stator salient. The modification to account for stator saliency has been considered in Section 3.1.4. The third and final complication is due to the length of the machine, which is only 1.5 cm; this makes the end effects more important and these are not explicitly modelled.

4.3 The Test Motors

Six nominally identical motors were supplied by the manufacturer. Because of normal manufacturing tolerances each one differed slightly from the other. The table of machine data in 4.3 gives the mean values of the various parameters of interest. The manufacturer also supplied data concerning the conductivity of the rotor bars, the magnetic characteristics of the laminations and all the machine dimensions.

4.4 Experimental Apparatus and Technique

The torque speed characteristics along with the input power and current were measured using a 'Magtrol' system, which has a manufacturer's quoted accuracy of 0.25% of full scale. The dynamometer used is rated at 18m Nm which means that the measurements

Rated voltage	220 V
Frequency	50 Hz
Number of poles	2
Number of rotor bars	16
Airgap length	0.4 mm
Machine length	15 mm
Rotor skew	1.6 slots
Number of turns on stator winding	2000
Stator winding resistance at 90°C	680 ohm
Rotor bar conductivity at 90°C	2.77×10^{2} s/m
Endring conductivity at 90°C	2.77×10^{2} s/m
Shading ring resistance at 90°C	2.57×10^{-4} ohm
Interbar resistance	3.2×10^{-4} ohm-m

Table 4.3

should be accurate to within 0.045mNm. All six motors were tested at their normal operating temperature, which was found to be 76°C. A first set of tests was carried out with the stator slot wedges in place and a second set with them removed. A reduced voltage test was also performed on the motor with the wedges in. The data from the 'Magtrol' system was recorded on a Gould OS4020 oscilloscope that was connected to an LSI-11 mini computer. The tests performed using this system were found to be very repeatable. For example, if the same test was performed twice on the same motor then the recorded performance characteristics would not vary by more than 2%.

4.4.1 Friction and Windage: The torque predicted by the theoretical method is usually the electromagnetic torque. This will always be larger than the shaft torque since it does not include the losses due to friction and windage. These losses must therefore be measured and subtracted from the computed torques. The friction and windage torques can be calculated if the inertia of the rotor of the machine, and the inertia of the dynamometer, is used with the information obtained from a run down test. The inertia of the rotor was measured. This figure was added to the manufacturers quoted value for the inertia of the dynamometer. The friction torque was then calculated from

$$T_f = J\ddot{\theta} \qquad (4.1)$$

$\ddot{\theta}$ was found by running the motor up to speed on the dynamometer then switching the dynamometer off and recording the decay of speed with time. $\ddot{\theta}$ is then obtained by measuring the gradient of this curve. The variations of T_f with speed are shown for the motor with the

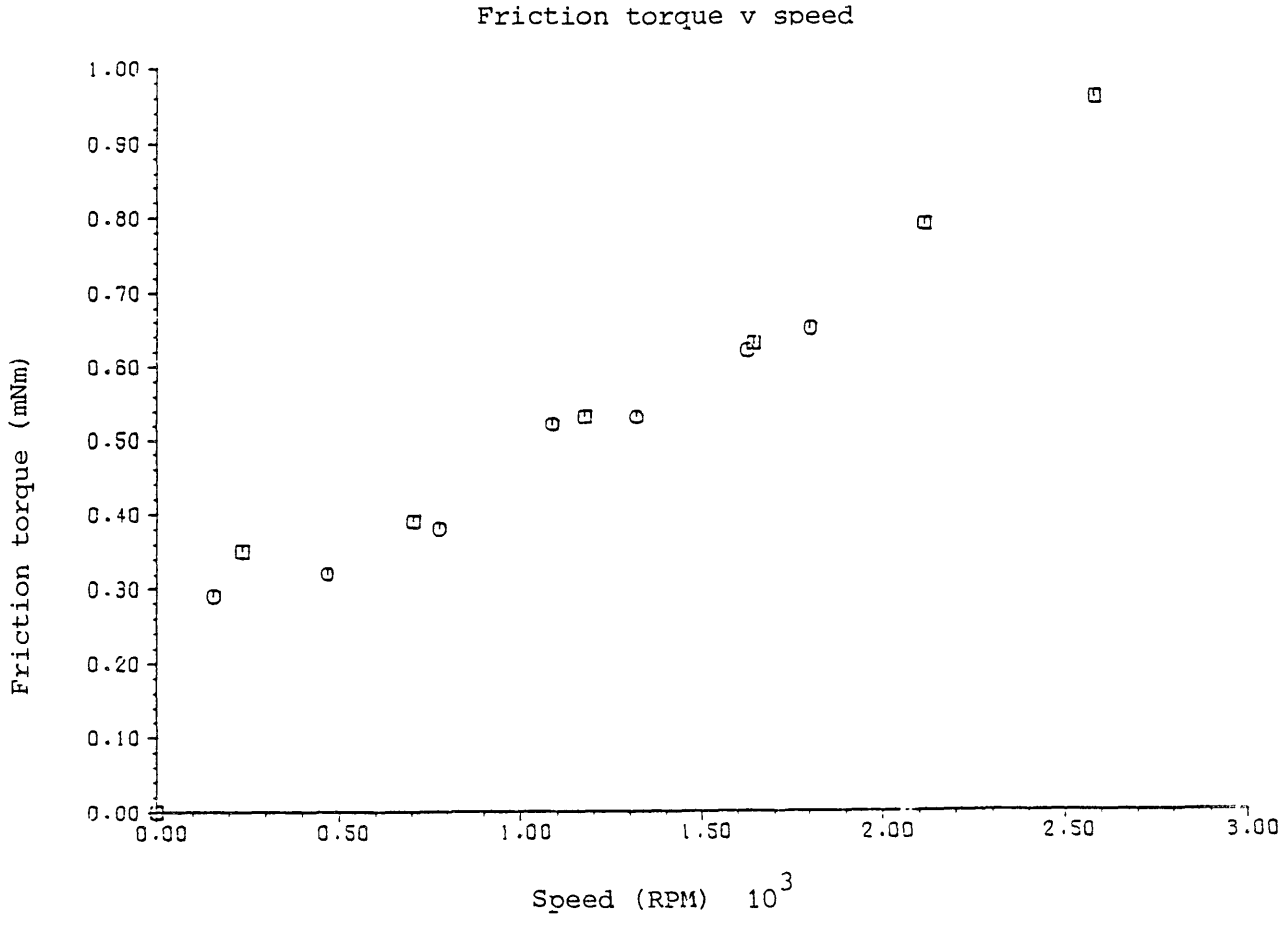


Fig. 4.8

□ with wedges in place

o with wedges removed

wedges in and without the wedges in Figure 4.8. These characteristics were subtracted from the torques calculated in the program.

4.4.2 Inter-bar Resistance: If the value of inter-bar resistance is known then the bar impedances can be modified as outlined in Section 3.1.8 to take account of the presence of inter-bar currents. The difficulty with inter-bar resistance is that its value is very uncertain and can vary a great deal depending on how the rotor was formed. For instance if during the pressure casting process some molten aluminium is forced in between the rotor laminations more inter-bar current will result because of the reduced iron path.

For the present work the inter-bar resistance was determined by turning the endrings off the rotor and measuring it in the same way as in reference [44]. The value obtained by this method was then used in the calculations. In addition calculations were made using inter-bar resistances of 10 times and a 10th of the measured value. This was done in order to assess the sensitivity of the design to this essentially indeterminate parameter.

4.4.3 Rotor End-ring Resistance: This can be calculated using the technique of Trickey [48]. However, the method outlined in Chapter 6 was preferred since it was thought that this would lead to higher accuracy. The results obtained in Chapter 6 are incorporated in the program by means of a look up table and are added to the bar resistance to give an effective value of bar resistance for each harmonic.

4.5 Comparison of Computed and Experimental Results

The finite element meshes used for the motor with the wedges present and absent were topologically the same. The grid used is shown in Figure 4.9 and is known as the 'full bar' model. It was thought that the position of the rotor may influence the computed results obtained from a steady state analysis. The rotor mesh was therefore moved round by one half of a rotor slot pitch giving what is termed as the 'half bar' model, shown in Figure 4.10.

4.5.1 The Full Bar Model: Figures 4.11-4.13 compare the computed results and the experimental measurements of input power, input current and torque for the motor with the wedges removed. Only two sets of experimental results are shown on each graph, although six motors were tested, these define the largest differences found between the motors tested under the same conditions. From the graphs it can be seen that excellent agreement is obtained between the experimental and computed curves for input power and current with errors typically being in the region of 3%. In the case of the torque curve the computed result lies in between the limits of the experiment, but has a slightly different shape. This is thought to be due to under prediction of the third harmonic torques. Only one computed curve is shown in each graph because varying the inter-bar resistance was found not to affect the characteristics significantly. The absence of a variation is thought to be due to the rotor being short when compared to its pole pitch. Figures 4.14-4.15 give typical flux plots at the instants of peak and zero voltage for the full bar model.

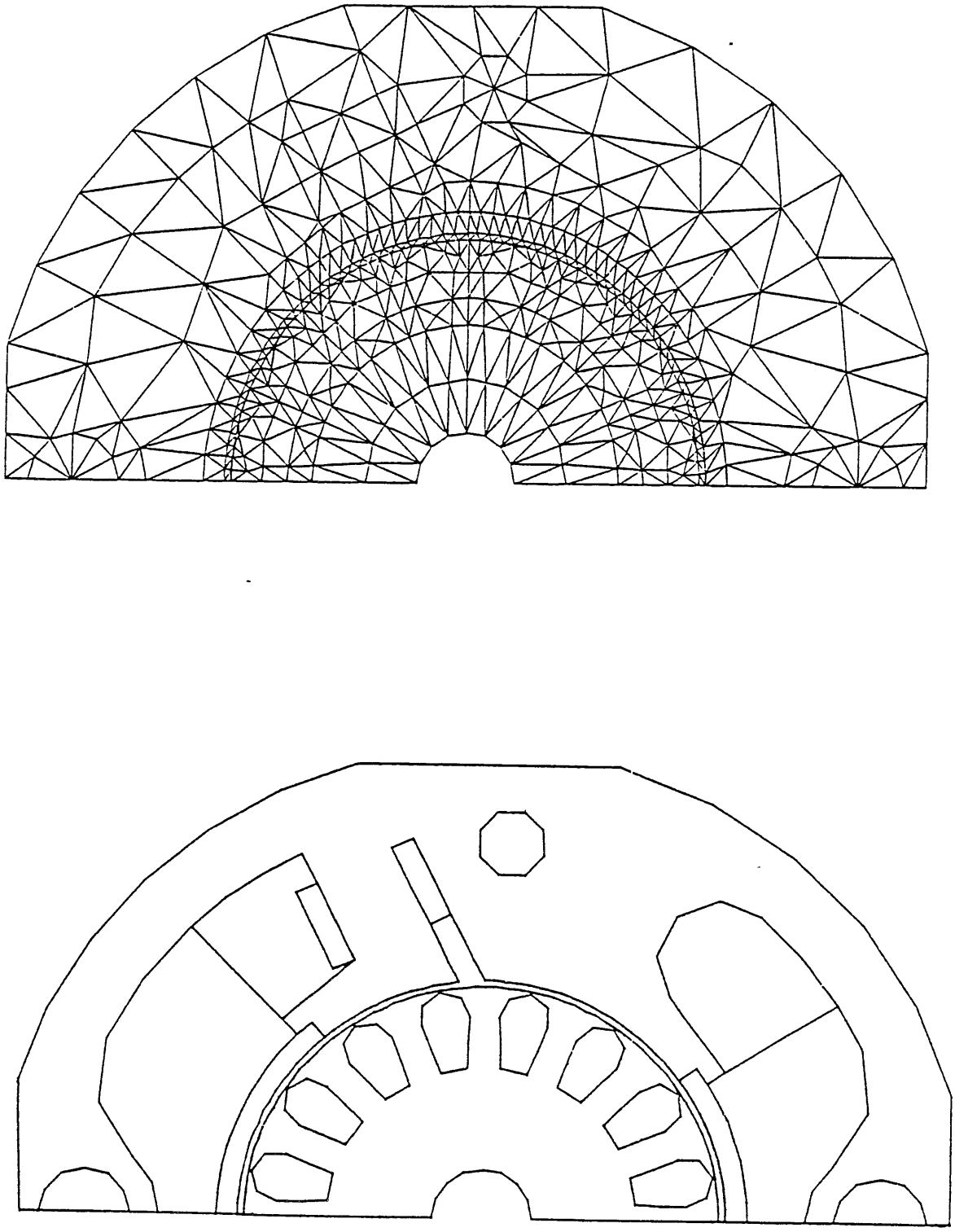


Fig. 4.9 An Outline of the Full Bar Model Together with the Finite Element Mesh.

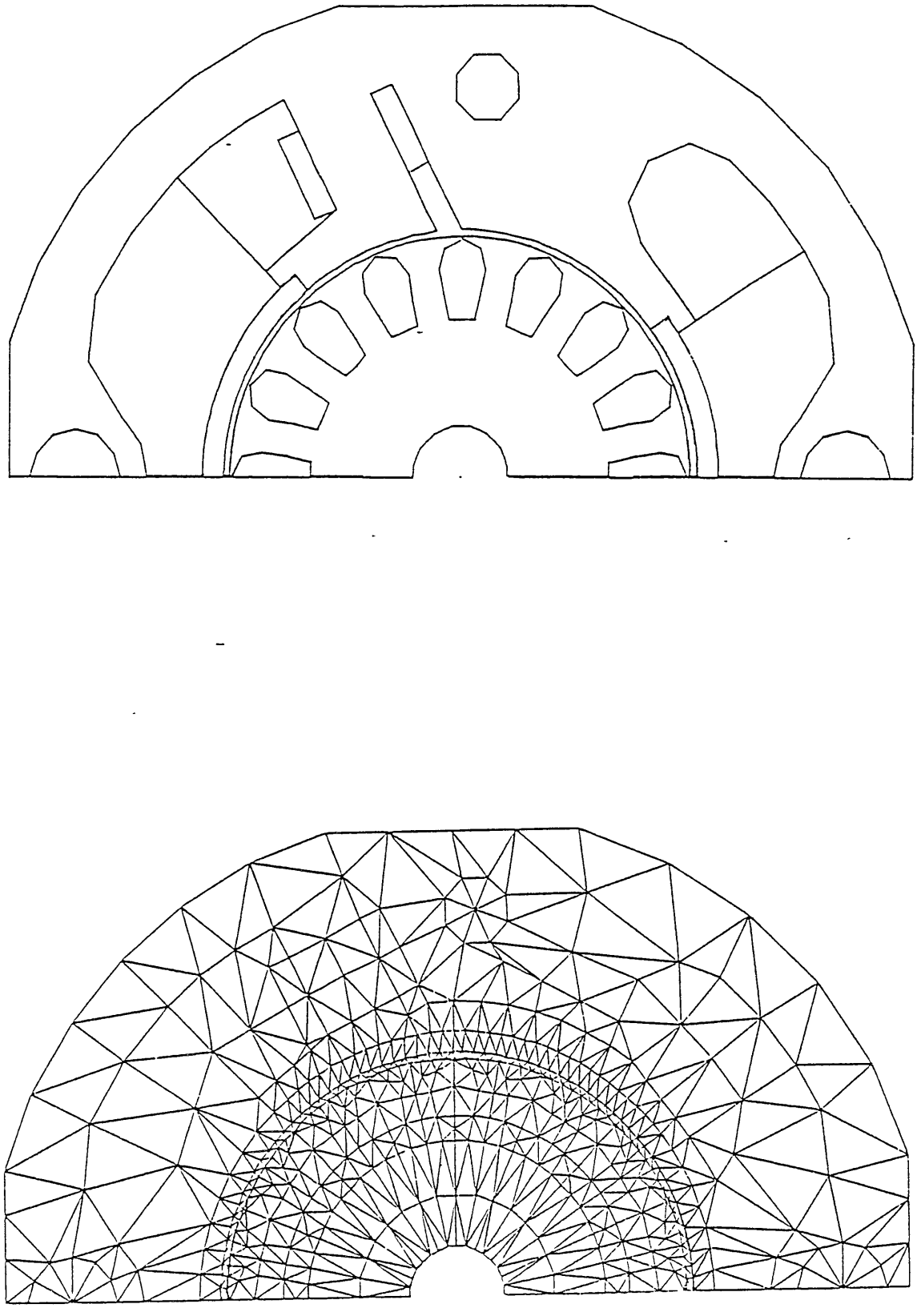


Fig. 4.10 An outline of the half bar model together with its finite element mesh.

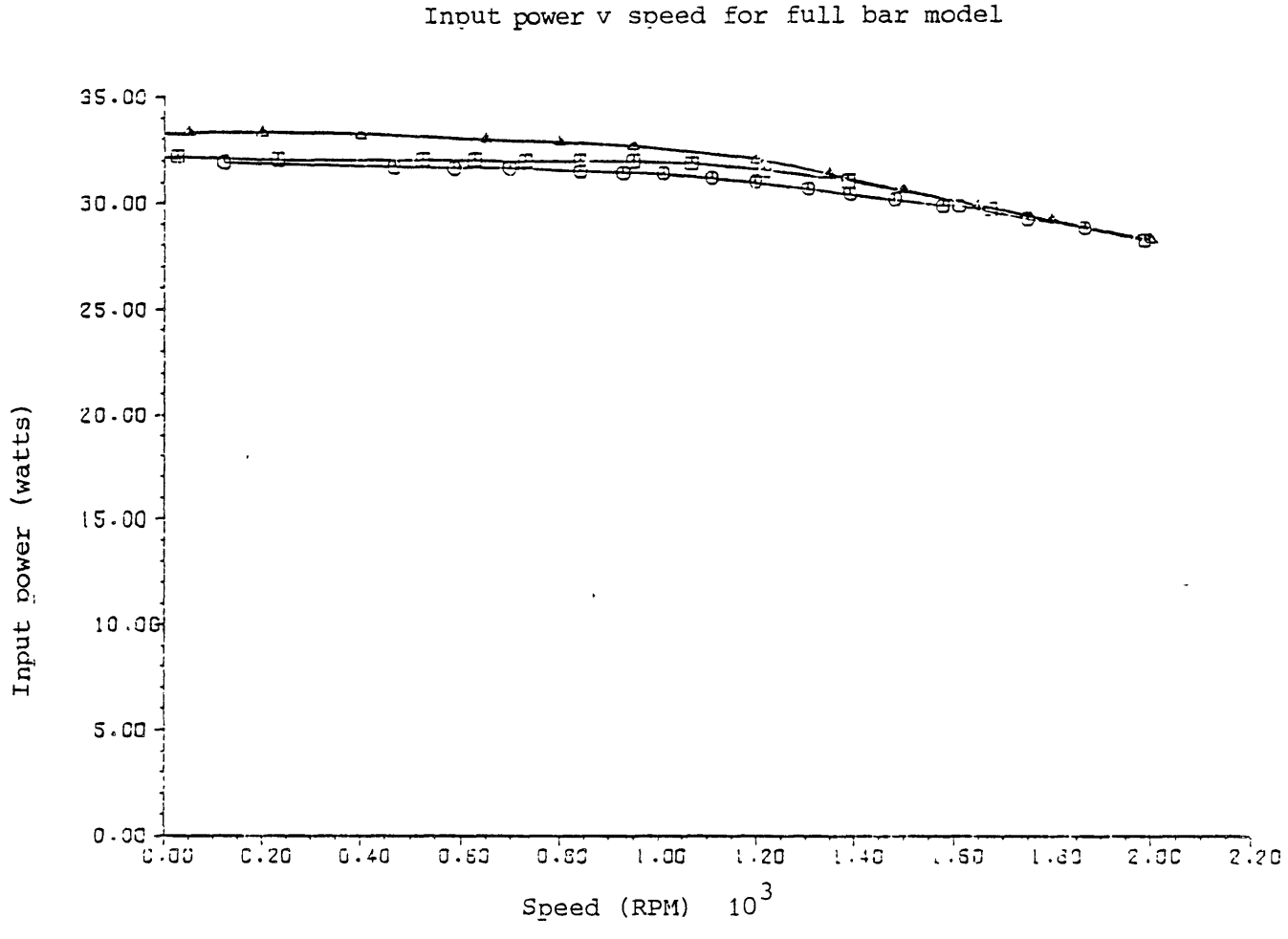


Fig. 4.11

□ Upper experimental limit

o Lower experimental limit

Δ Computed

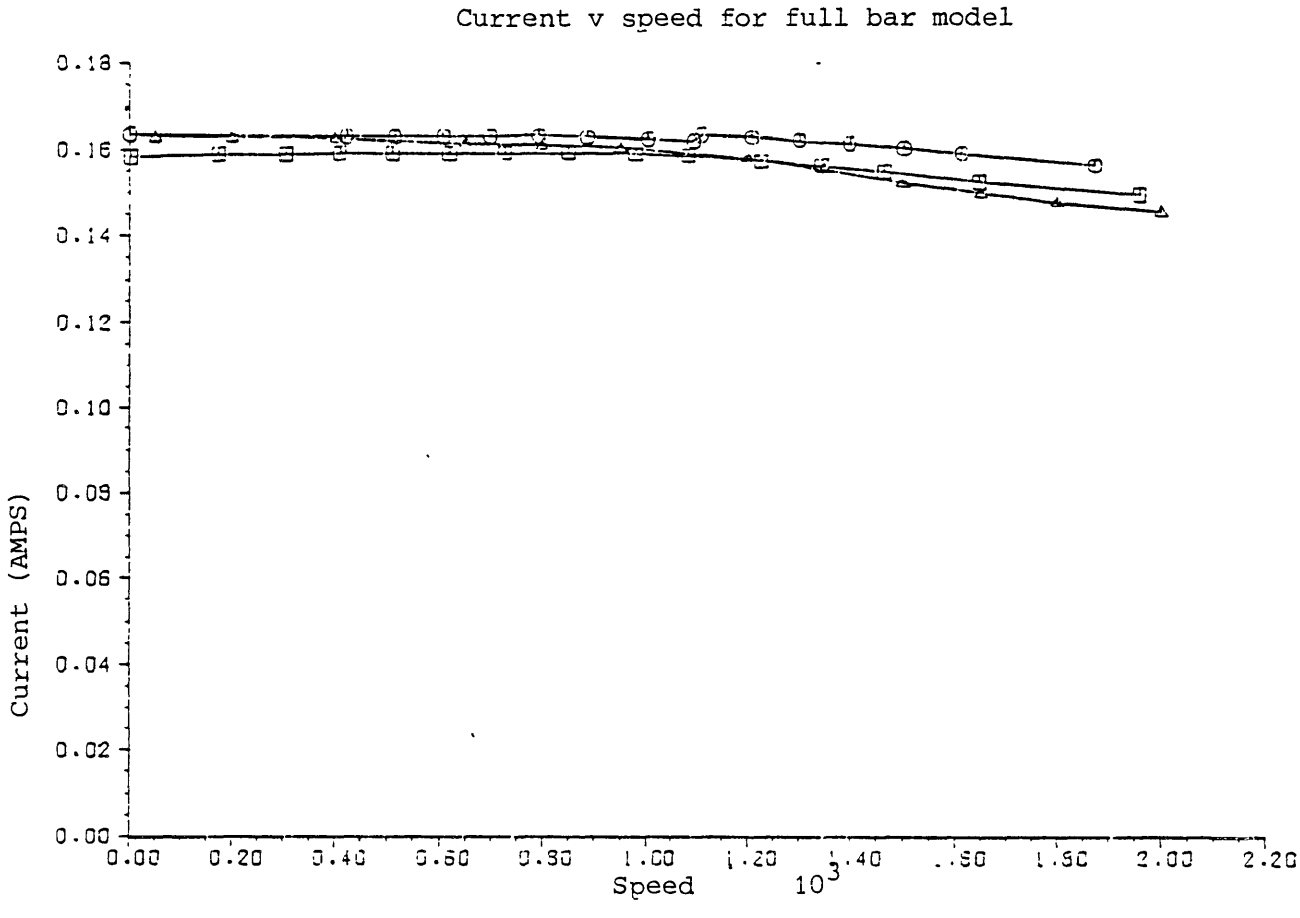


Fig. 4.12

o Upper experimental limit

□ Lower experimental limit

Δ Computed

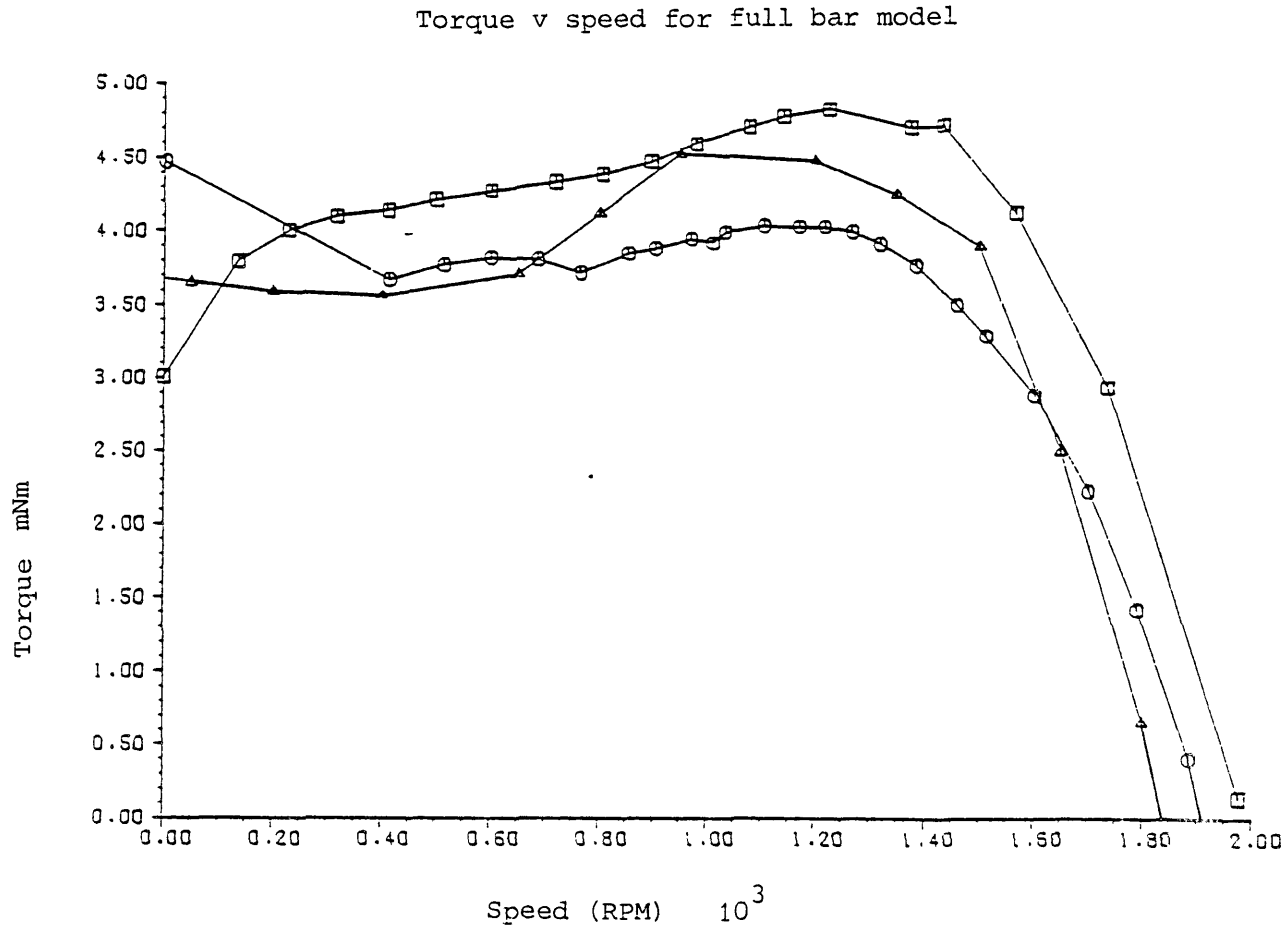


Fig. 4.13

□ Upper experimental limit

o Lower experimental limit

Δ Computed

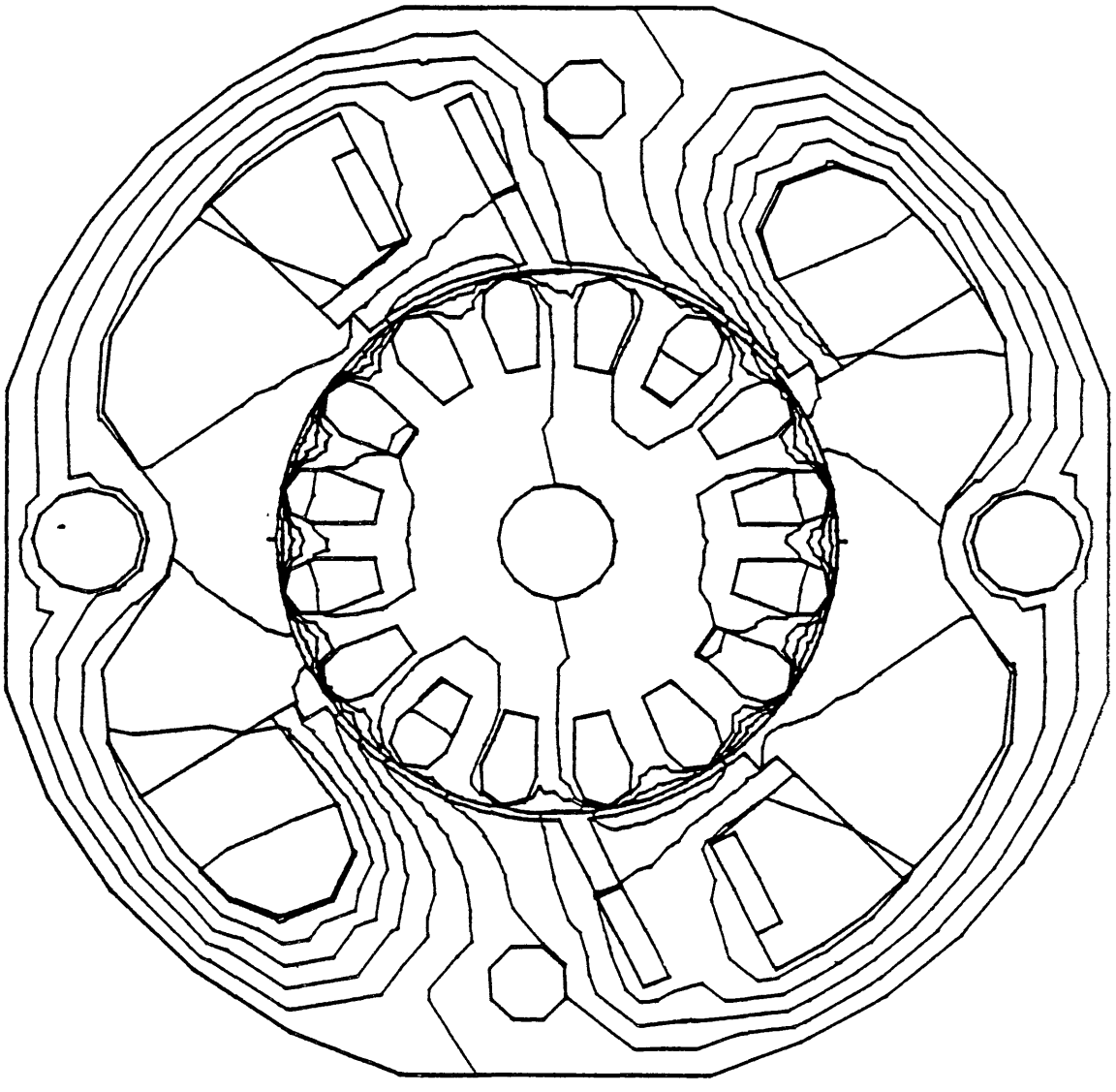


Fig. 4.14 Flux plot for instant of peak voltage

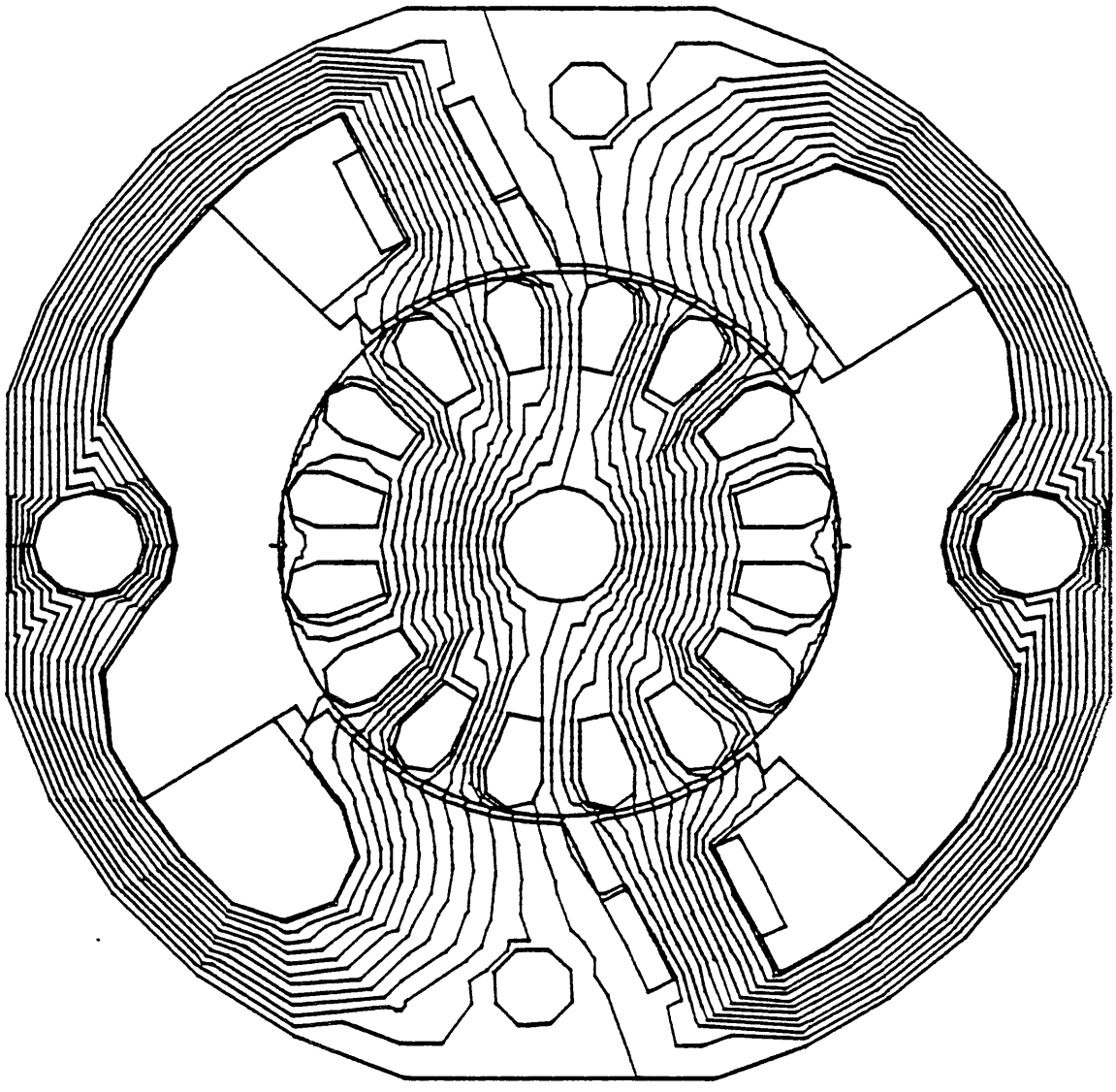


Fig. 4.15 Flux plot for instant of zero voltage

4.5.2 The Half Bar Model: The rotor was moved round by one half of a rotor slot pitch and the characteristics were recomputed. The graphs of power and current against speed can be found in Figures 4.16-4.17. Comparison of these with figures 4.11-4.12 reveals that the position of the rotor has not affected the input power and current significantly. Again only one computed result is shown since various values of inter-bar resistance did not influence them at all. The torque calculation, on the other hand, was affected by moving the rotor but the characteristic produced still lay between the experimental limits in Figure 4.18. It is the change in shape of the torque that is noticeable. This is thought to be mainly due to the change in the magnetic flux paths in the rotor which will produce a change in the coupling impedances and therefore a change in the magnitude of the harmonic currents that will be reflected in the torque calculation in equation (3.44). Typical flux plots for the half bar model are shown in Figures 4.19 and 4.20. The observable feature of Figure 4.21 is that the different values of inter-bar resistance produce a dip in the characteristic at about 1200 r.p.m.. This again is thought to be attributable to the changes in the flux paths modifying the coupling impedances and making the impedance matrix more sensitive to small changes due to, for example, the inclusion of inter-bar currents.

4.5.3 Modelling the Motor with the Wedges in Place: This was considered to be more difficult than when the wedges were not present because of the cut in the wedge, which makes the motor three dimensional in terms of the analysis. The details of the modelling of the wedge can be found in Appendix 8.2. Just as in the previous example the rotor was modelled in two different positions so that the importance of the rotors position in space could be assessed. Three

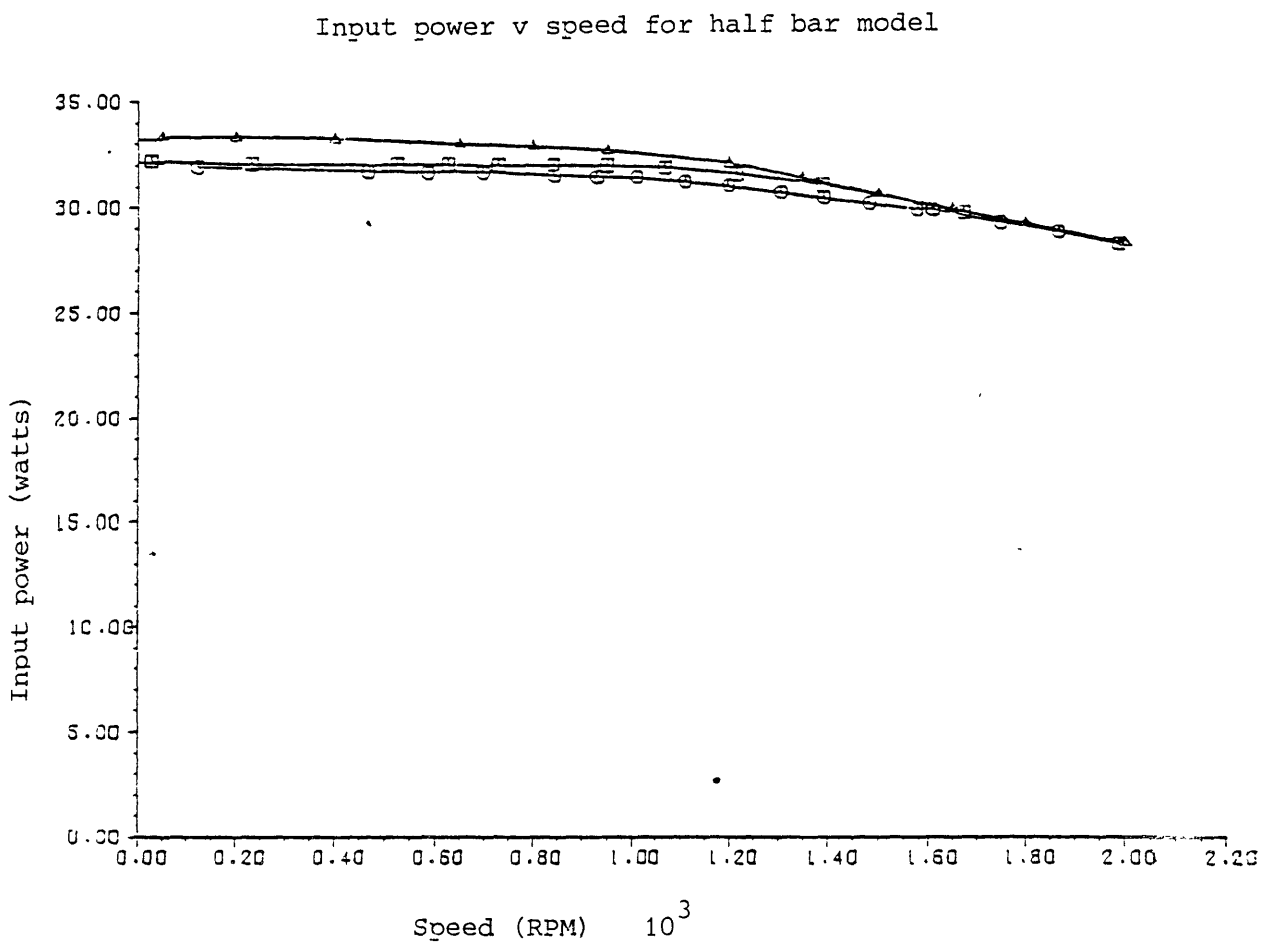


Fig. 4.16

□ Upper experimental limit

o Lower experimental limit

Δ Computed

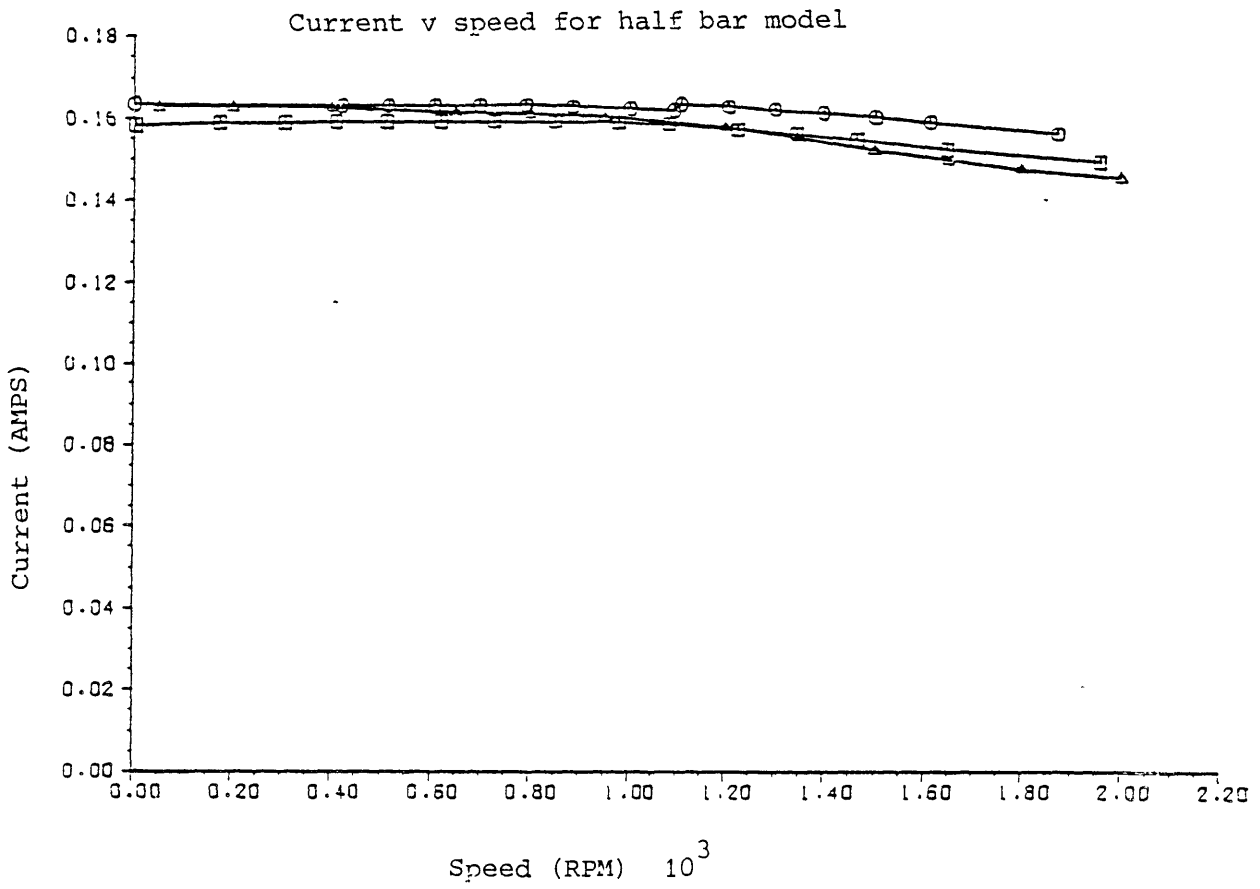


Fig. 4.17

o Upper experimental limit

□ Lower experimental limit

Δ Computed

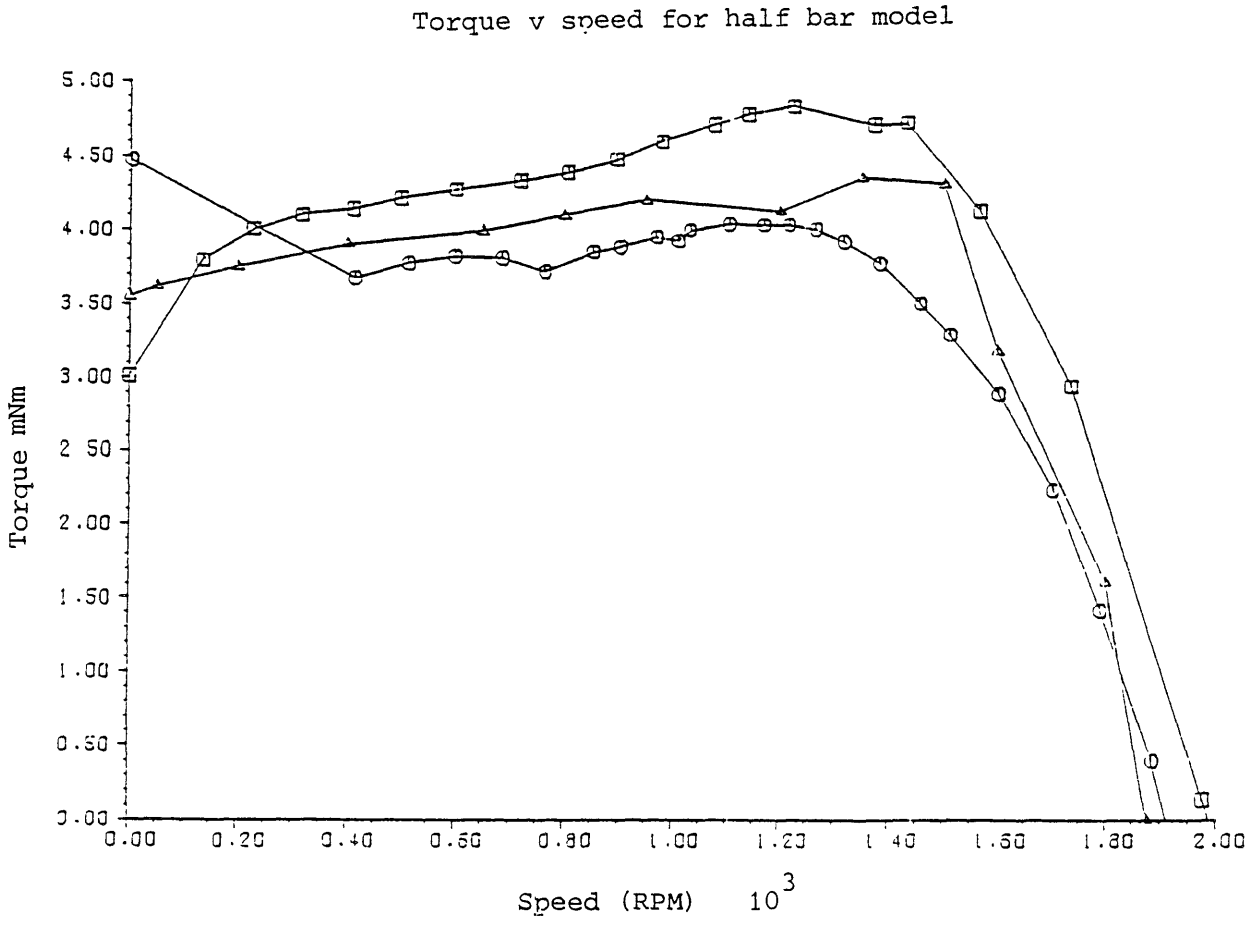


Fig. 4.18

□ Upper experimental limit

o Lower Experimental limit

Δ Computed

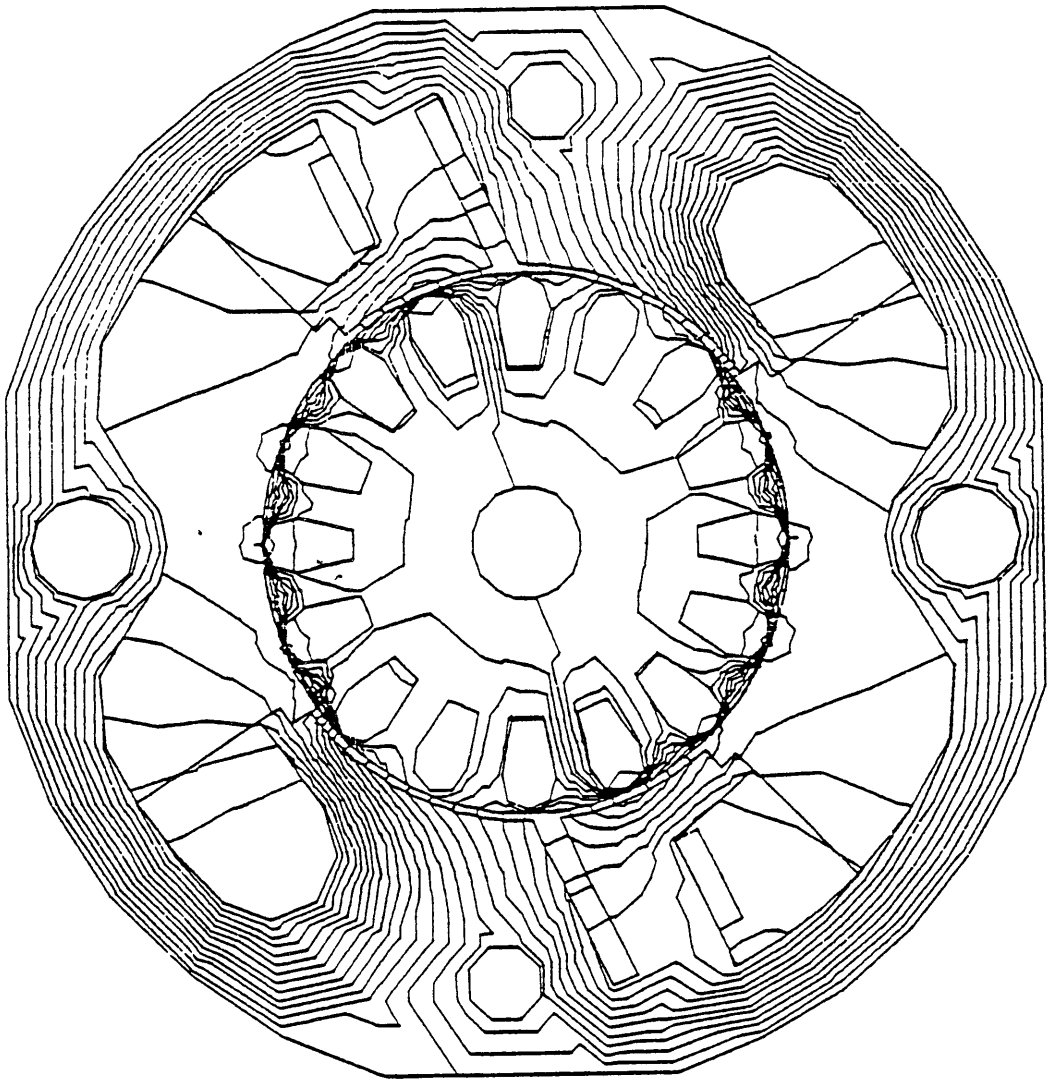


Fig. 4.19 Flux plot for peak voltage

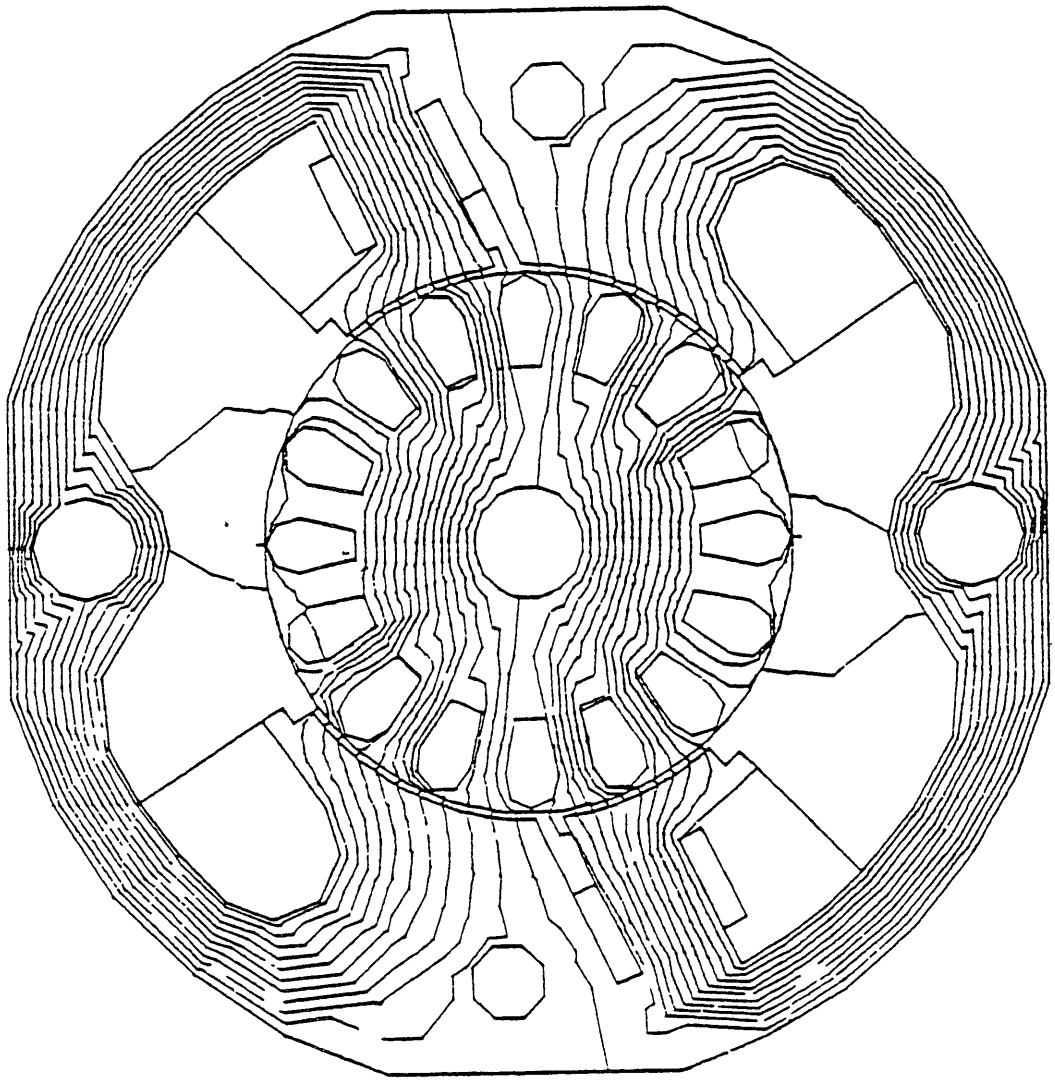


Fig 4.20 Flux plot for zero voltage

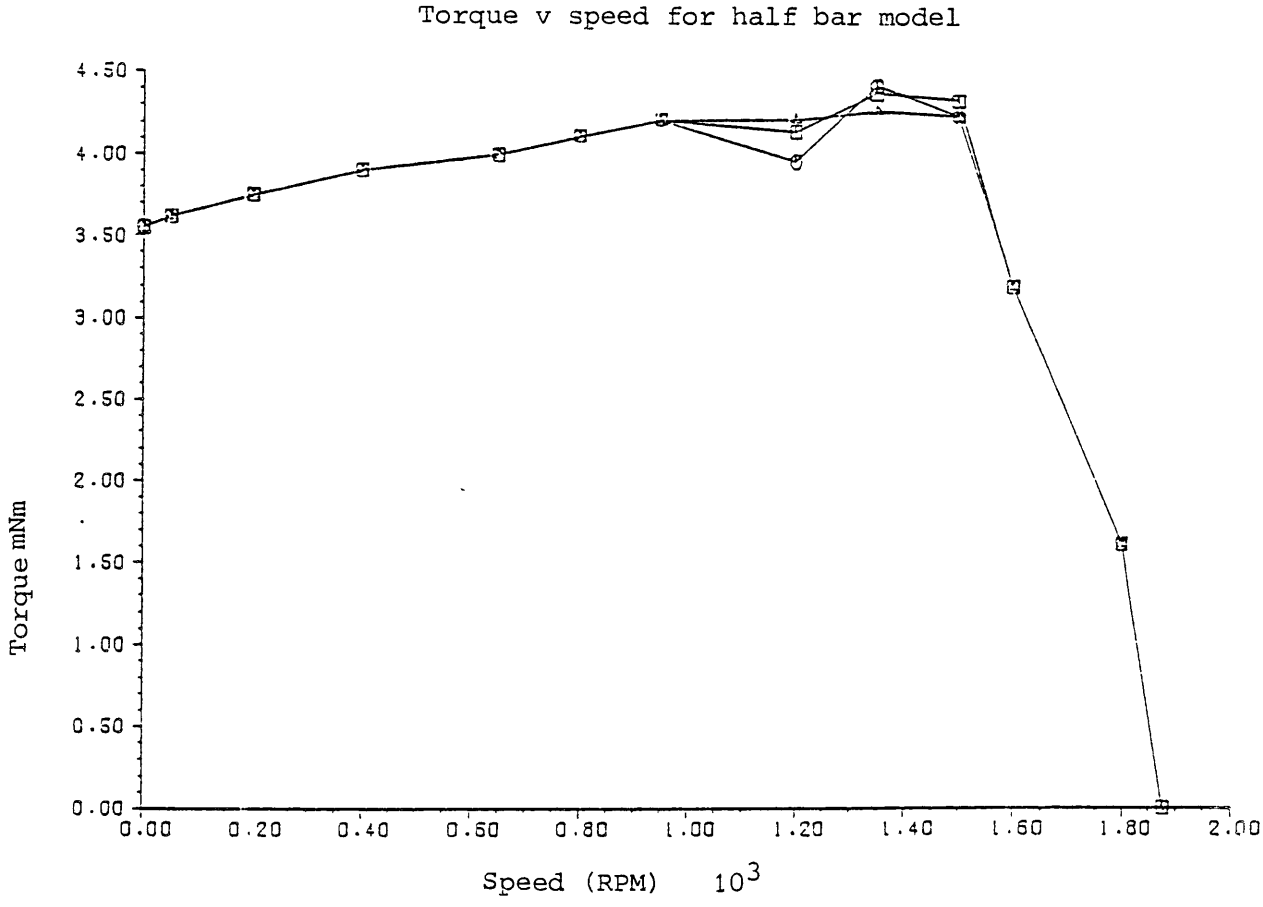


Fig. 4.21

□ Inter bar resistance = 3.2×10^{-3} Ohm-m

○ Inter bar resistance = 3.2×10^{-4} Ohm-m

Δ Inter bar resistance = 3.2×10^{-5} Ohm-m

different values of the inter-bar resistance were also tried to examine the influence of inter-bar currents on the motors performance. Results were also produced from the analysis for the machine when it was run at a reduced voltage of 170V to check that the program still predicted its performance adequately when the motor came out of saturation. Figures 4.22 - 4.24 show the input power, input current and torque characteristics for the full bar model run at its normal voltage of 220V along with the experimental limits. It was again found that inter-bar currents did not significantly affect the input power and current curves. The variation of torque with inter-bar resistance is shown in Figure 4.25. From these graphs it is evident that, although the agreement between experimental and computed results is quite good, the program over-estimates the torque and under-estimates the power and current. This discrepancy is thought to be due to the iron losses in the magnetic slot wedge being larger than calculated. More stator losses would have the effect of bringing the torque down and pushing the power and current up. The difference in the torque could also be due to higher harmonic effects that could not be calculated since the number of rotor bars limits the number of samples available for the Fourier analysis. Higher harmonics would have the effect of pulling the middle portion of the torque speed graph down. Figures 4.26-4.29 are the same as figures 4.22-4.25, except that the voltage has been reduced to 170V. The match between experimental and computed results is again thought to be quite good for this type of motor. The difference between the experimental and computed results is, as in the previous example, thought to be due to inadequate modelling of the magnetic slot wedge coupled with higher harmonic effects.

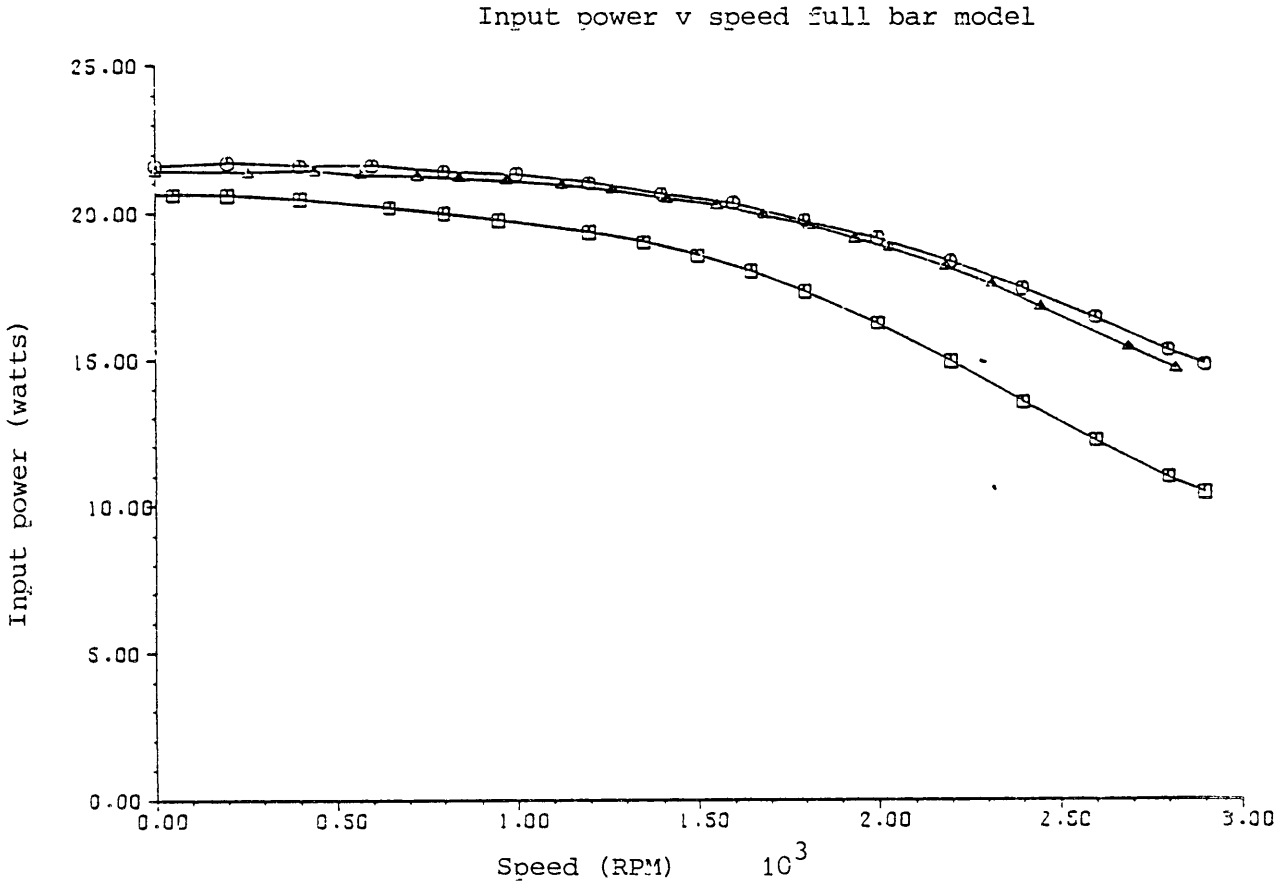


Fig. 4.22

o Upper experimental limit

Δ Lower experimental limit

□ Computed

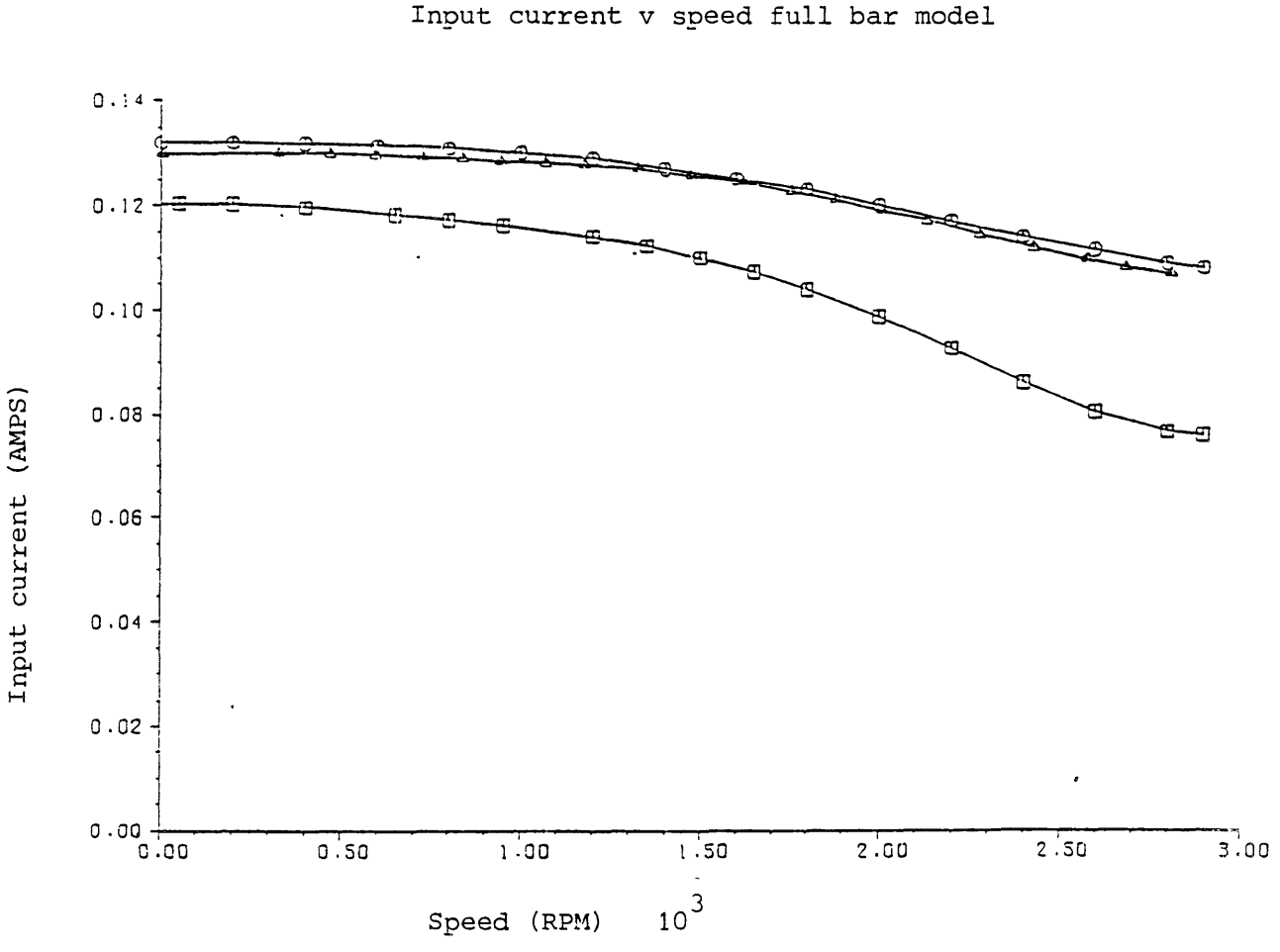


Fig. 4.23

o Upper experimental limit

Δ Lower experimental limit

□ Computed

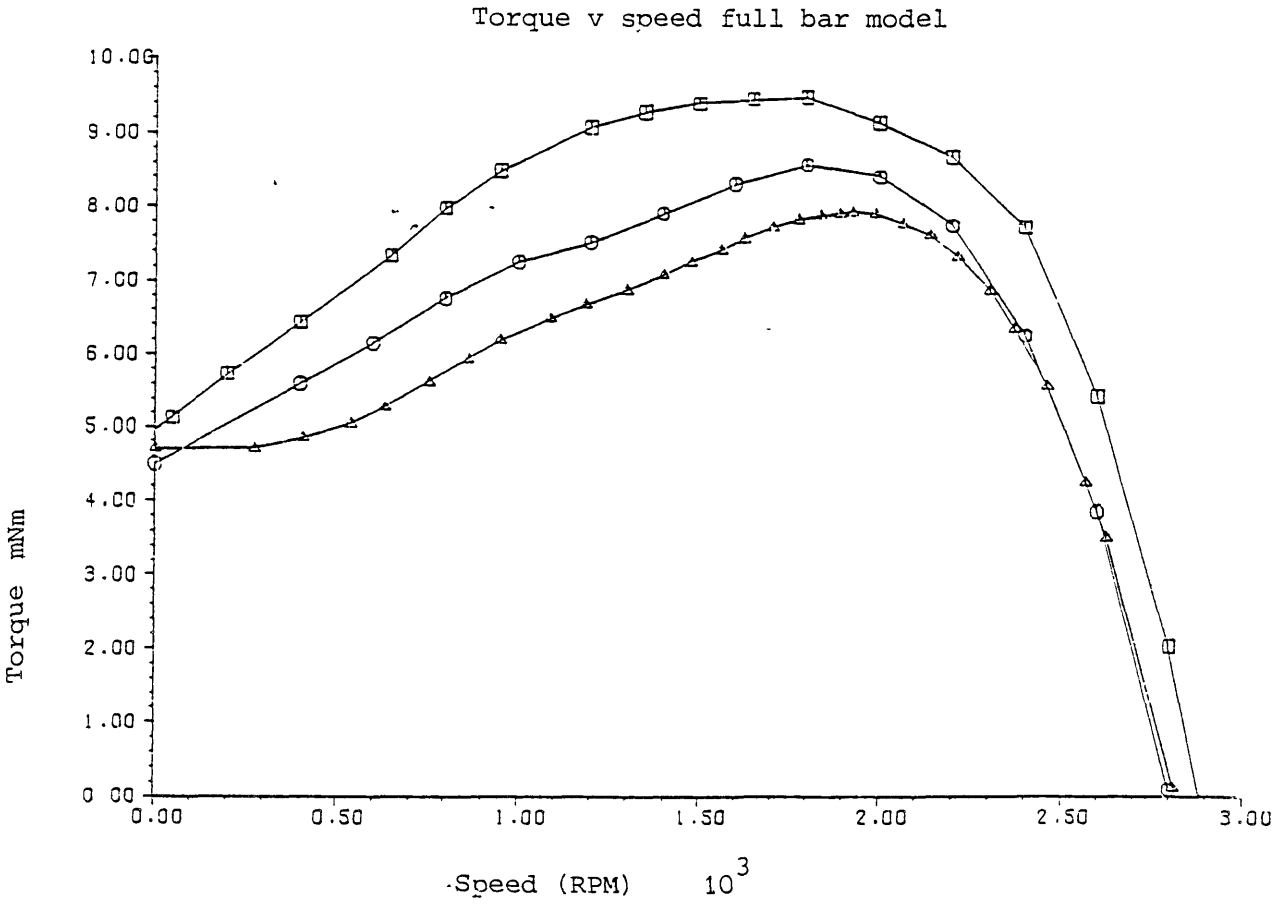


Fig. 4.24

o Upper experimental limit

Δ Lower experimental limit

□ Computed

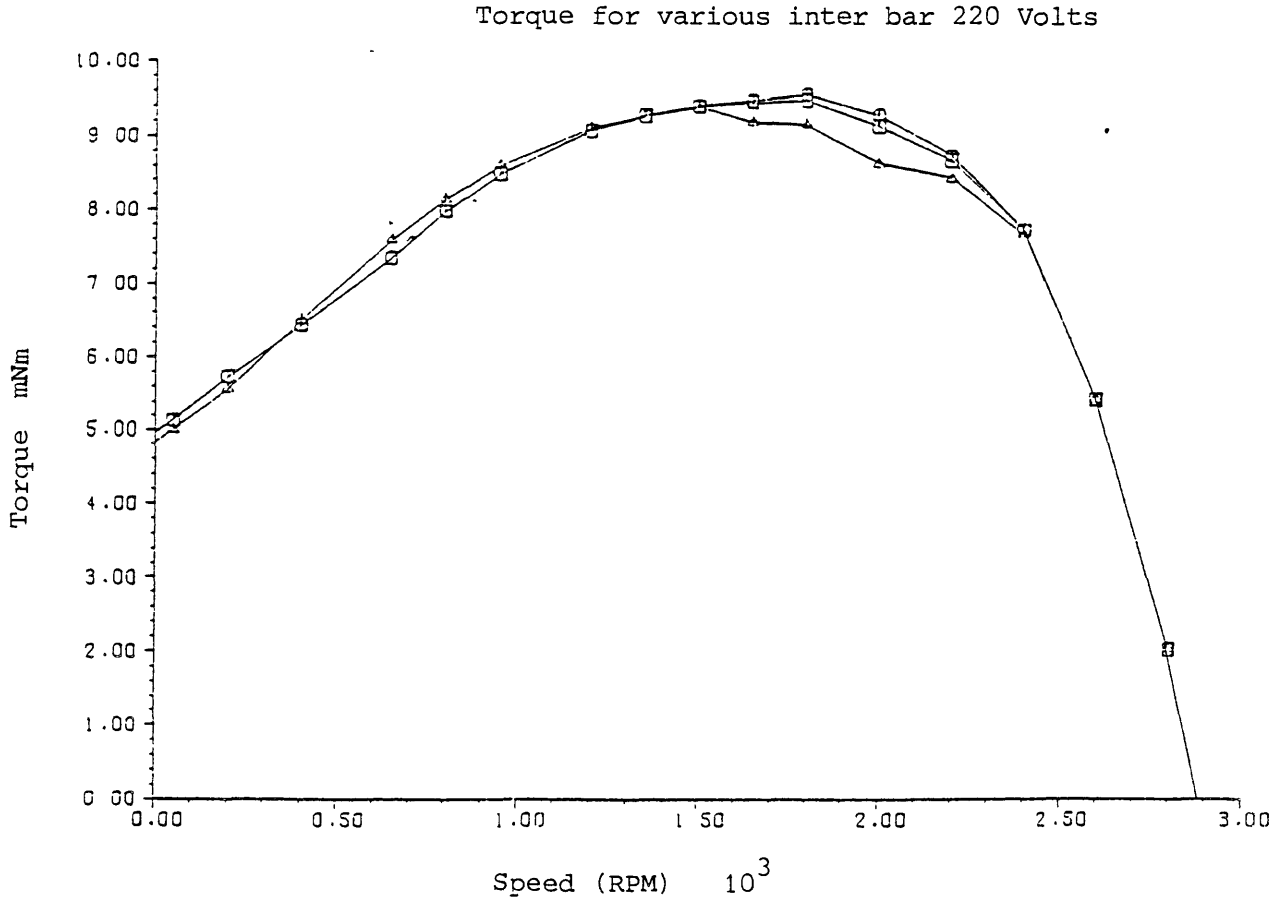


Fig. 4.25

□ Inter bar resistance = 3.2×10^{-3} Ohm-m

o Inter bar resistance = 3.2×10^{-4} Ohm-m

Δ Inter bar resistance = 3.2×10^{-5} Ohm-m

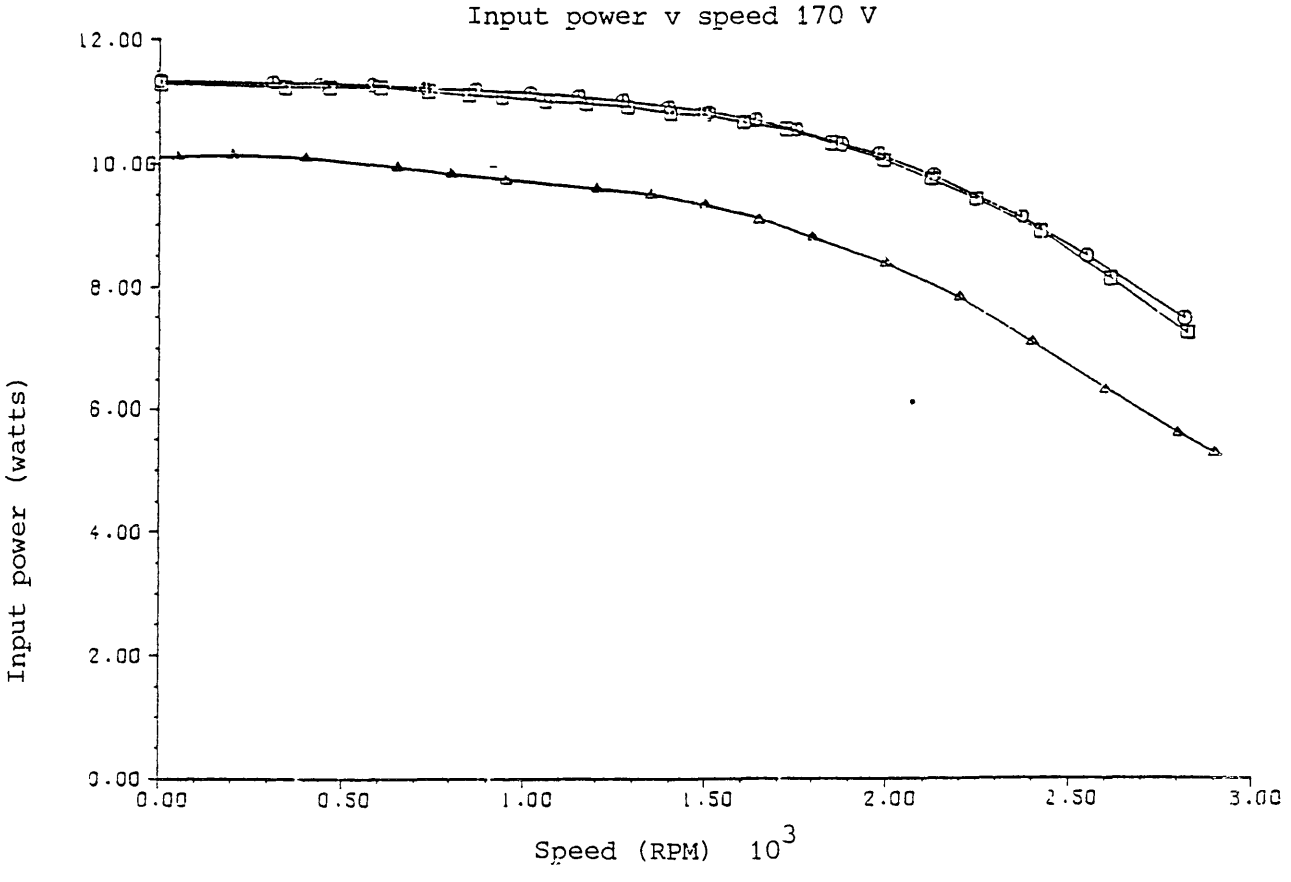


Fig. 4.26

o Upper experimental limit

□ Lower experimental limit

Δ Computed

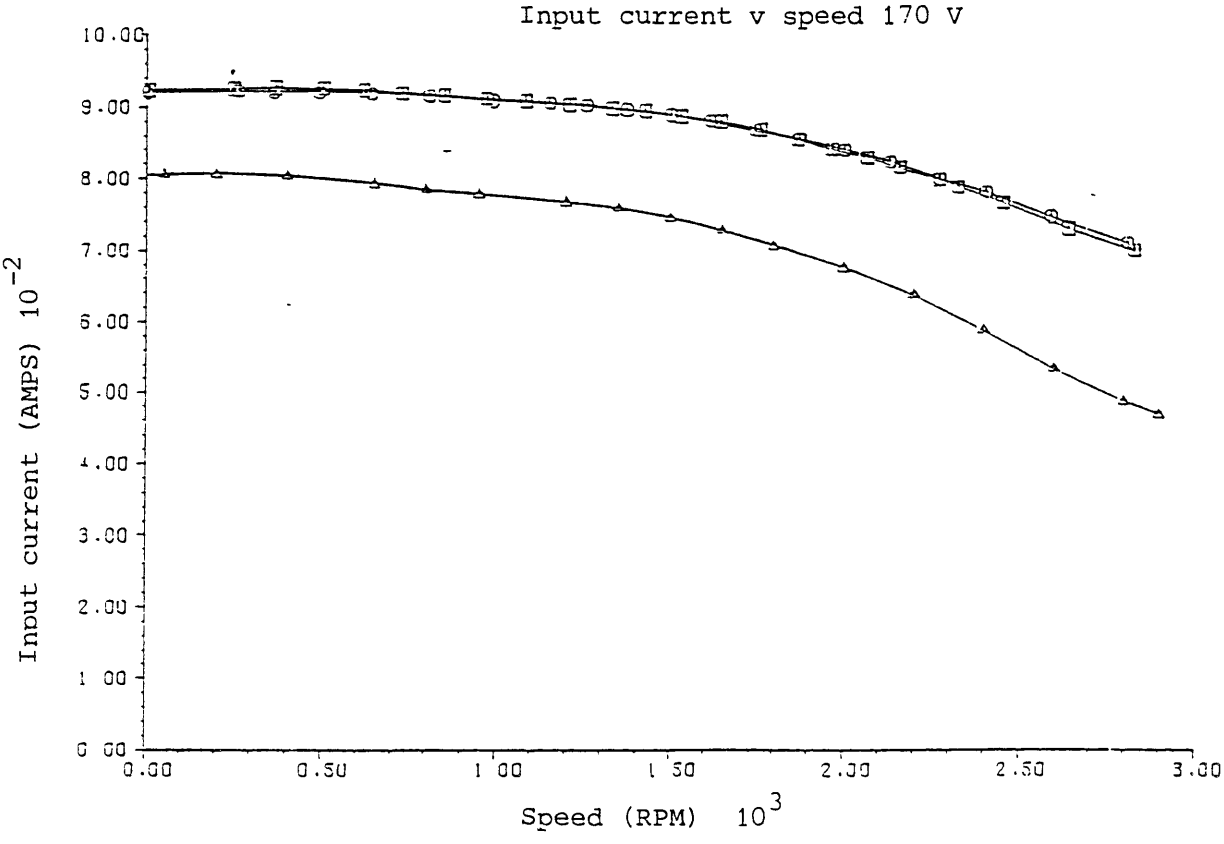


Fig. 4.27

□ Upper experimental limit

o Lower experimental limit

Δ Computed

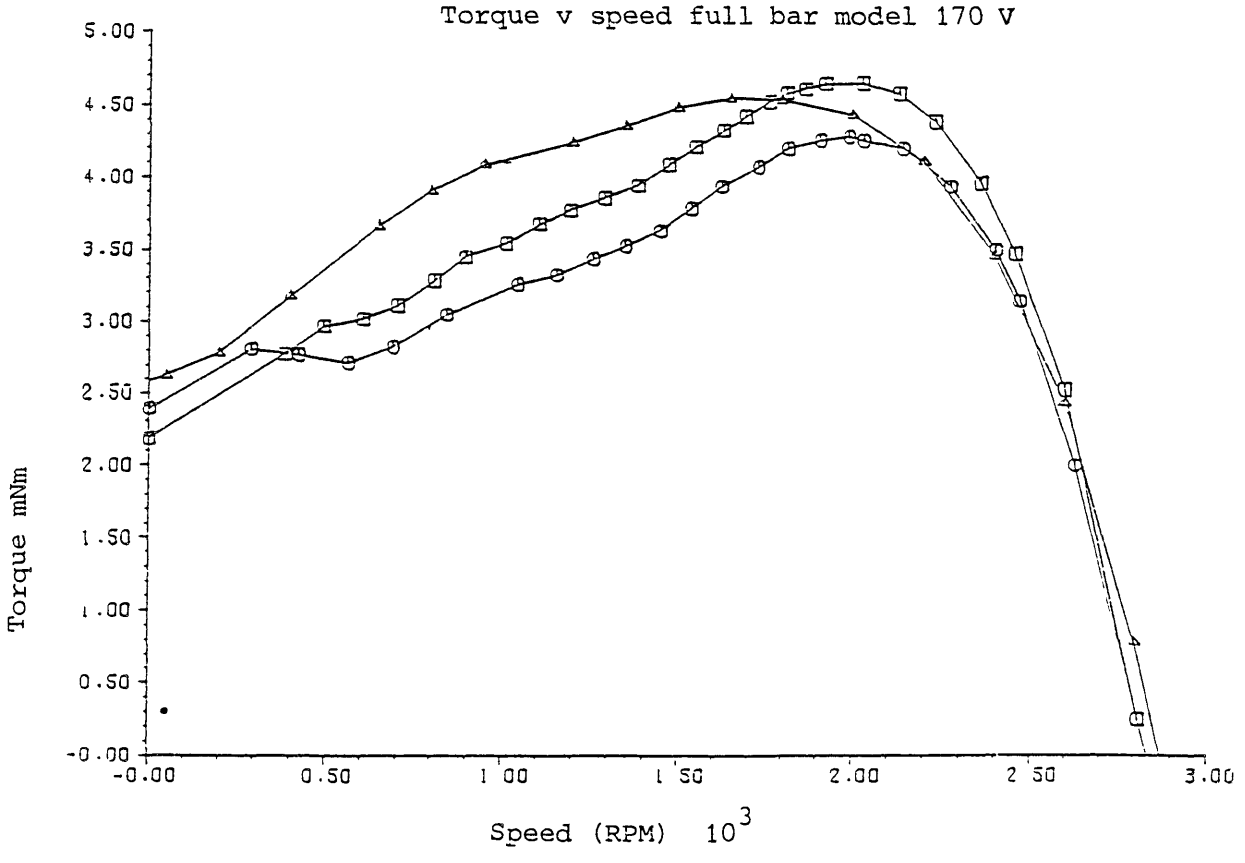


Fig. 4.28

□ Upper experimental limit

o Lower experimental limit

Δ Computed

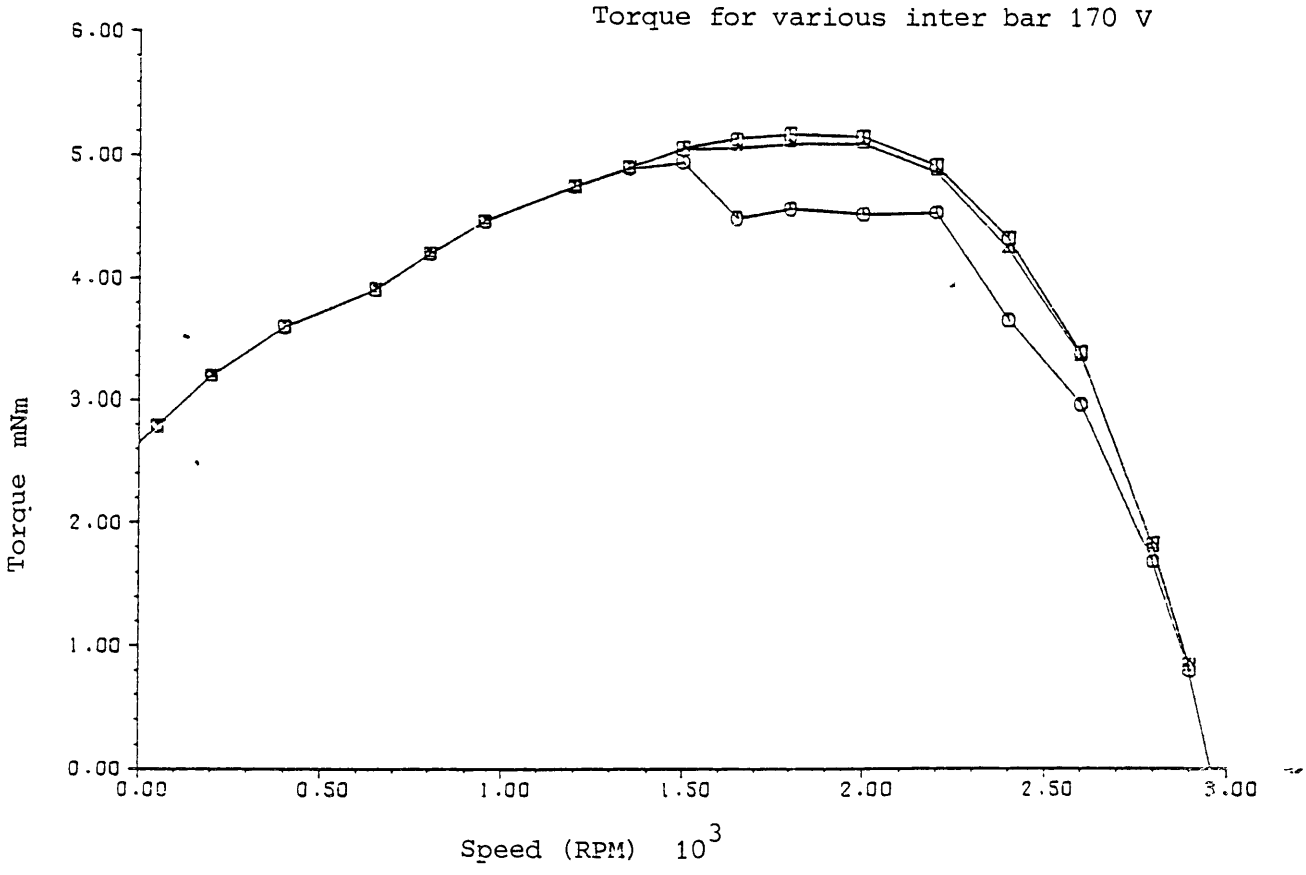


Fig. 4.29

□ Inter bar resistance = 3.2×10^{-3} Ohm-m

o Inter bar resistance = 3.2×10^{-4} Ohm-m

Δ Inter bar resistance = 3.2×10^{-5} Ohm-m

4.5.4 Comparison of Full and Half Bar Results: To complete the results section a comparison of the full and half bar models was thought to be necessary. Figure 4.30 shows the curves for the two different models for the 220V terminal conditions for one value of inter-bar resistance. The important thing to be noticed from this diagram is that the full and half bar models give practically identical results. This is to be expected since the placement of a magnetic slot wedge between the stator poles has the effect of spreading the flux more evenly over the rotor. Consequently the region through which the rotor moves is more magnetically homogeneous which means that approximating the motion by frequency scaling in the rotor is more valid. Figures 4.31-4.32 show two typical flux plots for the motor with the wedges in place.

4.6 Conclusions to Chapter 4 and Suggestions for Further Work

This chapter has presented the results of a combined fields and circuits approach applied to the analysis of two shaded pole motors. Shaded pole motors were chosen because they represent one of the most difficult motors to analyse by conventional means. Although it is felt that the results are quite good for this type of analysis there is still room for further development of the technique.

One improvement that could be made would be a more detailed analysis of the magnetic slot wedge, which has been found to be crucially important in determining the behaviour of the motor analysed in this chapter. Another extension of the work would be to apply the technique to three phase motors. This would be a useful development because a field-based model is capable of assessing the iron losses

which are important in determining the loadings that can be applied to such a machine. Finally, the method could be modified to operate in three dimensions. This would allow more detailed consideration of end effects, which are important in some types of machine. Some of the work carried out in this chapter, and in Chapter Three, was presented at the 1985 Compumag Conference and will be published in the IEEE Transactions on Magnetics. The paper is appended at the end of this thesis.

Comparison of full and half bar models

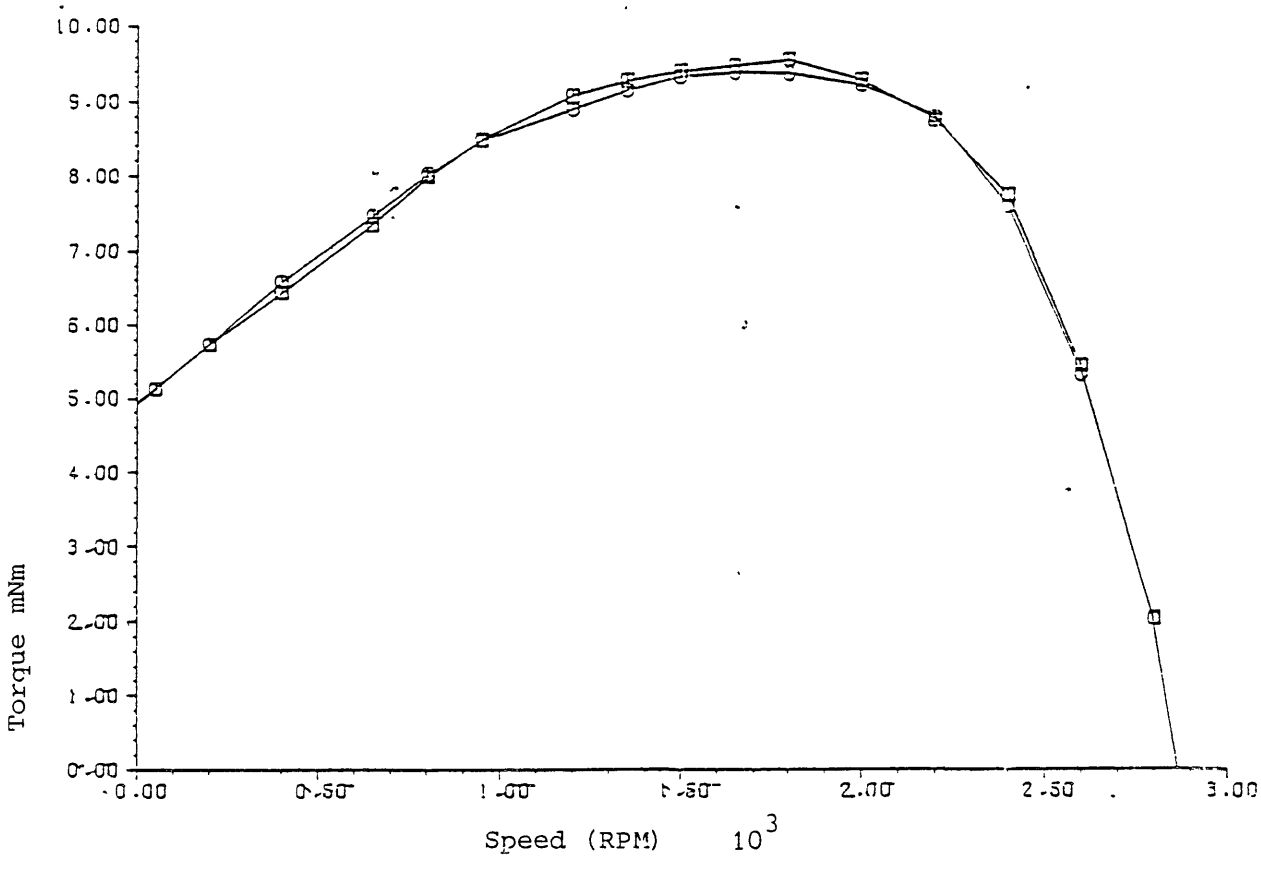


Fig. 4.30

□ Full bar model

o Half bar model

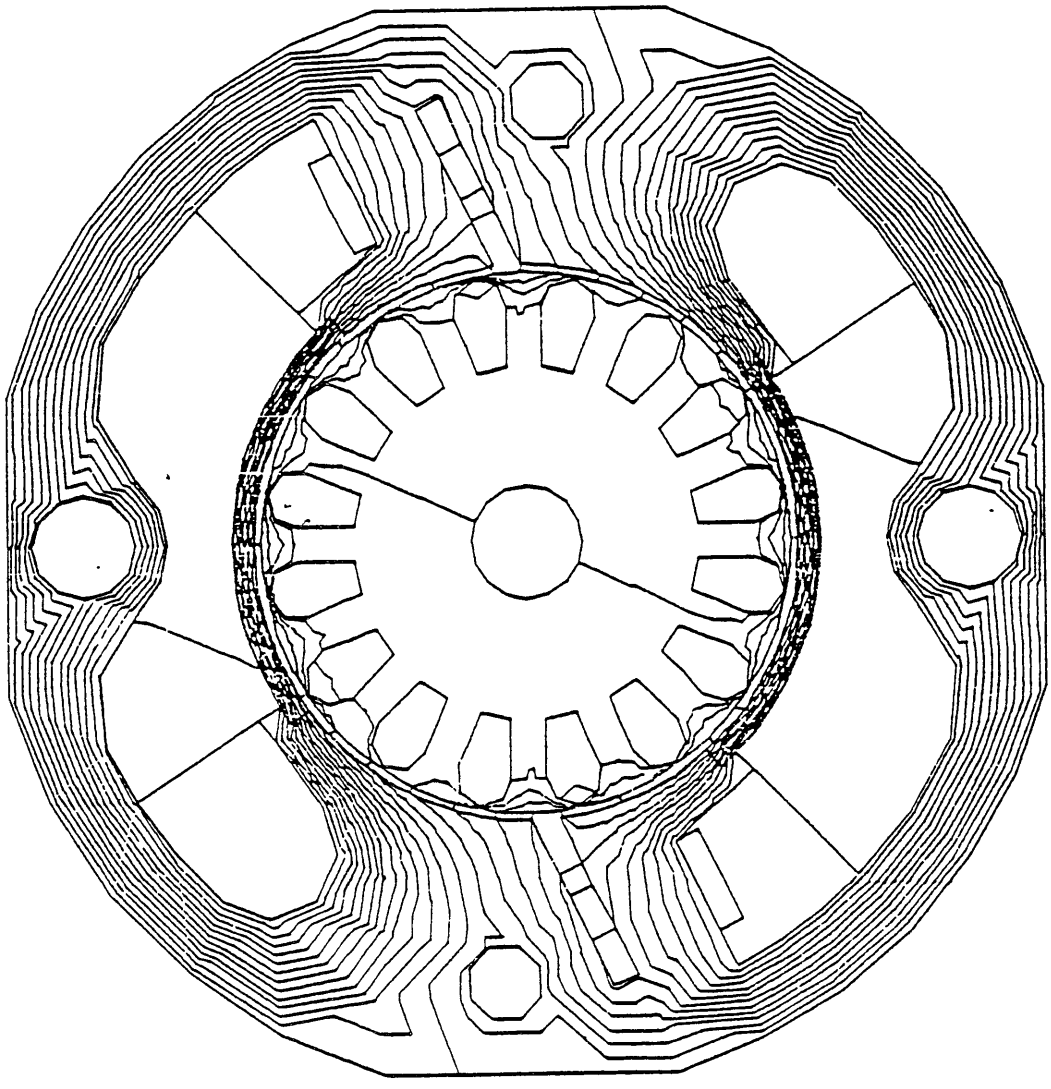


Fig. 4.31 Flux plot at peak voltage

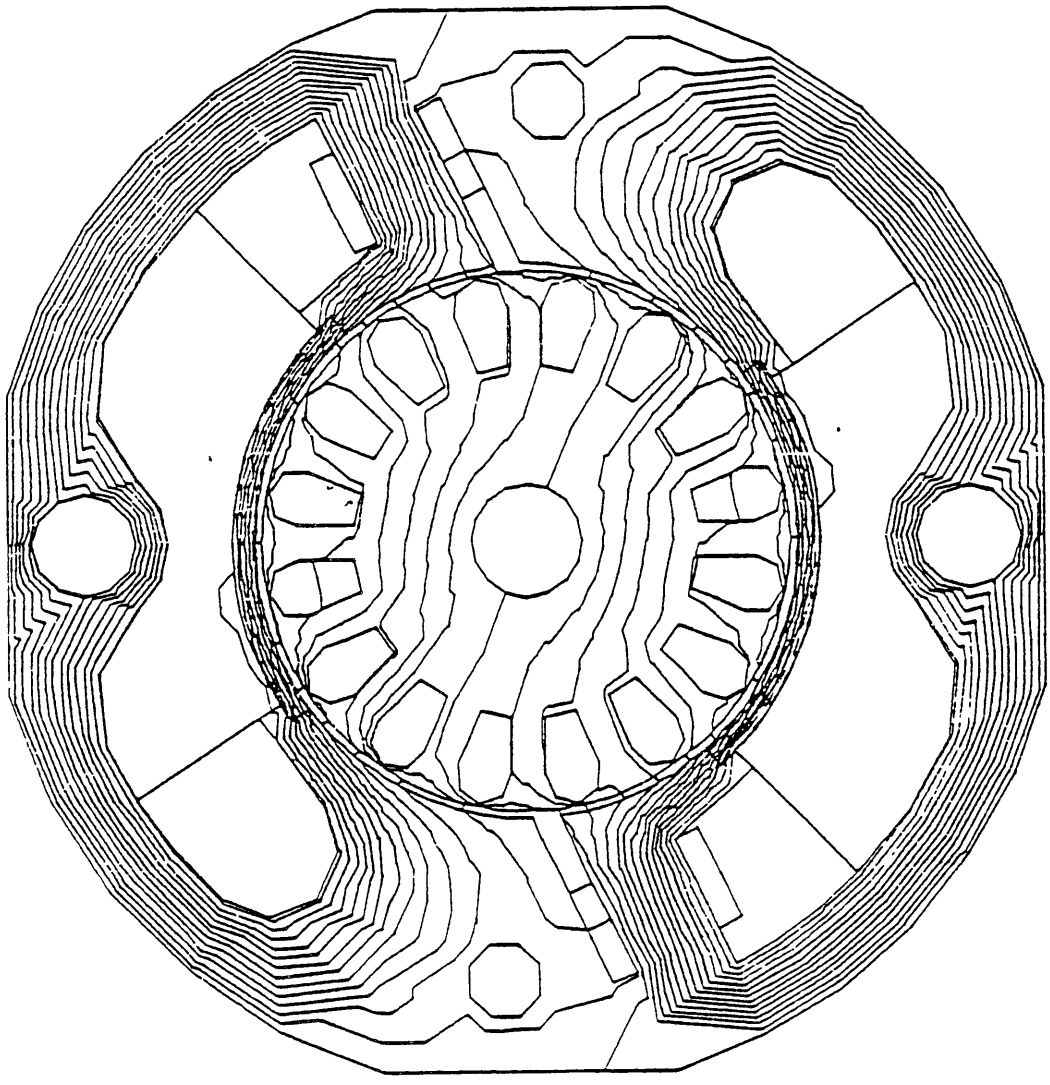


Fig. 4.32 Flux plot at zero voltage

CHAPTER FIVE

CALCULATION OF THE BAR RESISTANCE AND LEAKAGE REACTANCE OF CAGE ROTORS WITH CLOSED SLOTS

5.1 Introduction

Closed rotor slots are found in cage motors with ratings ranging from the very lowest powers up to several kilowatts. The reasons for using closed slots are diverse, although the main reasons appear to be mechanical. The closed slot holds the conductor in place, allows accurate machining of the rotor surface, and may ease the problems of diecasting by preventing the molten aluminium from running out. In addition, a smooth rotor surface reduces the flux pulsations caused by rotor slotting, resulting in lower surface losses and reduced acoustic noise. In large machines with deep, narrow slots, the bridge permeance may be relatively small when compared with the overall leakage permeance of the slot, whilst in small machines, which are particularly relevant to this thesis, the aspect ratio of the slots is different and the bridge permeance may dominate.

The authors main motivation in attempting to model closed slots was the idea of being able to include the parameters obtained from the analysis as a look up table in the main finite element program for simulating the performance of induction machines. This is useful because it allows an isolated slot to be modelled in a far more

detailed manner than would be practicable in the main simulation package since doing this would require all the slots in a pole-pitch to be analysed in the same detail, which would be uneconomic.

Birch and Butler [35] have described a numerical method for calculating bridge permeance as a function of slot current. Their method involves a notional division of the bridge into parallel strips, and an iterative procedure to relate m.m.f. drop across each strip to the current which flows in each slot. Whilst Birch and Butler's work was undoubtedly a significant advance on what had gone before, their method still left some scope for improvement. Firstly, the m.m.f. drop in the rotor teeth and core was neglected, all the slot m.m.f. being assumed to be available for driving flux through the bridge. Secondly, the effect of the stator m.m.f. on the rotor slot bridge saturation was ignored, the stator being modelled as an infinitely permeable smooth block.

The purpose of this chapter is to present a general method by which an accurate value of rotor bar resistance and leakage reactance can be obtained, taking magnetic saturation and deep bar effect into account. The work is specifically directed at the calculation of impedances for use in an equivalent circuit model, such as the one used in the finite element motor simulation package, that is excited from a sinusoidal voltage supply. The method described enables the rotor resistance and leakage reactance per bar to be calculated as a function of bar current and rotor frequency, for any shape of rotor bar. The examples presented in this chapter will be exclusively concerned with rotors having closed slots; this is mainly because the

actual motor simulated had closed rotor slots. However, the general method described is as applicable to open slots as it is to closed ones.

5.2 Theoretical Development

5.2.1 General Description and Consideration of Boundary Conditions:

In order to avoid the need to make subjective judgements regarding the extent of the saturated part of the slot bridge, and to represent the rotor in a more realistic manner than previously attempted, the model adopted comprises a section of a rotor corresponding to a complete rotor slot pitch. A typical model used for this purpose is illustrated in Figure 5.1, in which alpha is the rotor slot pitch, measured in mechanical radians.

The level of saturation in the rotor depends not only on the rotor m.m.f., but also on that produced by the stator. These two m.m.f.'s are almost equal and opposite, with the relatively small difference between them being sufficient to produce the air-gap flux. If the stator m.m.f. was ignored and field calculations made using the rotor currents as the only m.m.f. source, then the tooth fluxes obtained would far exceed those found in practice and the rotor would be heavily saturated. It is therefore necessary to specify an appropriate boundary condition along the arc CDE (Figure 5.1) to produce an air-gap flux that is commensurate with the current flowing in the rotor bars. To this end, the single rotor bar used in the model is regarded as one of Nb bars in a symmetrical rotor cage, which carries a 2p-pole current wave of r.m.s. magnitude $\bar{I}$. If the

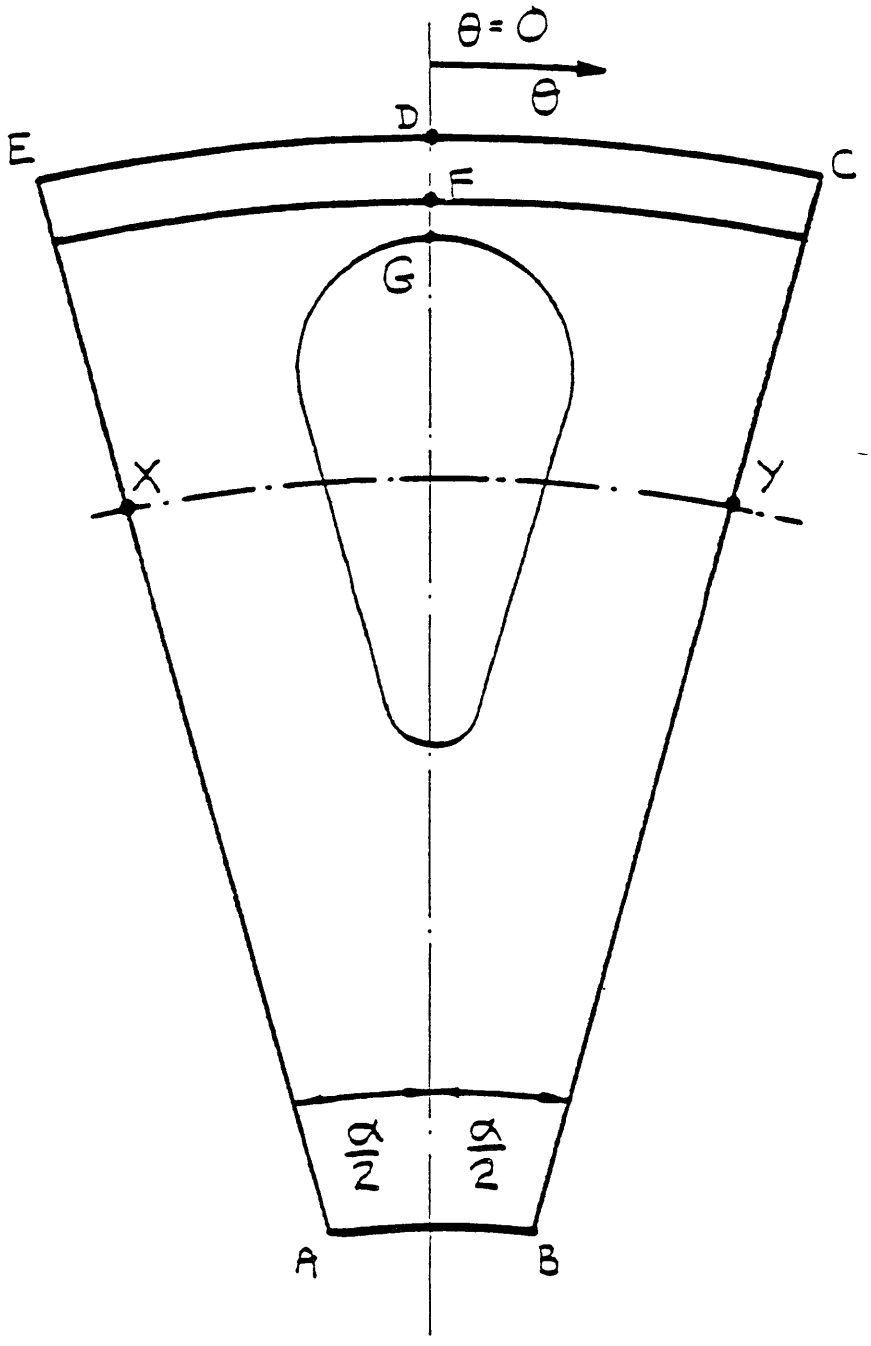


Fig. 5.1 Typical rotor tooth-pitch model

rotor leakage impedance per bar presented to this assumed current distribution is $\bar{Z}_b$, then the e.m.f. induced in the bar by the air-gap flux is given by

$$\bar{E}_b = \bar{I}_b \bar{Z}_b = \bar{I}(R_b + j\omega L_b) \qquad (5.1)$$

in which R_b and L_b are the effective bar resistance and leakage inductance respectively.

The 2p-pole flux density wave rotating in the air-gap may be written in the general form

$$b(\theta,t) = R_e\{\sqrt{2}\ \bar{B}\ e^{j(\omega t+p\theta)}\} \qquad (5.2)$$

where the circumferential coordinate θ is measured in the rotor reference frame so that the frequency ω is the rotor frequency. The flux density, $\bar{B}$, is related to the induced bar e.m.f. through the flux cutting rule

$$\bar{E}_b = \frac{\omega d W \bar{B}}{2p} \qquad (5.3)$$

Combining equations 5.1 and 5.3 gives

$$\bar{B} = \frac{2p}{Wd\omega}\ \bar{I}\ \bar{Z}_b \qquad (5.4)$$

The stator is assumed to produce a sinusoidal m.m.f. wave, which may be represented as a surface current density distribution which, when viewed from the rotor, is of the form

$$j_s(\theta,t) = R_e\{\sqrt{2}\ \bar{J}_s\ e^{j(\omega t - p\theta)}\} \qquad (5.5)$$

The rotating flux density wave in the air-gap may, finally, be related to the combined m.m.f.'s of the rotor and stator, by applying Ampere's law around a closed path which crosses the airgap twice (see [27]).

$$\bar{J}_s = \frac{N_b \bar{I}}{\pi d} = -\frac{j2\mu_o p \bar{B}}{d} \qquad (5.6)$$

Combining equations 5.6 and 5.4 the required equation for J_s is obtained

$$\bar{J}_s = -\frac{\bar{I}}{\pi d}\ \{N_b + \frac{j4\mu_o p^2 \pi}{dW\omega}\ \bar{Z}_b\} \qquad (5.7)$$

Provided $\bar{Z}_b$ is known, equations 5.5 and 5.7 enable the appropriate boundary condition to be specified along the boundary CDE in Figure 5.1. The problem, however, is that it is the value of $\bar{Z}_b$ that is not known. Therefore for each rotor current it is necessary to adopt an iterative approach. $\bar{Z}_b$ is initially estimated by some convenient method, to allow a boundary condition to be specified. The field is then solved and $\bar{Z}_b$ recalculated as described below. This procedure is repeated until satisfactory convergence is achieved. In practice this is found to occur within two or three iterations.

The boundary conditions imposed along the radial boundaries, AE and BC in figure 5.1, must reflect the fact that the bar modelled is part of a complete squirrel cage which carries a 2p-pole current

distribution. This is accomplished by using periodicity conditions along these boundaries. The magnetic vector potentials at the two similar boundary points X and Y are related by the equation

$$\bar{A}_y = \bar{A}_x \, e^{-j\alpha p} \tag{5.8}$$

The boundary AB corresponds to the rotor shaft, which is assumed to be impermeable to flux. AB therefore becomes a flux line, which is specified as A = constant.

5.3 The Governing Field Equations

The governing differential equation for a two dimensional current forced skin effect problem was shown by Konrad [36] to be of the form

$$\frac{\partial}{\partial x}\left(\nu \frac{\partial \bar{A}}{\partial x} \right) + \frac{\partial}{\partial y}\left(\nu \frac{\partial \bar{A}}{\partial y} \right) = - \bar{J}_o + j\omega\sigma(\bar{A} - \bar{A}_o) \tag{5.9}$$

For the deep bar problem being considered here, the right hand side of equation 5.9 is non zero only over the bar cross sectional area. $\bar{J}_o$ is the uniform current density that would be obtained if the bar carried the same r.m.s. current $\bar{I}$, at a frequency low enough for skin effect to be negligible, i.e.

$$\bar{J}_o = \frac{\bar{I}}{S_b} \tag{5.10}$$

where S_b is the cross sectional area of the bar. $\bar{J}_o$ is the field source term. The remaining term on the right hand side of equation 5.9 represents the modification to the uniform current density, due to skin effect. $\bar{A}_o$ is the average value of magnetic vector potential over the bar area

$$\bar{A}_o = \frac{1}{S_b} \int_{S_b} \bar{A} \, dS \tag{5.11}$$

5.4 The Finite Element Solution

Equation 5.9 may be conveniently solved by the finite element method. The general form of the first-order elemental equation, derived from equation (5.9) using standard, may be written as

$$\{\nu[S] + j\omega\sigma[C]\} \{\bar{A}\} = \{\bar{J}\} \tag{5.12}$$

The elements of the real matrices [S] and [C], and of the complex vectors $\bar{A}$ and $\bar{J}$, are listed in reference [38]. If the elemental equations, such as (5.12), are assembled to form the global set of equations describing the whole field solution, then that set of equations takes on the usual form

$$GA = J \tag{5.13}$$

In order to allow for magnetic saturation, equation (5.13) must be solved in a non-linear sense, with the reluctivities of the iron elements varying with flux density in accordance with some form of magnetisation characteristic. It has been implicitly assumed in

equations 5.9 to 5.13 that all magnetic field quantities, including the m.m.f., vary sinusoidally in time, whereas magnetic saturation prevents this from being possible. It will be recalled, however, that the objective of this work is to determine reactances and resistances for use in equivalent circuits for sinusoidally excited machines. It is appropriate, therefore, to use reluctivity values which relate the fundamental frequency component of magnetic field strength to the local magnitude of the assumed sinusoidally time varying flux density. Suitable values may be derived from standard d.c. magnetisation characteristics for the laminated iron, by determining the H versus time variation and then calculating the magnitude of the fundamental component of $\overline{H}$ by the use of Fourier analysis. However, it was decided, in this case, to use a less accurate but much simpler approach, based on the use of a.c. magnetisation characteristics. Such characteristics give the specific apparent power as a function of the peak of the sinusoidal flux density [37]. They may, therefore, be used to obtain the r.m.s. value of $\overline{H}$ as a function of the r.m.s. value of $\overline{B}$. The ratio of these two quantities gives a suitable value of reluctivity for use in equation 5.12. In fact the reluctivity so obtained is somewhat larger than that required, but provided that the combined r.m.s. of the harmonic components of $\overline{H}$ is less than 46% of the r.m.s. fundamental component, then the error in ν will be less than 10%.

A suitable Newton-Raphson algorithm for solving equation 5.13 in the nonlinear sense has been described by Ralph and Williamson [38] and has already been described in Chapter 2. In this section the situation is complicated still further by the use of periodicity boundary conditions, such as those on AE and BC in Figure 5.1, which produce a general phase shift across the two boundaries rather than a

straight equality or negative equality. Such a condition produces additional coupling between the real and imaginary parts of the solution, and results in a system of equations with an asymmetrical coefficient matrix. The details of how these boundary conditions are incorporated in the solution can be found in Appendix 8.3.

Having solved for the field with both stator and rotor m.m.f. sources present, it is then necessary to distinguish between stator-driven and rotor-driven fluxes, so that the rotor bar leakage reactance may be calculated. This is most easily accomplished by re-solving equation 5.13 in a linear sense, with the rotor bar current as the only m.m.f. source, and with the reluctivity of each iron element in the model set at the value determined during the nonlinear solution. For this purpose the stator is regarded as being infinitely permeable so that a homogeneous Neumann boundary condition, which is natural to the finite element technique, is now specified along the arc CDE in Figure 5.1. In effect, the non-linear solution is used to set the elemental reluctivities to the appropriate values, and the linear solution to determine the rotor-driven flux. A similar method has been used by Ralph and Williamson [7] to distinguish between un-skewed stator fields and skewed rotor fields in induction motor analysis.

5.5 Calculation of the Rotor Leakage Impedance Per Bar, $\bar{Z}_b$

5.5.1 Bar Resistance, R_b: The complex current density in the rotor bar is given by

$$\bar{J} = \bar{J}_o - j\omega\sigma(\bar{A} - \bar{A}_o) \qquad (5.14)$$

The Joule loss per unit length is

$$W = \int_{S_b} \frac{|\bar{J}|^2}{\sigma} \, dS \qquad (5.15)$$

Substituting equation 5.14 into 5.15, and simplifying gives

$$W = |\bar{J}_o|^2 \frac{S_b}{\sigma} - \omega^2\sigma \, |\bar{A}_o|^2 \, S_b + \omega^2\sigma \int_{S_b} |\bar{A}|^2 \, dS \qquad (5.16)$$

This must equal I^2R_b, from which

$$R_b = R_o \left\{1 - \left| \frac{\omega}{\bar{I}R_o} \right|^2 \left(|\bar{A}_o|^2 - \frac{1}{S_b} \int_{S_b} |\bar{A}|^2 \, dS\right)\right\} \qquad (5.17)$$

R_o is the resistance per bar at low frequencies. The integral contained within equation 5.17 is evaluated using a summation over the bar elements as follows

$$\int_{S_b} |\bar{A}|^2 \, dS = \frac{1}{6} \sum_e \Delta_e \, R_e \left\{ \sum_{i=1}^{3} \sum_{j=1}^{3} \bar{A}_{ie} \, \bar{A}^*_{je} \right\} \qquad (5.18)$$

where Δ_e is the area of the e^{th} bar element. For use in equation 5.7 the bar resistance is calculated in accordance with equation 5.17 should be augmented by the effective end ring resistance, in the usual manner [39].

5.5.2 Bar Leakage Inductance: For the calculation of bar leakage reactance, it is convenient to partition the leakage flux into separate components, as in traditional calculation methods. The advantage of this approach is that the components of leakage flux are affected differently by the various geometrical factors relating to rotor design.

Slot leakage inductance, L_{slot}: this is due to all the rotor driven flux that crosses the slot. It may be evaluated by calculating the energy stored in the slot and equating it to the energy stored in an equivalent inductance.

$$L_{slot} = \frac{W}{\mu_0 I^2} \int_{S_b} |\bar{B}|^2 \, dS \tag{5.19}$$

which in finite element terms becomes

$$L_{slot} = \frac{W}{\mu_0 I^2} \sum_{e} \Delta_e R_e \{(\bar{A})_e^T (\bar{S})_e (\bar{A})^*\} \tag{5.20}$$

Bridge leakage inductance, L_{bridge}: this is due to all the rotor driven flux that passes over the top of the slot, through the closed slot bridge. It is evaluated from the flux that passes between F and G in Figure 5.1

$$L_{bridge} = \frac{W}{I} R_e \{ \bar{A}_F - \bar{A}_G \} \tag{5.21}$$

Airgap leakage inductance, L_{gap}: this is due to all the rotor driven flux that passes over the top of the slot, through the airgap. It is evaluated from the flux that passes between D and F in Figure 5.1

$$L_{gap} = \frac{W}{I} R_e \{\bar{A}_D - \bar{A}_F\} \tag{5.22}$$

The calculation of these three inductance components is one of the main objectives of this section, and their sum is referred to below as the 'combined' leakage inductance, L_c

$$L_c = L_{slot} + L_{bridge} + L_{gap} \tag{5.23}$$

The bar leakage inductance, L_b, which is required for the calculation of $\bar{Z}_b$ for use in equation (5.7) also includes two components which are not derivable from the field plots. The largest of these is the differential leakage inductance, which on a per bar basis is given by [40]

$$L_{diff} = \frac{\pi d \mu_o W}{4 g N_b} \left\{ \text{cosec}^2\left(\frac{P\pi}{N_b}\right) - \left(\frac{N_b}{P\pi}\right)^2 \right\} \tag{5.24}$$

The second component not included in L_c is the end-ring leakage reactance. This component, however, is usually much smaller than the rest and may be neglected. With this assumption

$$L_b = L_c + L_{diff} \tag{5.25}$$

5.6 Examples

The accuracy with which the rotor bar resistance and leakage reactance presented to a sinusoidal current distribution may be calculated is difficult, if not impossible, to verify experimentally, and so alternative means must be found if the validity of the method described in Section 5.2 is to be established. To this end three examples are presented in the following sections. The first two examples are of impedance calculations in commonly employed slot geometries. The relationship between the results and those calculated using certain analytical expressions that are found in the literature, is discussed. The third example is of one of the bars, which has special relevance to this thesis, of a machine which has been simulated in Chapter 4.

5.6.1 Round Rotor Bars: Round bars with closed slots are used in the rotors of small single phase and three phase motors. Figure 5.2 defines the geometric variables referred to in this section, and figure 5.3 illustrates the triangular mesh used in the field analysis.

Figure 5.4 shows the computed variations of the combined leakage inductance with mean bar current density $\bar{J}_o$, for bridge depths, b, of 0.1 mm and 0.5 mm. $\bar{J}_o$ is used as the independent variable in Figure 5.4 and elsewhere in preference to the r.m.s. bar current because it is thought that this parameter gives a clearer indication of the currents likely to be encountered in a well designed machine. The effects of magnetic saturation are clearly evident, with inductance falling as the bar current increases. In order to investigate this phenomenon further, the three constituent

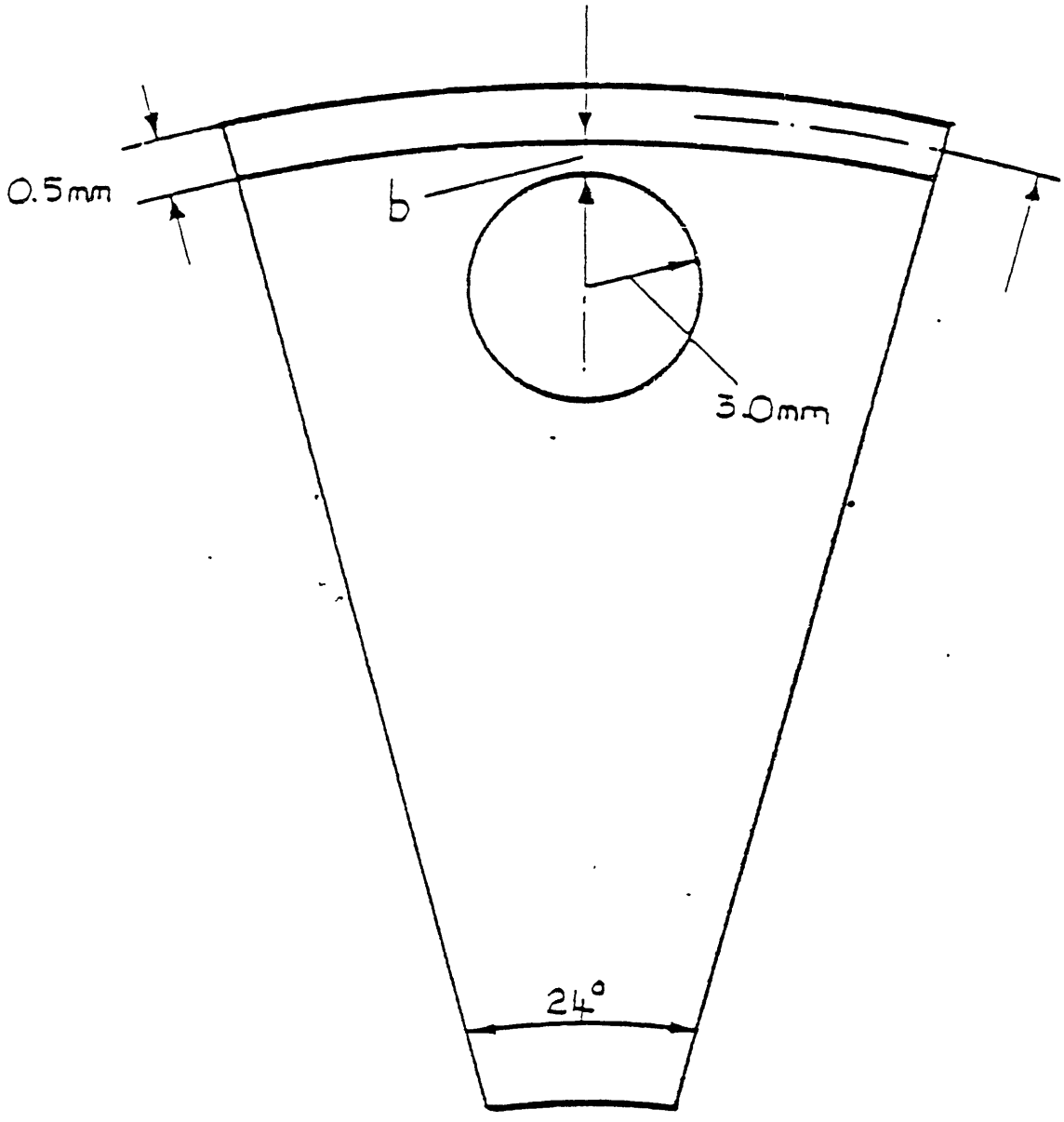


Fig. 5.2 Round Bar Geometry

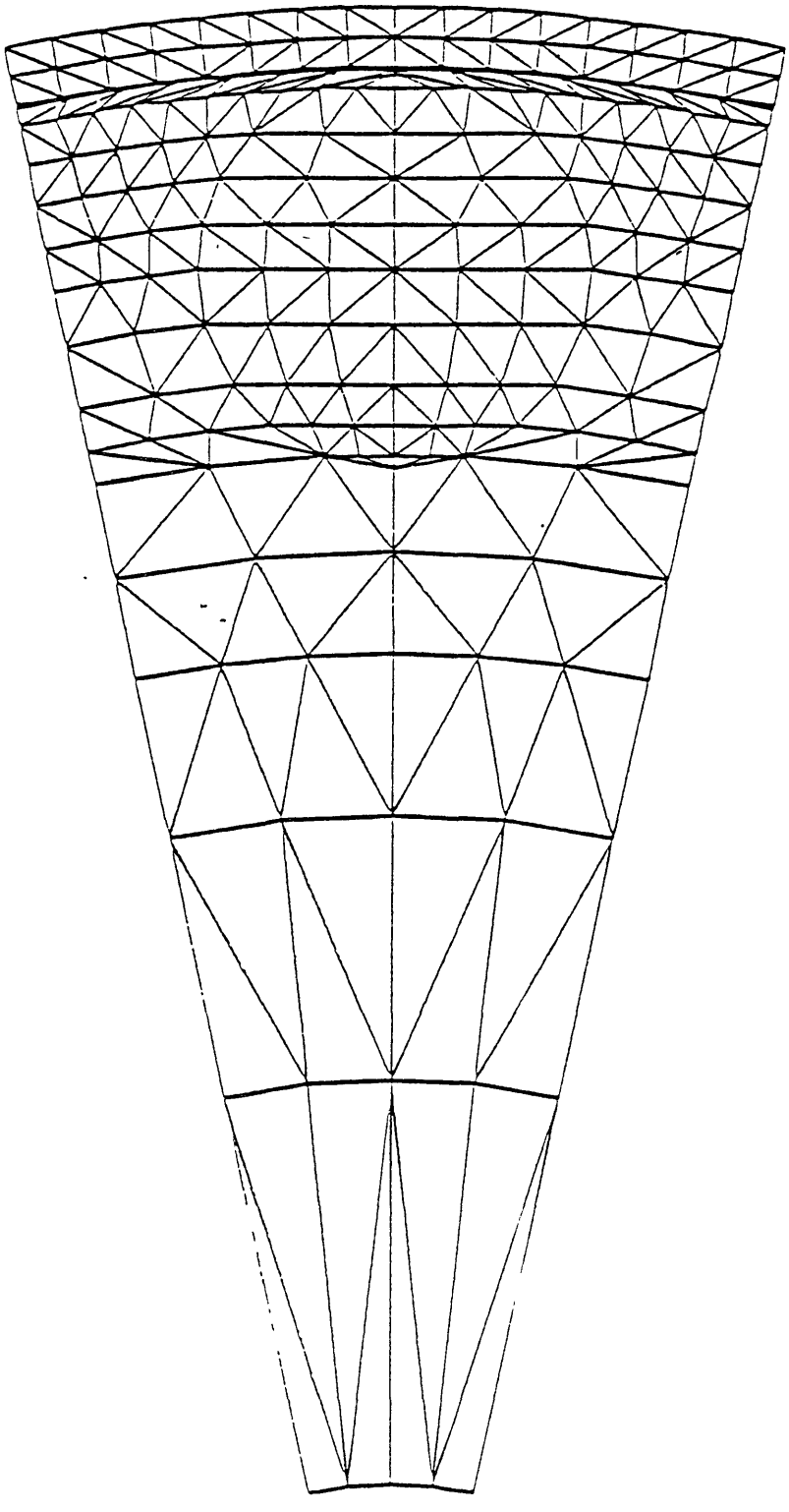


Fig. 5.3 Round Bar Mesh

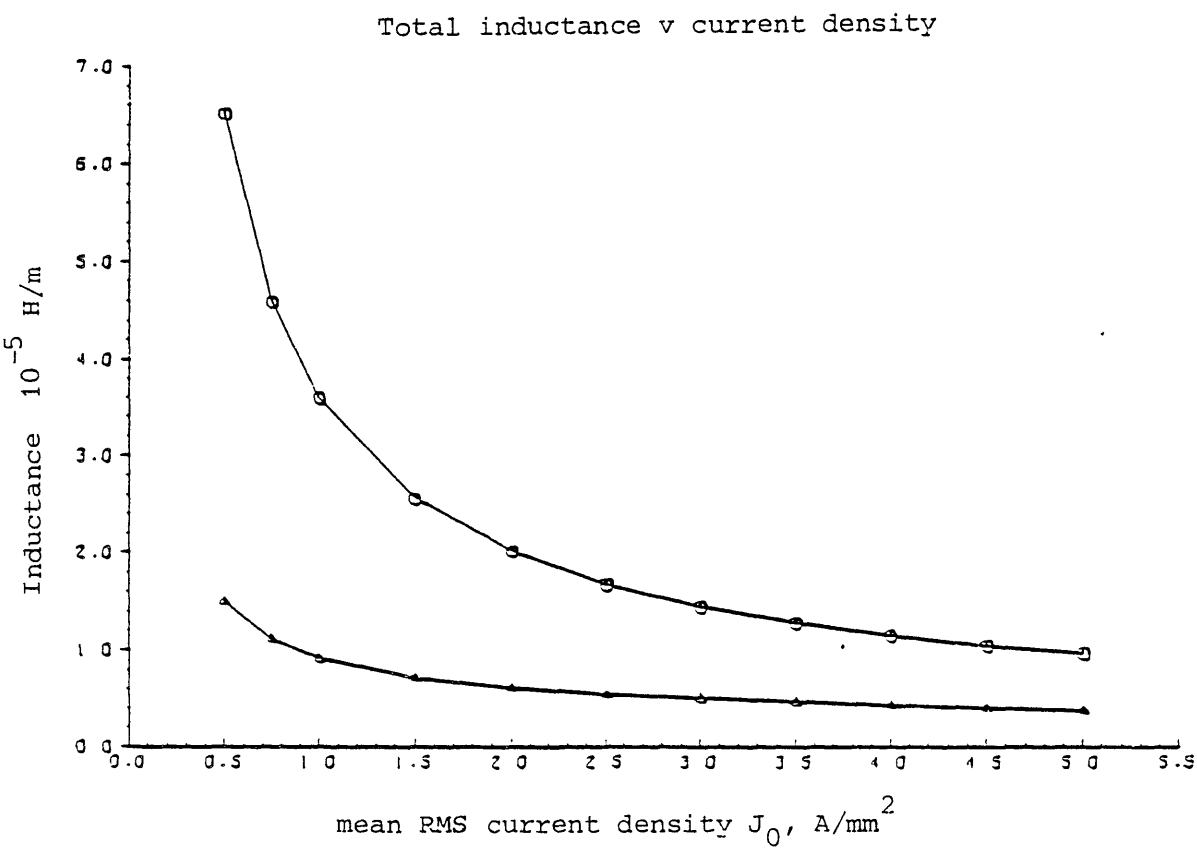


Fig. 5.4

o bridge depth = 0.5 mm

Δ bridge depth = 0.1 mm

components are given separately in Table 5.1. Inspection of Table 5.1 shows that whilst the bridge leakage dominates, and is the most susceptible to magnetic saturation, the other components of leakage inductance also fall as the current increases. This is thought to be due to the saturation of the main flux paths. For example, with a 0.5 mm slot bridge the bar impedance falls by 85% when $\bar{J}_0$ is increased from 0.5 to 5.0 Amm-2. The impedance drop in the bar, however, has increased by at least 47%, with a corresponding increase in the airgap tooth flux.

Changes in rotor frequency were found to have little effect on the bridge and airgap components of leakage inductance, whereas the slot component was affected in the manner illustrated in Figure 5.5 This figure shows relatively small changes in what is itself a small component of leakage inductance. The characteristics of Figure 5.5 clearly indicate the influence of saturation on what is normally held to be a non-saturable component of leakage inductance. Increasing the bar current at constant bridge depth is seen to produce a reduction in slot leakage inductance, due to the increased saturation of the surrounding iron paths. Similarly, when the bar current is kept constant but the bridge depth is increased, the tooth saturation is also increased and the slot leakage inductance falls. This figure also provides a convenient means of relating the present work to what has gone before. Analytical expressions for the impedance of circular bars in semi-closed slots have been published by a number of authors [41 -43]. Whilst these authors assumed the surrounding iron to be infinitely permeable and presented results which are valid only for semi-closed slots, their formulae included a $\frac{\sin\theta}{\theta}$ term, where 2θ is the angle subtended at

Leakage Inductance Component ($\mu H\ m^{-1}$)		Mean Current Density (J_o) (Amm^{-2})		
		0·5	2·5	5·0
L_{slot}	b = 0·5 mm	1·07	0·88	0·77
	b = 0·1 mm	1·29	1·29	1·07
L_{gap}	b = 0·5 mm	0·30	0·23	0·17
	b = 0·1 mm	0·55	0·55	0·47
L_{bridge}	b = 0·5 mm	63·73	15·59	8·65
	b = 0·1 mm	13·08	3·57	2·16
L_c	b = 0·5 mm	65·09	16·70	9·58
	b = 0·1 mm	14·70	5·41	3·71

Table 5.1

Variation of leakage inductance components with d.c. current density and slot bridge depth for the round bar (f = 50 Hz)

the bar centre by the slot opening. Setting $\frac{\sin\theta}{\theta} = 1$ therefore produces a result which, whilst not strictly valid, should give a reasonable approximation to the unsaturated slot inductance with a closed slot. The variation of slot inductance with frequency, obtained in this way, is also included in figure 5.5.

The relationship between this unsaturated characteristic and those calculated by the method proposed in this chapter is as one would expect: the unsaturated inductances are of similar magnitude but larger than their saturated counterparts. The correspondence between these characteristics is thought to be evidence of the validity of the proposed method.

Figure 5.6 shows the calculated variation of bar resistance with frequency, for slot bridge depths of 0.5 mm and 1.0 mm, and mean current densities of 0.5 and 5.0 Amm-2, together with the variation calculated using the approximate method described above. The results show that magnetic saturation has relatively little effect on the bar resistance, suggested that the current flow paths are unchanged and that variations in inductance present in Figure 5.5 are produced chiefly by changes in the flux paths. Figure 5.6 also includes the calculated variation of resistance with frequency using the approximate method referred to above. The method described in this chapter and the approximate method, produce closely similar results over the frequency range of principal interest to the induction motor analyst.

Whilst the finite element method described in Section 5.2 uses a single slot pitch model, it will be appreciated that the imposition of periodicity boundary conditions along the radial boundaries means

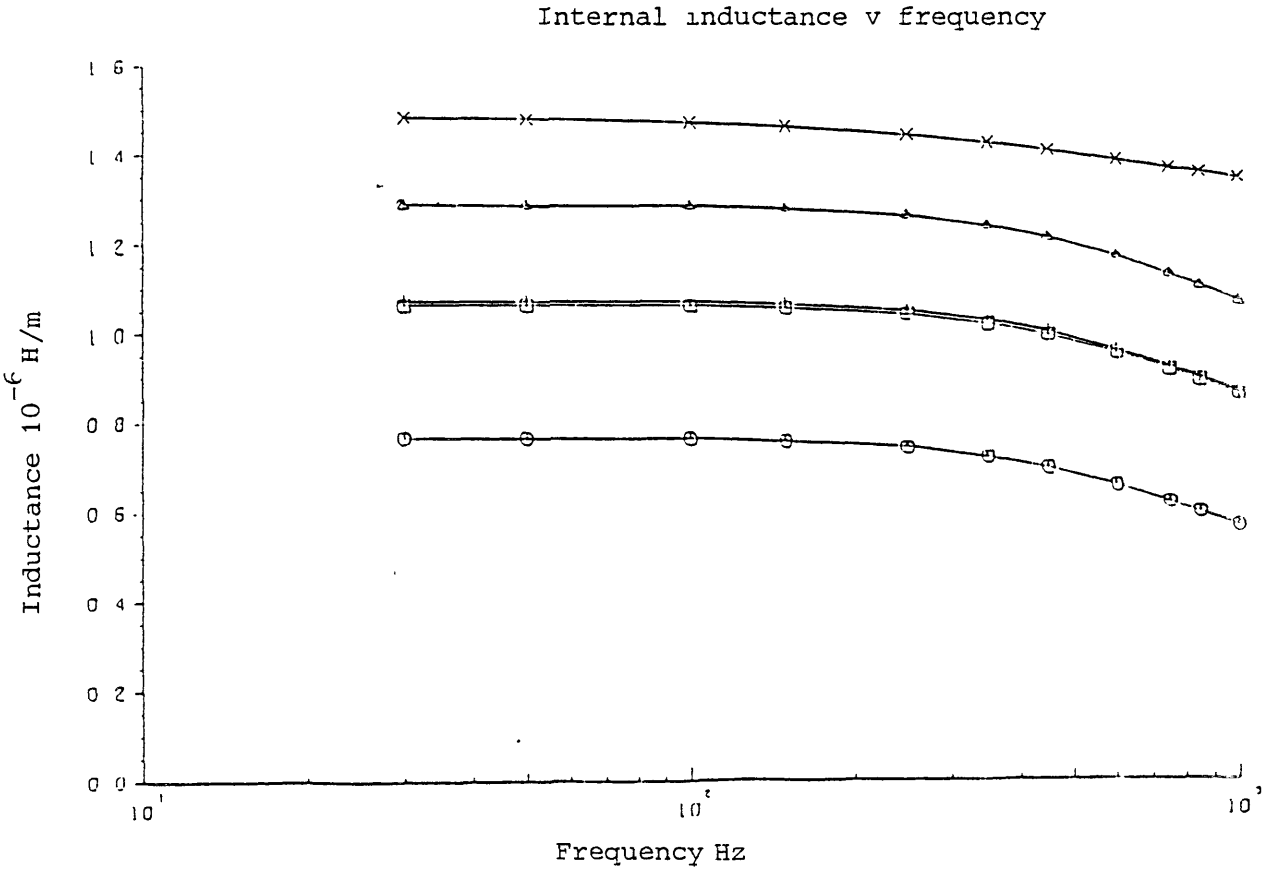


Fig. 5.5

x approximate method

Δ bridge depth = 0.1 mm, J_0 = 0.5 A/mm^2

\+ bridge depth = 0.1 mm, J_0 = 5.0 A/mm^2

□ bridge depth = 0.5 mm, J_0 = 0.5 A/mm^2

○ bridge depth = 0.5 mm, J_0 = 5.0 A/mm^2

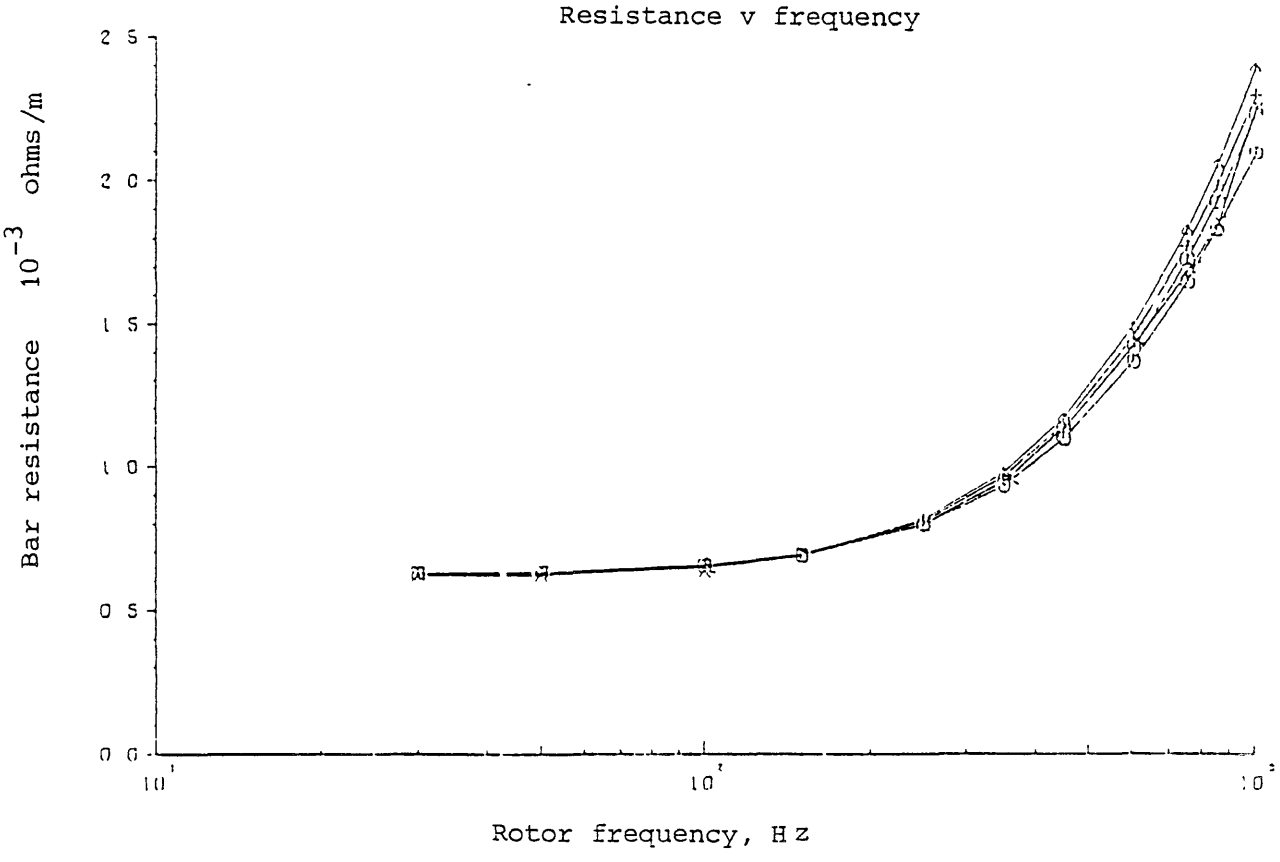


Fig. 5.6

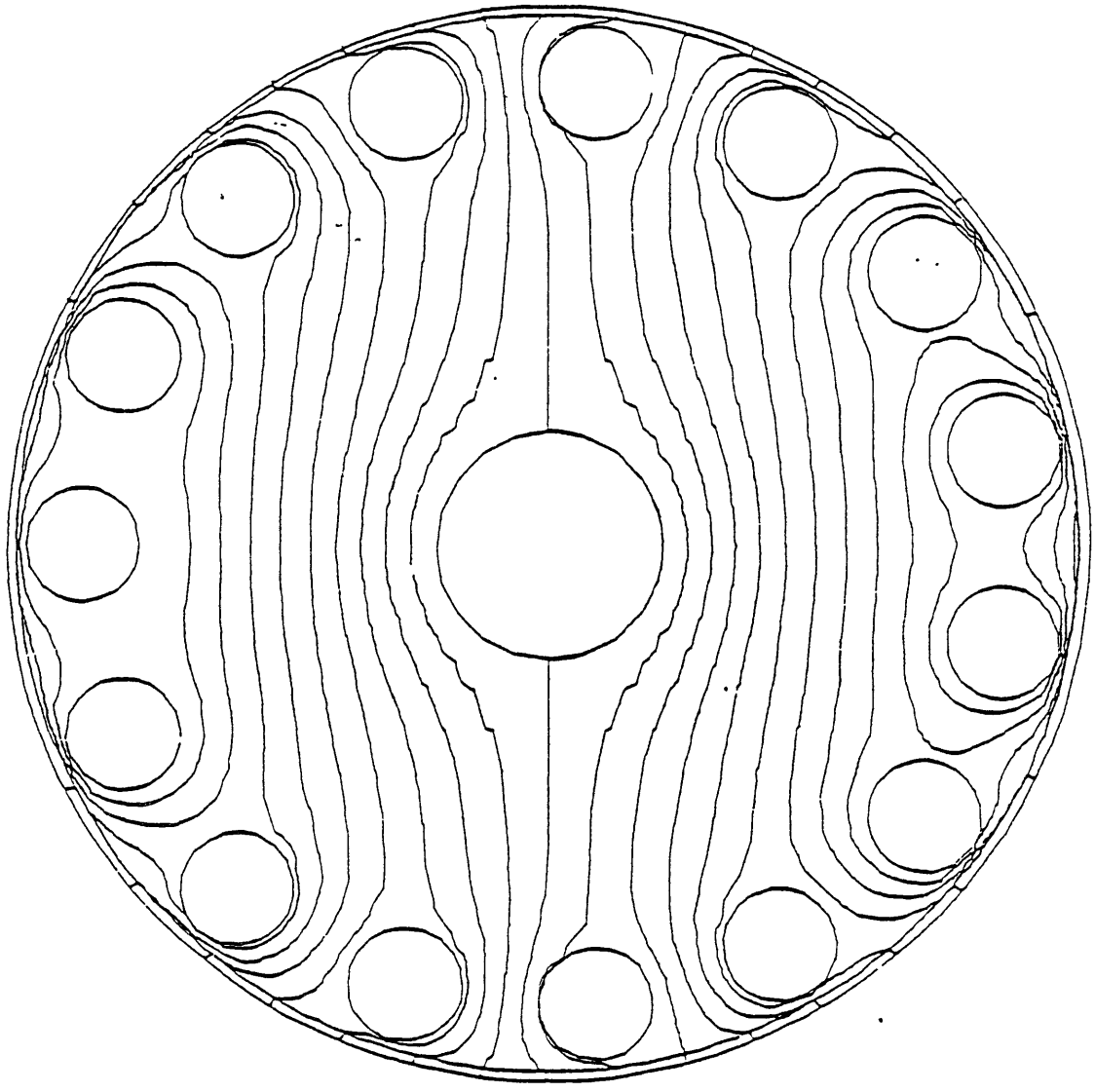
x Approximate method

Δ Bridge depth = 0.1 mm, J_0 = 0.5 A/mm^2

\+ Bridge depth = 0.1 mm, J_0 = 5.0 A/mm^2

□ Bridge depth = 0.5 mm, J_0 = 0.5 A/mm^2

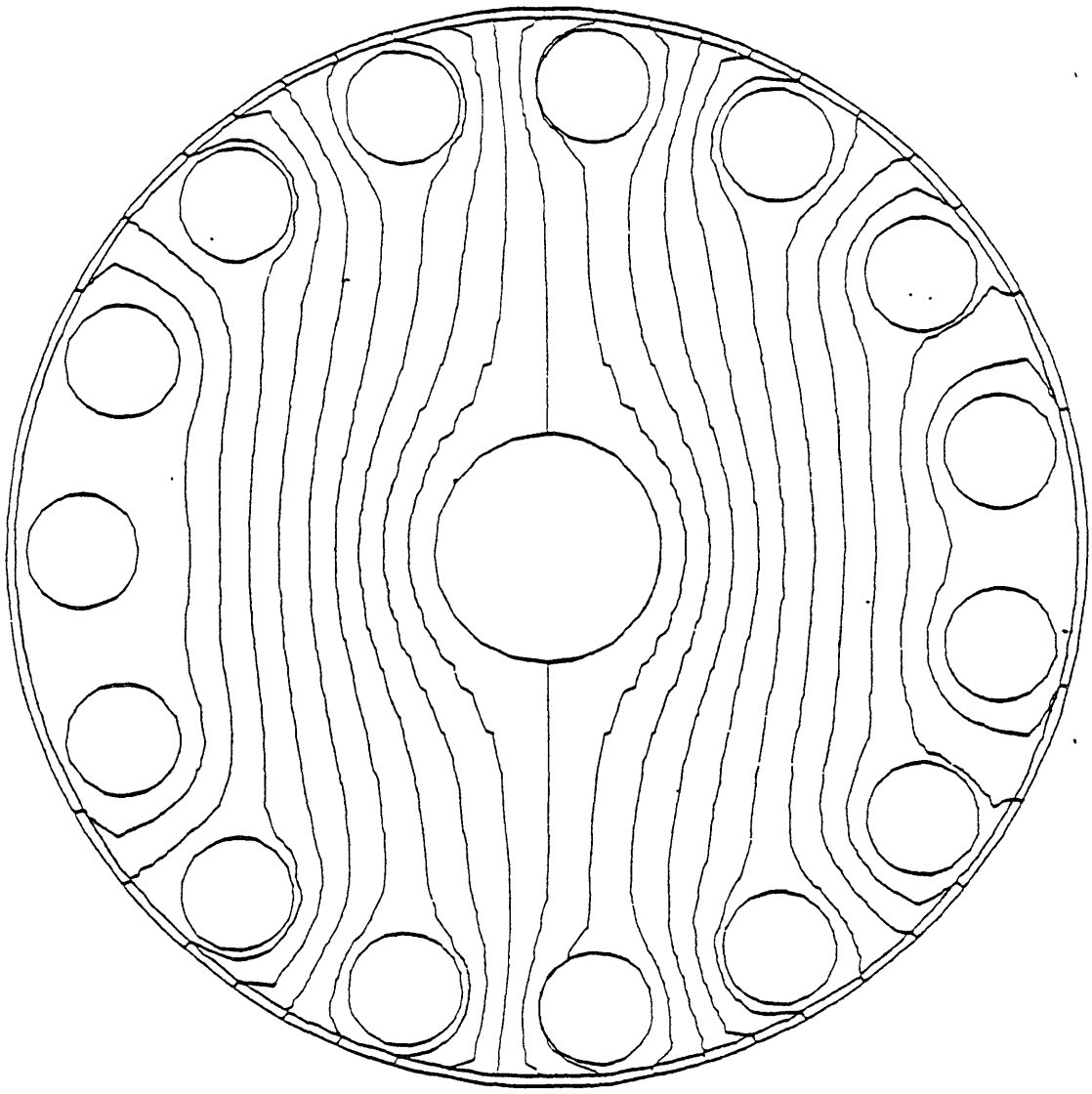
o Bridge depth = 0.5 mm, J_0 = 5.0 A/mm^2



The Datum = - 35.4383E-04
The Step Length = 29.5319E-05
A Maximum = 29.7188E-04
A Minimum = 0

Contours of A at 50 Hz
0.5 mm Bridge Thickness
Current density = 0.5 Amps/mm^2

Fig. 5.7



The Datum = - 26.6353E-03
The Step Length = 22.1961E-04
A Maximum = 23.0358E-03
A Minimum = 0

Contours of A at 1 KHz
0.5 mm bridge thickness
Current density = 5.0 Amps/mm^2

Fig. 5.8

that the whole rotor is implicitly modelled. The complete rotor flux pattern can be recovered by using appropriate phase shifts on the single slot solution. As an example, Figure 5.7 illustrates the field due to the rotor currents for a two pole 50 Hz excitation with an r.m.s. bar current of 14.1 A. Figure 5.8 illustrates that a similar field pattern is produced when an r.m.s bar current is increased to 141 A, with the exception that the bridge leakage flux is no longer in evidence. This may be explained by reference to the interval between adjacent flux lines, which is 0.30 mWb/m in Figure 5.7 and 2.20 mWb/m in Figure 5.8. Increasing the bar current by a factor of ten has produced relatively little change in the bridge leakage flux, which is now a smaller proportion of the total flux produced by the rotor currents. The difference between Figure 5.7 and 5.8 is therefore a clear indication of increasing slot bridge saturation.

5.6.2 Parallel-sided Bars with Rounded Ends: Figure 5.9 defines the geometry of a parallel-sided bar that is used in three phase machines by at least one leading British manufacturer. Figure 5.10 shows the mesh used in the finite element analysis, with Figure 5.11 being a detail of the mesh close to the slot bridge.

Figure 5.12 shows the variation of the combined leakage inductance with current for slot bridge depths of 0.1 mm and 0.55. As before, the effects of magnetic saturation are clearly evident. Table 5.2 gives the individual components of leakage inductance, showing that the bridge inductance is much more saturated than it was in the case of the round bar. This may be accounted for by comparing the cross sectional areas of the two bars. The parallel sided bar has almost five times the cross sectional area of the round bar, so that for a

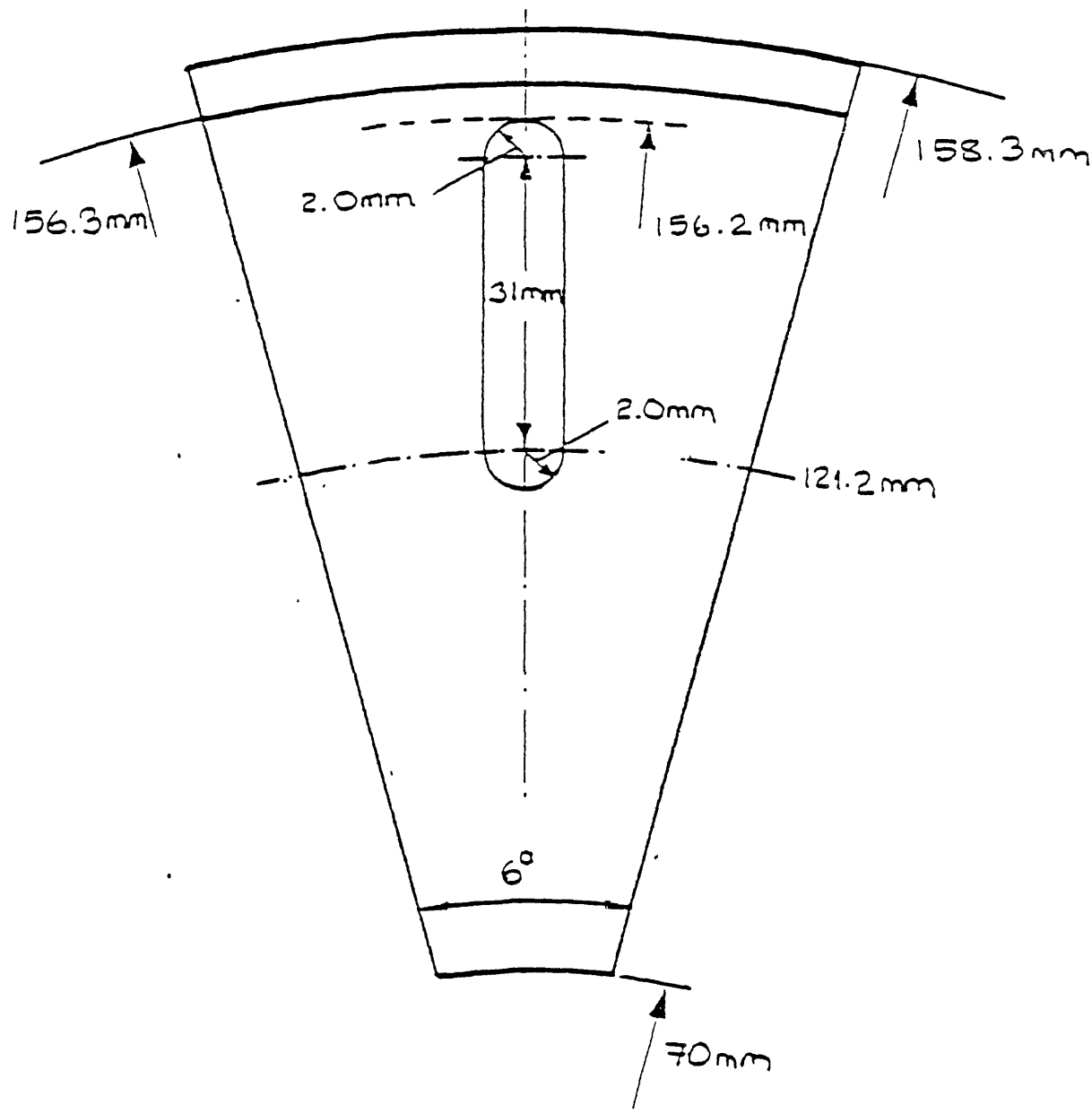


Fig. 5.9 Parallel-sided bar geometry

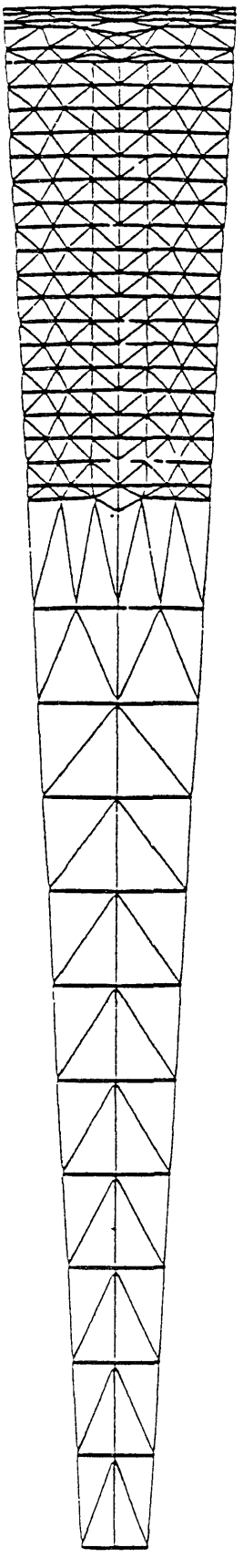


Figure 5.10 Parallel-sided bar mesh

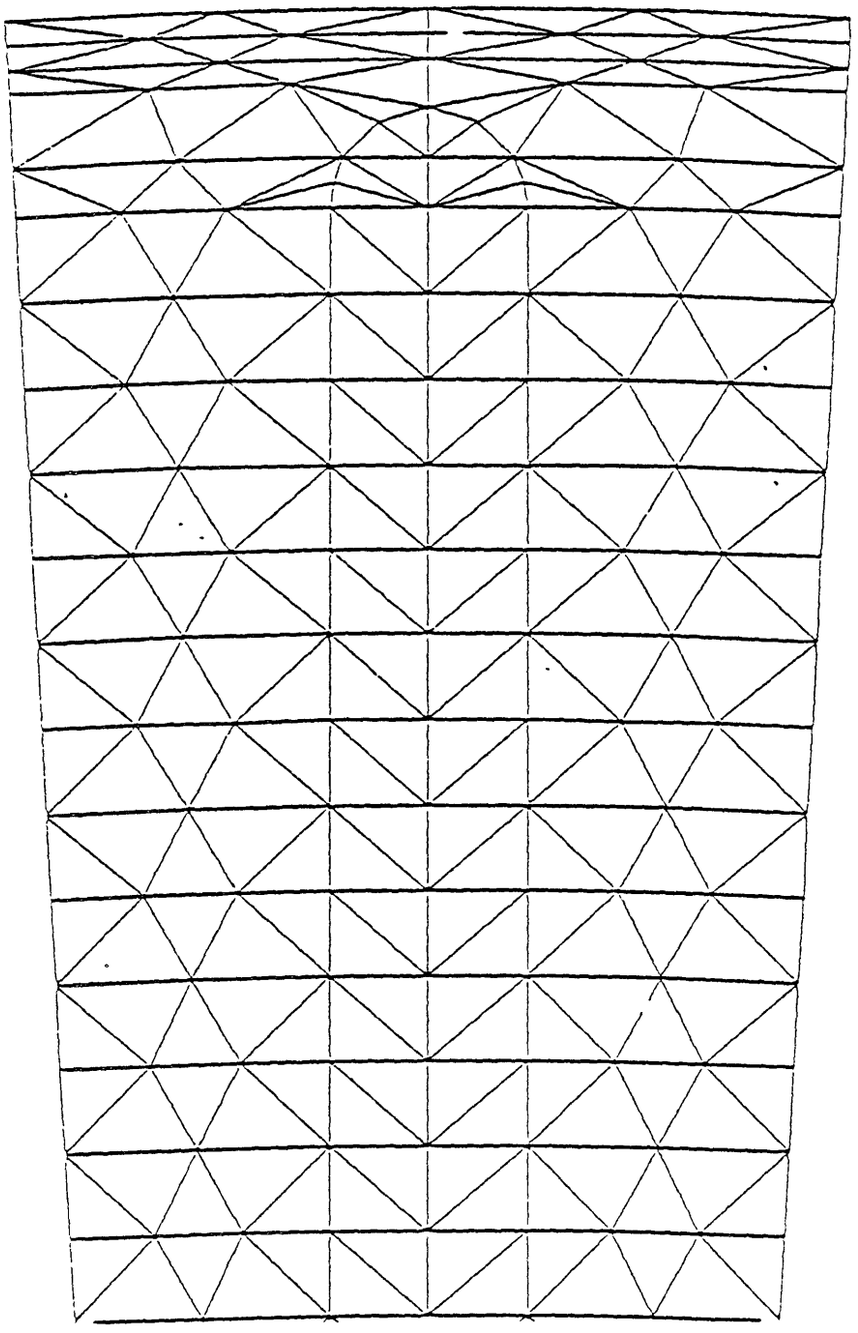


Fig. 5.11 Parallel-sided bar mesh, detail

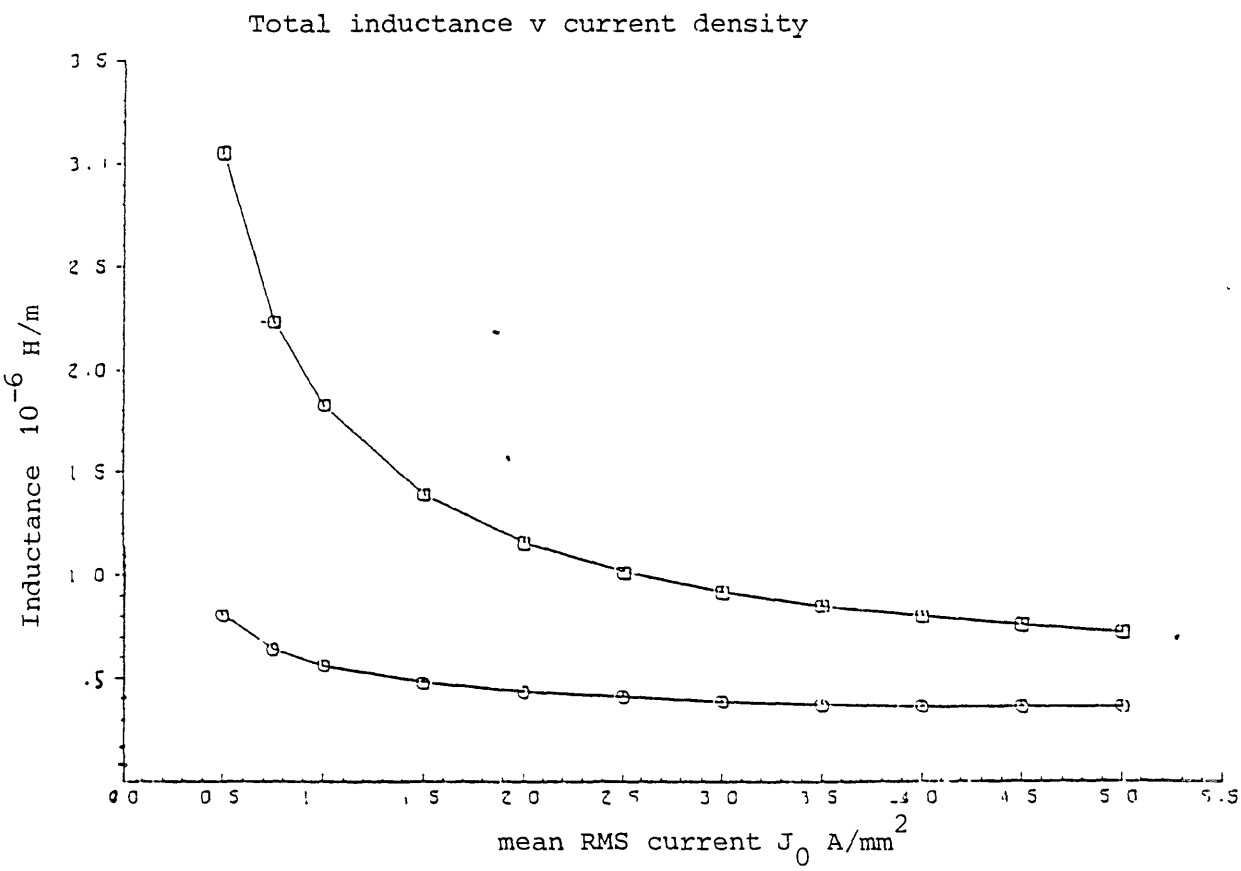


Fig. 5.12

Frequency = 50 Hz

□ bridge depth = 0.5 mm

0 bridge depth = 0.1 mm

Leakage Inductance Component ($\mu H\ m^{-1}$)		Mean Current Density (J_o) (Amm^{-2})		
		0·5	2·5	5·0
L_{slot}	b = 0·5 mm	2·17	1·91	2·00
	b = 0·1 mm	2·21	2·18	2·30
L_{gap}	b = 0·5 mm	0·18	0·16	0·14
	b = 0·1 mm	0·18	0·18	0·17
L_{bridge}	b = 0·5 mm	28·15	8·05	5·10
	b = 0·1 mm	5·66	1·72	1·14
L_c	b = 0·5 mm	30·50	10·12	7·24
	b = 0·1 mm	8·05	4·09	3·61

Table 5.2

Variation of leakage inductance components with d.c. current density and slot bridge depth for a parallel-sided slot with rounded ends.

given mean current density the m.m.f. available for driving flux through the bridge is increased by that factor. With a 0.1 mm thick slot bridge, the bridge leakage inductance is seen to be less than the slot leakage inductance. Table 5.2 also shows that the slot component appears to increase at higher current levels for both thickness of slot bridge. Closer examination of this phenomenon showed that the teeth had become so saturated that the m.m.f. drop down the teeth was sufficient to make the flux taking the parallel radial path down the slot a non-negligible quantity. This radial slot flux is included in the slot leakage inductance calculation, as defined by equation 5.19.

Figure 5.13 gives the variation with frequency of the combined leakage inductance, together with its constituent components.

This shows that because the slot leakage is, in this instance, a large proportion of the whole, the combined inductance is now strongly frequency dependent.

As in the case of the round bar, the slot leakage inductance calculation affords some means of comparison with previous work on a similar, though not identical, geometry.

The analysis of deep bar effect in a parallel-sided bar which fills an open slot has been carried out by Alger [39]. The expressions he derives for effective bar resistance and bar leakage reactance are

$$R_b = R_o \frac{\xi}{2} \left[\frac{\sinh\xi + \sin\xi}{\cosh\xi - \cos\xi} \right] \qquad (5.26)$$

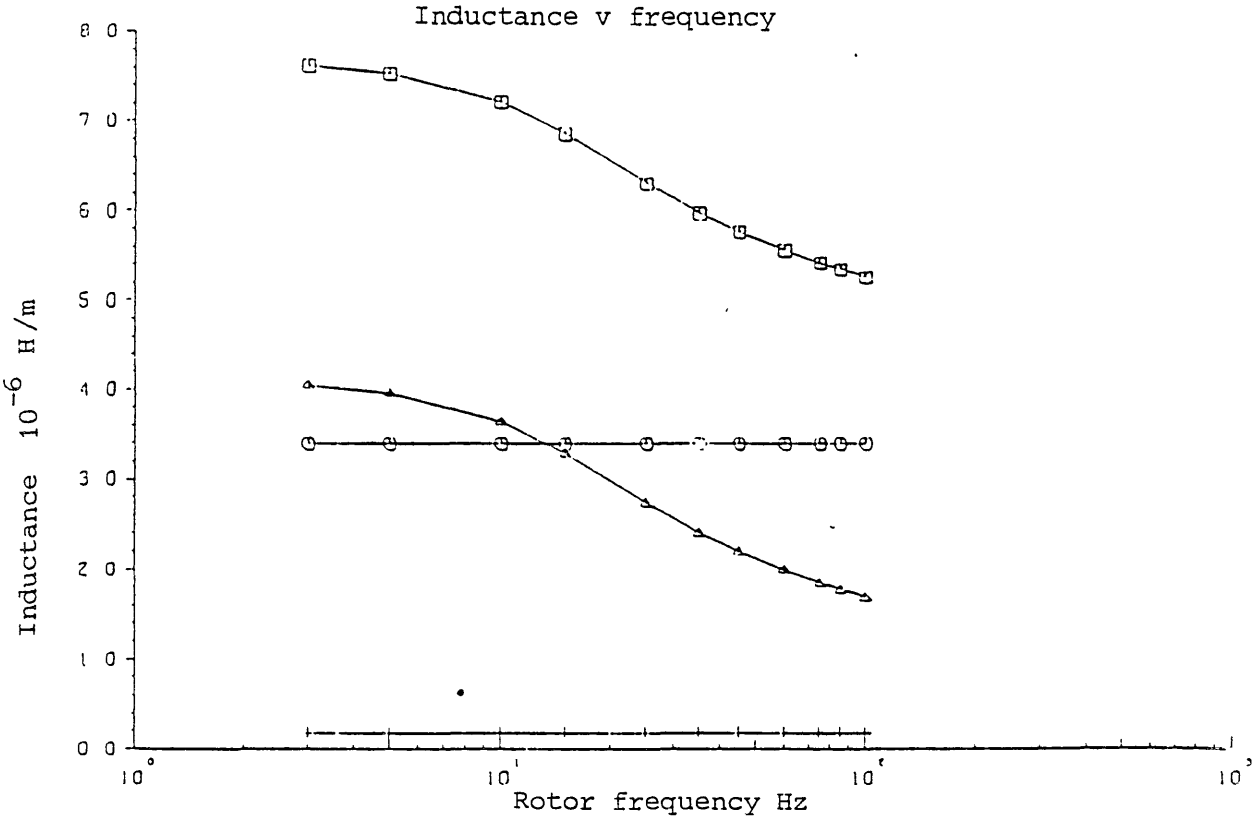


Fig. 5.13

Variation of bar leakage inductance, and its constituent components, with frequency. Parallel-sided bar with round ends J_0= 2.5 A/mm^2, bridge depth = 0.1 mm

$$L_{slot} = L_o \frac{3}{\xi} \left[\frac{\sinh\xi - \sin\xi}{\cosh\xi - \cos\xi} \right] \qquad (5.27)$$

where R_o and L_o are the low frequency values of R_b and L_{slot} respectively, and

$$\xi = 2d \sqrt{\frac{\omega \mu_o \sigma}{2}}$$

d is the bar depth, and σ its conductivity.

Figure 5.14 compares the frequency dependence of the slot component of leakage inductance calculated using the method described in this section with that calculated using equation 5.27. As before, the agreement is thought to be surprisingly good, in view of the vastly different boundary conditions at the top end of open and closed slots. It will be appreciated, in this respect, that the flux at the top of the slot links all the current at all frequencies, and therefore makes a significant contribution to the inductance. Figure 5.15 similarly compares the bar resistance calculated by the two methods showing that the open slot approximation gives excellent agreement with the more detailed finite element approach. To investigate this situation further, the variation with distance along the slot of the magnitude and phase of the bar current density were computed using both methods. The results are presented in Figures 5.16 and 5.17 which show that the current distributions are sensibly identical, with slight differences being produced at the slot top.

5.6.3 Elliptical bars: These are the type of bars used in a small shaded-pole motor, which is in mass production and was simulated in Chapter 4. One of the main reasons for performing the deep-bar work

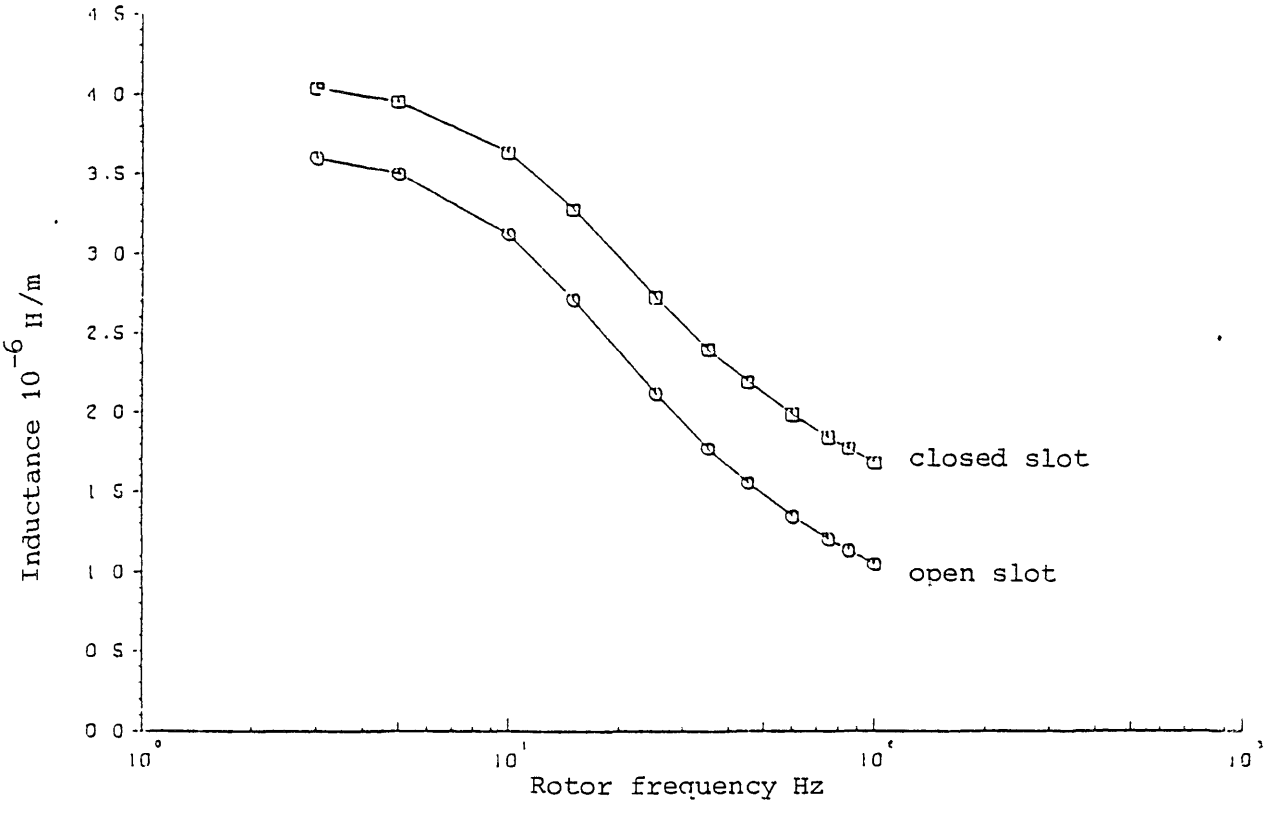


Fig. 5.14

Variation of slot leakage inductance with frequency. Parallel-sided bar with round ends and with open ends, J_0 = 2.5 A/mm^2, bridge depth = 0.1 mm

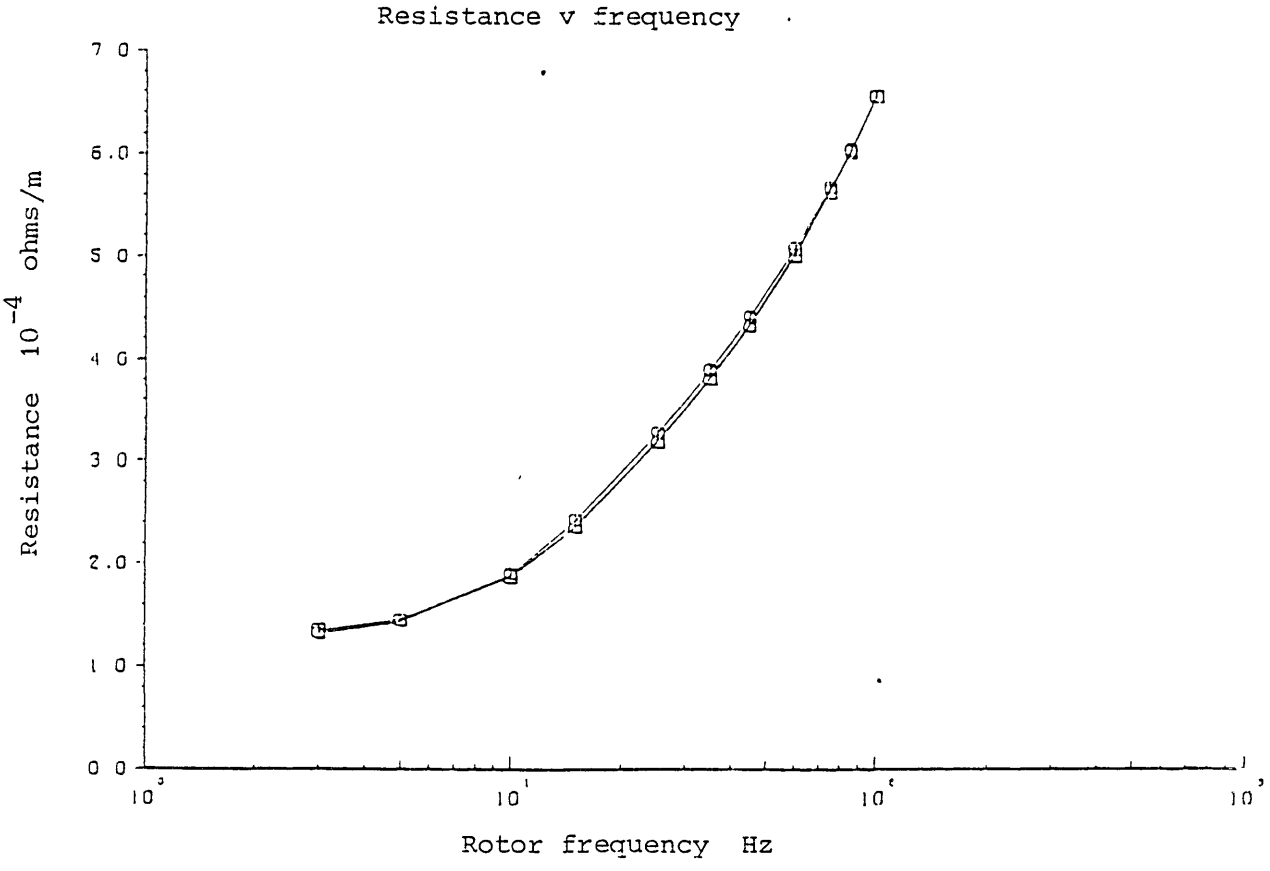


Fig. 5.15

Parallel-sided bar with round ends J_0=2.5 A/mm^2

bridge depth = 0.1 mm

□ closed slot

o open slot

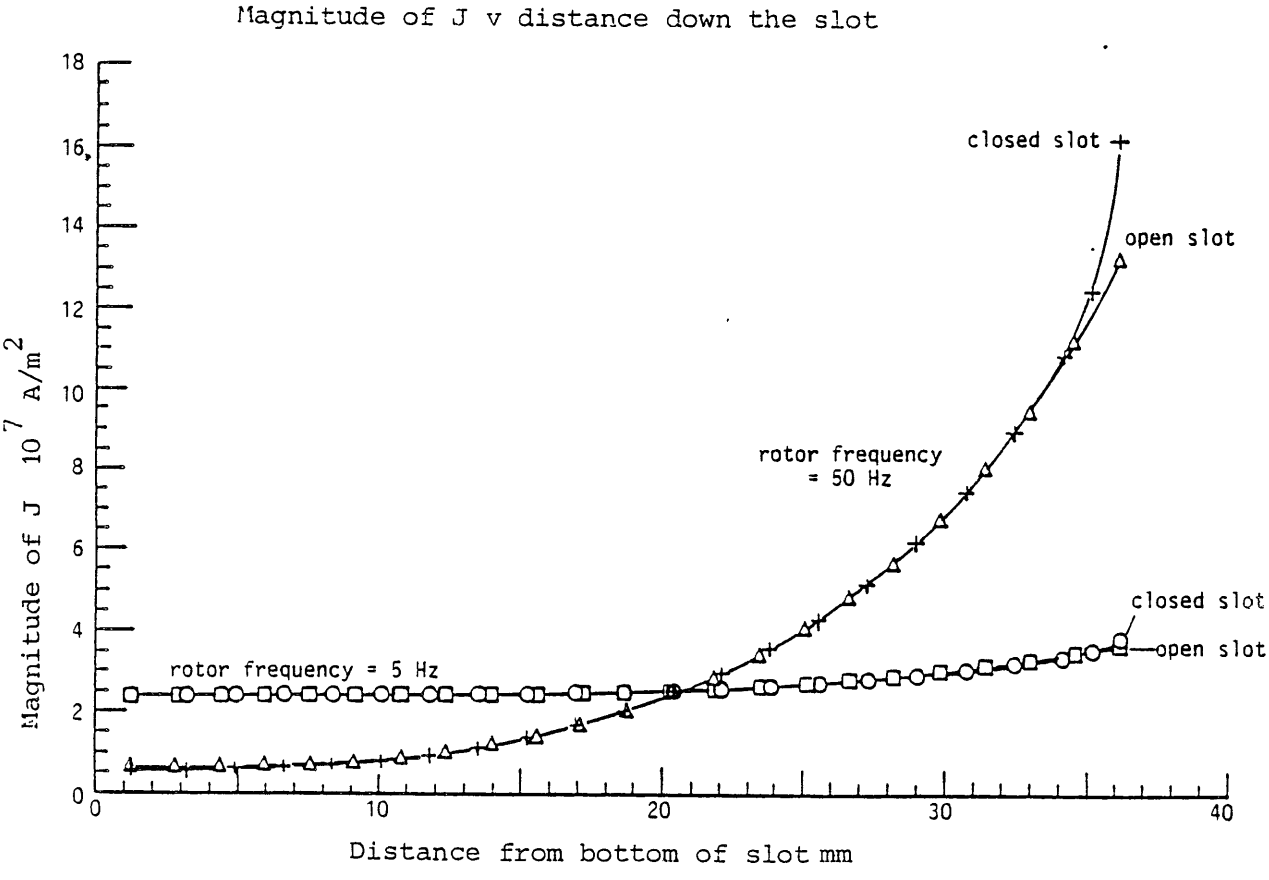

Magnitude of J v distance down the slot
Magnitude of J 10^7 A/m^2
Distance from bottom of slot mm
closed slot
open slot
rotor frequency = 50 Hz
rotor frequency = 5 Hz
closed slot
open slot
0
2
4
6
8
10
12
14
16
18
0
10
20
30
40

Fig. 5.16

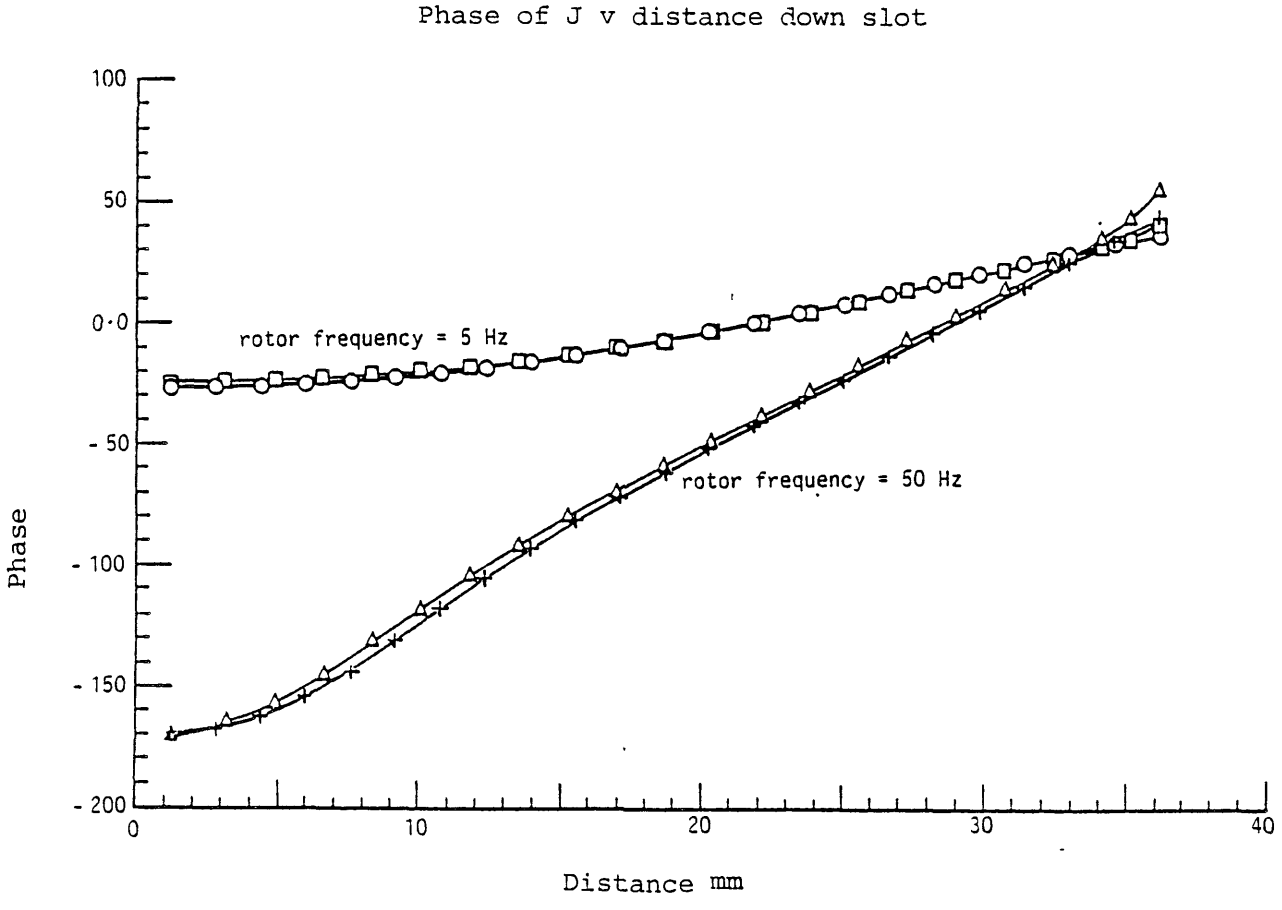

Phase of J v distance down slot
100
50
0·0
- 50
- 100
- 150
- 200
Phase
rotor frequency = 5 Hz
rotor frequency = 50 Hz
0
10
20
30
40
Distance mm

Fig. 5.17

was to more accurately determine the effects of saturation on the rotor of this machine. The results from the analysis being used as input to the simulation program. The slot and its leading dimensions are shown in Figure 5.18 and a drawing of the mesh used in the analysis is presented in Figure 5.19. From Figure 5.18 it can be seen that the bar is only 5.5 mm deep. At a frequency of 50 Hz the skin depth of Aluminium is 12 mm, thus at the rotor frequencies of interest skin-effect would not be expected to be significant. The variation of bar-resistance with frequency is shown in Figure 5.20 and demonstrates, that the resistance varies very little over the range of interest.

The values of the individual components of inductance as function of frequency are shown in Figure 5.21. It can be seen from this graph that none of the components is substantially affected by frequency in the range considered, and that the bridge leakage inductance dominates the other components.

The effects of current on the parameter values is however more interesting. Examination of Figure 5.22 reveals that the bridge-leakage inductance is strongly dependent on current, since the bridge saturates out as the current is raised. Hence the bridge-leakage component, and therefore the total leakage inductance, falls dramatically with increasing current. This variation in inductance is important when analysing induction machines, since the rotor bar current varies considerably between starting and steady-state operation.

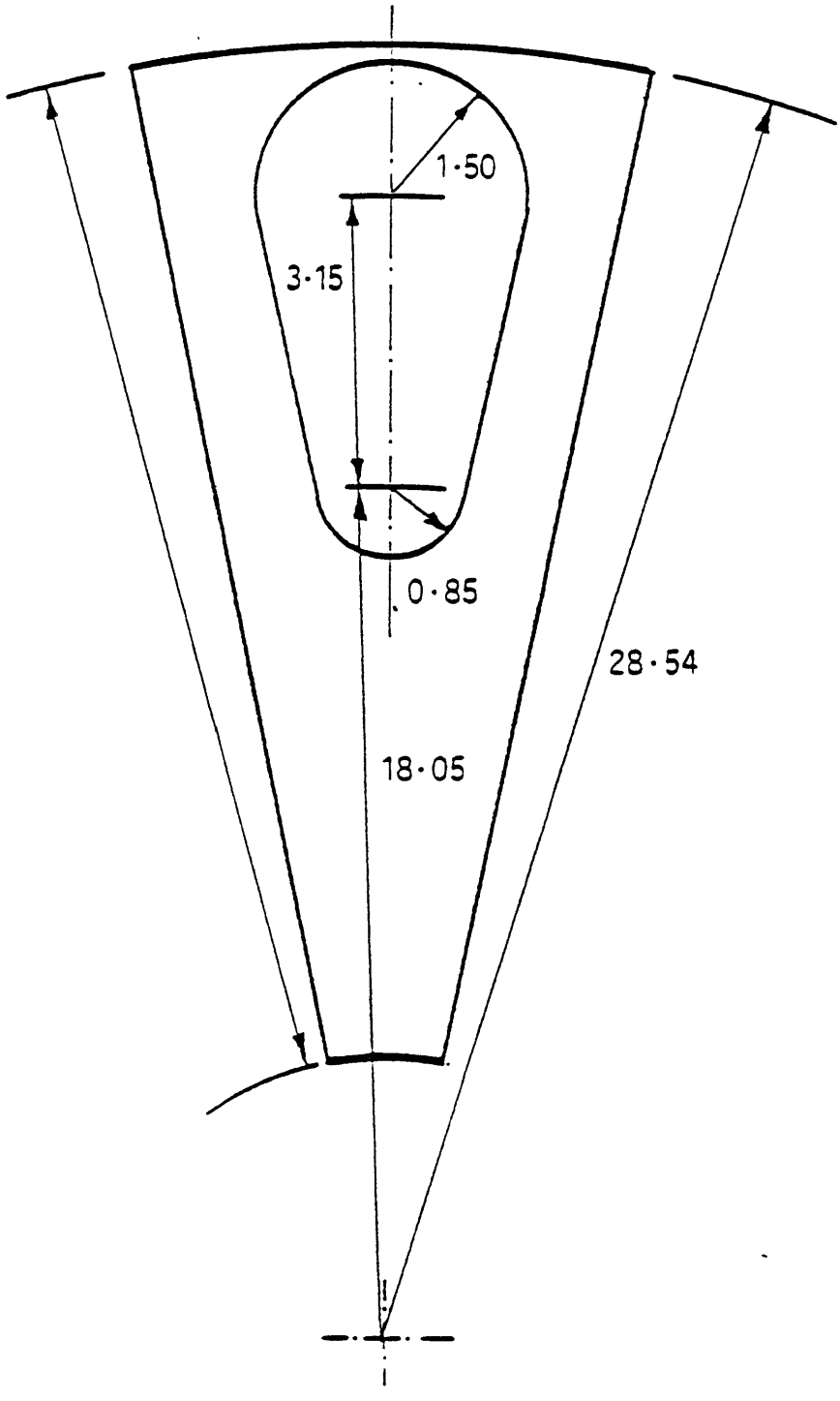


Fig. 5.18 Elliptical slot geometry

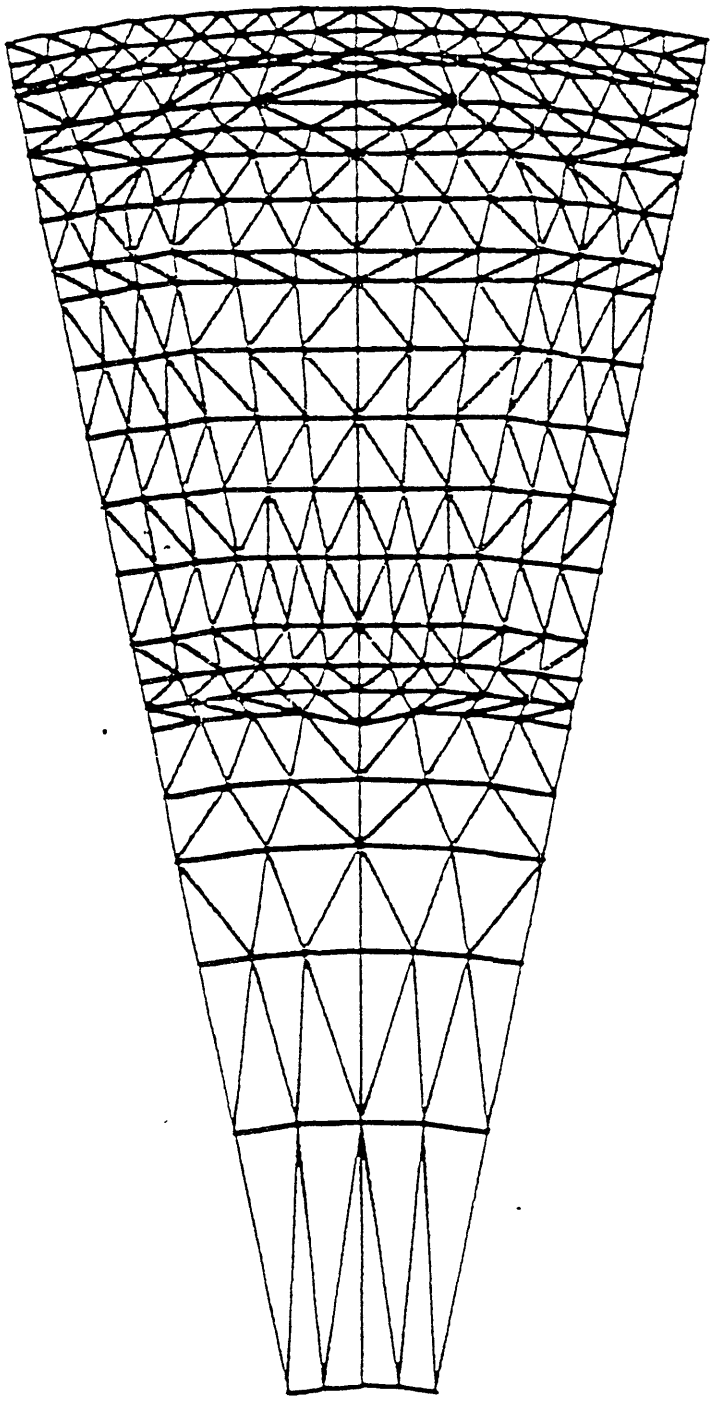


Fig. 5.19 Elliptical slot mesh

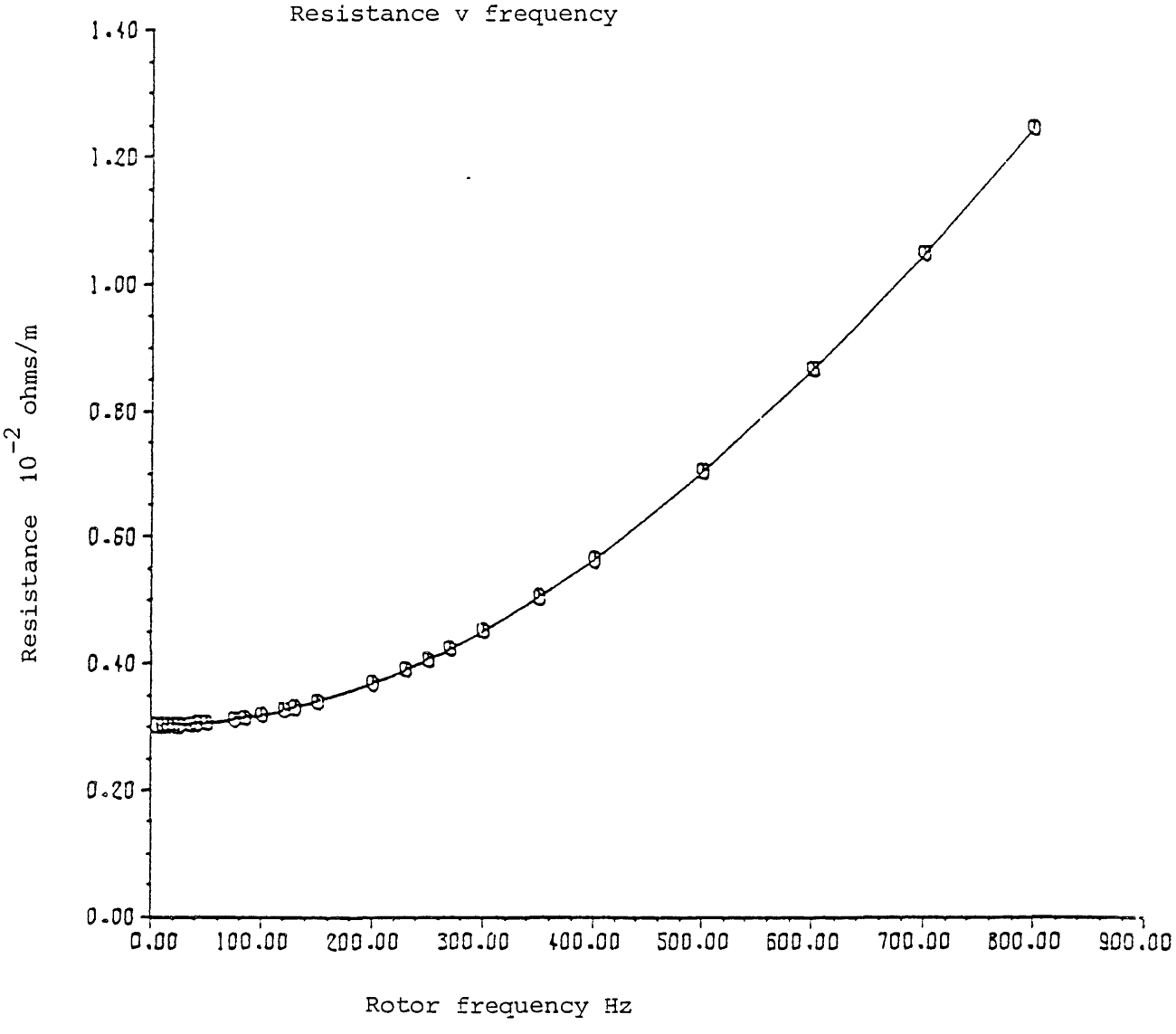


Fig. 5.20

Variation of bar resistance with frequency
R.M.S. current density J_0 = 0.5 A/mm^2

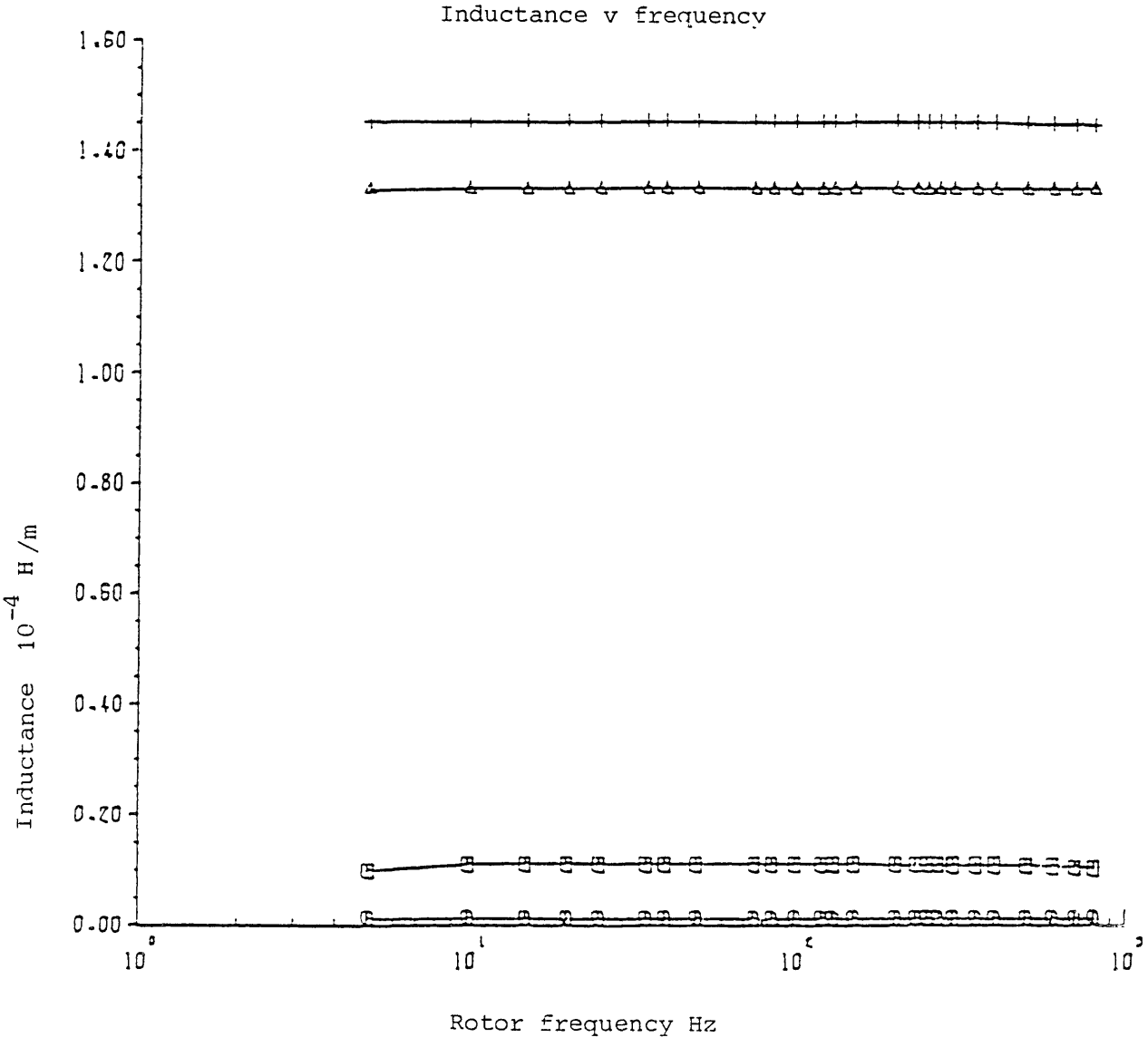


Fig. 5.21

R.M.S. current density J_0 = 0.5 A/mm^2

□ Slot leakage inductance

o Airgap leakage inductance

Δ Bridge leakage inductance

\+ Total leakage inductance

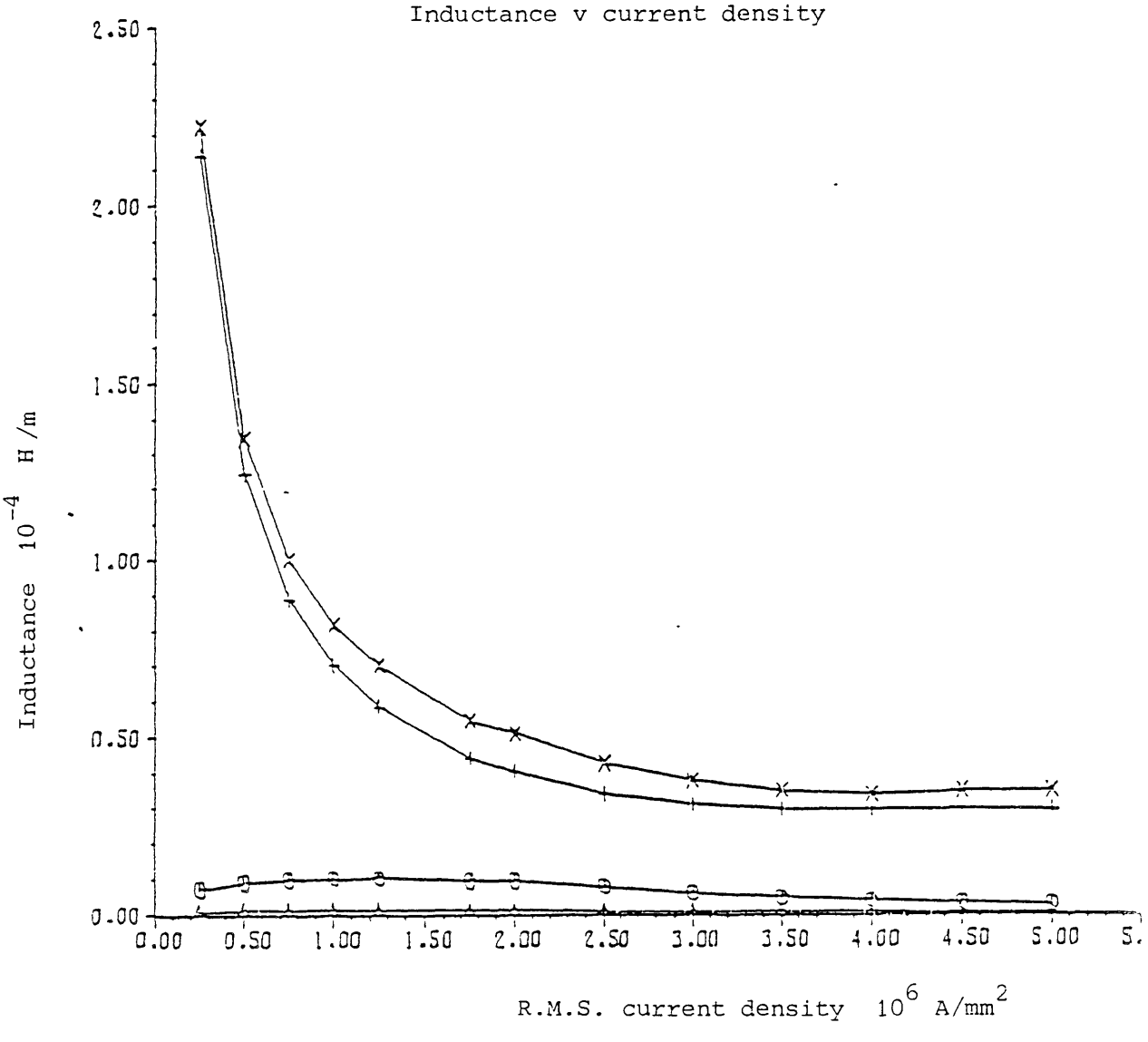


Fig. 5.22

o Slot leakage inductance

Δ Airgap leakage inductance

\+ Bridge leakage inductance

x Total leakage inductance

Further consideration of 5.21 shows that the slot-leakage and airgap-leakage components also fall slightly with increasing current. This, as earlier, is attributed to the saturation of the main flux paths.

The resistance of the bars is unaffected by variations in current. This means that the current flow paths are not affected by saturation of the rotor.

5.7 Conclusions

This chapter has described a method for calculating the leakage impedances of cage rotors with closed slots; taking into account magnetic saturation in the rotor and skin effect in the bars. The method is quite general in that any combination at bar and slot stage can be analysed. However the method is limited to analysing situations where the saturation on the rotor teeth is fairly uniform over a pole pitch, which would be the case if poly-phase induction motors were being examined. But when machines such as the one in Chapter 4 are analysed, it is found that the distribution of saturation in the rotor is important and therefore the results from this chapter were not used to predict the slot leakage reactance of that machine. The values of resistance, on the other hand, were incorporated in Chapter 4 since they were found to be substantially independent of rotor saturation.

The work carried out in this chapter has been published as an IEE paper which is appended at the end of this thesis.

CHAPTER SIX

THE CALCULATION OF THE RESISTANCE OF INDUCTION MOTOR ENDRINGS

6.1 Introduction

As has been pointed out in an earlier section there are some machine parameters that cannot be calculated directly from a two dimensional field model of the motor. The resistance of the endrings of an induction motor is one of these. It is therefore necessary to either calculate the value of this resistance by using an empirical formula or by some other means and then to add it to the values already calculated in the field model. This chapter is devoted to calculating the value of harmonic endring resistance in a more accurate manner than has previously been attempted.

The induced currents which flow axially through the bars of a cage rotor complete their closed paths by passing circumferentially around the endrings. The endrings offer resistance to the passage of current, which is traditionally accounted for by making a modification to the bar resistance. This is done by equating the joule losses in the real cage to those in an equivalent cage which carries the same current distribution but which has zero-resistance endrings. By this technique, the effective bar resistance can be shown to be given by (see Appendix 8.4)

$$R'_b = R_b + \frac{R_e}{2N_b \sin^2(\frac{P\pi}{N_b})} \qquad (6.1)$$

This expression shows that the contribution made by the endring to the effective bar resistance depends not only on its physical dimensions, but also on the number of poles. Different harmonic current distributions in the same cage will 'see' different effective resistances. This feature has prompted some authors to suggest that in single-phase machines, in which stator m.m.f. harmonics are always present, the appropriate resistance required for the fundamental should be obtained using relatively low resistance bars and high resistance endrings, so that the harmonic resistances are made smaller [47,48]. This option, however, must be exercised with caution, because excessively high resistance endrings may promote inter bar currents.

In order to make use of equation 6.1 it is necessary to be able to calculate the endring resistance, R_e. A method for doing this was described in a classical paper by P.H. Trickey, in 1936 [49]. Trickey used the model illustrated in Figure 6.1. It consists of a half pole-pitch arc of an annulus, the inner radius of which is equal to that of the endring, whilst its outer radius is given by the rotor bar pitch-circle radius. Laplace's equation in two dimensions may be solved inside such a region provided appropriate boundary conditions are stipulated. To this end, Trickey represented the injection of currents from the bars, into the ring, by a sinusoidally distributed current density which flows radially inwards over the length of the arc AB. This assumed current density distribution enables boundary conditions to be specified along three of the region boundaries, whilst that along the fourth (i.e. the arc CD) derives from it being a conductor/air interface through which current cannot pass. The

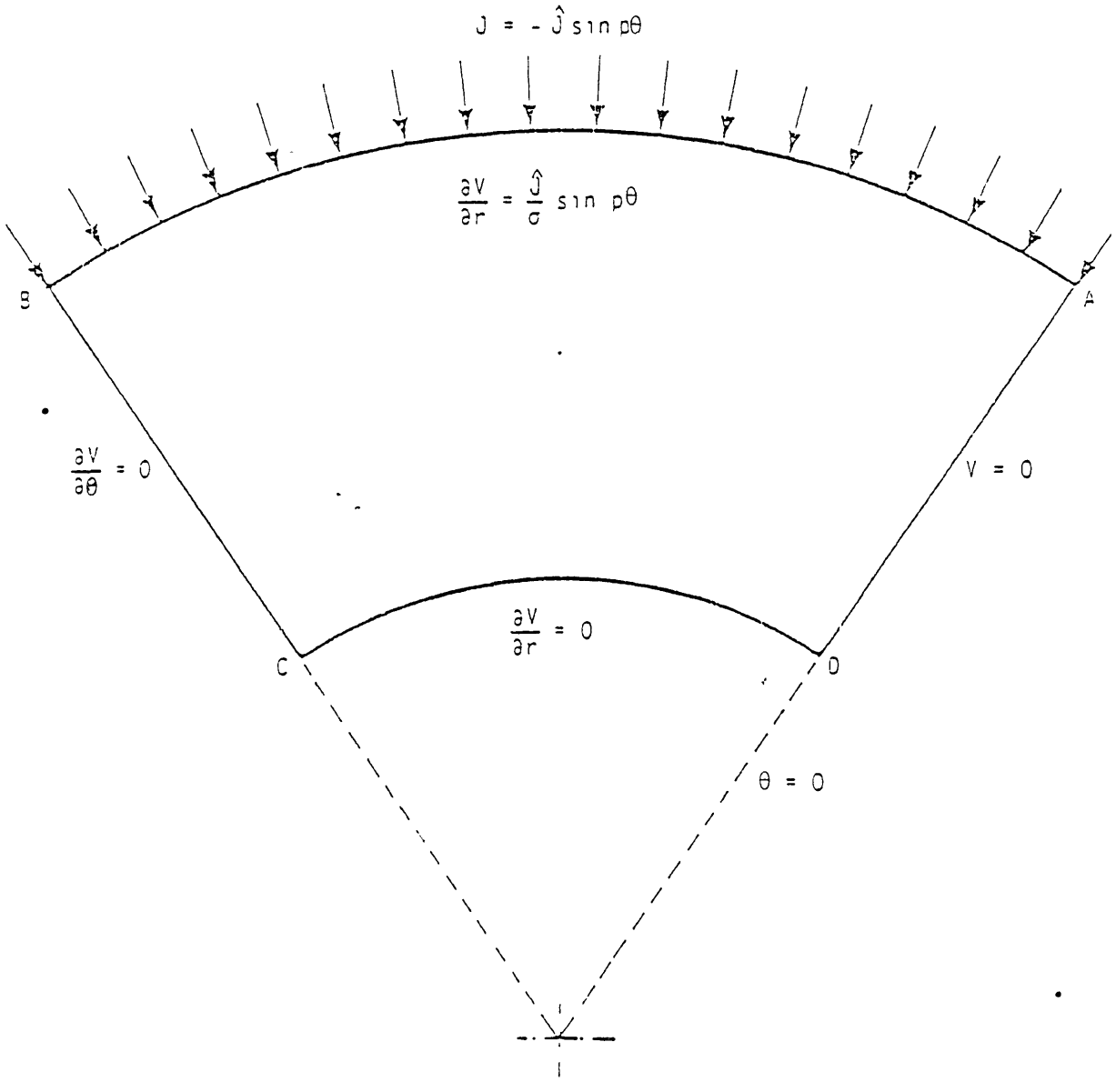


Fig. 6.1 Trickey's model for ending resistance calculations

resulting boundary conditions are indicated on Figure 6.1. Using this model Trickey showed that the endring resistance should be calculated according to the equation

$$R_e = \frac{2\pi D_r \rho}{t(D_r - D_i)} K_{ring} \qquad (6.2)$$

where K_{ring} is a correction factor for wide endrings given by

$$K_{ring} = P \left(\frac{1 + \left(\frac{D_i}{D_r} \right)^{2p}}{1 - \left(\frac{D_i}{D_r} \right)^{2p}} \right) \left(1 - \frac{D_i}{D_r} \right) \qquad (6.3)$$

The great strength of Trickey's method is that his correction factor K_{ring} has an analytical expression which is simple to evaluate and may be used to generate design curves for regular design office use. Its main weakness, on the other hand, is that the technique by which the bar currents are introduced into the endring is somewhat artificial, suggesting that simplicity might have been achieved at the cost of accuracy.

The purpose of this chapter is to describe a new method for calculating endring resistance, based on a more realistic model of the endring. The results obtained using the new method are verified by comparison with experimental data obtained from a specially constructed test-rig and are compared with the results obtained using Trickey's method.

6.2 Method of Analysis

6.2.1 Model and Assumptions: The first assumption made is that the thickness of the endrings is small when compared with their radial width and to the pole-pitch. This assumption, which is also implicit in Trickey's work, enables the current flow in the endrings to be regarded as essentially two dimensional. The model adopted is illustrated in Figure 6.2. It consists of a sector of an endring which corresponds to one rotor slot pitch. The outer and inner radii of the model are those of the real endring, the sector is symmetrically disposed with respect to the intersection of one rotor bar. The cross hatched area in Figure 6.2 which corresponds to this intersection is designated Region 2. The rotor bar current is introduced into the model as a specified current density, which enters Region 1 normally to the paper. It is assumed that deep bar effects may be neglected, so that the injected current density distribution is uniform over the whole of Region 1. The potential distribution in the endring is therefore give by

$$\frac{\partial^2 \bar{v}}{\partial x^2} + \frac{\partial^2 \bar{v}}{\partial y^2} = \frac{I_b S}{t S_b} \qquad \text{Region 1} \qquad (6.4)$$

$$\frac{\partial^2 \bar{v}}{\partial x^2} + \frac{\partial^2 \bar{v}}{\partial y^2} = 0 \qquad \text{Region 2} \qquad (6.5)$$

The curved boundaries A'B' and C'D' correspond to the outside and inside boundaries of the endring, and are consequently impervious to current flow. A homogeneous Neumann boundary condition should therefore be enforced along these two boundaries. Whilst only one rotor bar is present to inject current into the endring, it is assumed that this forms part of a cage of N_b bars, which carries a

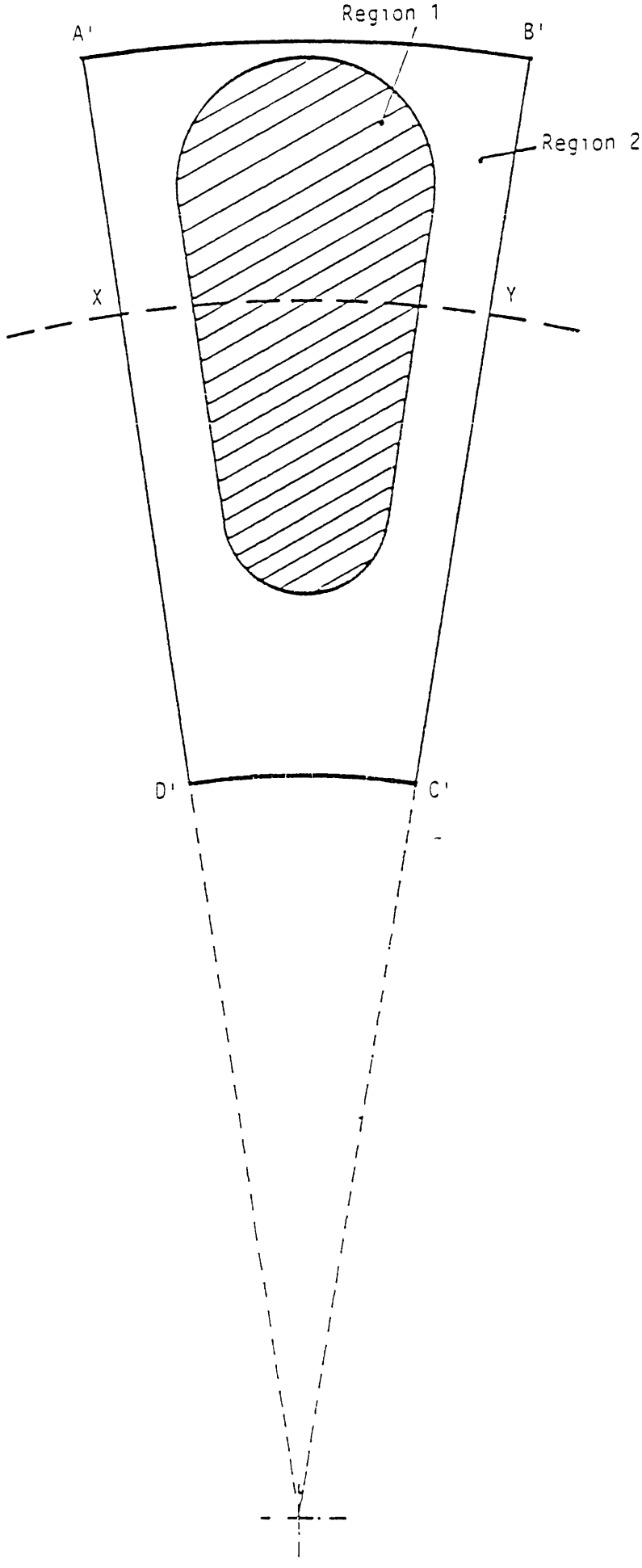


Fig. 6.2 Model used for finite-element method for calculating endring resistance

2p-pole current distribution. Under these circumstances, the potential distribution in the endring will be circumferentially periodic, and a periodicity condition may be specified between the boundaries A'D' and B'C'. For example, the potentials of the corresponding points X and Y in Figure 6.2 are related by the equation

$$\bar{V}_x = \bar{V}_y \, e^{j\frac{2\pi p}{N_b}} \tag{6.6}$$

It is to enable this form of boundary condition to be imposed that the potential function has been designated as complex in equation 6.4. Imposition of this boundary condition and how it relates to the uniqueness of the final solution is further discussed in Appendix 8.5.

6.3 Calculation of Endring Resistance

Equations 6.4 and 6.5 must be solved, subject to the boundary conditions discussed in the previous section. First order finite elements were chosen as a convenient method for achieving this [49]. The end result of the finite-element solution is a set of nodal potentials, and the object of this section is to derive an expression to enable the endring resistance to be calculated from this set.

The complex distribution over the j^{th} element is given by

$$\bar{V}_j(x,y) = \sum_{i=1}^{3} \bar{V}_{ji} \, N_{ji}(x,y) \tag{6.7}$$

where the shape functions have the usual form [49]

$$N_{ji}(x,y) = \frac{1}{2S_j} (a_{ji} + b_{ji}x + c_{ji}y) \tag{6.8}$$

The joule loss in this element is given by

$$P_j = \frac{t}{\rho} \int_{j^{th}\text{element}} \bar{E}\cdot\bar{E}^* \, dx \, dy = \frac{t}{\rho} \int_{j^{th}\text{ element}} (\nabla\bar{V}_j)\cdot(\nabla\bar{V}_j)^* \, dx \, dy \tag{6.9}$$

But

$$(\nabla\bar{V}_j)(\nabla\bar{V}_j)^* = \frac{1}{4S_j^2} \left\{ \left| \sum_{i=1}^{3} \bar{V}_{ji} b_{ji} \right|^2 + \left| \sum_{i=1}^{3} \bar{V}_{ji} C_{ji} \right|^2 \right\} \tag{6.10}$$

so that the terms under the integral sign in equation 6.9 are independent of x and y. The power loss in an endring is obtained by summing all the elemental contributions in one slot pitch, and then multiplying by the number of rotor bars.

$$P_e = Nb \sum_{j=1}^{\text{all elements}} P_J \tag{6.11}$$

As shown in Section 6.1, this may be related to the endring resistance by the equation

$$P_e = I_e^2 R_e = \frac{I_b^2 R_e}{4\sin^2\left(\frac{P\pi}{N_b}\right)} \tag{6.12}$$

Finally, combining equations 6.9-6.12

$$R_e = \frac{N_b t}{I_b^2 \rho} \sin^2 \left(\frac{P\pi}{N_b} \right) \sum_{j}^{\text{all elements}} \frac{1}{S_j} \left(\left| \sum_{i=1}^{3} \bar{V}_{ji} b_{ji} \right|^2 + \left| \sum_{i=1}^{3} \bar{V}_{ji} C_{ji} \right|^2 \right) \quad \ldots\ldots (6.13)$$

6.4 Experimental Verification

6.4.1 The object of the experiments was to obtain measurements of endring resistance so that comparisons could be made with both Trickey's technique and the finite element method. The endring resistance was determined indirectly, by making relatively few measurements on a simple test-rig, and invoking the principles of superposition.

The physical model of the endring, which was used for the experimental investigation, is illustrated in Figure 6.3. This model which was machined from a single block of aluminium alloy, is intended to represent an annular endring and the ends of sixteen rotor bars that are joined to it. Current was injected into the ring and collected from it by means of flat copper electrodes, which were clamped to the flat faces of the rotor bars. The electrode to bar contact surfaces were coated with an electrical jointing compound, in order to reduce contact resistance and to help ensure a uniform current distribution over the bar cross-section. The potential difference between bars was measured by means of potential contacts which were soldered into small holes made in the outer curved surfaces of the bars, close to the endring.

Figure 6.4 shows a schematic representation of the endring model, with current being injected into one bar and being collected from another which is diametrically opposite to it. Potential differences

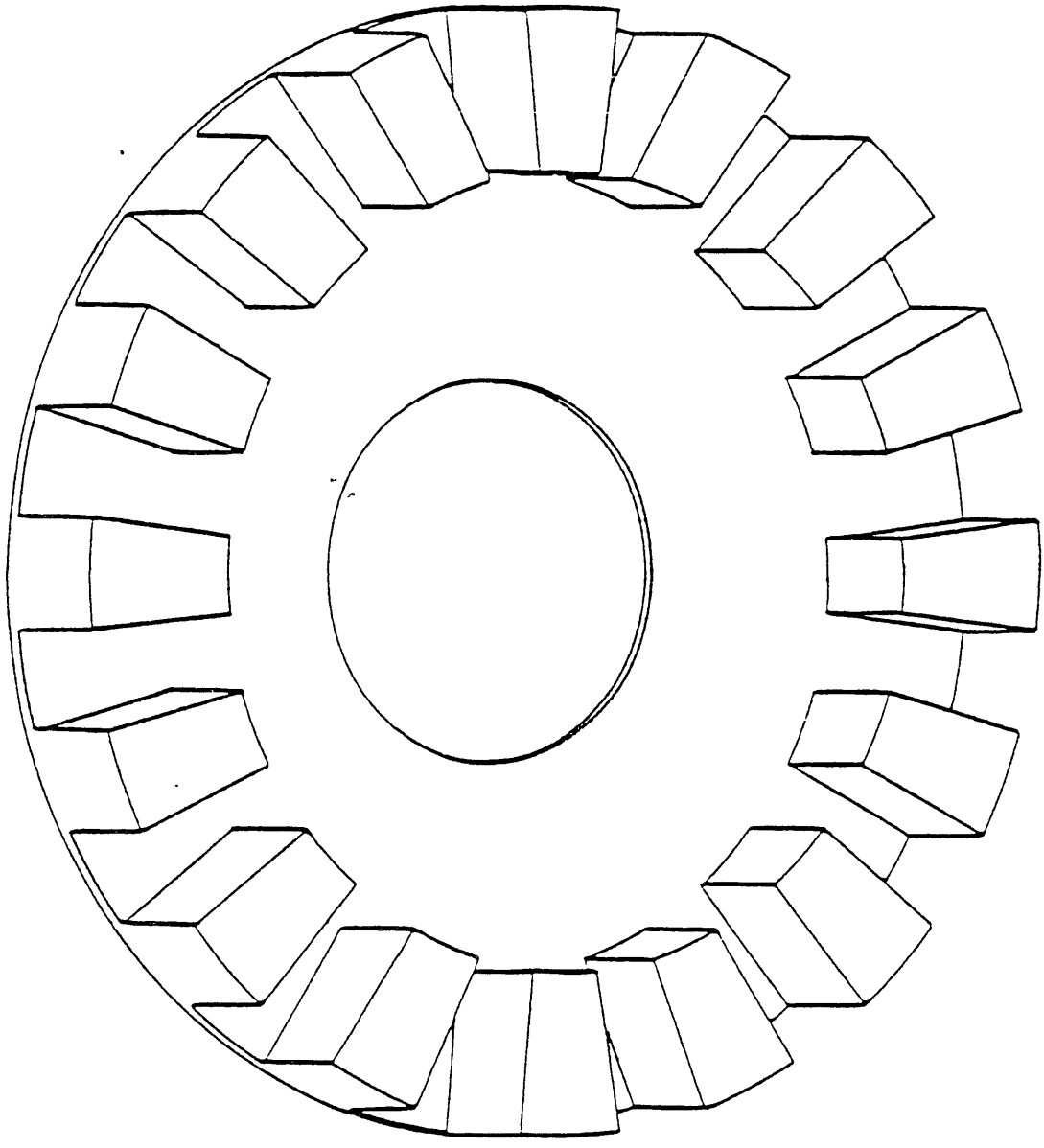


Fig. 6.3 Model endring used for experimental verification

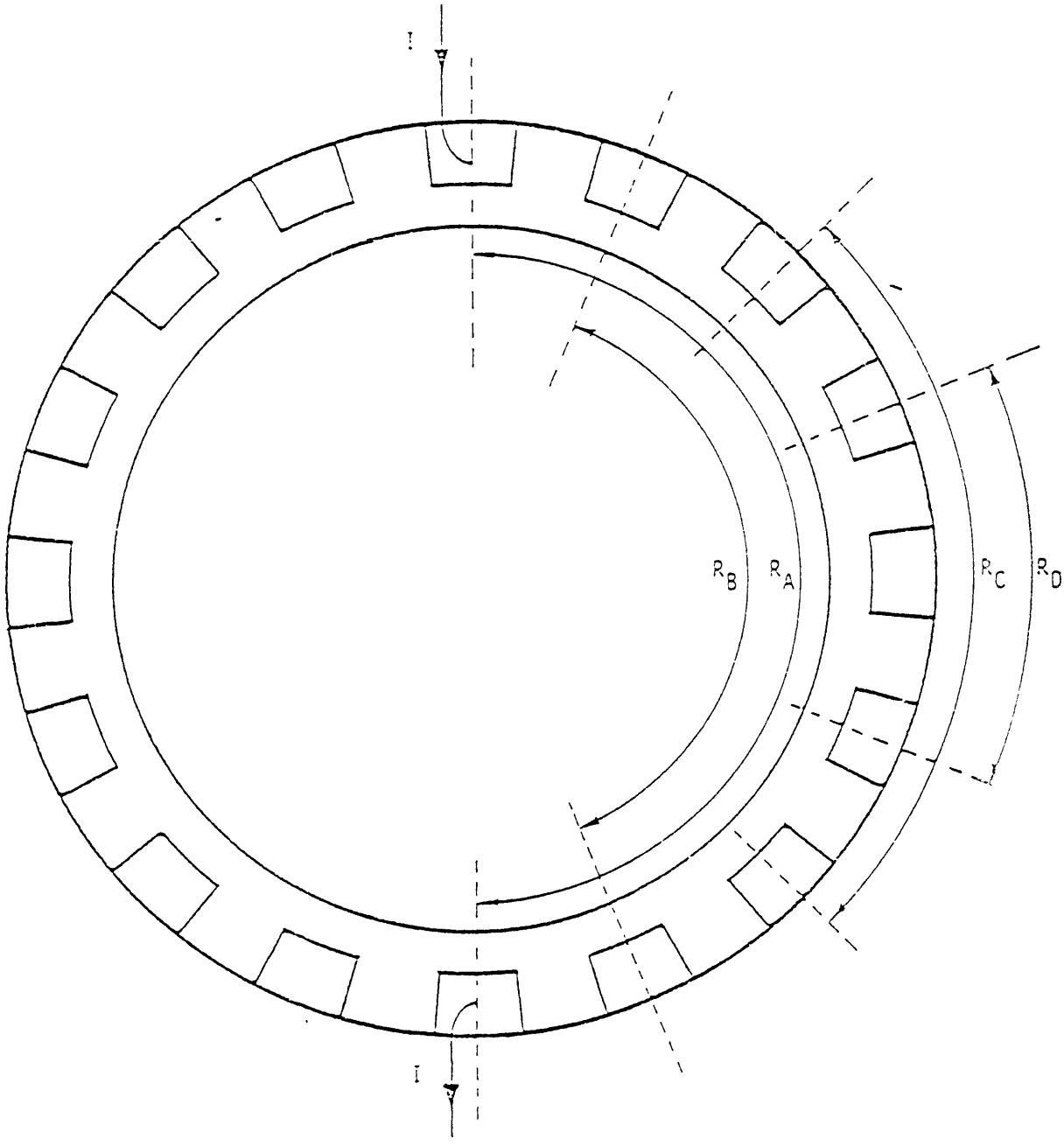


Fig. 6.4 Two-pole feed for measuring endring resistance

may be measured between pairs of bars and used to determine 'apparent' resistance R_A, R_B, R_C, R_D, such that the potential differences between the two corresponding bars is IR_A, IR_B, and so forth. This simple single diametric feed system may be used as a building block for a more complicated arrangement, provided that the current injected into one bar is removed from that at the opposite end of the diameter. With this proviso, the principle of superposition may be invoked to show that the power loss in the endring is given by

$$P_e = \sum_{i=1}^{8} I_i \{R_A I_i + 2R_B I_{i+1} + 2R_C I_{i+2} + 2R_D I_{i+3}\} \qquad (6.14)$$

subject to $I_i + 8 = -I_i$ (see Appendix 8.6) (6.15)

where I_i is the current injected into the i^{th} bar. Let, now, the bar currents form part of a 2p-pole pattern, so that

$$I_i = \sqrt{2} I_b \cos\left(\omega t + \frac{\pi P i}{8}\right) \qquad (6.16)$$

Reference to the requirements embodied in equation 6.15 shows that p=1, 3, 5, 7 ... (2n+1). Substitution from equation 6.16 into equation 6.14 reveals that the power loss in one endring is given by

$$P_e = 8I_b^2 \{R_A + 2R_B \cos\left(\frac{P\pi}{8}\right) + 2R_C \cos\left(\frac{P\pi}{4}\right) + 2R_D \cos\left(\frac{3P\pi}{8}\right)\} \qquad (6.17)$$

This power loss is also given by

$$P_e = I_e^2 R_e = \frac{I_b^2 R_e}{4\sin^2(\frac{P\pi}{N_b})} \qquad (6.18)$$

so that, with $N_b = 16$, we obtain

$$R_e = 32 \sin^2\left(\frac{P\pi}{16}\right)\left\{R_A + 2R_B \cos\left(\frac{P\pi}{8}\right) + 2R_C \cos\left(\frac{P\pi}{4}\right) + 2R_D \cos\left(\frac{3P\pi}{4}\right)\right\} \qquad .... \quad (6.19)$$

Equation 6.19 shows that the endring resistance can be obtained for pole numbers that are odd multiples of two, by making just four voltage measurements. In practice, however, each apparent resistance was calculated as the average of sixteen measurements made using different pairs of bars for current injection and collection. This was done in order to minimise the effects of experimental error.

Figure 6.5 shows a schematic of the endring model with a primitive four-pole current feed. With this type of feed two apparent resistances R_A' and R_B' may be defined, and used to determine the endring resistance for pole numbers that are odd multiples of four

$$R_e = 32\sin^2\left(\frac{P\pi}{16}\right)\left\{R_A' + 2R_B'\cos\left(\frac{P\pi}{8}\right)\right\} \qquad (6.20)$$

$$P = 2, 6, 10, \ldots, 4n+2$$

6.4.2 Comparison Between Experiment and Calculation: The procedure outlined in Section 6.3.1 was used to determine the resistance of the model endring, the dimensions of which are marked on Figure 6.6. The endring resistance was also calculated by Trickey's method and by the finite element method. The results obtained are shown in Tables 6.1

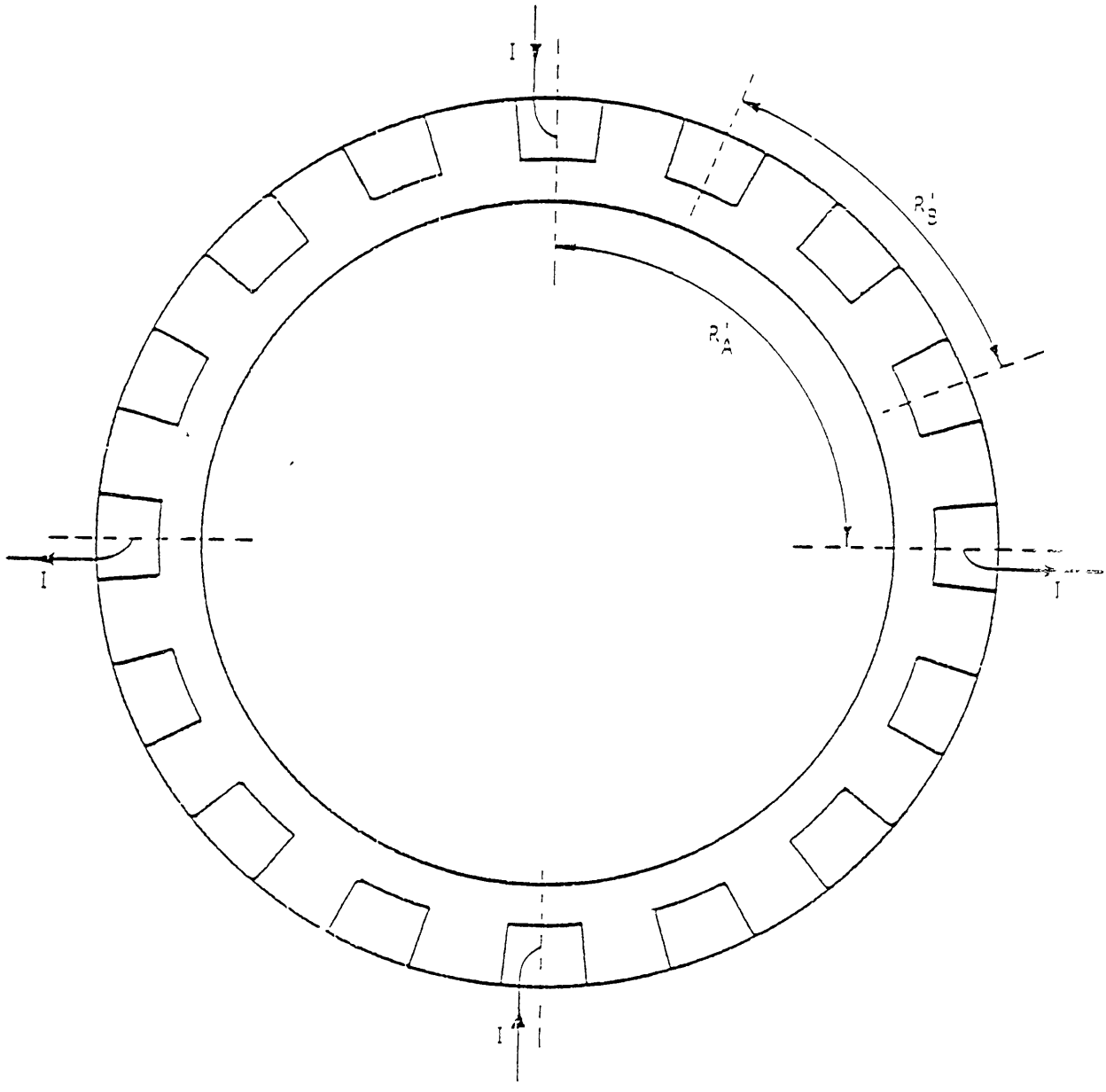


Fig. 6.5 Four-pole feed for measuring endring resistance

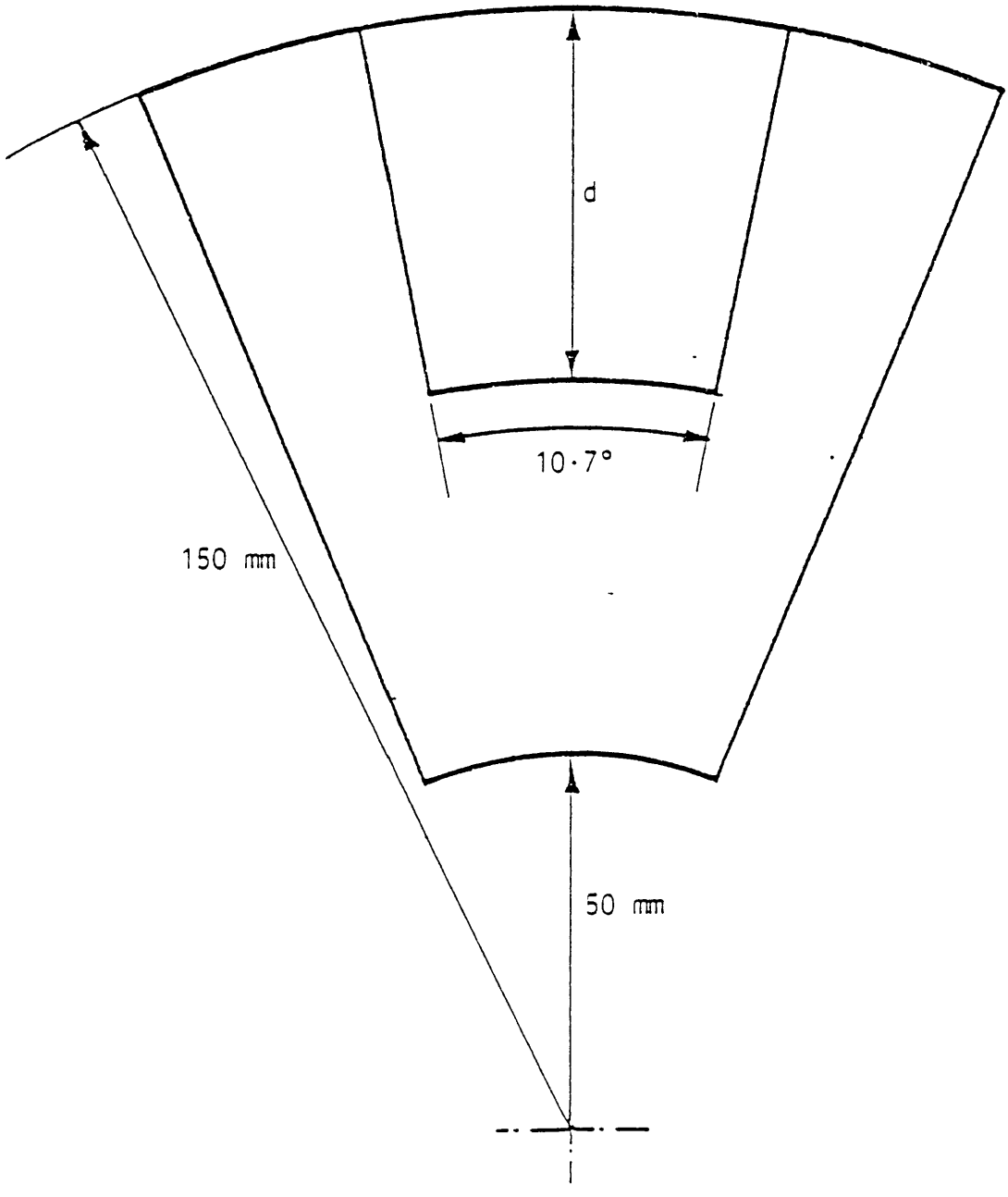


Fig. 6.6 Model of endring test-rig used for F.E. analysis

Number of poles	Experimentally-Determined Value (μΩ)	Caculated by Trickey's Method		Calculated by Finite Element Method	
		Value (μΩ)	Error (%)	Value (μΩ)	Error (%)
2	159.3	153.2	- 3.8	154.3	- 3.1
4	185.6	233.5	+ 25.8	193.6	+ 4.3
6	222.0	335.6	+ 51.2	222.7	+ 0.3
8	-	444.3	-	235.5	-
10	263.4	554.8	+ 110.6	254.1	- 3.5
12	266.8	665.7	+ 149.5	266.2	- 0.2

Table 6.1

Comparison of endring resistance, calculated by Trickey's method and by the finite-element method, with experimental results.

Geometry as shown in Fig 6 with d = 50 mm.

Number of poles	Experimentally-Determined Value (μΩ)	Calculated by Trickey's Method		Calculated by Finite Element Method	
		Value (μΩ)	Error (%)	Value (μΩ)	Error (%)
2	193.6	206.5	+ 6.6	195.4	+ 0.9
4	277.8	330.1	+ 18.8	286.1	+ 3.0
6	341.1	481.3	+ 41.1	369.2	+ 8.2
8	-	639.5	-	427.8	-
10	433.5	799.0	+ 84.3	463.2	+ 6.9
12	470.6	958.7	+ 103.7	481.8	+ 2.4

Table 6.2

Comparison of endring resistance, calculated by Trickey's method and by the finite-element method, with experimental results.

Geometry as shown in Fig 6 with d = 20 mm.

and 6.2 for bar depths, d, of 50 mm and 20 mm respectively. These tables show that the finite element calculation agrees very well with the measured values, for both rotor bar depths and over the full range of pole numbers. Trickey's method, however, does not fare so well, giving an unacceptably high error as the pole number increases. The probable reason for this lies in Trickey's assumption that the bar currents are introduced into the rotor as a smooth sinusoidally distributed current density. Clearly, when the number of bars per pole is low this assumption becomes unrealistic. The second of Trickey's main assumptions is that all the current is injected into the endrings along the circumference of the rotor slot pitch circle. This assumption becomes more approximate when rotor bar depth is large compared to the ring width, suggesting that with fixed ring dimensions Trickey's method is favoured by bars which are of small depth. This observation is borne out by comparison between Tables 6.1 and 6.2, which shows that Trickey;s method is more accurate for the 20 mm bar depth than for the 50 mm.

6.5 Practical Example

Figure 6.7 gives the dimensions of a particular rotor bar and the endring to which it is joined. The rotor has a total of sixteen bars and is used in a commercially manufactured two-pole shaded-pole motor. It is in fact the rotor from the motor which was simulated in chapter [4] and the values of endring resistance calculated in this section were used in the simulation. The bar resistance for this rotor is 4.35*10**-5 ohms, and the endring thickness (t) is 3.5 mm.

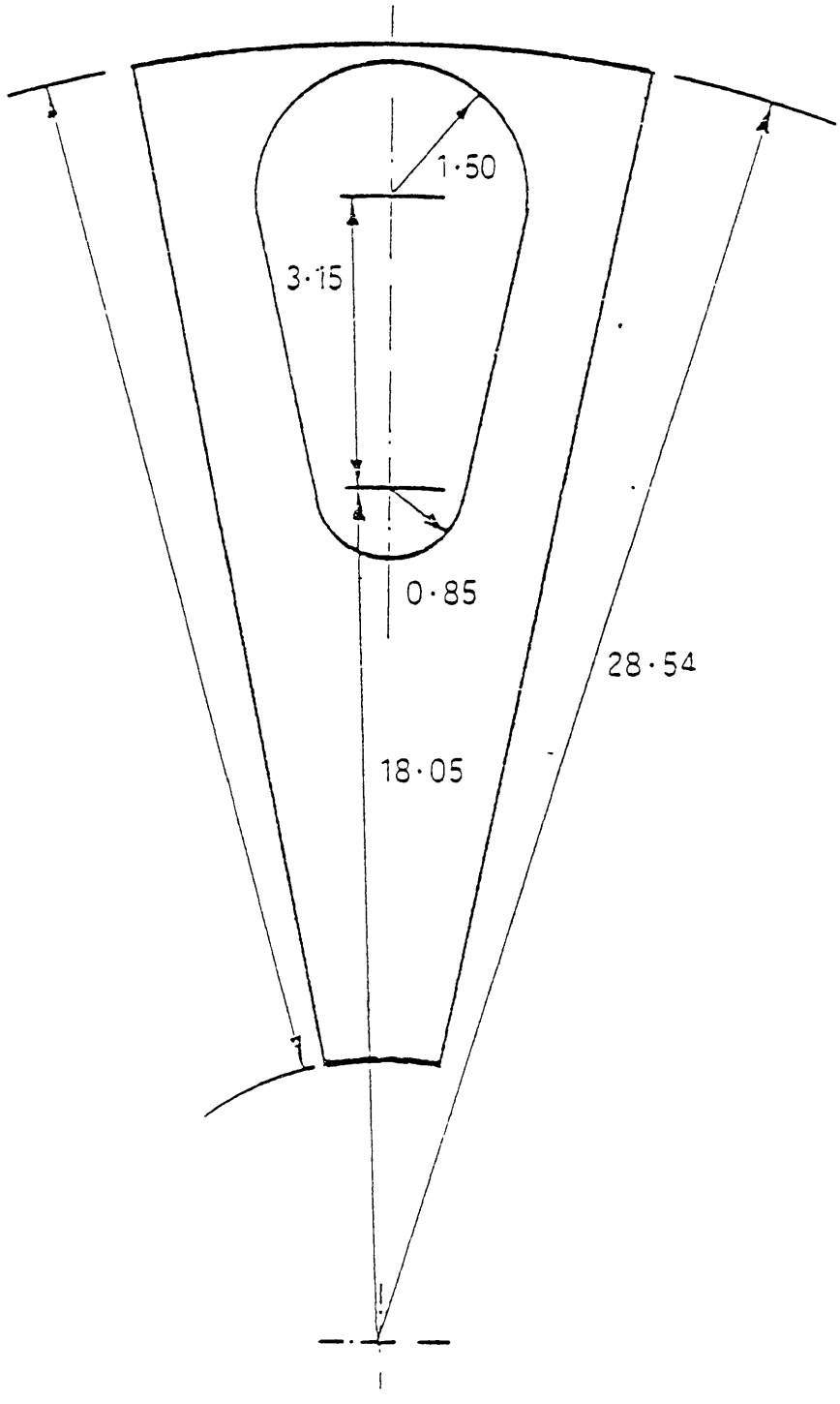


Fig. 6.7 Model of endring used for theoretical investigation (dimensions in mm)

Figure 6.8 shows the variation of R_e with endring width (w) for the fundamental rotor current distribution and its first three harmonics, calculated using the finite element method. As would be expected, R_e decreases as the endring width is increased, but it also shows that for each pole number R_e falls asymtotically towards a minimum beyond which the addition of further material to the endrings has no effect. The endring width at which the minimum resistance is reached decreases as the pole number is increased. This phenomenon, which was also discussed by Trickey [48], may be examined further with reference to the equipotential plots shown in Figures 6.9 and 6.10, which correspond respectively to a fundamental and a fifth harmonic current distribution with an endring width of 11.25 mm. The map for the two-pole distribution shows that the endring current penetrates the full ring width, whereas that for the ten pole distribution indicates that there will be relatively little current penetration below the radius corresponding to the bottom of the slots. The deciding factor for utilisation of material close to the inside diameter of the endrings is clearly the relative sizes of endring and pole pitch. The potential maps shown in Figures 6.9 and 6.10 are obtained using the solution for a single slot pitch model, as described in Section 6.2, and employing an appropriate phase rotation to synthesise the complete endring map.

The results of Figure 6.8 may also be used to investigate the contribution made by the endrings to the effective rotor bar resistance. With reference to equation 6.1 we may write

$$R'_b = R_b + R_{be} \qquad (6.21)$$

where

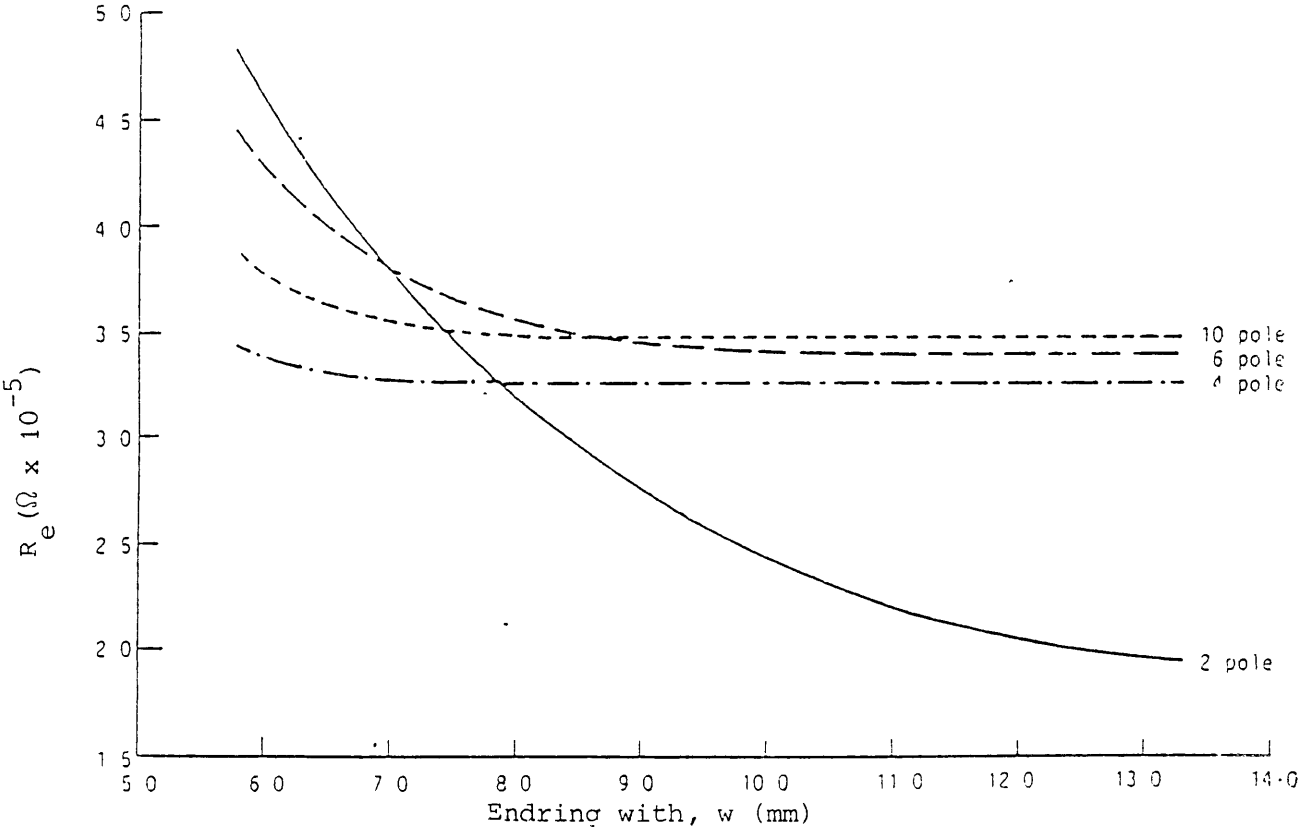


Fig. 6.8 Variation of R_e with w

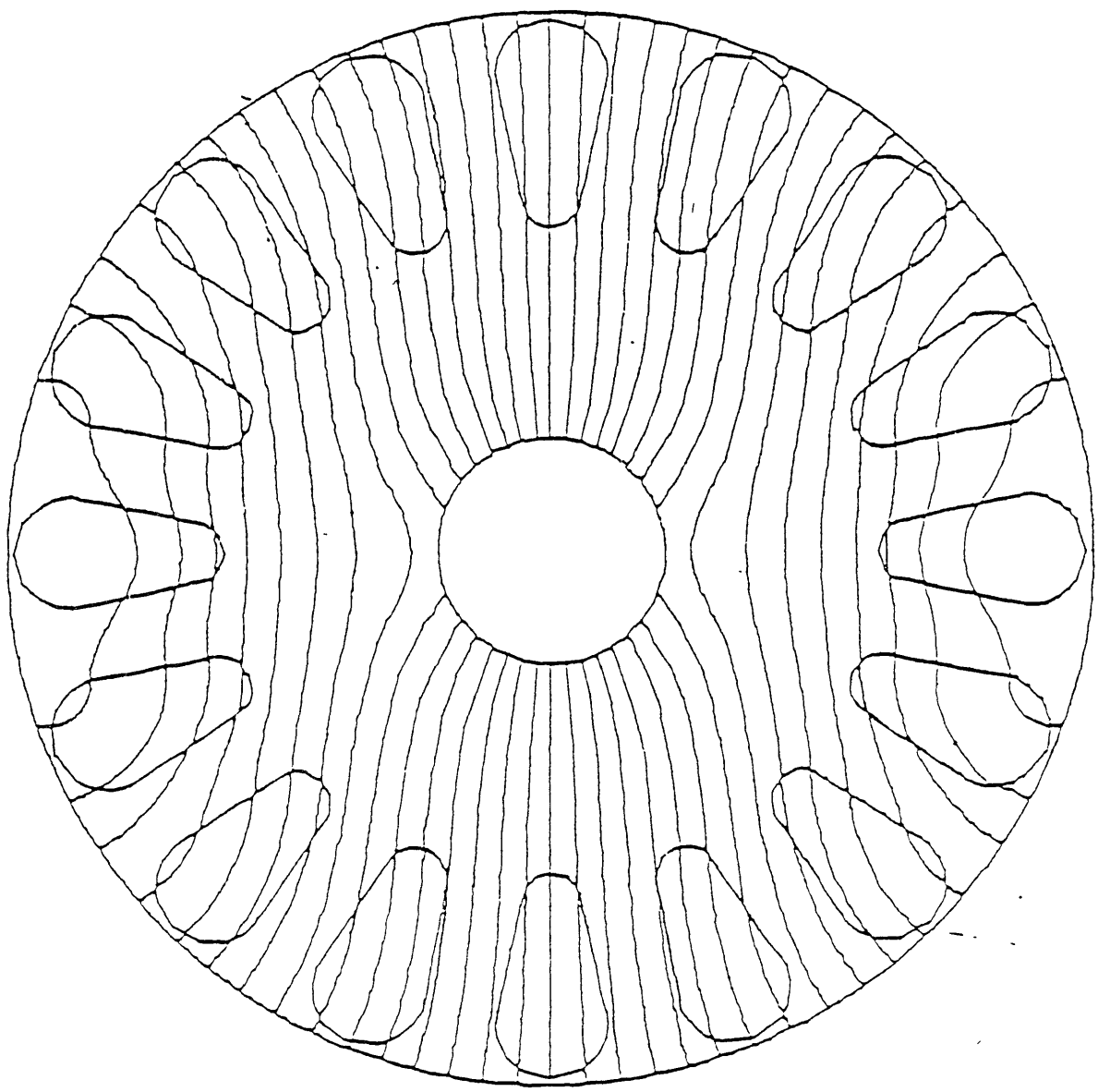


Fig. 6.9 Equipotential lines with an 11.25 mm wide endring and a 2-pole current distribution

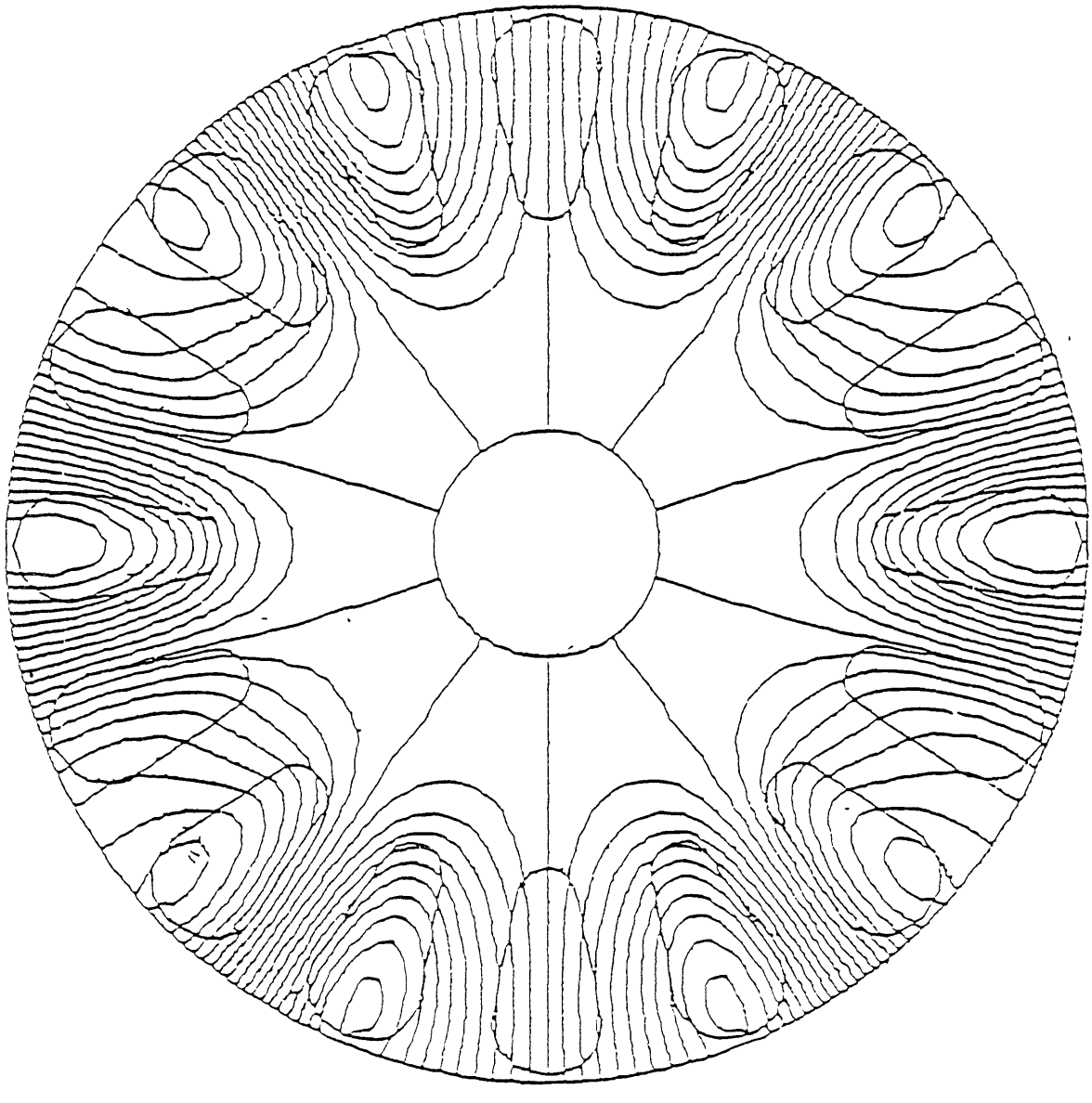


Fig. 6.10 Equipotential lines with an 11.25 mm wide endring and a 10-pole current distribution

$$R_{be} = \frac{R_e}{2N_b \sin^2\left(\frac{P\pi}{N_b}\right)} \qquad (6.22)$$

Figure 6.11 illustrates the variation of R_{be} with endring width, showing that for the rotor under investigation the endrings make a contribution of less than 10% to the harmonic bar resistances, but can contribute from 30% to 50% of the resistance presented to the fundamental. The designer is clearly free to adjust the fundamental bar resistance over a wide range without influencing the harmonic resistance to any real extent.

Alternatively, in a machine where harmonic influences are absent, the designer may wish to choose a value of R_b' and then set the endring dimensions to achieve this value. Obviously, an infinite number of solutions exist, as there is a trade off between endring thickness and width. This point may be illustrated with reference to Figure 6.12, which gives the variation of endring volume with endring width for different values of R_{be}. As the endring width is increased, the volume is shown as diminishing, indicating that the endring thickness is being reduced. These characteristics show that for reasons of material economy relatively wide, thin endrings are favoured. In machines in which harmonic fields play an important part, such an option may not be acceptable, because reducing endring thickness will increase the harmonic resistances, whilst the increased width has little effect. A shaded pole motor is always heavily influenced by harmonic fields, and so the 'minimum' cost option may be particularly unsuitable. In the real machine from which the rotor in this section is taken, for example, the designer has set the endring width to 5.75 mm; this represents use of a thin endring and potential maps of the ring corresponding to 2 pole and 10 pole current distributions

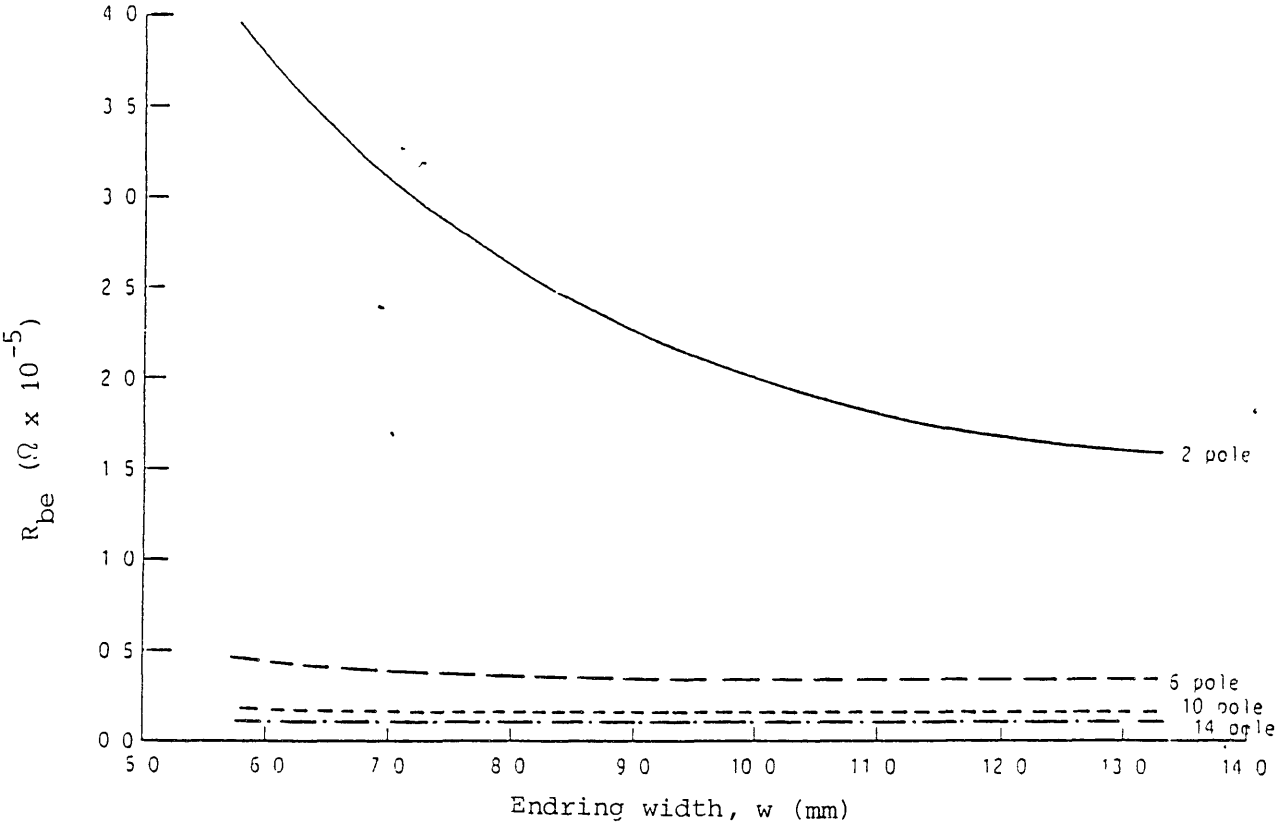


Fig. 6.11 Variation of R_{be} with w, for geometry of Figure 6.7

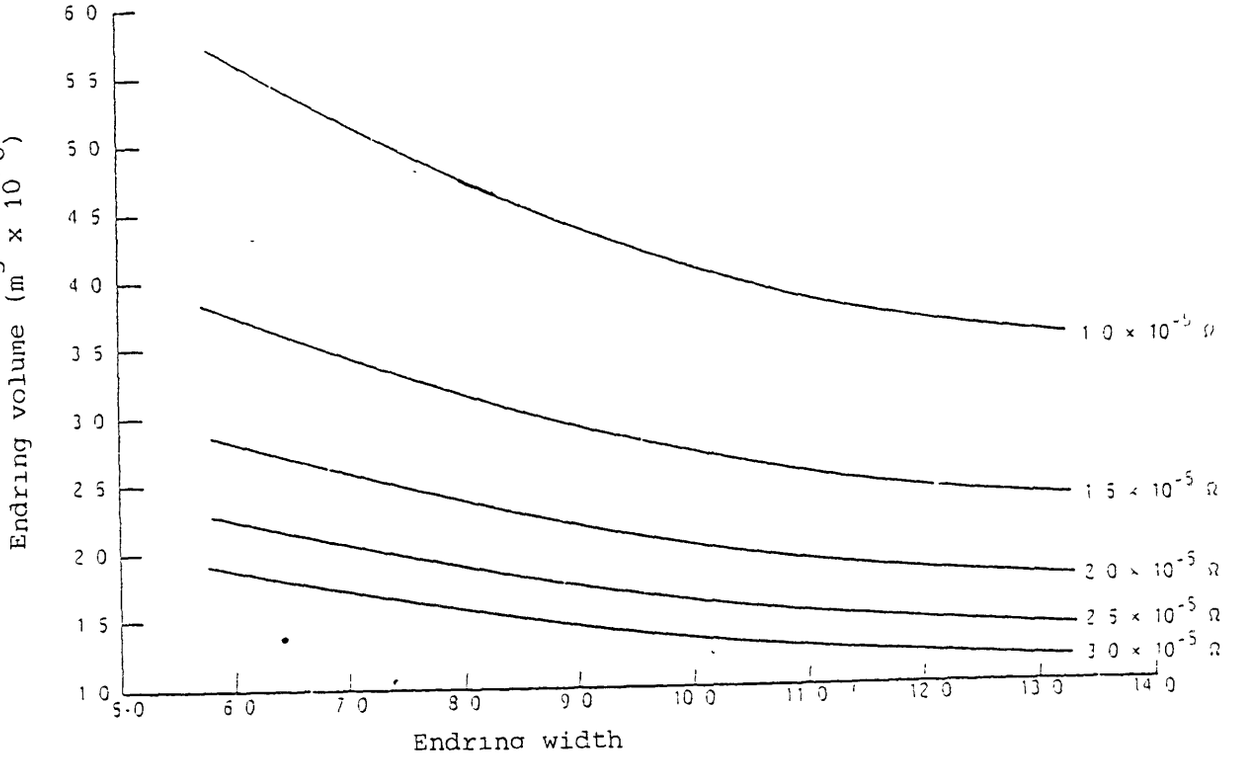


Fig. 6.12 Variation of endring volume with endring width for different values of R_{be} for a 2-pole distribution

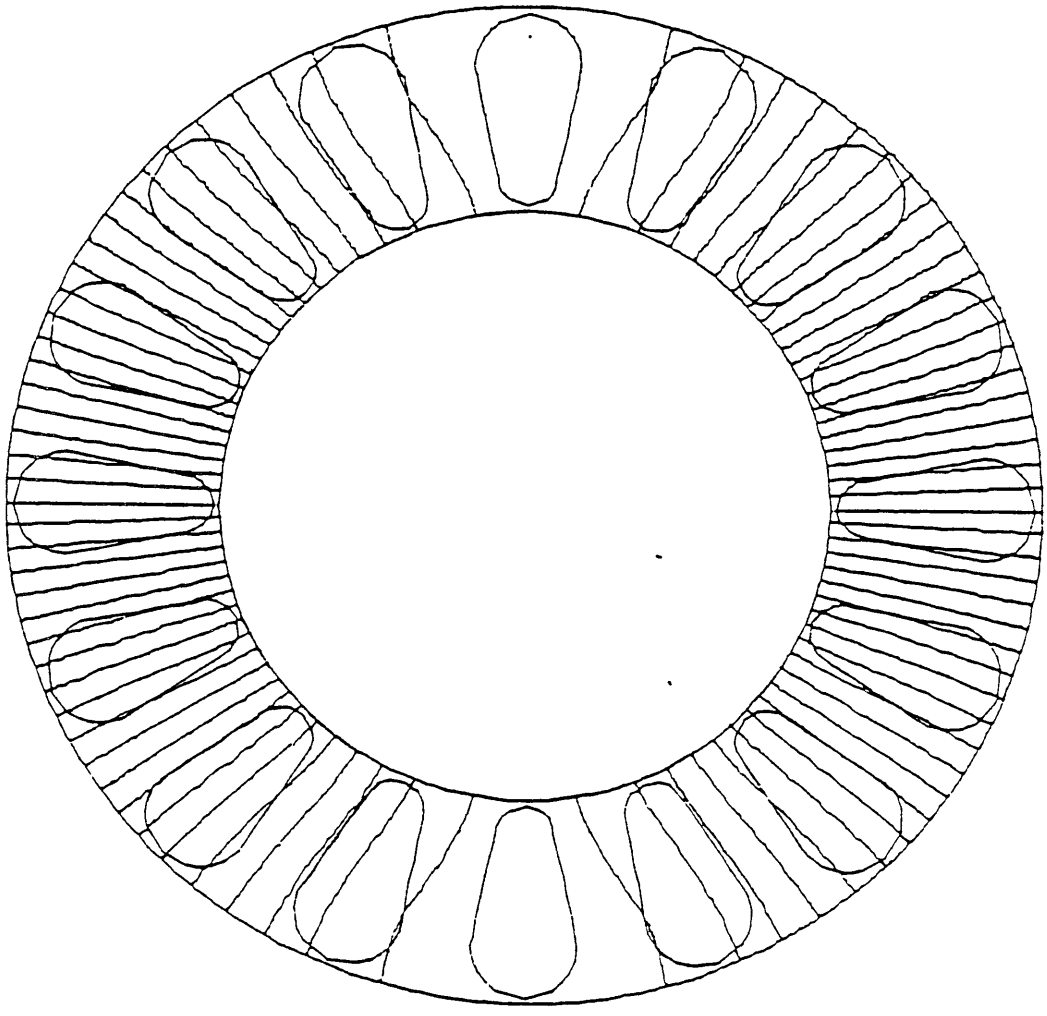


Fig. 6.13

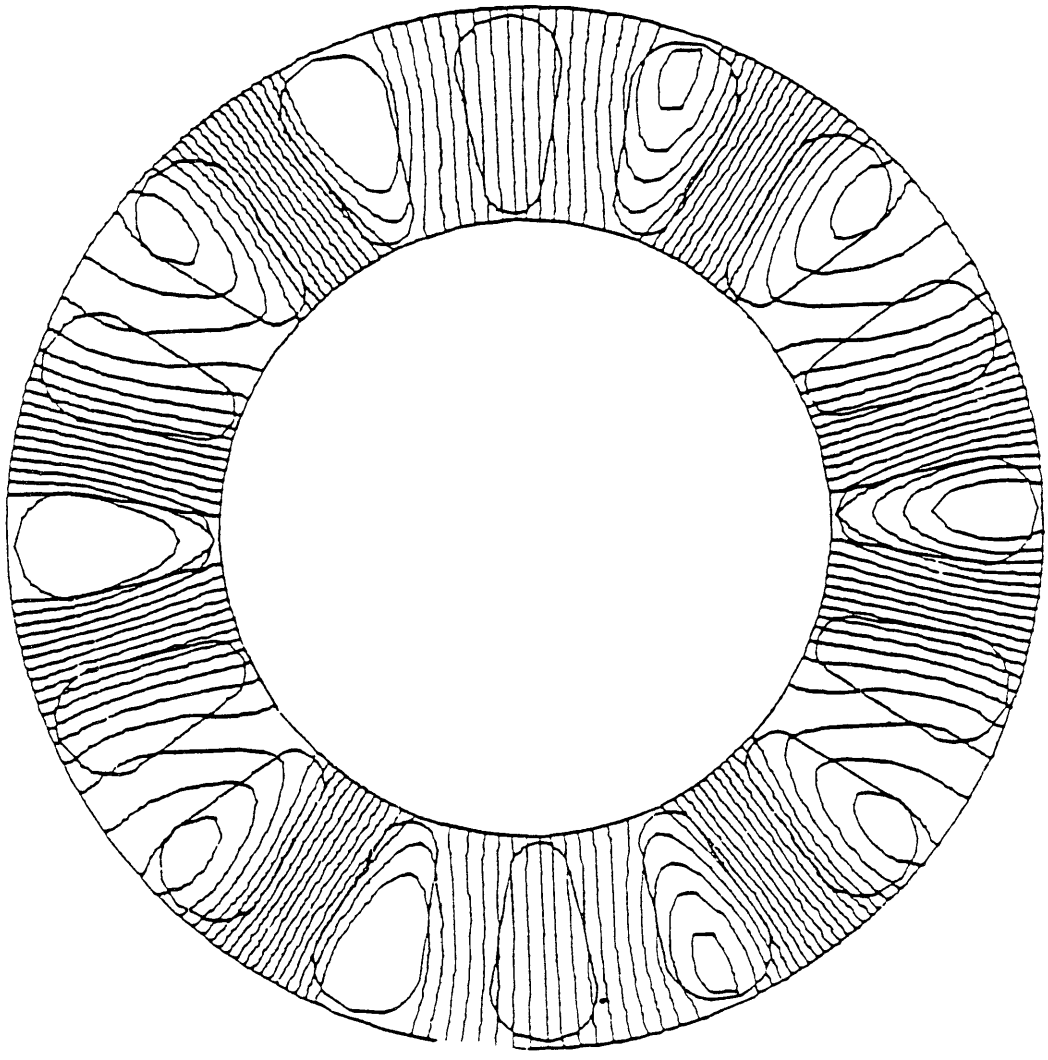


Fig. 6.14

are shown in Figures 6.13 and 6.14. It can be seen from these that no material has been wasted since the lines of constant potential are everywhere dense. The endring resistance has thus been chosen to be relatively high.

6.6 Conclusions

The work contained in this chapter describes a method for calculating endring resistance, based on the use of finite elements. The method uses a more realistic model than its predecessor, and has been shown to be capable of producing more accurate results. In finite element terms the problems tackled were quite small and the amount of computer time required to obtain a solution is therefore small.

The endring studied in Section 6.4 required a mesh of 252 nodes and 442 elements, and each solution took 1.14 cpu seconds of CPU time on a CDC 6600 machine. The results from the analysis of the elliptical bar imbedded in an endring were used in Chapter 4 and were included in the analysis by means of a look-up table.

Suggestions for Further Work

All the examples given in this chapter were modelled with two assumptions.

Firstly it was assumed that the skin effect was negligible and would not significantly effect the ring resistance.

.

The second assumption was that the endrings were thin and hence they could be modelled in two dimensions.

From these assumptions, it is clear that a quantitative assessment of influence of skin effect would be worth doing. This could be done by using the analysis of Chapter Five to predict the current distribution and then injecting these currents into the endring model and calculating the resistance.

Another extension would be to model the endring in three dimensions to assess the importance of neglecting the fact that currents must flow round a sharp bend as they leave the rotor bar and enter the endring, rather like a fluid encountering a T-junction. Such a model would not present major difficulties in terms of analysis since it could all be done in terms of a scalar potential.

CHAPTER SEVEN

REFERENCES

[1] Trickey, P.H., 'An analysis of the shaded pole motor', AIEE Trans., Vol 55, September 1936, pp 1007-14.

[2] Eastham, J.F. and Williamson, S., 'Generalised theory of induction motors asymmetrical airgaps and primary windings', Proc. IEE, Vol 120, No 7, July 1973.

[3] Eastham, J.F. and Williamson, S., 'Design and analysis of close ratio two-speed shaded-pole induction motors', Proc. IEE, Vol 120, No 10, October 1973.

[4] Poloujadoff, M. and Perret, R., 'Measurement of iron losses in single phase squirrel cage motors', Electrical Machines and Electromagnetics: an International Quarterly, 4, pp 165-175.

[5] Perret, R. and Poloujadoff, M., 'Characteristic analysis of saturated shaded pole induction motors', Trans. IEEE on Power Apparatus and Systems, Vol PAS-95, No 4, July/August 1976.

[6] Williamson, S. and Ralph, J.W., 'Finite element analysis for nonlinear magnetic field problems with complex current sources', Proc. IEE, Part A, Vol 129, No 6, pp 391-395, August 1982.

[7] Williamson, S. and Ralph, J.W., 'Finite element analysis of an induction motor fed from a constant voltage source', Proc. IEE, Part B, Vol 130, No 1, pp 18-24, January 1983.

[8] Williamson, S. and Ostojic, M., 'Reversing shaded pole motor with effective ring shift', Electric Power Applications, February 1978, Vol 1, No 1.

[9] Oden, J.T., 'Finite elements of nonlinear continua', McGraw-Hill, New York, 1972.

[10] Strang, G. and Fix, G.J., 'An analysis of the finite element method', Englewood Cliffs, N.J., Prentice-Hall, Inc., 1973.

[11] Demerdash, N.A. and Nehl, T.W., 'An evaluation of the methods of finite elements and finite differences in the solution of nonlinear electromagnetic fields in electrical machines', IEEE Trans., Vol PAS-98 (1), 1979, pp 74-87.

[12] Biddlecombe, C.S., Heighway, E.A., Simkin, J. and Trowbridge, C.W., 'Methods for Eddy Current Computation in Three Dimensions', Proc. Compumag, Chicago 1981.

[13] Rodger, D. and Eastham, J.F., 'Finite element solution of 3D eddy current flow in magnetically linear conductors at power frequencies', Proc. Compumag, Chicago 1981.

[14] Carpenter, C.J. and Wyatt, E.A., 'Efficiency of numerical techniques for computing eddy currents in two and three dimensions', Proc. Compumag, Oxford, 31 March - 2 April, 1976.

[15] Pillsbury, R.D. Jr., 'A three-dimensional eddy current formulation using two potentials: the magnetic vector potential and total magnetic scalar potential', Compumag, Genoa, 30 May - 2 June 1983.

[16] Emson, C.R.I., Simkin, J. and Trowbridge, C.W., 'Further developments in three dimensional eddy current analysis', Proc. Compumag, Fort Collins, USA, 1 June - 5 June, 1985.

[17] Sherer, G.H. and Herzog, G.E., 'The calculation of shaded pole motor performance by the use of a digital computer', AIEEE Rotating Machinery Paper 59-1137, October 11, 1959.

[18] NAG, Numerical Algorithms Group Library Manual, Oxford University Computer Laboratory.

[19] Peckham, G., 'A new method for minimising a sum of squares without calculating gradients', The Computer Journal, Vol 13, No 4, November 1970.

[20] Zienkiewicz, O.C., 'The finite element method', 3rd edition, McGraw-Hill, New York, 1977.

[21] Silvester, P. and Chari, M.V.K., 'Finite element solution of saturable magnetic field problems', Ibid, PAS-90, (5), 1971, pp 2362-2372.

[22] Chari, M.V.K. and Silvester, P., 'Analysis of turboalternator magnetic fields by finite elements', Ibid, PAS-90, (2), 1971, pp 2362-2372.

[23] Du Terrail, Y., Sabonnadiere, J-C., Masse, P., Coulomb, J.L., 'Nonlinear complex finite elements analysis of electromagnetic field in steady-state AC devices', Trans. IEEE, Vol MAG 20, No 4, July 1984.

[24] Strang, G., 'Linear algebra and its applications', Second Edition, Academic Press, London.

[25] Cuthill, E. and McKee, J., 'Reducing the bandwidth of sparse symmetric matrices', Proc. 24th National Conference of the ACM, ACM Publ. P-69, 1969.

[26] Liu, W-H. and Sherman, A.H., 'Comparative analysis of the Cuthill-McKee and the Reverse Cuthill McKee ordering algorithms for Sparse Matrices', SIAM J. Numer. Anal., Vol 13, No 2, April 1976.

[27] Williamson, S. 'Power factor improvement in cage-rotor induction motors', Proc. IEE, Vol 130, Pt B, No 2, March 1983.

[28] Williamson, S. and Laithwaite, E.R. 'Generalised harmonic analysis for the steady state performance of sinusoidally-excited cage induction motors', Proc. IEE, Vol 132, Pt B, No 3, May 1985.

[29] Duff, I.S., 'A survey of sparse matrix research', IEEE Proc., Vol 65, No 4, April 1977.

[30] Gibbs, N., Poole, W. and Stockmeyer, P., 'An algorithm for reducing the bandwidth and profile of a sparse matrix', SIAM J. Numer. Anal., Vol 13, No 2, April 1976.

[31] Jacobs, D.A.H., 'Preconditioned conjugate gradient methods for solving systems of algebraic equations', C.E.R.L. Lab. note No. RD/L/N193/80, October 1980.

[32] Meijerink, J.A. and Van der Vorst, H.A., 'An iterative solution method for linear systems of which the coefficient matrix is a symmetric M-matrix', Mathematics of Computation, Vol 31, No 137, pp 148-62, 1977.

[33] Kershaw, D.S., 'The incomplete Cholesky-conjugate gradient method for iterative solution of systems of linear equations', Journal of Computational Physics, Vol 26, pp 43-65, 1978.

[34] Markham, G., 'The CG-squared method for solving asymmetric systems of linear equations', C.E.R.L. Lab note No. TPRD/L/APM/012, November 1983.

[35] Birch, T.S. and Butler, O.I., 'Permeance of closed-slot bridges and its effect on induction-motor current computation', Proc. IEE, 1971, 118, (1), pp 169-172.

[36] Konrad, A., 'The numerical solution of steady-state skin effect problems - an intergrodifferential approach', IEEE Trans., 1981, MAG 17, (1), pp 1148-1152.

[37] British Standards: BS601:1973, 'Specification for steel sheet and strip for magnetic circuits and electrical apparatus', Part 5, methods of test, British Standards Inst. 2 Park Street, London W1A 2BS.

[38] Ralph, J.W., and Williamson, S., 'Solution of two-dimensional nonlinear field problems with sinusoidal excitation sources using first-order finite elements', IEEE Trans., 1983, MAG-19, PP 2433-2436.

[39] Alger, P.L., 'Induction machines', Gordon and Breach, New York, 1970).

[40] Williamson, S. and Smith, A.C., 'Field analysis for rotating induction machines and its relationship to the equivalent circuit method', IEE Proc. B, Electr. Power Appl., 1980, 127, pp 83-90.

[41] Swann, S.A. and Salmon, J.W., 'Effective resistance and reactance of a solid cylindrical conductor embedded in a semi-closed slot, Proc. IEE, 1962, 109C, pp 611-615.

[42] Annell, H., The alternating current impedance of a solid conductor of circular cross-section placed in a semi-closed circular slot', Trans. R Inst. Tech., 1963, 200, pp 1-33.

[43] El-Markabi, M.H.S. and Freeman, E.M., 'Normalised impedance if circular, trapezoidal and rectangular conductors in semi-closed slots: a unified transmission line approach', IEE Proc., A, 1984, 131, (3), pp 129-139.

[44] Weppler, R., 'Influence of interbar rotor currents on the performance of single-phase and polyphase induction motors', Siemens Forschu-u. Entwickl-Ber., bd 4, 1975, Nr. 2, Springer-Verlag, 1975.

[45] Subba Rao, V. and Butler, O.I., 'Stray losses of polyphase cage-induction motors with particular reference to the condition of imperfect rotor-bar-iron insulation', Ibid, 1969, 116, (5), pp 737-751.

[46] Chang, S.S.L., 'Equivalent circuits and their application to designing shaded-pole motors', AIEE Trans., 1951, 70, Part 1, pp 690-699.

[47] Williamson, S. and Breese, P., 'Evaluation of the reluctance augmentation principle in shaded-pole motors', Proc. IEE, 1978, 125, (9), pp 831-835.

[48] Trickey, P.H. 'Induction motor resistance ring width', Trans. AIEE, 1936, Vol 55, pp 144-150.

[49] Silvester, P.P. and Ferrari, R.L., 'Finite elements for electrical engineers', Cambridge University Press, Cambridge, 1983.

[50] Segerlind, L.J., 'Applied finite element analysis', John Wiley and Sons Inc., 1976.

CHAPTER EIGHT

8.1 Finite Elements

The basis of the finite element method is that a continuous field may be approximated by a collection of discrete subdomains over which there is an assumed variation of potential. This variation is normally expressed by a polynomial. The method solves Poisson's equation by minimising a functional which may be obtained by use of the governing partial differential equation and the Euler-Lagrange equation. If a functional for a given problem is not readily available the method of Galerkin, which is a weighted residual method may be applied instead. For two dimensional magnetisation problems the functional to be minimised over each finite element is as in equation 8.1.

$$\iint_{\Delta} \left(\int_{0}^{B} \nu b \, db \right) dx \, dy - \iint_{\Delta} JA \, dx \, dy \qquad (8.1)$$

If a simplex triangular element such as the one in Figure 8.1 is used and the variation in that element is expressed by a polynomial of the form

$$A(x,y) = \alpha_1 + \alpha_2 x + \alpha_3 y \qquad (8.2)$$

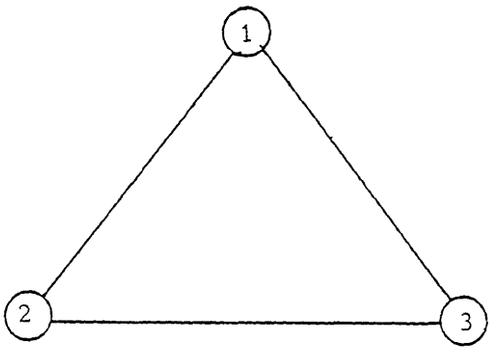


Fig. 8.1 A Single Finite Element

is assumed; then is may be shown, [50], that (8.2) may be rewritten as

$$A(x,y) = \frac{1}{2\Delta} \sum_{i=1}^{3} (a_i + b_i x + c_i y) A_i \qquad (8.3)$$

where $a_1 = X_2 Y_3 - X_3 Y_2$

$b_1 = Y_2 - Y_3$

$c_1 = X_3 - X_2$

in which 1,2 and 3 refer to the vertices of the triangle as in Figure 8.1 and X and Y are the coordinates. Δ is the triangle area.

The minimisation process reduces equation 8.4 to an elemental system of equations

$$\nu[S]\{A\} = \{J\} \qquad (8.4)$$

in which the stiffness matrix

$$[S] = \frac{1}{4\Delta^3} \begin{bmatrix} b_2^2+c_1^2 & b_1b_2+c_1c_2 & b_1b_3+c_1c_3 \\ b_2b_1+c_2c_1 & b_2^2+c_2^2 & b_2b_3+c_2c_3 \\ b_3b_1+c_3c_1 & b_3b_2+c_3c_2 & b_3^2+c_3^2 \end{bmatrix} \qquad (8.5)$$

$$\{A\} = \begin{Bmatrix} A_1 \\ A_2 \\ A_3 \end{Bmatrix} \tag{8.6}$$

$$\{J\} = \frac{J}{3} \begin{Bmatrix} 1 \\ 1 \\ 1 \end{Bmatrix} \tag{8.7}$$

From this it can be seen that [S] is symmetric, and since it minimises the energy of the system it will be positive definite.

8.2 Modelling of Magnetic Slot Wedges

The difficulty with representing the magnetic slot wedge is that it is a three-dimensional object. Therefore, no matter how it is modelled in two dimensions, there will always be an error involved. The method chosen to model the wedge is as follows.

Consider the diagram of the wedge shown in Figure 8.2

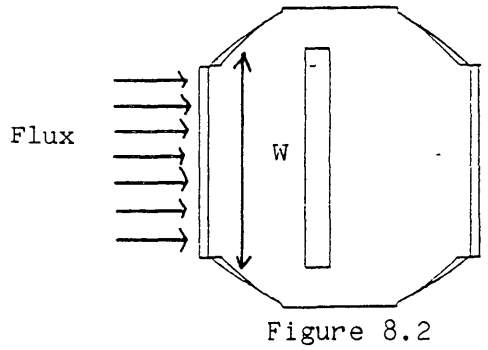


Figure 8.2

then the flux density will tend to be higher at the edges of the wedge that surrounds the cut in it, because there is less magnetic material there.

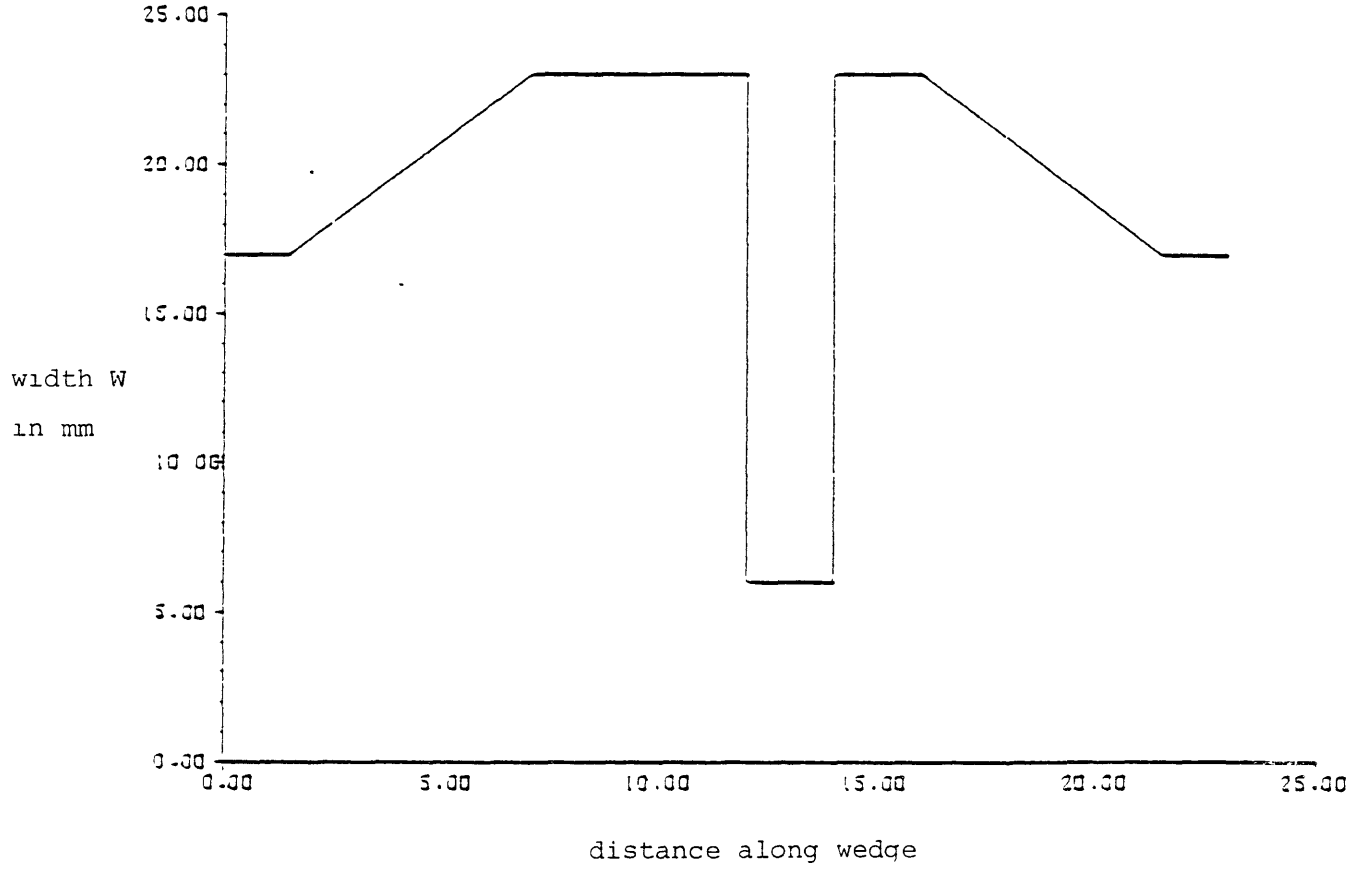

25.00
20.00
15.00
10.00
5.00
0.00
width W
in mm
0.00
5.00
10.00
15.00
20.00
25.00
distance along wedge

Figure 8.3

One way, therefore, of modelling the wedge is to work out the nett thickness, W, as a function of θ, this is shown in Figure 8.3, and to use W to define a wedge factor that is used to correct the flux density in the wedge before the next value of reluctivity is calculated using that flux density. The wedge factor, W_f, is defined as

$$W_f = \frac{W_{max}}{W(\theta)} \tag{8.8}$$

and $B_w = B_{calculated} \times W_f$ (8.9)

from this

$$B_w^2 = B_{calculated}^2 W_f^2 \tag{8.10}$$

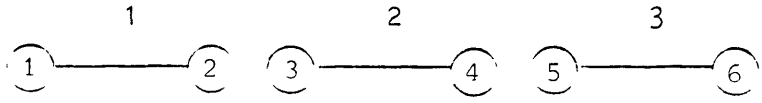
and $\nu = \nu(B_w^2)$ (8.11)

The magnetic characteristics of the wedge are input as a cubic spline to the program of Chapter 4.

The use of a wedge factor allows some account of the wedge to be taken in a two-dimensional analysis.

8.3 Incorporation of Complex Periodicity

Consider the following collection of one-dimensional elements



If the above system is such that the potentials at the nodes conform to the following restrictions

$$\bar{A}_2 = \bar{A}_3 \tag{8.12}$$

$$\bar{A}_4 = \bar{A}_5 \tag{8.13}$$

$$\bar{A}_6 = \overline{kA_1} \quad \text{where } \bar{k} \text{ is a complex phase shift.} \tag{8.14}$$

Then the relationship between the potentials, for the above disjointed system, may be written in matrix form as

$$\begin{bmatrix} \bar{A}_1 \\ \bar{A}_2 \\ \bar{A}_3 \\ \bar{A}_4 \\ \bar{A}_5 \\ \bar{A}_6 \end{bmatrix} = \begin{bmatrix} 1 & 0 & 0 \\ 0 & 1 & 0 \\ 0 & 1 & 0 \\ 0 & 0 & 1 \\ 0 & 0 & 1 \\ \bar{k} & 0 & 0 \end{bmatrix} \begin{bmatrix} \bar{A}_1 \\ \bar{A}_2 \\ \bar{A}_4 \end{bmatrix} \tag{8.15}$$

disjoint

of $[\bar{A}] = [C]\,[\hat{\bar{A}}]$

where [C] is called the connectivity matrix.

The global stiffness matrix for the above disjoint system may be written as

$$[S]_{disjoint} = \begin{bmatrix} S^1_{11} & S^1_{12} & 0 & 0 & 0 & 0 \\ S^1_{21} & S^1_{22} & 0 & 0 & 0 & 0 \\ 0 & 0 & S^2_{11} & S^2_{12} & 0 & 0 \\ 0 & 0 & S^2_{21} & S^2_{22} & 0 & 0 \\ 0 & 0 & 0 & 0 & S^3_{11} & S^3_{12} \\ 0 & 0 & 0 & 0 & S^3_{21} & S^3_{22} \end{bmatrix} \qquad (8.16)$$

$[S]_{disjoint}$ may be compressed into a connected system [S] by doing the following

$$[S] = \begin{bmatrix} 1 & 0 & 0 & 0 & 0 & \bar{k}^* \\ 0 & 1 & 1 & 0 & 0 & 0 \\ 0 & 0 & 0 & 1 & 1 & 0 \end{bmatrix} \begin{bmatrix} S^1_{11} & S^1_{12} & 0 & 0 & 0 & 0 \\ S^1_{21} & S^1_{22} & 0 & 0 & 0 & 0 \\ 0 & 0 & S^2_{11} & S^2_{12} & 0 & 0 \\ 0 & 0 & S^2_{21} & S^2_{22} & 0 & 0 \\ 0 & 0 & 0 & 0 & S^3_{11} & S^3_{12} \\ 0 & 0 & 0 & 0 & S^3_{21} & S^3_{22} \end{bmatrix} \begin{bmatrix} 1 & 0 & 0 \\ 0 & 1 & 0 \\ 0 & 1 & 0 \\ 0 & 0 & 1 \\ 0 & 0 & 1 \\ \bar{k} & 0 & 0 \end{bmatrix}$$

.... (8.17)

after multiplication, this becomes

$$[S] = \begin{bmatrix} S^1_{11} + \overline{kk}^* S^3_{22} & S^1_{12} & \bar{k}^* S^3_{21} \\ S^1_{21} & S^1_{22} + S^2_{11} & S^2_{12} \\ \bar{k} S^3_{12} & S^2_{21} & S^2_{22} + S^3_{11} \end{bmatrix} \qquad (8.18)$$

with $kk^* = 1$

Here $[S] = [C]^H [S]_{disjoint} [C]$

where $[C]^H$ denotes the Hermitian conjugate of C. [S] may then be separated into real and imaginary parts to fit in with the Newton-Raphson algorithm.

8.4 Derivation of Basic Endring Formulae

Figure 8.4 is a circuit representation of the junction between a rotor bar and an end-ring. If the rotor carries a uniform 2p-pole current distribution, then the phase angle between the current in successive segments of the end-ring is the same as that between successive bars of the cage, i.e. $2\pi p/N_b$ radians, as shown. Applying Kirchhoff's nodal law at this junction

$$\bar{I}_b + \bar{I}_e = \bar{I}_e \, e^{j\frac{2\pi p}{N_b}} \qquad (8.19)$$

from which the relationship between the R.M.S. magnitudes may be derived

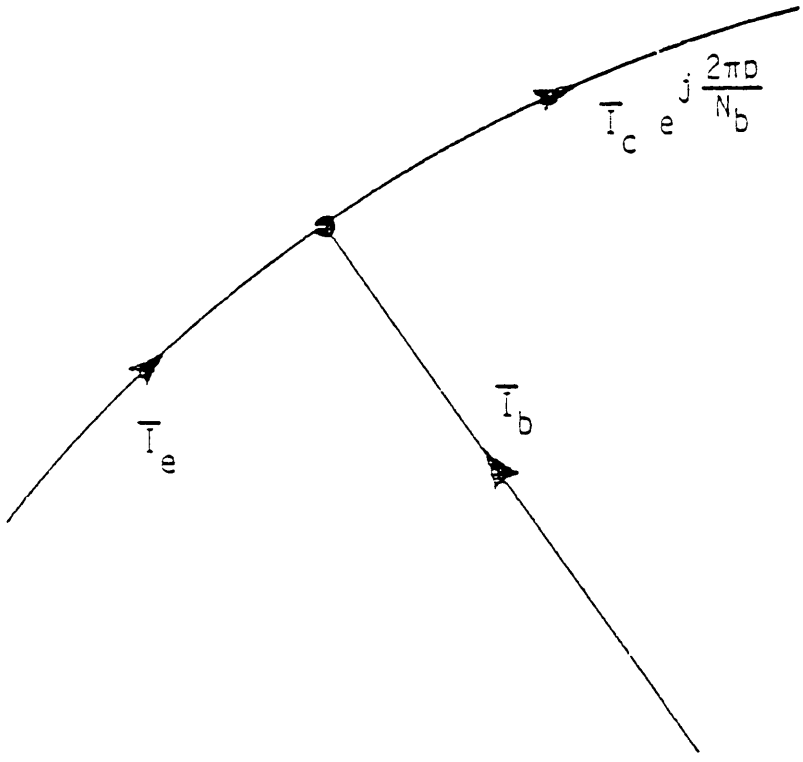


Fig. 8.4

$$I_e = \frac{I_b}{2 \sin\left(\frac{\pi p}{N_b}\right)} \tag{8.20}$$

The joule loss in the cage is given by

$$P = 2I_e^2 R_e + N_b I_b^2 R_b \tag{8.21}$$

$$P = N_b I_b^2 \left[R_b + \frac{R_e}{2N_b \sin^2\left(\frac{\pi p}{N_b}\right)} \right] \tag{8.22}$$

which is equivalent to the loss that would obtain in a cage having zero resistance endrings, and a bar resistance by equation 6.1.

8.5 Uniqueness of Solution

Consider the arrangement shown below

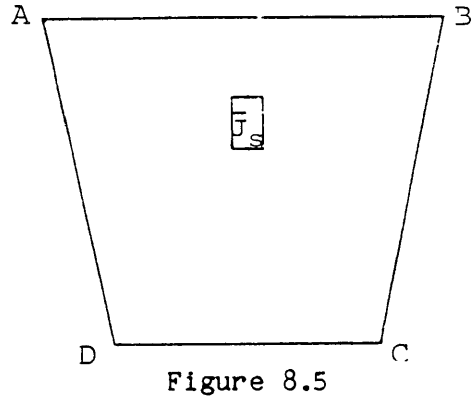


Figure 8.5

We are seeking a solution to Poisson equation

$$\nabla^2 \bar{V} = \frac{\bar{J}_s}{\sigma} \tag{8.23}$$

in the domain defined by the boundaries AB, BC, CD and DA subject to the following boundary conditions

$$\text{on boundaries AB and CD} \quad \frac{\partial \bar{V}}{\partial n} = 0 \tag{8.24}$$

$$\text{on boundaries BC and DA} \quad \bar{V}_{BC} = \bar{k}\,\bar{V}_{DA} \tag{8.25}$$

A problem now arises from the fact that the value of the potential $\bar{V}$ does not appear to have been fixed anywhere. It was therefore thought necessary to prove that the solution obtained using these boundary conditions was unique.

Firstly, suppose that there are two solutions $\bar{V}_1$ and $\bar{V}_2$ for the above conditions. Then the difference between solutions is

$$\bar{V} = (\bar{V}_1 - \bar{V}_2) \quad \text{on DA} \tag{8.26}$$

$$\bar{V} = \bar{k}(\bar{V}_1 - \bar{V}_2) \quad \text{on BC} \tag{8.27}$$

Applying the divergence theorem to $\bar{V}$ gives

$$\int_{\Gamma} \nabla\cdot(\bar{V}^*\nabla\bar{V})\, d\Gamma = \int_{S} \bar{V}^* \frac{\partial \bar{V}}{\partial n}\, dS \tag{8.28}$$

but

$$\int_{\Gamma} \nabla\cdot(\bar{V}^*\nabla\bar{V})\, d\Gamma = \int_{\Gamma} \{\, \bar{V}^*\nabla\cdot(\nabla\bar{V}) + \nabla\bar{V}(\nabla\bar{V})^* \}\, d\Gamma \tag{8.29}$$

$$\text{however } \nabla\cdot(\nabla\bar{V}) = \nabla^2(\bar{V}_1-\bar{V}_2) = \frac{\bar{J}_s}{\sigma} - \frac{\bar{J}_s}{\sigma} = 0 \tag{8.30}$$

$$\therefore \int_\Gamma |\nabla\bar{V}|^2 \, d\Gamma = \int_S \bar{V}^* \frac{\partial\bar{V}}{\partial n} \, dS \tag{8.31}$$

evaluating the second integral along DA and CB only, since $\frac{\partial\bar{V}}{\partial n} = 0$ on the other boundaries, gives

$$\int_S \bar{V}^* \frac{\partial\bar{V}}{\partial n} \, dS = \int_{DA} \bar{V}^* \frac{\partial\bar{V}}{\partial n} \, dS - \int_{BC} \bar{k}^* \bar{V}^* \frac{\partial(\bar{k}\bar{V})}{\partial n} \tag{8.32}$$

and since $\bar{k}$ is a complex constant equation (8.32) becomes

$$\int_S \bar{V}^* \frac{\partial\bar{V}}{\partial n} \, dS = \int_{DA} \bar{V}^* \frac{\partial\bar{V}}{\partial n} \, dS - \int_{BC} |\bar{k}|^2 \bar{V}^* \frac{\partial\bar{V}}{\partial n} \, dS = 0 \tag{8.33}$$

since $|\bar{k}|^2 = 1$.

Using this result (8.31) becomes

$$\int_V |\nabla\bar{V}|^2 \, dV = 0 \tag{8.34}$$

$$\text{which implies } \nabla\bar{V} = 0 \tag{8.35}$$

$$\text{which implies } \bar{V} = \text{constant} \tag{8.36}$$

but $\bar{V} = (\bar{V}_1 - \bar{V}_2)$

and $(\bar{V}_1 - \bar{V}_2) \neq$ constant.

Hence there is a contradiction and $\bar{V}_1$ and $\bar{V}_2$ cannot both be solutions to (8.23). Therefore the solution is unique.

8.6 Power Dissipation

Consider the endring as shown below

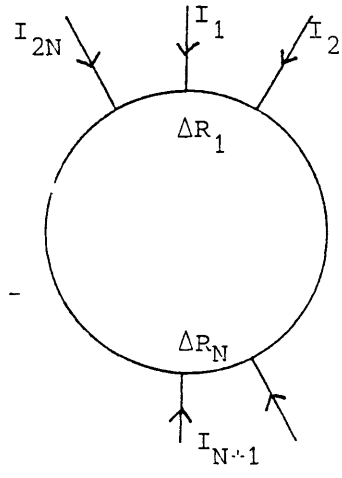


Figure 8.6

The system has 2N currents which enter and leave diametrically thus $I_{N+1} = -I_1$.

The total power consumed by the endring can be obtained from equation (8.37)

$$P_e = V_{1,N+1}\, I_1 + V_{2,N+2}\, I_2 + \ldots + V_{N,2N}\, I_N \qquad (8.37)$$

If the ΔR_n are obtained by feeding a current into bar one and extracting it from bar N+1, then apparent incremental resistances can be defined by (8.38)

$$\Delta R_n = \frac{\Delta V_n}{I_1} \qquad (8.38)$$

Using these apparent resistances we can substitute for the voltage in equation (8.37) and express the power in the endring as

$$P_e = \sum_{i=1}^{N} I_i^2 S_1 + 2 \sum_{n=1}^{\frac{N}{2}} S_n \sum_{i=1}^{N} I_i I_{i+(n-1)} \qquad (8.39)$$

$$\text{where } S_n = \sum_{i=n}^{N+1-n} \Delta R_i \qquad 1 \leq n \leq \frac{N}{2} \qquad (8.40)$$

$$S_n = 0 \quad n = \frac{N}{2} + 1 \qquad (8.41)$$

This allows the endring resistance to be inferred from experimental measurements. However the question arises as to whether it is the instantaneous power or the average power that is being used to calculate the endring resistance.

Assuming that

$$I_i = \hat{I} \cos(\omega t + \phi + \frac{2\pi pi}{2N}) \qquad (8.42)$$

then the first summation of equation (8.39) becomes

$$\sum_{1=1}^{N} I_1^2 S_1 = S_1 \left[\sum_{i=1}^{N} \frac{\hat{I}^2}{2} + \frac{\hat{I}^2}{2} \cos(2\omega t + 2\phi + \frac{2\pi pi}{2N}) \right] \qquad (8.43)$$

changing notation allows (8.43) to be expressed as

$$\sum_{i=1}^{N} I_1^2 S_1 = \frac{\hat{I}^2}{2} S_1 \left[\sum_{i=1}^{N} 1 + \sum_{i=1}^{N} R_e \left\{ e^{j(2\omega t+2\phi)} e^{\frac{j^2\pi pi}{N}} \right\} \right]$$

$$= \frac{N\hat{I}^2}{2} S_1 \qquad (8.44)$$

Taking the second summation of equation (8.39) and forming the typical product

$$I_i \, I_{i+j} \qquad (8.45)$$

gives

$$\frac{\hat{I}^2}{2} \left[\cos(2\omega t + 2\phi + \frac{2\pi pi}{N} + \frac{\pi pj}{N} + \cos\left(\frac{\pi pj}{N} \right) \right] \qquad (8.46)$$

which yields (8.47) when summed to N terms.

$$\frac{N\hat{I}^2}{2} \cos\left(\frac{\pi p_j}{N} \right) \qquad (8.47)$$

Neither equations (8.44) nor (8.47) depend on time so the use of D.C. current feeds yields the average power which is the required result.

The restriction on the above analysis is that only pole numbers of order 2,6,10,...,4n+2 may be used when doing the experiment.

Presented at the 1985 Compumag Conference

ANALYSIS OF CAGE INDUCTION MOTORS - A COMBINED FIELDS AND CIRCUITS APPROACH

S. Williamson and M.C. Begg

Abstract - The paper develops the general idea of using a combination of field and circuit analysis to solve the class of eddy-current problems in which the current flow paths are well-defined. The method described is particularly suitable for electromagnetic devices which are excited from voltage sources and which may have external impedances connected in their circuits. The method is illustrated with reference to the analysis of a single-phase cage induction motor.

INTRODUCTION

The equation which relates the magnetic vector potential to the current density in a slowly time-varying field, and which forms the basis of many eddy-current formulations, is

$$\nabla \times \nu\nabla \times \mathbf{A} = \mathbf{J} \qquad (1)$$

As a first step, it is usual to resolve J into 'source' and 'induced' components, giving an equation of the form

$$\nabla \times \nu\nabla \times \mathbf{A} = \mathbf{J}_0 - \sigma\left\{\dot{\mathbf{A}} + (\mathbf{v}.\nabla)\mathbf{A} + \nabla\varphi\right\} \qquad (2)$$

(2) may be solved for a wide class of two-dimensional problems, involving relative motion, non-linear material properties, and time-variation. Many electromagnetic devices, however, have essentially three-dimensional features which exert a considerable influence on their performance, and a two-dimensional eddy-current formulation is not appropriate. Whilst three-dimensional eddy-current formulations have been developed, their practical applications are still restricted to relatively simple devices. An alternative approach is to acknowledge the generality of (1) and to make no distinction between source and induced currents, at least as far as the field solution is concerned. The difference between the two can then be embodied in a circuit model, which is used in conjunction with the field model and which also takes time-variation and relative motion into account. This technique is, of course, the basis of the familiar equivalent-circuit representations of electrical devices, which enable performance to be simulated using equivalent-circuit parameters that are obtained from (usually simplistic) field models. Indeed, one course of action would be to adopt the conventional equivalent-circuit models and to use a detailed field solution to attempt to obtain more accurate values for the equivalent circuit parameters. Such parameters, however, generally comprise summations of notional components, which may be difficult to segregate from a complete field solution.

The purpose of this paper is to identify a class of problem for which a mixed circuit and fields analysis may be suitable, and to develop a general method of solution. The technique is illustrated with reference to the analysis of a single-phase cage induction motor.

CLASS OF PROBLEM AND GENERAL METHOD

The general method which is outlined in this paper may be used for any eddy-current problem in which the current flow paths are well-defined.

The authors are with Imperial College of Science and Technology, London SW7 2BT.

Under this circumstance the distinction between source and induced currents may be regarded as somewhat artificial, and (1) used as the defining field equation. The currents are related to the applied terminal voltages by means of circuit equations, which may refer to steady-state or transient behaviour. In this paper, however, we shall concentrate exclusively on steady-state performance and sinusoidally time-varying excitation. With this restriction the circuit equations may be written in the general coupling impedance form

$$\begin{pmatrix} \bar{V}_1 \\ \bar{V}_2 \\ \bar{V}_3 \\ \vdots \\ \bar{V}_n \end{pmatrix} = \begin{pmatrix} \bar{Z}_{11} & \bar{Z}_{12} & \bar{Z}_{13} & \cdots & \bar{Z}_{1n} \\ \bar{Z}_{21} & \bar{Z}_{22} & \bar{Z}_{23} & & \bar{Z}_{2n} \\ \bar{Z}_{31} & \bar{Z}_{32} & \bar{Z}_{33} & & \bar{Z}_{3n} \\ \vdots & & & & \vdots \\ \bar{Z}_{n1} & & & & \bar{Z}_{nn} \end{pmatrix} \begin{pmatrix} \bar{I}_1 \\ \bar{I}_2 \\ \bar{I}_3 \\ \vdots \\ \bar{I}_n \end{pmatrix} \qquad (3)$$

in which a total of n current variables has been assumed. The elements of this matrix may be evaluated from a set of linear field solutions in a systematic manner. If all the currents except $\bar{I}_n$ are set to zero, then the emf induced in the m-th circuit is given by

$$\bar{E}_{mn} = -\bar{I}_n \bar{Z}_{mn} \qquad (4)$$

from which $\bar{Z}_{mn}$ may be calculated. The essence of the method is to calculate the coupling impedances using a finite-element field model. Components, such as resistance, which are outwith the field solution are subsequently added to the relevant impedances.

The impedance equation (3) may be solved directly, if all applied winding voltages are specified. Should the windings be interconnected, then it will be necessary to transform from branch to loop variables before solving, but in either respect the set of winding currents $\bar{I}_1$ --- $\bar{I}_n$ can be determined. If, as is usual, the device contains magnetically saturable material, then the impedances will themselves be functions of current, and an iterative procedure must be adopted. Starting with a guessed or estimated set of currents, (1) is initially solved in a non-linear sense, i.e. allowing the reluctivity of the saturable elements to vary. This step, in effect, sets the level of saturation to that appropriate for the latest estimate to the unknown currents. The coupling impedances are then determined by means of a series of linear solutions, one for each current, with all reluctivities frozen at the values determined during the above non-linear solution. Solution of the impedance matrix then gives an improved estimate for the winding currents. The new current set is now used to up-date the elemental reluctivities via a new non-linear field solution, and the process repeated until consistent results are obtained.

EXAMPLE - SHADED-POLE MOTOR ANALYSIS

The general procedure outlined above was developed for the study of cage induction machines, and so these devices provide a suitable illustration of the method.

Figure 1 is a cross-section through a shaded-pole motor. The main winding is excited from a sinusoidal voltage source, and the starter winding has degenerated to a single turn copper loop, or shading ring, which embraces part of the pole. The rotor consists of a cast aluminium cage embedded in slots in a laminated core. The device is seen to consist of a complex arrangement of different materials.

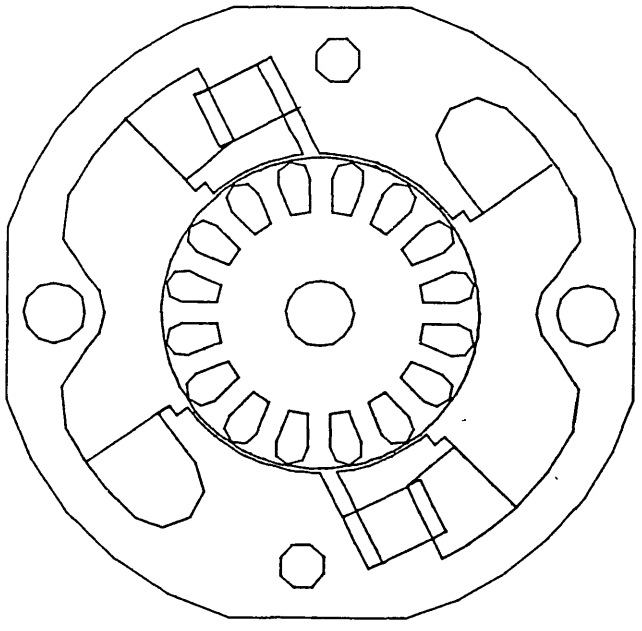


Fig. 1. Section through 2-pole shaded-pole motor.

Furthermore, the machine has two features which make it essentially three-dimensional in nature. The first is the fact that the conducting bars in the rotor are joined at their ends by conducting rings, which exert a significant influence on the current flowing in the bars. The second is the fact that the rotor is skewed, so that successive cross-sections of the rotor cage would show the bars at different positions relative to the stator. This is done to reduce the effect of the space-harmonic fields, and changes the effective coupling between the stator and rotor. An eddy-current model which incorporates both of these features must necessarily be three-dimensional in nature, and it is thought that a full field solution of this type is not yet economically viable.

The use of the combined fields and circuits approach reduces the complexity of the field solution if a three-dimensional model is to be employed, by virtue of the simpler formulation (1), but the modelling problem is still formidable and a two-dimensional model has been adopted. The term 'circuit' is clearly applicable to the stator winding and the short-circuited shading-ring, but as the current flow paths are not uniquely defined in the rotor, some further consideration is required. Here, we resolve the rotor bar currents into space-harmonic distributions.

Suppose, for example, that six rotor harmonic current distributions are thought to be necessary to model the rotor accurately. Let their pole numbers be denoted p_1, p_2 --- p_6. The current flowing in the first rotor bar (or reference bar) will be of the form

$$i_1(t) = \mathrm{Re}\,\sqrt{2}\left\{\bar{I}_{p_1} e^{j\omega_{p_1} t} + \bar{I}_{p_2} e^{j\omega_{p_2} t} + \bar{I}_{p_3} e^{j\omega_{p_3} t} + \text{--- } \bar{I}_{p_6} e^{j\omega_{p_6} t}\right\} \quad (5)$$

if there are N_b rotor bars, then denoting $\alpha = \pi/N_b$, the current in the second rotor bar is

$$i_2(t) = \mathrm{Re}\,\sqrt{2}\left\{\bar{I}_{p_1} e^{j(\omega_{p_1} t + \alpha p_1)} + \bar{I}_{p_2} e^{j(\omega_{p_2} t + \alpha p_2)} + \text{--- } \bar{I}_{p_6} e^{j(\omega_{p_6} t + \alpha p_6)}\right\} \quad (6)$$

that in the third bar is

$$i_3(t) = \mathrm{Re}\,\sqrt{2}\left\{\bar{I}_{p_1} e^{j(\omega_{p_1} t + 2\alpha p_1)} + \bar{I}_{p_2} e^{j(\omega_{p_2} t + 2\alpha p_2)} + \text{--- } \bar{I}_{p_6} e^{j(\omega_{p_6} t + 2\alpha p_6)}\right\} \quad (7)$$

and so on. These equations show that provided the pole numbers are known (and these are assumed at the outset) then it is necessary only to calculate the harmonic currents (I_{p_1}, I_{p_2} --- I_{p_6}) in the reference bar in order to specify the complete rotor current distribution. The frequency terms (ω_{p_1}, ω_{p_2} --- ω_{p_6}) are also known when the rotor speed is specified. The concept of a circuit on the rotor therefore becomes equated to the idea of a harmonic current distribution. This, in fact, is most fortuitous, because the modification for end-ring resistance depends on pole-number, and the modification to coupling produced by rotor skew is also readily accommodated on a harmonic basis.

Impedance Calculations

The coupling impedances are calculated directly from the linear field solutions by evaluating induced emfs, in accordance with (4). The emfs induced in the shading ring and exciting winding are obtained by integrating the magnetic vector potential over the relevant cross sectional area, taking winding sense into account

$$\bar{E} = \frac{j\omega w N}{S} \int \mathbf{A} \cdot d\mathbf{S} \quad (8)$$

If the source of the flux which induced this emf resides on the rotor, then the value obtained using (8) must be multiplied by the appropriate harmonic skew factor.

The calculation of emf induced in the rotor must relate to the harmonic decomposition of the bar currents, so that it is necessary to determine the various harmonic components of emf induced in the reference bar. For a rotor with open slots one possible method is to resolve the airgap field into its space-harmonic components, and to calculate the harmonic components of emf induced in the reference bar by means of the flux-cutting rule [1]. The elements of rotor self-impedance due to flux which does not cross the airgap are then calculated using either classical techniques or by separate field solutions [2] and are added to the airgap impedances. The machine used for illustrative purposes in this paper, however, has closed rotor slots, so that not all the flux which crosses the gap will link with the rotor bars, and so an alternative method has to be employed. The procedure adopted is to determine the emf induced in every bar, using (8) with the turns number (N) set to unity. The harmonic components are

then recovered by means of a discrete Fourier transform of these bar emfs. If the reference bar is positioned at $\vartheta = \vartheta_0$, and the total emf induced in the n-th bar is denoted $\bar{E}_{bn}$, then the p-th harmonic of emf in the reference bar is given by

$$\bar{E}_p = \frac{1}{N_b} \sum_{n=1}^{N_b} \bar{E}_{bn} e^{-jp(\vartheta_0 + (n-1)\alpha)} \qquad (9)$$

The number of harmonic components which may be recovered via (9) is limited by the number of sampling points, i.e. the number of rotor bars. As before, if the source of the field lies on the opposite side of the airgap (i.e. on the stator) then the harmonic emfs must be modified by the appropriate harmonic skew factor. It should also be noticed that for induced emfs in the rotor bars the frequency term (ω) in (8) will be different for each harmonic. A convenient approach is to calculate the harmonic emfs at supply-frequency, and then to scale each harmonic component using the slip. This frequency transformation takes account of the relative motion between stator and rotor, so that for the purposes of the field solution, the rotor is modelled in a fixed position with respect to the stator.

The harmonic decomposition of the rotor currents enables deep-bar effect to be modelled by changing resistance using factors that are calculated by classical methods. The end-ring resistance is similarly taken into account by means of corrections to bar resistance that are made on a harmonic-by-harmonic basis.

Calculation of Torque

The torque/speed characteristic of an induction motor is a key performance index, and the calculation of torque is therefore an important requirement. The radial airgap length of an induction motor is very small when compared to its mean diameter, so that if torque is to be determined by numerical integration from the field in the gap, a very large number of elements must be clustered in and around it. The circuit theory model of the induction machine provides an alternative method for torque calculation, based on the harmonic components of rotor loss. The electro-magnetic torque is given by

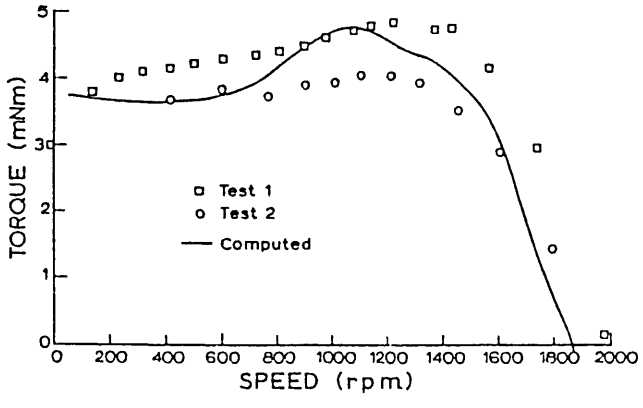


Fig 2. Comparison between experimentally-measured and computed torque/speed characteristics.

$$T = N_b \sum_{i=1}^{6} \frac{p_i I_{p_i}^2 R_{bp_i}}{\omega - p_i \omega_r} \qquad (10)$$

where R_{bp_i} is the effective bar resistance for the p_i-th harmonic, and ω_r is the rotor speed. The use of this expression relaxes the requirement for detailed field calculation in the gap, so that the authors use a single row of elements in this region.

Sample Results

The motor depicted in Fig. 1 is a two-pole 220 V, 50 Hz machine, with a rated output of about 18 W. The production model incorporates magnetic slot wedges, which have been removed for the purpose of this illustration. Removal of the wedges seriously degrades the performance, giving torque/speed characteristics which are susceptible to manufacturing tolerances. This point is illustrated in Fig. 2, which shows measured torque/speed characteristics for two nominally identical machines. The torque/speed characteristics computed using the method described in this paper are also included in Fig. 2, showing agreement with measurement that is very good for this class of machine. Figures 3 and 4

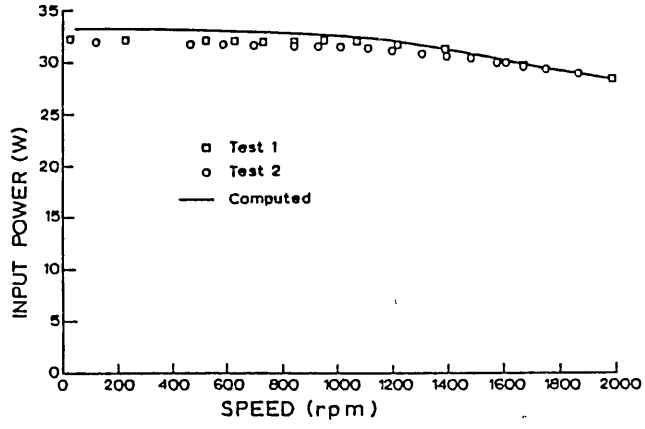


Fig. 3. Comparison between experimentally measured and computed power/speed characteristics.

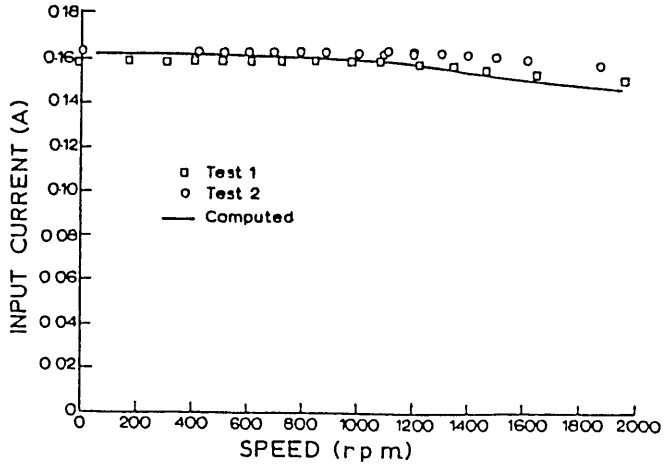


Fig. 4. Comparison between experimentally measured and computed current/speed characteristics.

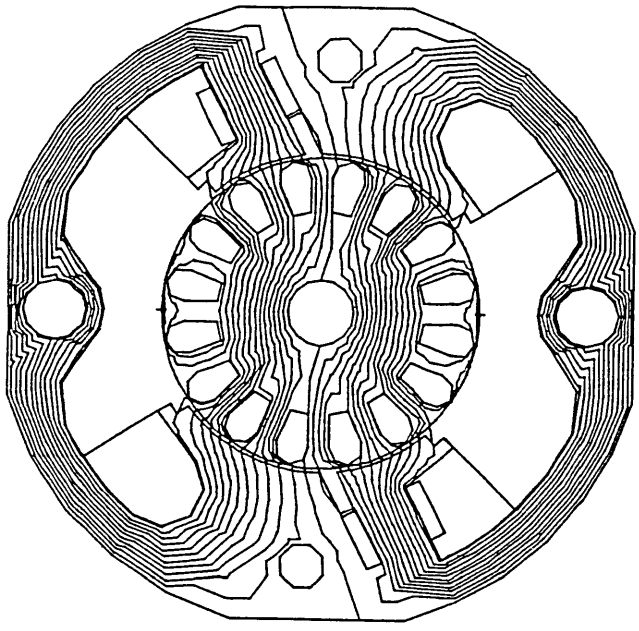


Fig. 5. Typical flux plot for instant of zero supply voltage at 50 rpm.

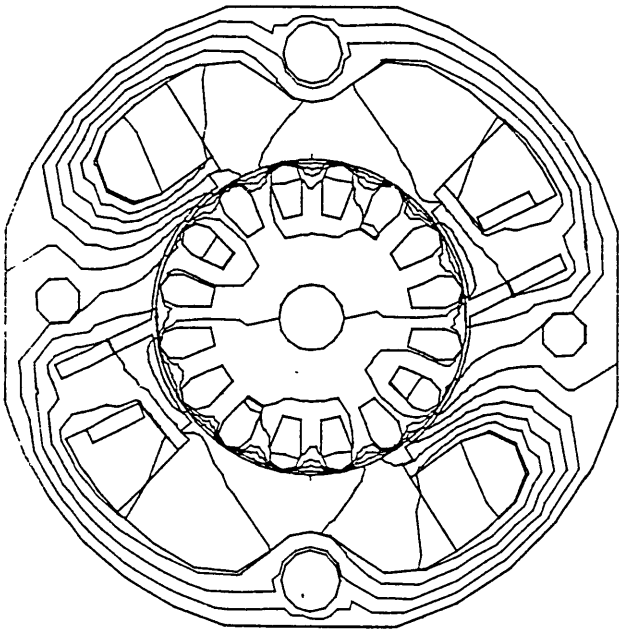


Fig. 6. Typical flux plot for instant of maximum supply voltage at 50 rpm.

give predicted and measured input power and current vs speed characteristics, and show equally good agreement. Typical flux plots are illustrated in Figs. 5 and 6, which show the instants of zero and peak supply voltage, respectively.

The finite-element field solution used for the test-motor employed first-order triangles, with a total of 455 nodes and 855 elements. Advantage was taken of the symmetry of the stator lamination, so that only half of the motor was modelled. The mesh used is illustrated in Fig. 7. Each point on the performance characteristics required a total of 61·6 cp secs on a CDC 855 Cyber.

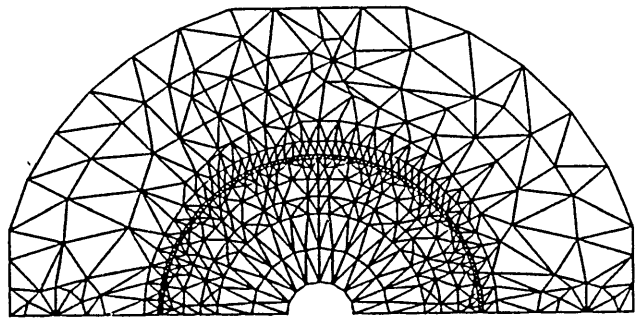


Fig. 7. Mesh used for finite-element field solution.

CONCLUSIONS

The general method of combining circuit and field analyses has been outlined with reference to the performance prediction on a cage motor. The advantages claimed for this method are

(i) The use of magnetostatic conditions means that the field solution is simplified.

(ii) The method may be used in both 2-D and 3-D problems.

(iii) The method automatically enables voltage-forced conditions to be simulated.

(iv) The circuit relationships usually enable the desired terminal quantities (current, power, torque) to be calculated in a simple manner.

REFERENCES

[1] S. Williamson and J.W. Ralph, "Finite-element analysis of an induction motor fed from a constant-voltage source," IEE Proc., Vol.130, Pt.B, No.1, pp.18-24, Jan. 1983.

[2] S. Williamson and M.C. Begg, "Calculation of the bar resistance and leakage reactance of cage rotors with closed slots," IEE Proc., Vol.132, Pt.B, No.3, pp.125-132, May 1985.

Calculation of the bar resistance and leakage reactance of cage rotors with closed slots

S. Williamson, Ph.D., A.C.G.I., D.I.C., C.Eng., M.I.E.E., and M.C. Begg, B.Sc.(Eng.)

Indexing term: *Induction motors*

Abstract: The paper describes a technique for calculating the leakage reactance and resistance per bar of a cage rotor with closed slots. The method is based on the use of a finite-element field calculation which enables the precise slot geometry to be modelled accurately, and includes the effects of tooth saturation and stator magnetomotive force. The method is illustrated by means of two examples, which are also used to provide a comparison with previous work on similar geometries. The method may be used to generate reactance against frequency and current characteristics, for design office use.

Principal symbols

A = magnetic vector potential
b, B = flux density
d = mean diameter of airgap
E = rotor bar induced EMF (RMS)
I = rotor bar current, RMS
j_s, J_s = rotor surface current density
J_0 = average (or direct) current density in rotor bar
N_b = number of rotor bars
p = number of pairs of poles
R_0 = bar resistance at low frequency
S_b = cross-sectional area of rotor bar
t = time
w = effective axial length of rotor
$\bar{Z}_b$ = rotor leakage impedance, per bar
α = rotor slot pitch, mechanical radians
θ = circumferential co-ordinate
ν = reluctivity
σ = conductivity
ω = angular frequency of rotor currents, rad/s
$\bar{}$ denotes complex sinusoidal quantities
$*$ denotes complex conjugate
Re denotes 'real part of'

1 Introduction

Closed rotor slots are found in cage motors with ratings ranging from the very lowest powers up to several tens of kilowatts. The stated reasons for using closed slots are diverse, although the main reasons appear to be mechanical. The closed slot holds the conductor in place, allows accurate machining of the rotor surface, and may ease the problems of diecasting by preventing the molten aluminium from running out. In addition, a smooth rotor surface reduces the flux pulsations caused by rotor slotting, resulting in lower surface losses, and attenuating some components of acoustic noise. In large machines with deep, narrow slots, the bridge permeance may be relatively small when compared with the overall leakage permeance of the slot, but in small machines the aspect ratio of the slots is different, and the bridge permeance may dominate.

Birch and Butler [1] have described a numerical method for calculating bridge permeance as a function of slot current. Their method involves a notional division of the bridge into parallel strips, and an iterative procedure to relate the MMF drop across each strip to the current which flows in the slot. Although Birch and Butler's work was undoubtedly a significant advance on what had gone before, their method still left some scope for improvement. First, the MMF drop in the rotor teeth and core was neglected, all the slot MMF being assumed to be available for driving the flux through the bridge. Secondly, the effect of the stator MMF on the rotor slot bridge saturation was ignored, the stator being modelled as an infinitely permeable smooth block.

The purpose of this paper is to present a general method by which an accurate value of rotor bar resistance and leakage reactance can be obtained, taking magnetic saturation and deep bar effect into account. The work is specifically directed at the calculation of impedances for use in the standard equivalent circuit, excited from a sinusoidal supply. The method described enables the rotor resistance and leakage reactance per bar to be calculated as a function of bar current and rotor frequency, for any shape of rotor bar. This paper is concerned exclusively with rotors having closed slots which are completely filled with conductor. It should be pointed out, however, that the general method described is equally applicable to semi-closed or open slots, which may be completely or partially filled.

2 Theoretical development

2.1 General description and consideration of boundary conditions

To avoid the need to make subjective judgments regarding the extent of the saturated part of the slot bridge, and to represent the rotor in a more realistic manner than previously attempted, the authors have adopted a model which comprises a section of a rotor corresponding to a complete rotor slot pitch. A typical model used for this purpose is illustrated in Fig. 1, in which α is the rotor slot pitch, measured in mechanical radians.

The level of saturation in the rotor depends not only on the rotor MMF, but also on that produced by the stator. These two MMFs are almost equal and opposite, with the relatively small difference between them being sufficient to produce the airgap flux. If the stator MMF were ignored and field calculations made using the rotor currents as the only MMF source, then the tooth fluxes obtained would far exceed those found in practice and the rotor would be heavily saturated. It is necessary, therefore, to specify an appropriate boundary condition along the arc CDE

Paper 3798B (P1), first received 6th August 1984 and in revised form 11th January 1985

The authors are with the Department of Electrical Engineering, Imperial College of Science & Technology, Exhibition Road, London SW7 2BT, United Kingdom

(Fig. 1) to produce an airgap flux that is commensurate with the current flowing in the rotor bars. To this end, the

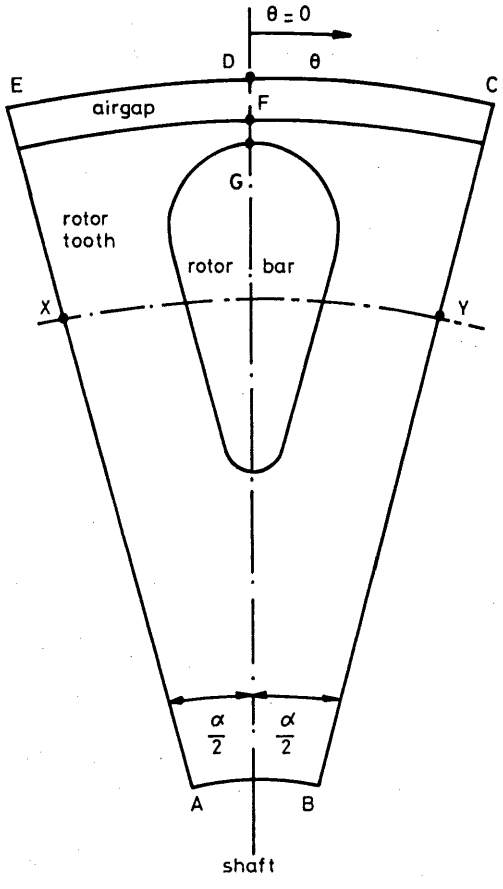


Fig. 1 *Typical rotor tooth-pitch model*

single rotor bar used in the model is regarded as one of N_b bars in a symmetrical rotor cage, which carries a $2p$-pole current wave of RMS magnitude I. If the rotor leakage impedance per bar presented to this assumed current distribution is $\bar{Z}_b$, then the EMF induced in the bar by the airgap flux is given by

$$\bar{E}_b = \bar{I}\bar{Z}_b = \bar{I}(R_b + j\omega L_b) \tag{1}$$

in which R_b and L_b are the effective bar resistance and leakage inductance, respectively.

The $2p$-pole flux density wave rotating in the airgap may be written in the general form

$$b(\theta, t) = \text{Re}\ \{\sqrt{2}\,\bar{B}e^{j(\omega t - p\theta)}\} \tag{2}$$

where the circumferential co-ordinate θ is measured in the rotor reference frame, so that the frequency ω is the rotor frequency. The flux density, $\bar{B}$, is related to the induced bar EMF through the flux-cutting rule

$$\bar{E}_b = \frac{\omega d w}{2p}\bar{B} \tag{3}$$

Combining eqns. 1 and 3,

$$\bar{B} = \frac{2p}{wd\omega}\bar{I}\bar{Z}_b \tag{4}$$

The stator is assumed to produce a sinusoidal MMF wave, which may be represented by a surface current density distribution, which, when viewed from the rotor, is of the form

$$j_s(\theta, t) = \text{Re}\ \{\sqrt{2}\,\bar{J}_s e^{j(\omega t - p\theta)}\} \tag{5}$$

The rotating flux density wave in the airgap may, finally, be related to the combined MMF of rotor and stator, by applying Ampère's law around a closed path which crosses the airgap twice (see, for example, Reference 2):

$$\bar{J}_s + \frac{N_b\bar{I}}{\pi d} = -\frac{2j\mu_0 p}{d}\bar{B} \tag{6}$$

Combining eqns. 6 and 4 we obtain the required equation for $\bar{J}_s$:

$$\bar{J}_s = -\frac{\bar{I}}{\pi d}\left\{N_b + \frac{4j\mu_0 p^2\pi}{dw\omega}\bar{Z}_b\right\} \tag{7}$$

Provided $\bar{Z}_b$ is known, eqns. 5 and 7 enable the appropriate boundary condition to be specified along the boundary CDE in Fig. 1. The problem, however, is that the very object of this paper is to develop a method by which $\bar{Z}_b$ may be determined. For each rotor current, therefore, it is necessary to adopt an iterative approach. $\bar{Z}_b$ is initially estimated by any convenient means, to enable a boundary condition to be specified. The field is then solved and $\bar{Z}_b$ recalculated as described below. This procedure is repeated until satisfactory convergence is achieved. In the practical examples described in Section 3, satisfactory convergence was found to occur in two or three iterations.

The boundary condition imposed along the radial boundaries, AE and BC in Fig. 1, must reflect the fact that the bar modelled is one in a complete cage which carries a $2p$-pole current distribution. This is accomplished by using a periodicity condition along these boundaries. The magnetic vector potentials at the two similar boundary points X and Y are related by the equation

$$\bar{A}_Y = \bar{A}_X e^{-j\alpha p} \tag{8}$$

The boundary AB corresponds to the rotor shaft, which is assumed to be impermeable to flux. AB, therefore, becomes a flux line, which is specified as $\bar{A}$ = constant.

2.2 Finite-element field solution

The governing differential equation for two-dimensional skin-effect problems was shown by Konrad [3] to be of the form

$$\frac{\partial}{\partial x}\left(\nu\frac{\partial\bar{A}}{\partial x}\right) + \frac{\partial}{\partial y}\left(\nu\frac{\partial\bar{A}}{\partial y}\right) = -\bar{J}_0 + j\omega\sigma(\bar{A} - \bar{A}_0) \tag{9}$$

For the deep-bar problem being studied in this paper, the right-hand side of eqn. 9 is non-zero only over the bar cross-sectional area. $\bar{J}_0$ is the uniform current density that would be obtained if the bar carried the same RMS current $\bar{I}$, at a frequency low enough for skin effect to be negligible, i.e.

$$\bar{J}_0 = \frac{\bar{I}}{S_b} \tag{10}$$

where S_b is the cross-sectional area of the bar. $\bar{J}_0$ is the field source term. The remaining term on the right-hand side of eqn. 9 represents the modification to the uniform current density, due to skin effect. $\bar{A}_0$ is the average value of magnetic vector potential over the bar area

$$\bar{A}_0 = \frac{1}{S_b}\int_{S_b}\bar{A}\,dS \tag{11}$$

Eqn. 9 may conveniently be solved by the finite-element method. The general form of the first-order elemental equation, derived from eqn. 9 using standard techniques, may be written

$$\{\nu[S] + j\omega\sigma[C]\}\{\bar{A}\} = \{\bar{J}\} \tag{12}$$

The elements of the real matrixes $[S]$ and $[C]$, and of the complex vectors $\bar{A}$ and $\bar{J}$, are listed in Reference 4. If the elemental equations, such as eqn. 12, are assembled to form the global set of equations describing the whole-field solution, then that set of equations takes on the usual form, i.e.

$$KA = J \tag{13}$$

To allow for magnetic saturation, eqn. 13 must be solved in a nonlinear sense, i.e. with the reluctivities of the iron elements varying with flux density in accordance with some form of magnetisation characteristic. In fact, it has been implicitly assumed in eqns. 9 to 13 that all magnetic field quantities (including MMF) vary sinusoidally in time, whereas magnetic saturation prevents this from being possible. It will be recalled, however, that the objective of this work is to determine reactances and resistances for use in equivalent circuits for sinusoidally excited machines. It is appropriate, therefore, to use reluctivity values which relate the fundamental-frequency component of magnetic field strength to the local magnitude of the assumed sinusoidally time-varying flux density. Suitable values may be derived from standard DC magnetisation characteristics for the laminated iron, by determining the H against time variation (in much the same way that magnetising current may be determined in single-phase transformers) and then calculating the magnitude of the fundamental component of H by the use of Fourier analysis. A less accurate, but somewhat simpler, method was chosen by the authors, based on the use of AC magnetisation characteristics. Such characteristics give the specific apparent power as a function of the peak of the sinusoidal flux density [4]. They may, therefore, be used to obtain the RMS value of H as a function of the RMS value of (sinusoidal) B. The ratio of these two quantities gives a suitable value of reluctivity for use in eqn. 12. In fact the reluctivity so obtained is somewhat larger than that required, but provided that the combined RMS of the harmonic components of H is less than 46% of the RMS fundamental component, then the error in ν will be less than 10%.

A suitable Newton–Raphson algorithm for solving eqn. 13 in the nonlinear sense has been described by Ralph and Williamson [5]. Their method requires the resolution of the field equations into real and imaginary components which are coupled together only through the gradient or tangent matrix. In this present study, the situation is further complicated by the use of periodicity boundary conditions (along AE and BC in Fig. 1) which produce a general phase shift rather than equality or negative equality. Such a condition produces additional coupling between the real and imaginary parts of the solution, and results in a set of system equations with an asymmetrical coefficient matrix.

Having solved for the field with both stator and rotor MMF sources present, it is necessary to distinguish between stator-driven and rotor-driven fluxes, so that the rotor bar leakage reactance may be calculated. This is most conveniently done by resolving eqn. 13 in a linear sense, with the rotor bar current as the only MMF source, and with the reluctivity of each iron element in the model set as the values determined during the nonlinear solution. For this purpose the stator is regarded as infinitely permeable, so that a homogeneous Neumann boundary condition is now specified along the arc CDE in Fig. 1. In effect, the nonlinear solution is used to set the elemental reluctivities to the appropriate value, and the linear solution to determine the rotor-driven flux. A similar method has been used by Williamson and Ralph [6] to distinguish between unskewed stator fields and skewed rotor fields in induction motor analysis.

2.3 Calculation of the rotor leakage impedance per bar $\bar{Z}_b$

The leakage impedance per bar has resistive and reactive components which may be determined from the finite-element field solution.

2.3.1 Bar resistance, R_b : The complex current density in the rotor bar is given by

$$\bar{J} = \bar{J}_0 - j\omega\sigma(\bar{A} - \bar{A}_0) \tag{14}$$

The Joule loss per unit length is

$$W = \int_{S_b} \frac{|\bar{J}|^2}{\sigma}\, dS \tag{15}$$

Substituting from eqn. 14 in eqn. 15, and simplifying, we obtain

$$W = |\bar{J}_0|^2 \frac{S_b}{\sigma} - \omega^2\sigma|\bar{A}_0|^2 S_b + \omega^2\sigma \int_{S_b} |\bar{A}|^2\, dS \tag{16}$$

This must equal I^2R_b, from which

$$R_b = R_0\left\{1 - \left[\frac{\omega}{IR_0}\right]^2\left(|\bar{A}_0|^2 - \frac{1}{S_b}\int_{S_b}|\bar{A}|^2\, dS\right)\right\} \tag{17}$$

R_0 is the resistance per bar at low frequencies. The integral contained within eqn. 17 is evaluated using a summation over the bar elements,

$$\int_{S_b} |\bar{A}|^2\, dS = \frac{1}{6}\sum_e \Delta_e \,\mathrm{Re}\left\{\sum_{i=1}^{3}\sum_{j=1}^{3} \bar{A}_{ie}\bar{A}^*_{je}\right\} \tag{18}$$

where Δ_e is the area of the eth bar element. For use in eqn. 7 the bar resistance calculated in accordance with eqn. 17 should be augmented by the effective end-ring resistance, in the usual manner [7].

2.3.2 Bar leakage inductance: For the calculation of bar leakage reactance, it is convenient to partition the leakage flux into separate components, as in traditional calculation methods. The advantage of this approach is that the components of leakage flux are affected differently by the various geometrical factors relating to rotor design.

(*a*) *Slot leakage inductance L_{slot}:* This is due to all the rotor-driven flux that crosses the slot. It may be evaluated by calculating the energy stored in the slot and equating it to the energy stored in an equivalent inductance.

$$L_{slot} = \frac{w}{\mu_0 I^2}\int_{S_b} |\bar{B}|^2\, dS \tag{19}$$

which in finite-element terms becomes

$$L_{slot} = \frac{w}{\mu_0 I^2}\sum_e \Delta_e \,\mathrm{Re}\,\{(\bar{A})_e^T(\bar{S})_e(\bar{A})^*\} \tag{20}$$

(*b*) *Bridge leakage inductance L_{bridge}:* This is due to all the rotor-driven flux that passes over the top of the slot, through the closed slot bridge. It is evaluated from the flux that passes between F and G (Fig. 1):

$$L_{bridge} = \frac{w}{I}\,\mathrm{Re}\,\{\bar{A}_F - \bar{A}_G\} \tag{21}$$

(*c*) *Air-gap leakage inductance L_{gap}:* This is due to all the rotor-driven flux that passes over the top of the slot,

through the airgap. It is evaluated from the flux that passes between D and F (Fig. 1):

$$L_{gap} = \frac{w}{I} \text{ Re } \{\bar{A}_D - \bar{A}_F\} \quad (22)$$

The calculation of these three inductance components is one of the main objectives of this paper, and their sum is referred to below as the 'combined' leakage inductance L_c:

$$L_c = L_{slot} + L_{bridge} + L_{gap} \quad (23)$$

The bar leakage inductance L_b which is required for the calculation of $\bar{Z}_b$ for use in eqn. 7 also includes two components which are not derivable from the field plots. The largest of these is the differential leakage inductance, which on a per-bar basis is given by [8]

$$L_{diff} = \frac{\pi d \mu_0 w}{4gN_b} \left\{ \text{cosec}^2 \left(\frac{p\pi}{N_b}\right) - \left(\frac{N_b}{p\pi}\right)^2 \right\} \quad (24)$$

The second component not included in L_c is the end-ring leakage reactance. This component, however, is usually much smaller than the rest and may be neglected. With this assumption, therefore,

$$L_b = L_c + L_{diff} \quad (25)$$

3 Examples

The accuracy with which the rotor bar resistance and leakage reactance presented to a sinusoidal current distribution may be calculated is difficult, if not impossible, to verify experimentally, and so alternative means must be found if the validity of the method described in Section 2 is to be established. To this end the authors present two examples of impedance calculations for commonly-employed bar geometries. The relationship between the results and those calculated using certain analytical expressions that are found in the literature is discussed.

3.1 Round rotor bars

Round bars with closed slots are used in the rotors of small single-phase and three-phase motors. Fig. 2A defines the geometric variables referred to in this Section, and Fig. 2B illustrates the triangular mesh used in the field analysis.

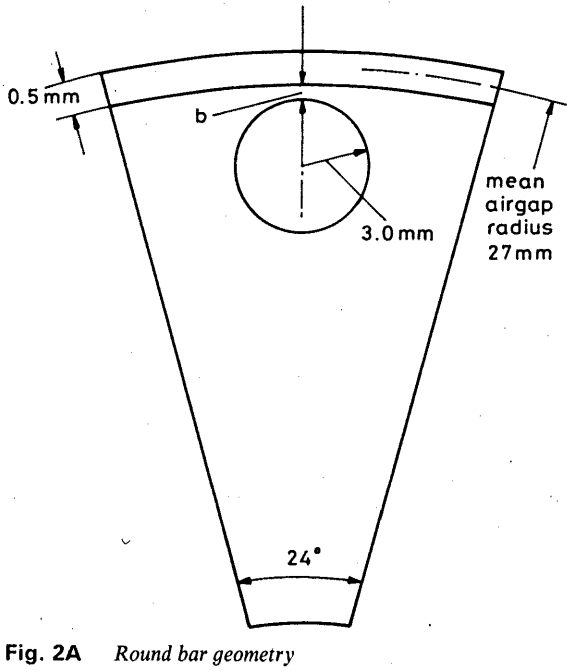


Fig. 2A *Round bar geometry*

Fig. 3 shows the computed variations of the combined leakage inductance with mean bar current density J_0 for

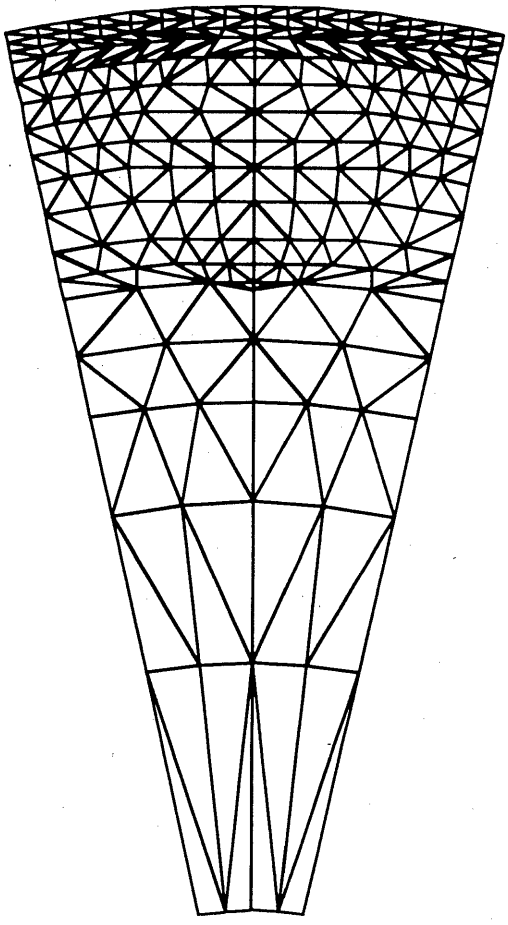


Fig. 2B *Round bar mesh*

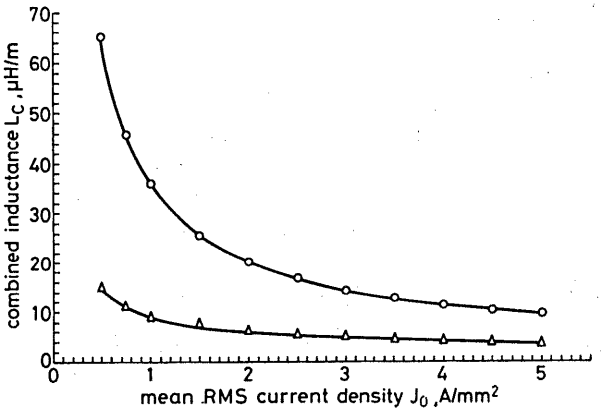


Fig. 3 *Variation of combined leakage inductance with mean current density for round bar of Fig. 2B*

$f = 50$ Hz
○ $b = 0.5$ mm
△ $b = 0.1$ mm

bridge depths b of 0.1 mm and 0.5 mm. J_0 is used as the independent variable in Fig. 3 and elsewhere in preference to the RMS bar current, i.e. $J_0 S_b$, because it is thought that this parameter gives a clearer indication of the range of currents likely to be encountered in a well designed machine. The effects of magnetic saturation are clearly evident, with inductance falling as the bar current increases. To investigate this phenomenon further, the three constituent components are given separately in Table 1. Inspection of Table 1 shows that, although the bridge leakage inductance dominates, and is the most susceptible to magnetic saturation, the other components of leakage

Table 1: Variation of leakage inductance components with mean current density and slot bridge depth for the round bar: $f = 50$ Hz

Leakage inductance component, μH/m		Mean current density J_0, A/mm^2		
		0.5	2.5	5.0
L_{slot}	$b = 0.5$ mm	1.07	0.88	0.77
	$b = 0.1$ mm	1.29	1.29	1.07
L_{gap}	$b = 0.5$ mm	0.30	0.23	0.17
	$b = 0.1$ mm	0.55	0.55	0.47
L_{bridge}	$b = 0.5$ mm	63.73	15.59	8.65
	$b = 0.1$ mm	13.08	3.57	2.16
L_c	$b = 0.5$ mm	65.09	16.70	9.58
	$b = 0.1$ mm	14.70	5.41	3.71

inductance also fall as the current increases. This is thought to be due to the saturation of the main flux paths. For example, with a 0.5 mm slot bridge, the bar impedance (which is reactance dominated) falls by 85% when J_0 is increased from 0.5 to 5.0 A/mm^2. The impedance drop in the bar, however, has increased by at least 47%, with a corresponding increase in the airgap and tooth flux.

Changes in rotor frequency were found to have little effect on the bridge and airgap components of leakage inductance, whereas the slot component was affected in the manner illustrated in Fig. 4. This Figure shows relatively

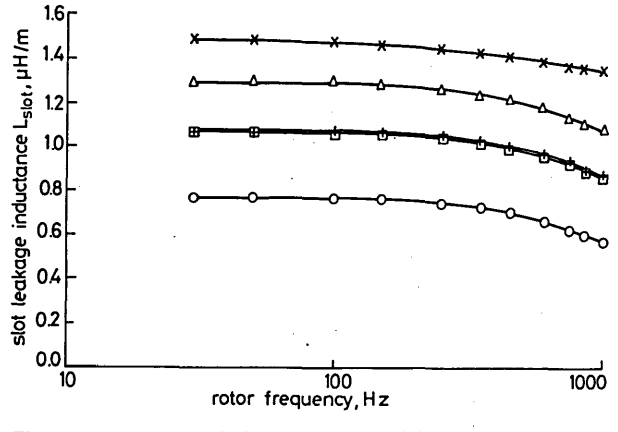


Fig. 4 *Variation of slot component of leakage inductance with frequency, for round bar of Fig. 2A*

× Approximate method
△ $b = 0.1$ mm, $J_0 = 0.5$ A/mm^2
\+ $b = 0.1$ mm, $J_0 = 5.0$ A/mm^2
□ $b = 0.5$ mm, $J_0 = 0.5$ A/mm^2
○ $b = 0.5$ mm, $J_0 = 5.0$ A/mm^2

small changes in what is itself a small component of the leakage inductance. The characteristics of Fig. 4 clearly indicate the influence of saturation on what is normally held to be a nonsaturable component of leakage inductance. Increasing the bar current at constant bridge depth is seen to produce a reduction in slot leakage inductance, due to the increased saturation of the surrounding iron paths. Similarly, when the bar current is kept constant but the bridge depth is increased, the tooth saturation is also increased, and the slot leakage inductance falls. This figure also provides a convenient means of relating the present work to that which has gone before. Analytical expressions for the impedance of circular bars in semiclosed slots have been published by a number of authors [9–11]. Whereas these authors assumed the surrounding iron to be infinitely permeable and presented results which are valid only for semiclosed slots, their formulas included a $\sin\theta/\theta$ term, where 2θ is the angle subtended at the bar centre by the slot opening. Setting $\sin\theta/\theta = 1$ therefore produces a result which, although not strictly valid, should give a reasonable approximation to the unsaturated slot inductance with a closed slot. The variation of slot inductance with frequency, obtained in this way, is also included in Fig. 4.

The relationship between this unsaturated characteristic and those calculated by the method proposed in this paper is as one would expect; i.e. the unsaturated inductances are of similar magnitude but larger than their saturated counterparts. The correspondence between these characteristics is thought to be evidence of the validity of the proposed method.

Fig. 5 shows the calculated variation of bar resistance

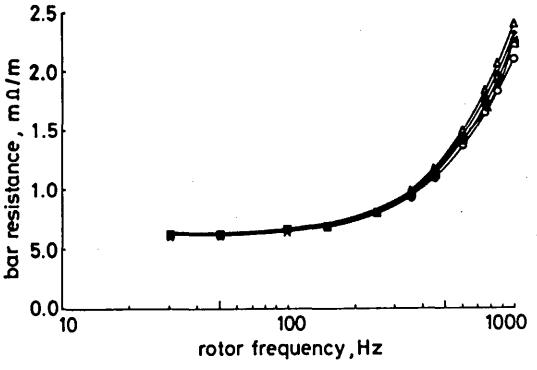


Fig. 5 *Variation of bar resistance with frequency, for round bar of Fig. 2A*

For key to symbols see Fig. 4

with frequency, for slot bridge depths of 0.5 and 0.1 mm, and mean current densities of 0.5 and 5.0 A/mm^2, together with the variation calculated using the approximate method described above. The results show that magnetic saturation has relatively little effect on the bar resistance, suggesting that the current flow paths are unchanged and that variations in inductance present in Fig. 4 are produced chiefly by changes in the flux paths. Fig. 5 also includes the calculated variation of resistance with frequency using the approximate method referred to above. The method

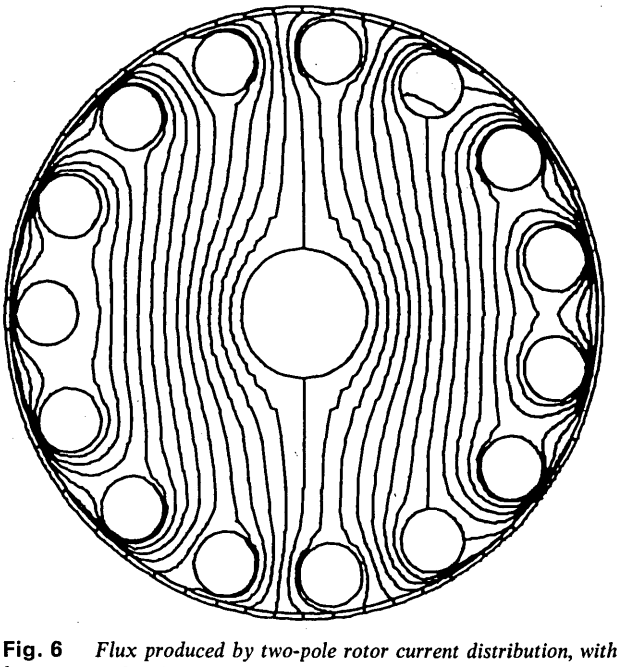


Fig. 6 *Flux produced by two-pole rotor current distribution, with RMS bar current of 14.1 A*

Interval between flux lines = 0.30 mWb/m

described in this paper, and the approximate method, produce closely similar results over the frequency range of principal interest to the induction motor analyst.

Although the finite-element method described in Section 2 uses a single slot-pitch model, it will be appreciated that the imposition of periodicity boundary conditions along the radial boundaries means that the whole rotor is implicitly modelled. The complete rotor flux pattern may be recovered by using appropriate phase shifts on the single slot solution. As an example, Fig. 6 illustrates the field due to the rotor currents only for a two-pole 50 Hz excitation with an RMS bar current of 14.1 A. Fig. 7 illustrates that a similar field pattern is produced when

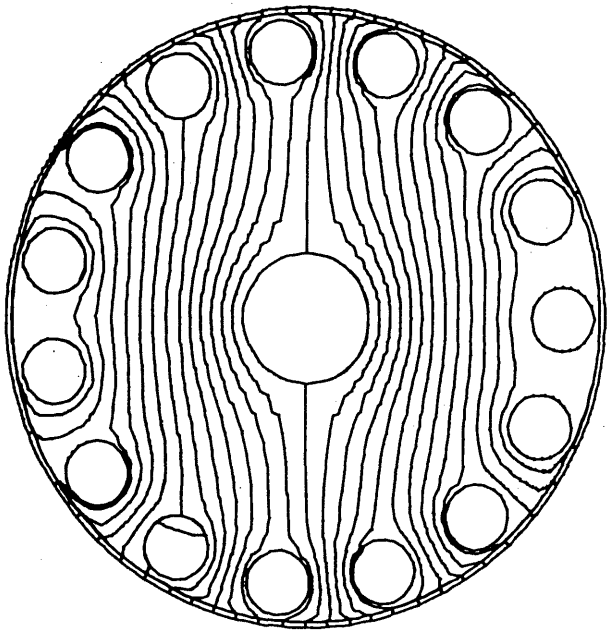


Fig. 7 *Flux produced by two-pole rotor current distribution, with RMS bar current of 141 A*
Interval between flux lines = 2.30 mWb/m

the RMS bar current is increased to 141 A, with the exception that the bridge leakage flux is no longer in evidence. This may be explained by reference to the interval between adjacent flux lines, which is 0.30 mWb/m in Fig. 6, and 2.20 mWb/m in Fig. 7. Increasing the bar current by a factor of ten has produced relatively little change in the bridge leakage flux, which is now a smaller proportion of the total flux produced by the rotor currents. The difference between Figs. 6 and 7 is therefore a clear indication of increasing slot bridge saturation.

3.2 Parallel-sided bars with rounded ends

Fig. 8A defines the geometry of a parallel-sided bar that is used in the three-phase machines by at least one leading British manufacturer. Fig. 8B shows the mesh used in the finite-element analysis, with Fig. 8C being a detail of the mesh close to the slot bridge.

Fig. 9 shows the variation of the combined leakage inductance with current for slot bridge depths b of 0.1 and 0.5 mm. As before, the effects of magnetic saturation are clearly evident. Table 2 gives the individual components of leakage inductance, showing that the bridge inductance is much more saturated than it was in the case of the round bar. This may be accounted for by comparing the cross-sectional areas of the two bars. The parallel-sided bar has almost five times the cross-sectional area of the round bar, so that, for a given mean current density, the MMF available for driving flux through the bridge is increased by that factor. With a 0.1 mm thick slot bridge, the bridge leakage inductance is seen to be less than the slot leakage inductance. Table 2 also shows that the slot component appears

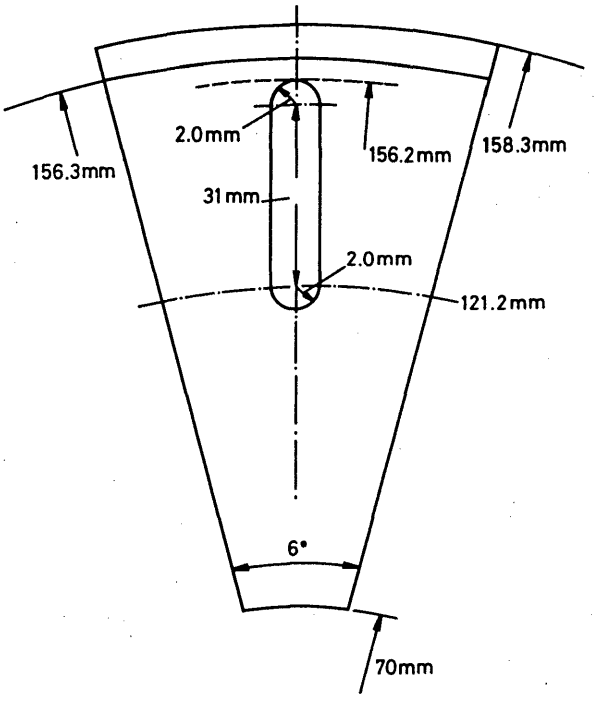


Fig. 8A *Parallel-sided bar geometry*

to increase at higher current levels for both thicknesses of slot bridge. Closer examination of this phenomenon showed that the teeth had become so saturated that the MMF drop down the teeth was sufficient to make the flux taking the parallel radial path down the slot a non-

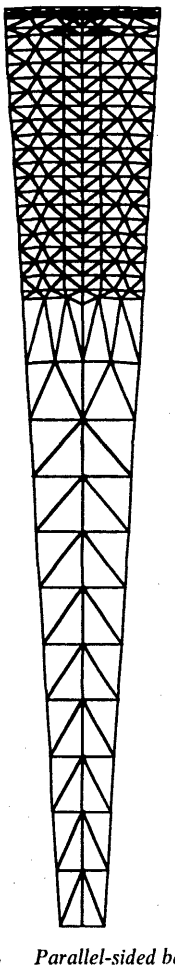


Fig. 8B *Parallel-sided bar mesh*

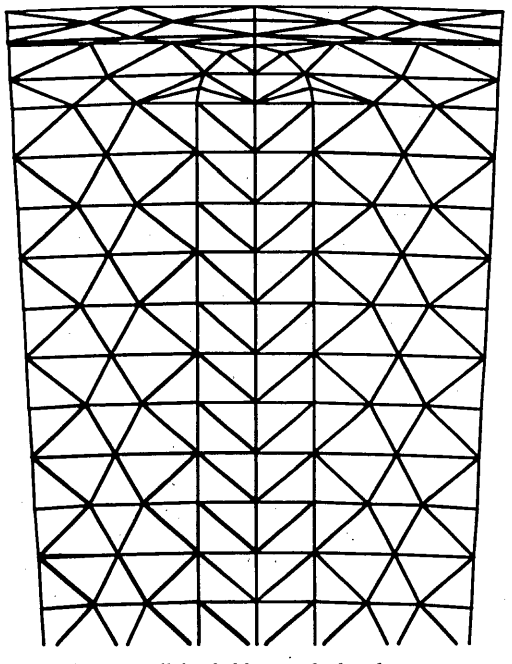


Fig. 8C *Parallel-sided bar mesh, detail*

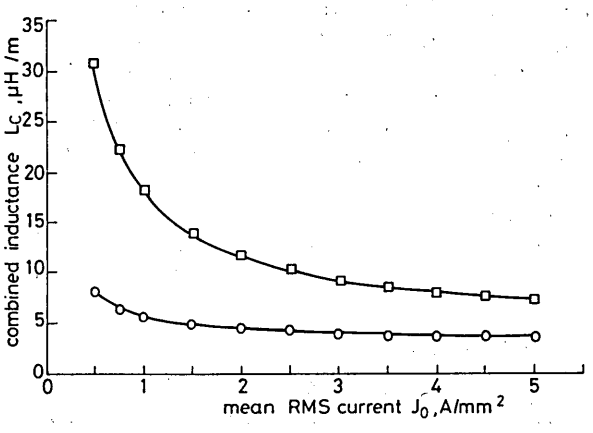


Fig. 9 *Variation of combined leakage inductance with mean current density for parallel-sided bar with round ends*

$f = 50$ Hz
□ $b = 0.5$ mm
○ $b = 0.1$ mm

negligible quantity. This radial slot flux is included in the slot leakage inductance calculation, as defined by eqn. 19.

Fig. 10 gives the variation with frequency of the combined leakage inductance, together with its constituent components. This Figure shows that, because the slot leakage inductance is, in this instance, a large proportion

Table 2: Variation of leakage inductance components with mean current density and slot bridge depth for a parallel-sided slot with rounded ends

Leakage inductance component, μH/m		Mean current density J_0, A/mm²		
		0.5	2.5	5.0
L_{slot}	$b = 0.5$ mm	2.17	1.91	2.00
	$b = 0.1$ mm	2.21	2.18	2.30
L_{gap}	$b = 0.5$ mm	0.18	0.16	0.14
	$b = 0.1$ mm	0.18	0.18	0.17
L_{bridge}	$b = 0.5$ mm	28.15	8.05	5.10
	$b = 0.1$ mm	5.66	1.72	1.14
L_c	$b = 0.5$ mm	30.50	10.12	7.24
	$b = 0.1$ mm	8.05	4.09	3.61

of the whole, the combined inductance is now strongly frequency dependent.

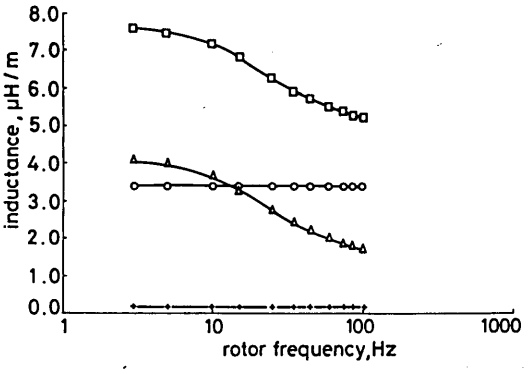


Fig. 10 *Variation of bar leakage inductance, and its constituent components, with frequency*

Parallel-sided bar with round ends $J_0 = 2.5$ A/mm², $b = 0.1$ mm
□ L_c
○ L_{bridge}
△ L_{slot}
+ L_{gap}

As for the round bar, the slot leakage inductance calculation affords some means of comparison with previous work on a similar, though not identical, geometry.

The analysis of deep bar effect in a parallel-sided bar which fills an open slot has been carried out by Alger [7]. The expressions he derives for effective bar resistance and leakage reactance are

$$R_b = R_0 \frac{\xi}{2}\left[\frac{\sinh \xi + \sin \xi}{\cosh \xi - \cos \xi}\right] \tag{26}$$

$$L_{slot} = L_0 \frac{3}{\xi}\left[\frac{\sinh \xi - \sin \xi}{\cosh \xi - \cos \xi}\right] \tag{27}$$

where R_0 and L_0 are the low-frequency values of R_b and L_{slot}, respectively, and

$$\xi = 2d\sqrt{\frac{\omega \mu_0 \sigma}{2}}$$

d is the bar depth, and σ its conductivity.

Fig. 11 compares the frequency dependence of the slot

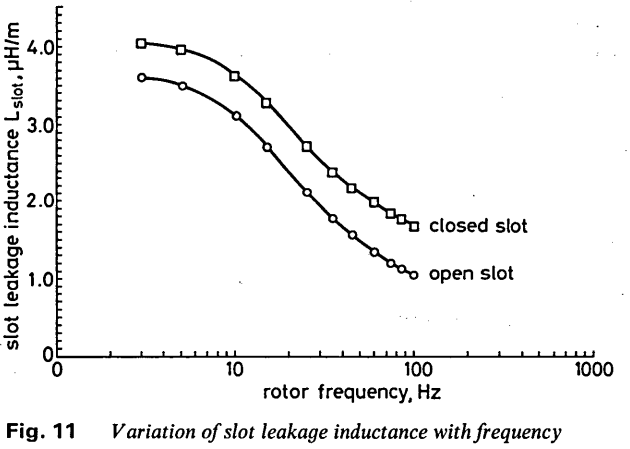


Fig. 11 *Variation of slot leakage inductance with frequency*

Parallel-sided bar with round ends and with open ends $J_0 = 2.5$ A/mm², $b = 0.1$ mm

component of leakage inductance calculated using the method described in this paper with that calculated using eqn. 27. As before, the agreement is thought to be surprisingly good, in view of the vastly different boundary conditions at the top of the open and the closed slots. It will be appreciated, in this respect, that the flux at the top of the slot links all the current at all frequencies, and there-

fore makes a significant contribution to the inductance. Fig. 12 similarly compares the bar resistance calculated by

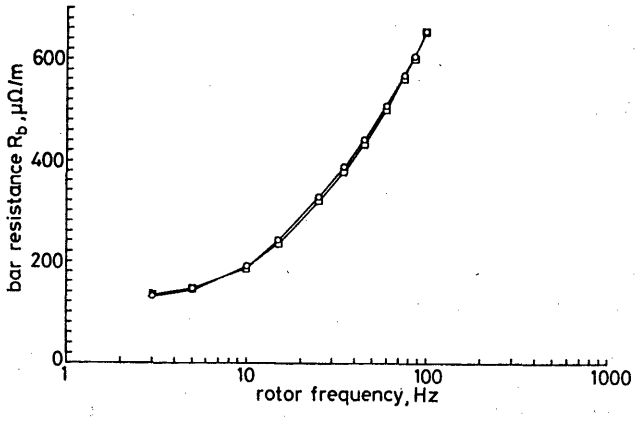


Fig. 12 *Variation of bar resistance with frequency*
Parallel-sided bar with round ends and with open ends $J_0 = 2.5$ A/mm², $b = 0.1$ mm
For key to symbols see Fig. 11

the two methods showing that the open-slot approximation gives excellent agreement with the more detailed finite element approach. To investigate this further, the variation with distance along the slot of the magnitude and phase of the bar current density were computed using both methods. The results are given in Figs. 13 and 14, which

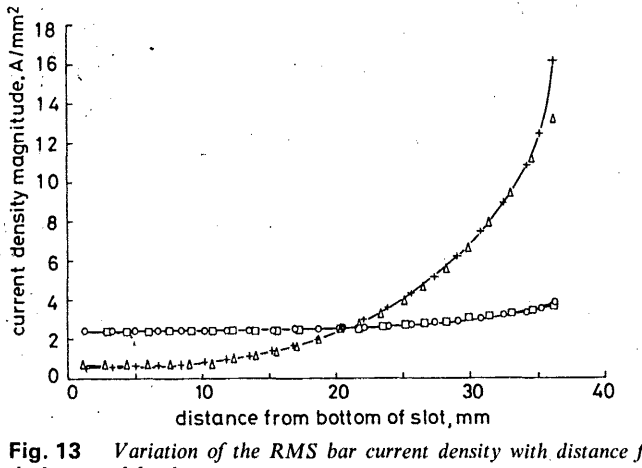


Fig. 13 *Variation of the RMS bar current density with distance from the bottom of the slot*
Parallel-sided bar with round ends and with open ends $J_0 = 2.5$ A/mm², $b = 0.1$ mm

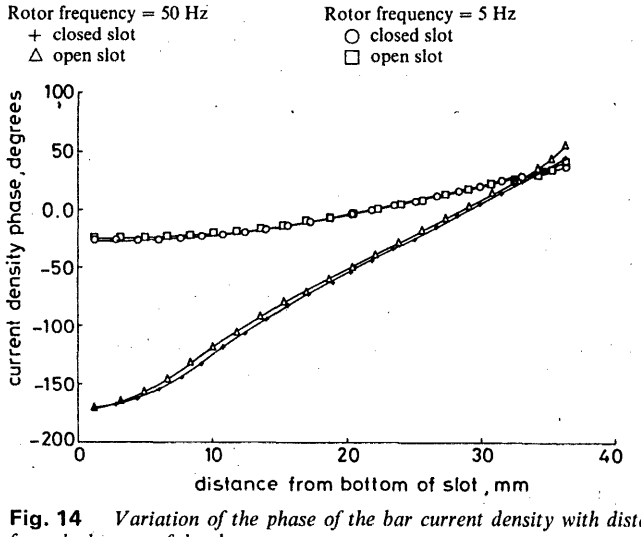


Fig. 14 *Variation of the phase of the bar current density with distance from the bottom of the slot*
Parallel-sided bar with round ends and with open ends $J_0 = 2.5$ A/mm², $b = 0.1$ mm
For key to symbols see Fig. 13

show that the current distributions are sensibly identical, with slight differences being produced at the slot top.

3.3 Computing time

The characteristics presented in this paper were obtained using a CDC 6600 machine, housed at Imperial College. The larger of the two meshes, that of the long slot (Fig. 8B), comprises 230 nodes and 382 elements. The number of complex potentials to be determined at each solution point was 189, corresponding to 378 real variables. This size of problem can be accommodated with ease on a medium-sized minicomputer. For this mesh, the time taken to obtain the first point on an impedance against frequency or impedance against current characteristic was typically 10.5 s, assuming that no previous solution was available, so that the iron reluctivities were all initialised to the same high value. After a first solution had been obtained, the calculated reluctivities could be used as a starting estimate for the field solution for the next point on the characteristic, so that the time taken for subsequent points fell to approximately 2.5 s.

4 Conclusions

This paper has described a method for calculating the leakage impedances of cage rotors with closed slots, taking into account magnetic saturation in the rotor iron and skin effect in the bars. The method is quite general, being capable of modelling any shape of bar placed in any shape of slot. Although the paper has concentrated on closed slots, the same technique may be applied to semiclosed and open slots.

The method may be used for the calculation of impedance variation curves for design-office use, or as part of a larger strategy for detailed machine analysis using finite elements.

5 Acknowledgment

The authors gratefully acknowledge the useful discussion held with Mr. K.F. Raby concerning the appropriate boundary condition to be placed at the stator surface.

6 References

1 BIRCH, T.S., and BUTLER, O.I.: 'Permeance of closed-slot bridges and its effect on induction-motor-current computation', *Proc. IEE*, 1971, **118**, (1), pp. 169–172
2 WILLIAMSON, S.: 'Power-factor improvement in cage-rotor induction motors', *IEE Proc. B, Electr. Power Appl.*, 1983, **130**, (2), pp. 121–129
3 KONRAD, A.: 'The numerical solution of steady-state skin-effect problems—an integrodifferential approach', *IEEE Trans.*, 1981, **MAG-17**, (1), pp. 1148–1152
4 British Standards: BS601:1973 'Specification for steel sheet and strip for magnetic circuits of electrical apparatus. Part 5. Methods of test', British Standards Institution, 2 Park Street, London W1A 2BS
5 RALPH, J.W., and WILLIAMSON, S.: 'Solution of two-dimensional nonlinear field problems with sinusoidal excitation sources using first-order finite elements', *IEEE Trans.*, 1983, **MAG-19**, pp. 2433–2436
6 WILLIAMSON, S., and RALPH, J.W.: 'Finite-element analysis of an induction motor fed from a constant-voltage source', *IEE Proc. B, Electr. Power Appl.*, 1983, **130**, (1), pp. 18–24
7 ALGER, P.L.: 'Induction machines' (Gordon and Breach, New York, 1970)
8 WILLIAMSON, S., and SMITH, A.C.: 'Field analysis for rotating induction machines and its relationship to the equivalent-circuit method', *IEE Proc. B, Electr. Power Appl.*, 1980, **127**, pp. 83–90
9 SWANN, S.A., and SALMON, J.W.: 'Effective resistance and reactance of a solid cylindrical conductor embedded in a semi-closed slot', *Proc. IEE*, 1962, **109C**, pp. 611–615
10 ANNELL, H.: 'The alternating current impedance of a solid conductor of circular cross-section placed in a semi-closed circular slot', *Trans. R. Inst. Tech.*, 1963, **200**, pp. 1–33
11 EL-MARKABI, M.H.S., and FREEMAN, E.M.: 'Normalised impedance of circular, trapezoidal and rectangular conductors in semiclosed slots: a unified transmission line approach', *IEE Proc. A*, 1984, **131**, (3), pp. 129–139